

THE STRUCTURE OF THE MAGNETOSPHERE AS DEDUCED FROM
MAGNETOSPHERICALLY REFLECTED WHISTLERS

A DISSERTATION
SUBMITTED TO THE DEPARTMENT OF ELECTRICAL ENGINEERING
AND THE COMMITTEE ON GRADUATE STUDIES
OF STANFORD UNIVERSITY
IN PARTIAL FULFILLMENT OF THE REQUIREMENTS
FOR THE DEGREE OF
DOCTOR OF PHILOSOPHY

By
Bruce Charles Edgar

March 1972

I certify that I have read this thesis and that in my opinion it is fully adequate, in scope and quality, as a dissertation for the degree of Doctor of Philosophy.

RA Helliwell

(Principal Adviser)

I certify that I have read this thesis and that in my opinion it is fully adequate, in scope and quality, as a dissertation for the degree of Doctor of Philosophy.

Joseph W. J. Rogers

I certify that I have read this thesis and that in my opinion it is fully adequate, in scope and quality, as a dissertation for the degree of Doctor of Philosophy.

Stephen E. Davis

Approved for the University Committee
on Graduate Studies:

Lincoln E. Moore

Dean of Graduate Studies

ABSTRACT

This dissertation investigates and interprets a very low frequency (VLF) electromagnetic wave phenomenon called the magnetospherically reflected (MR) whistler. This study utilizes VLF (0.3 to 12.5 kHz) data obtained from the Orbiting Geophysical Observatories (OGO) 1 and 3 from October 1964 to December 1966. MR whistlers are produced by the dispersive propagation of energy from atmospheric lightning through the magnetosphere to the satellite along ray paths which undergo one or more reflections due to the presence of ions.

The gross features of MR whistler frequency-time spectrograms are explained in terms of propagation through a magnetosphere composed of thermal ions and electrons and having small density gradients across L-shells. Irregularities observed in MR spectra are interpreted in terms of propagation through field-aligned density structures. Trough and enhancement density structures were found to produce unique and easily recognizable signatures in MR spectra. Sharp cross-field density drop-off produces extra traces in MR spectrograms.

The absence of the MR whistlers above $L \sim 2.4 - 2.6$ for periods of up to 12 days after severe magnetic storms is explained in terms of trapping of whistler rays by pronounced cross-field density dropoffs, typically at $L \sim 1.8$ and $L \sim 2.4$. Field-aligned density structures (troughs, enhancements, and dropoffs) between $L \sim 1.8$ and $L \sim 3$ deduced from MR spectra observed after this period are thought to be the vestiges of structures originally created by the magnetic storm. Such structures on some occasions persist for several weeks during quiet periods after magnetic storms and show strong longitude dependence.

The upper frequency cutoffs observed on MR whistler components are explained in terms of trapping of the frequency components above the cutoff by cross-field dropoffs. The lower frequency cutoffs are interpreted in terms of D-region absorption and defocusing of the MR whistler energy. The enhanced amplitudes observed on the upper frequency portions are explained in terms of a minimal defocusing of MR whistler rays, without invoking hot-plasma effects.

ACKNOWLEDGMENTS

The author wishes to thank Dr. R. A. Helliwell for his guidance and helpful discussions during the course of the research. The author is indebted to Dr. R. L. Smith for his assistance in ray tracing calculations and to Dr. J. J. Angerami for his advice in interpreting the data and close supervision during the writing of this dissertation. The assistance of Mr. John Katsufakis in supplying the experimental data and Mr. Jerry Yarbrough in the data reduction are gratefully acknowledged. Finally, the author wishes to thank his wife, Nancy, for her constant support and encouragement during the years of research and writing.

This research was supported by the National Aeronautics and Space Administration under Contract NAS 5-2131, Grant NGR 05-020-288 and Grant NgL 05-020-008. Computer facilities made available in part by the National Science Foundation Office of Computer Sciences under Grant NSF GP-948.

CONTENTS

	<u>Page</u>
I. INTRODUCTION	1
A. Purpose	1
B. The Structure of the Magnetosphere	1
C. Measurement of Magnetospheric Densities	3
D. The Whistler Method of Studying Magnetospheric Densities	6
E. Ground Observations of Whistlers	6
F. Satellite Observations	7
G. The Magnetospherically Reflected Whistler	10
H. Nonducted Whistler Ray Paths	10
I. Effect of Ions on Whistler Ray Paths	13
J. Organization Plan	17
K. Contributions of the Present Investigation	17
II. MR WHISTLER PROPAGATION IN A SMOOTH MAGNETOSPHERE	19
A. Introduction	19
B. Spacing Patterns in MR Whistler Components	19
C. The Reflection Process	25
D. Formation of the MR Nose Frequency	33
E. Density Models	37
F. Ray Tracing Calculations	39
G. Nighttime Models	46
H. Upper and Lower Frequency Cutoffs	46
I. Conclusions	50
III. EFFECTS OF SHARP IRREGULARITIES	53
A. Introduction	53
B. Models	53
C. Theoretical Basis for Other Types of Irregularities	57
D. Comparison with Other Models	61
E. Detection of Ducts by MR Whistlers	65
F. Detection of Ducts and Dropoffs	67
G. Effects of a Field-Aligned Trough on MR Whistlers	70
H. Summary	72

CONTENTS (Cont)

	<u>Page</u>
IV. OCCURRENCE OF MR WHISTLERS	73
A. Introduction	73
B. Occurrence of MR Whistlers in L-Shell--Latitude Space . .	73
C. Effect of the Plasmapause	78
D. Uses of the Data	80
V. MAGNETIC STORM EFFECTS ON MR WHISTLERS	81
A. Effect of Magnetic Storms on the Magnetosphere	81
B. A Case Study of MR Whistler Activity During the 17 to 18 April 1965 Magnetic Storm	81
C. MR Whistler Activity Levels: 14 to 30 April 1965	84
D. Models for Ray Tracing Calculations	89
E. Comparison of Computed and Measured Spectra	97
F. Alouette Topside Density Data	99
G. Behavior of MR Whistlers during Other Magnetically Disturbed Periods	99
H. Summary	101
VI. TRAPPING AND ITS RELATION TO THE STRUCTURE OF THE MAGNETOSPHERE	103
A. Introduction	103
B. Trapping Conditions	105
C. Effects of Magnetic Field "Curvature"	107
D. Consequence of Trapping	113
E. Comparison of Theoretical Results of Trapping with Observations	119
F. Observation of Magnetospheric Structure by Satellite	123
G. Summary	125
VII. CONCLUSIONS AND FUTURE WORK	127
A. Summary and Conclusions	127
B. Magnetospheric Density Structure	128
C. Applications of the Structure	130

CONTENTS (Cont)

	<u>Page</u>
D. The Boomerang Mode: A Future Experiment	131
E. Future Theoretical Work on Boomerang Mode	135
F. Proposals for Future Work on MR Whistlers	135
Appendix A. THE REFRACTIVE INDEX AND THE LOWER HYBRID RESONANCE	137
Appendix B. THE GROUP RAY REFRACTIVE INDEX	151
Appendix C. SIMPLE MODELS OF THE TURNAROUND MECHANISM	159
Appendix D. DETERMINATION OF THE PLANE OF STRATIFICATION	177
BIBLIOGRAPHY	181

TABLES

<u>Number</u>		
2.1	Defocusing loss (dB)	50
6.1	Observations of MR whistlers after the 17 to 18 April 1965 storm	119

ILLUSTRATIONS

<u>Figure</u>		<u>Page</u>
1.1	(a) Sketch of inner magnetosphere, showing the location of the topside ionosphere plasmasphere, and plasmopause. (b) Typical equatorial profile of density in the inner magnetosphere. (c) Sketch of the topside ionosphere illustrating the variation of H^+ and O^+ ions and electron density with altitude . . .	4
1.2	Variation of the thermal proton densities measured by the OGO-3 RF mass spectrometer during June to July 1966 at local dusk	5
1.3	Typical orbit of the OGO-3 satellite near perigee	8
1.4	Frequency-time spectrogram of a typical magnetospherically reflected (MR) whistler observed near the magnetic equator at $L \sim 2.4$	9
1.5	Sketch of the refractive index surface $(\mu)\psi$ for electrons only, which is open at wave normal angles near 90°	11
1.6	(a) Typical ray path through a model magnetosphere when the effect of the positive ions on the refractive index μ has been neglected. (b) Wave normal angle as a function of dipole latitude along path	12
1.7	Sketches of refractive index surfaces for ions plus electrons, and for electrons only	14
1.8	Sequence of refractive index surfaces at several frequencies for a point on the equator at $L \sim 2.4$	15
1.9	Typical ray path through a magnetosphere composed of positive ions and electrons	16
2.1	Ray paths for the first three components at 1.5 kHz, of MR whistlers received at four satellite locations . . .	20
2.2	(a) Snell's law for a simple case involving a sharp plane boundary between two different regions. (b) Geometric Snell's law construction illustrating the conservation of the refractive index component along the local stratification	27
2.3	Case 1 turnaround ("low frequency case")	28
2.4	Case 2 turnaround ("Gendrin mode")	29

ILLUSTRATIONS (Cont)

<u>Figure</u>		<u>Page</u>
2.5	Case 3 turnaround ("high frequency case")	31
2.6	Time history of wave normal behavior along an MR ray path illustrated for a wave at 2 kHz	32
2.7	(a) Ray paths for the 1^+ second component of an MR whistler as a function of frequency for a satellite location at the equator, $L \sim 2.4$. (b) Computed spectra corresponding to the ray paths in (a)	34
2.8	(a) Wave normal behavior for several frequencies associated with the ray paths of Fig. 2.7a. (b) Group ray refractive index vs dipole latitude along the path	36
2.9	(a) 3^- ray paths for three frequencies. (b) Spectra corresponding to the ray paths in (a)	38
2.10	Diffusive equilibrium models	40
2.11	Effect of shifting the satellite latitude on MR spectra calculations	41
2.12	Comparison of computed (dots) and observed (solid lines) MR whistler frequency-time spectra for several geomagnetic latitudes	43
2.13	(a) Relative variation of the electron density at 1000 km utilized in the ray tracing calculations compared to actual proton measurements by Taylor et al [1968b]. (b) Comparison of computed spectra (dots) using the density variation in (a) to the observed MR whistler spectra	45
2.14	Computed and observed MR whistler spectra using the nighttime model of 50% H^+ , 25% He^+ , and 25% O^+ at 1000 km with a base level density of 10^4 el/cc and a uniform temperature of $1600^\circ K$	47
2.15	Upper and lower frequency cutoffs	48
3.1	Illustration of effects on MR spectra of a rapid dropoff in density at $L \sim 1.8$	54
3.2	Theoretical effect of an enhancement at $L = 2.2$ upon MR whistler ray paths	58

ILLUSTRATIONS (Cont)

<u>Figure</u>		<u>Page</u>
3.3	Sequence of calculated $2^- 2^+$ MR spectrograms for the duct model of Fig. 3.2 compared to a sequence of observed $2^- 2^+$ MR whistlers which show similar spectral distortions	60
3.4	Characteristics of the 3^- MR component as predicted by four magnetospheric density models	62
3.5	Duct (enhancement) interaction with $1^- 1^+$, $3^- 3^+$ MR whistlers	64
3.6	Effects of an enhancement on 1^+ MR ray paths and spectrograms	66
3.7	Duct and dropoff density structure effects	68
3.8	(a) MR spectrogram showing effects of a cross-L density dropoff at $L \sim 1.9$ and a small duct at $L \sim 2.4$. (b) Sketch of the density profile at 1000 km deduced from (a)	69
3.9	(a) Example of a MR whistler with irregular spectra caused by a field-aligned trough. (b) Effect of a trough at $L \sim 2.2$ on MR whistler rays which have undergone one reflection. (c) The input latitude vs output L-shell along the equator characteristics for the ray paths in (b) show that there is a general focusing of the rays above the trough center allowing for three 1^+ rays to cross the satellite point at $L \sim 2.3$. (d) A calculated MR spectrogram using the trough model of (b)	71
4.1	Cumulative data coverage (shaded portions) in the magnetic meridian plane by (a) OGO-1 during October 1964 to June 1965; (b) OGO-1 during October 1965 to December 1966; and (c) OGO-3 during June to November 1966. (d) Plots in the magnetic meridian plane of typical orbits of OGO-1	74
4.2	Average occurrence levels of MR whistlers for the observation period October 1964 to December 1966 in the magnetic meridian plane	76
4.3	Average occurrence rates for MR whistlers with different numbers of components plotted vs L-shell	77
4.4	Average occurrence levels of MR whistlers in local time vs L-shell	79

ILLUSTRATIONS (Cont)

<u>Figure</u>		<u>Page</u>
5.1	L-shell-dipole latitude plot for April 14, 22, 25, 27 and 30, 1965 OGO-1 passes	82
5.2	Geomagnetic activity during the April 17 to 18 storm compared to the observed OGO-1 MR whistler activity . . .	83
5.3	Occurrence rates for MR whistlers observed on five OGO-1 passes before and after the 17 to 18 April storm	85
5.4	Frequency-time spectrograms of whistlers (not all are MR's) observed before and after the storm	86
5.5	Measurement of the depletion of density on 22 April above $L \sim 2.5$ as compared to density on 14 and 30 April	92
5.6	Ray paths for the outer and inner MR whistler modes, with wave normal directions indicated by the arrows along the paths	94
5.7	(a) Wave normal angle variation along the outer and inner mode MR ray paths of Fig. 5.6. (b) Calculated spectrograms for the outer and inner modes	95
5.8	Comparison of computed and measured spectrograms	98
5.9	Density measurements at 800 km made by the Alouette-1 satellite before, during, and after the 17 to 18 April storm	100
5.10	MR whistler activity levels during May 1965 correlated with the magnetic activity index K_p	102
6.1	Typical ray paths for 2 kHz in a "smooth" magneto-spheric model	103
6.2	(a) Illustration of the effects of an abrupt drop in density on the ray paths. (b) Input latitude vs L-shell along the equator	104
6.3	Condition for trapping a ray by a density dropoff	106
6.4	Examples of curvature effects on trapping of rays	108
6.5	(a) Trapping of rays by an abrupt density dropoff at $L \sim 1.8$. (b) Input latitude at 500 km vs output L-shell along the equator showing great defocusing for rays starting between 39° and 40°	112

ILLUSTRATIONS (Cont)

<u>Figure</u>	<u>Page</u>
6.6 Trapping of rays by an abrupt density dropoff at $L \sim 2.4$	114
6.7 (a) Trapping of rays by two density dropoffs at $L \sim 2.4$ and $L \sim 1.8$. (b) Trapping of rays by density dropoffs at the same location as in (a) but with an initial height variation	115
6.8 Cross-field penetration of 1^+ ray paths for a maximum starting latitude at 31°	117
6.9 $2^- 2^+$ MR whistler spectra produced by ray paths which have a maximum starting latitude of 31°	118
6.10 MR whistler spectra for 25 April 1965 showing the progressive disappearance of the high frequencies as the satellite moves to higher L-shells	120
6.11 $2^- 2^+$ MR whistler spectra produced by ray paths with a maximum starting latitude of 28°	122
6.12 A comparison of H^+ profiles	124
7.1 Sketches of electron density structures deduced from MR whistlers observed on four OGO-1 passes	129
7.2 Several boomerang ray paths from a satellite at the equator, for three different values of initial wave normal angle	132
7.3 (a) Boomerang ray path for a satellite sounder at $L \sim 3$ at the equator. (b) Corresponding spectrogram for the boomerang mode as seen by a satellite VLF receiver at the equator	134
B.1 (a) Group-ray refractive index as a function of frequency and wave normal angle. (b) Comparison of the several expressions for μ_{gr}	157
C.1 Penetration of the ray path across and along the field using the Lyons and Thorne approach	163
C.2 Penetration of the ray paths during turnaround across and along the field as predicted by the extension of the L & T approach	169
C.3 (a) Turnaround times compared using ray tracing results and our approximate expressions (C.23) and (C.24). (b) The comparison of the maximum penetration of the ray path along a field line during turnaround as computed by ray tracing and from Eq. (C.15)	176

I. INTRODUCTION

A. Purpose

The purpose of this dissertation is to describe and explain the observations of magnetospherically reflected (MR) whistlers made by the Orbiting Geophysical Observatories (OGO) 1 and 3. The data were obtained with the aid of broadband very-low-frequency (VLF) (0.3 to 12.5 kHz) receivers during the period between October 1964 and December 1966. Topics included under this general objective are: (1) the explanation of the general frequency-time characteristics of MR whistlers in terms of wave propagation through a "smooth" or slowly varying magnetosphere; (2) the investigation of the theoretical and observed sensitivity of the MR whistler frequency-time spectrograms to various models of irregular field aligned structure of the magnetospheric thermal plasma densities; (3) utilization of MR whistler observations from successive satellite passes to detect spatial and temporal variations in the magnetospheric density structure as a function of magnetic activity.

B. The Structure of the Magnetosphere

The magnetosphere [Gold, 1959] is defined as the region about the earth where the behavior of the plasma is controlled primarily by the geomagnetic field. At the outer edges of the magnetosphere, the magnetic field configuration is complex and is determined by the interaction between the geomagnetic field and the solar wind [Parker, 1963]. The geomagnetic field between $\sim 1.5 R_E$ and $4 R_E$ ($R_E \sim 6370$ km, an earth radius) from the center of the earth can be represented reasonably accurately by a dipole field. This dissertation will be primarily concerned with the region below $4 R_E$ which under average conditions is the plasmasphere.

The thermal plasma structure of the inner magnetosphere can be broken down into several altitude regions. At the lower boundary of the magnetosphere is the ionosphere which begins at ~ 100 km and extends up to ~ 1000 km. The F-2 ionization peak at approximately 300 km consists primarily of oxygen ions and electrons. Above the F-2 peak

the oxygen ion concentration decreases exponentially with altitude, while the hydrogen ion concentration increases with altitude. At some altitude between 500 km and 1000 km the oxygen and hydrogen ion concentrations are equal. This transition altitude depends upon latitude, local time, and geomagnetic conditions. Above the transition level the dominant ion is the hydrogen ion. The helium ion is also present in the transition region, but it is a minor constituent. The topside ionosphere is generally defined as the region above the F-2 layer peak and below the altitude where the hydrogen ion dominates. Above the topside ionosphere collisions help to establish a diffusive equilibrium distribution of density along magnetic field lines [Angerami and Thomas, 1964].

Angerami and Carpenter [1966] have given experimental support for the diffusive equilibrium model of densities in the inner magnetosphere. This model assumes that the partial pressures exerted by each ion constituent and by the electrons are balanced by the earth's gravitational field and the electric field due to charge separation. The motions of the ions and electrons are assumed to be confined to a magnetic line of force such that the density distribution along one field line may be different from that along an adjoining field line. Also the density distribution along a field line in the vicinity of the magnetic equator is nearly constant.

Since the earth's magnetic field influences the thermal density distribution, it is convenient to describe the magnetic field lines with the McIlwain L-parameter [McIlwain, 1961]. For a dipole field, the L-parameter is defined as $L = r/(r_E \cos^2 \lambda)$, where r is the geocentric distance, r_E is the radius of the earth, and λ is the magnetic latitude. In this case a particular L-parameter or L-shell identifies the magnetic field lines which cross the magnetic equator at a geocentric distance equal to the L-value multiplied by the radius R_E of the earth. For example, the $L = 4$ field line crosses the equator at a geocentric distance of $4 R_E$.

The thermal plasma which is characterized by its diffusive equilibrium properties often experiences a sharp dropoff in density levels at a field aligned boundary typically near $L \sim 4$. Inside this boundary the density at the equator is on the order of hundreds of electrons per cubic centimeter. Outside the density may drop two orders of magnitude [Carpenter, 1966]. The boundary is called the plasmapause, and the inner

region is called the plasmasphere. The plasmapause location is a function of local time and magnetic conditions. The structure of the plasmasphere below $L \sim 4$ will be one of the principal areas of interest in this dissertation. A representation of the plasmasphere and the earth's magnetic field is shown in Fig. 1.1.

C. Measurement of Magnetospheric Densities

During the past decade numerous satellite experiments have been devised to measure thermal ion and electron density levels in the topside ionosphere and magnetosphere. Techniques used for this purpose have included electrostatic electron probes [Brace and Reddy, 1965], RF ion mass spectrometers [Taylor et al, 1965, 1968b] and high frequency topside sounders [Colin and Chan, 1969]. The first two techniques suffer from one major drawback; the ion or electron density measurement is made at the satellite and could be affected by the spacecraft itself. The probe measurement accuracy is dependent upon the decoupling of the probe potential from the spacecraft potential and from potentials created by photoelectric emission [Shkarofsky, 1971]. The RF mass spectrometer has produced good usable data on ion densities, but the conversion from ion current to ambient ion density is dependent upon the spectrometer's efficiency and geometry, and upon the spacecraft's potential, velocity, and orientation. Considerable information on the upper ionosphere has been obtained from topside sounders. Here the main limitation is the altitude range, since the satellite sounds the plasma density below it. When sweeping frequency sounders are used (producing ionograms similar to the familiar ground-based counterparts) the spatial resolution is also a limitation.

A secondary problem is the length of time between individual measurements. For example Taylor et al [1971] found that high resolution data taken every 3.2 seconds by the OGO-4 polar orbiting satellite measures significant changes in ion densities in the topside ionosphere that might be overlooked by lower resolution data taken every 37 seconds. The high resolution data are taken every 0.2° of latitude along the orbit; whereas the lower resolution data are taken every 2.3° . The field-aligned

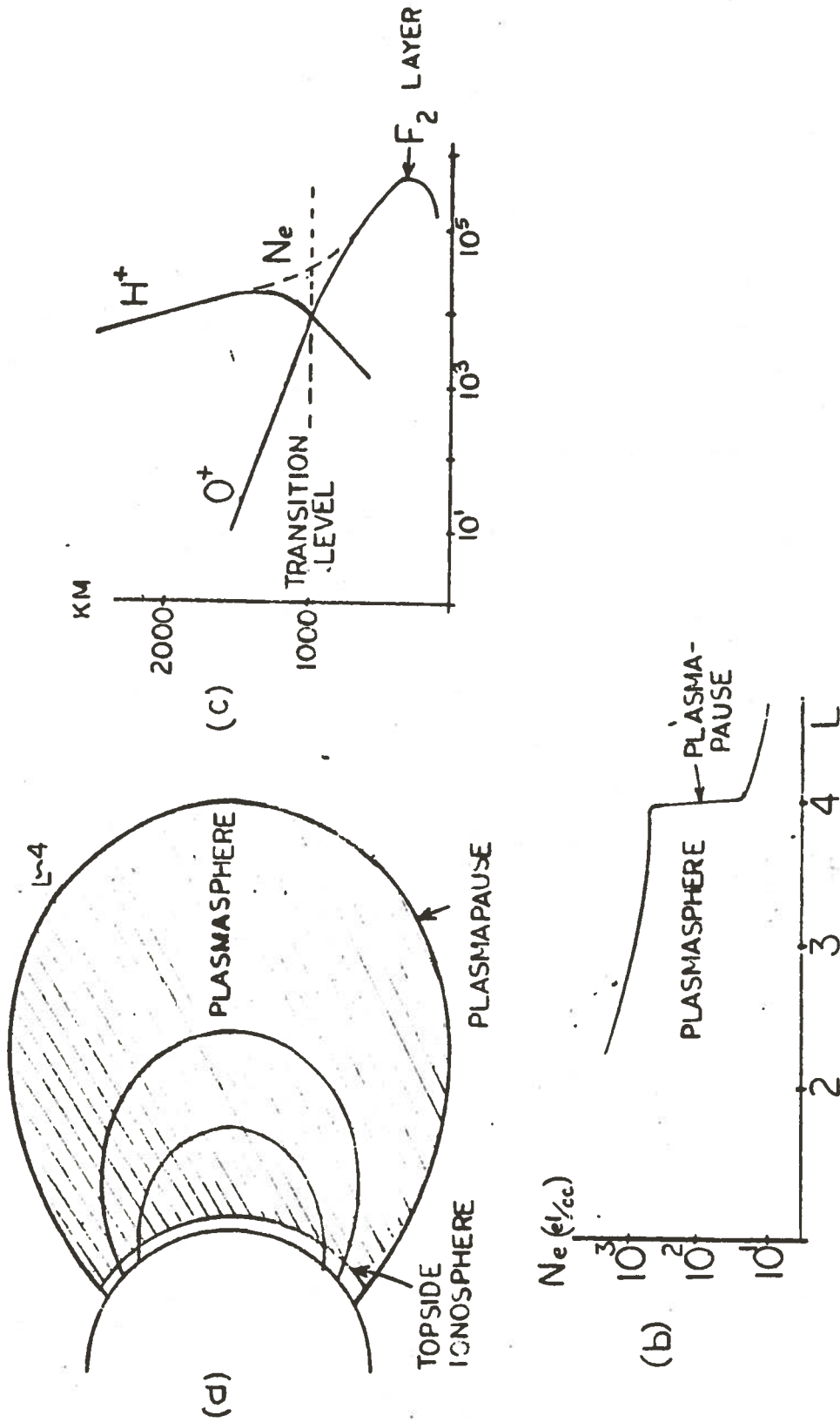


Fig. 1.1. (a) SKETCH OF INNER MAGNETOSPHERE, SHOWING THE LOCATION OF THE TOPSIDE IONOSPHERE PLASMASPHERE, AND PLASMAPAUSE. (b) Typical equatorial profile of density in the inner magnetosphere. (c) Sketch of the topside ionosphere illustrating the variation of H^+ and O^+ ions and electron density with altitude.

density structure as discussed in this report may have widths corresponding to 0.5° at 1000 km. Another problem found only in satellite measurements of densities in the plasmasphere is illustrated in Fig. 1.2. Because of limitations in satellite telemetry coverage near perigee, density measurements often do not extend below $L \sim 3 - 2.5$. Thus any significant density structure below the telemetry cutoff can not be observed.

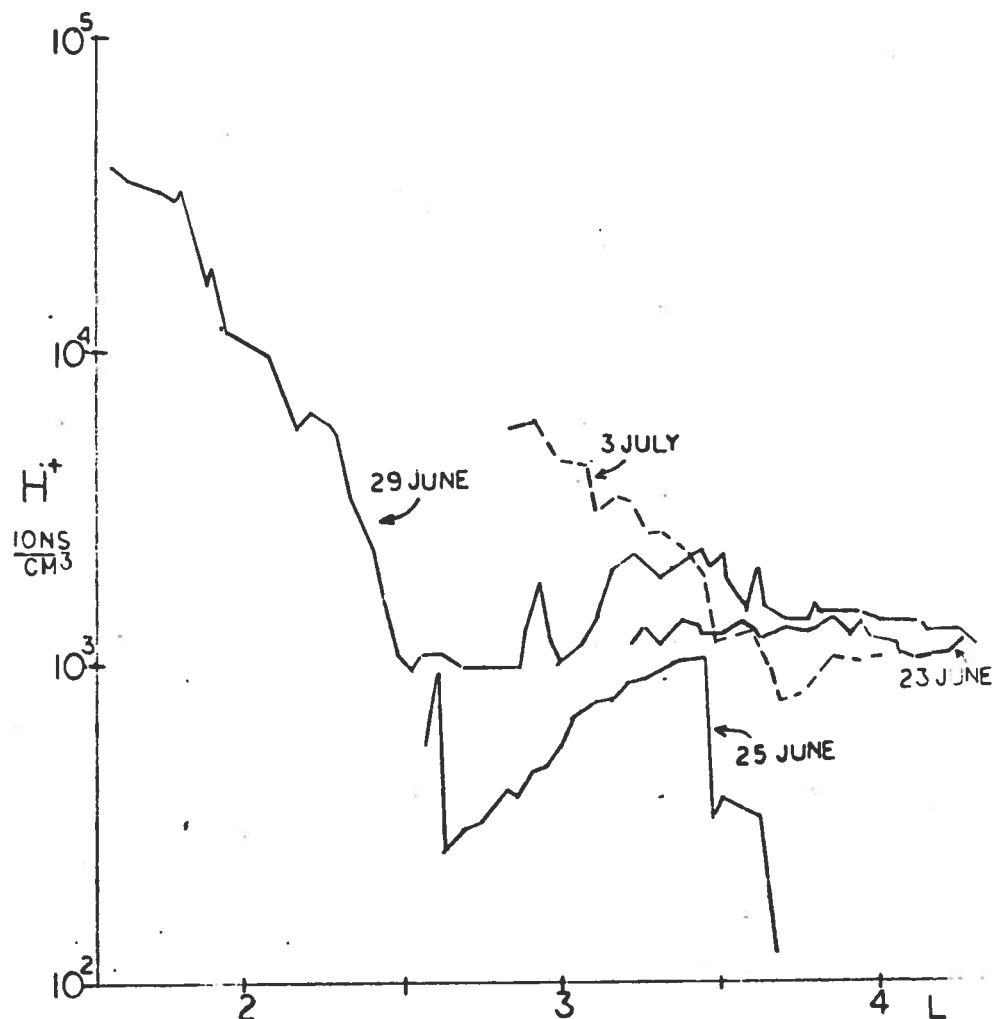


Fig. 1.2. VARIATION OF THE THERMAL PROTON DENSITIES MEASURED BY THE OGO-3 RF MASS SPECTROMETER DURING JUNE TO JULY 1966 AT LOCAL DUSK [Taylor et al, 1968b, 1970]. The plots show considerable irregular density structure in the magnetosphere.

D. The Whistler Method of Studying Magnetospheric Densities

Whistlers are naturally occurring VLF electromagnetic wave phenomena which are produced by atmospheric lightning strokes. The VLF portion of the electromagnetic energy produced by a lightning source may propagate across the ionosphere and enter the magnetosphere. At the end of the magnetospheric path a wide band VLF receiver, whether on the ground or in a satellite, detects a highly dispersed signal whose different frequency components arrive at different times. The resulting signal when played through an audio system produces a whistling sound, and thus these signals have been called whistlers [Helliwell, 1965].

The whistler method of measuring magnetospheric densities generally involves the identification of the path from the point of origin to the observation point and the measurement of the dispersion and travel time of the observed signal. These travel times can then be converted into electron density along the path by the suitable application of magnetospheric theory [Ratcliffe, 1959]. Since the density measurement depends on conditions along the propagation path, it is independent of local conditions at the reception point. Thus when the reception point is on a satellite, the density measurement is independent of spacecraft potential problems. The accuracy of the whistler method of measuring densities is however highly dependent upon correctly determining the propagation path.

E. Ground Observations of Whistlers

Whistlers were first heard by man at the end of the 19th century. From that time to the present whistler studies have progressed from crude experimental observations to a highly sophisticated scientific tool for exploring the ionosphere and magnetosphere [Helliwell, 1965]. From studies of the properties of whistlers observed on the ground, it was concluded that the paths of propagation were fixed in the magnetosphere and that these paths were contained within field-aligned enhancements of ionization or "ducts." Smith et al [1960] has shown that these ducts can trap whistler energy whose wave normals are confined within a small cone about the magnetic field. From accurate measurements of the

magnetospheric travel times and dispersions of ground observed whistlers, it is possible to determine the L-values of the field-aligned paths of propagation and the corresponding equatorial electron densities. Ground observations of ducted whistlers have yielded much useful information about density structure of the magnetosphere beyond $L \sim 3$, particularly about the plasmapause [Angerami and Carpenter, 1966].

When a lightning source illuminates the lower boundary of the ionosphere, the ducts which exist at the time can trap only a small portion of the radiated VLF energy. The ducts guide the VLF energy along field lines of the earth's magnetic field from the hemisphere of excitation to the opposite hemisphere. There the ducted whistler exits from the ionosphere and may then be detected on the ground. The "nonducted" energy follows paths not confined to single field lines and exhibits a wide range of wave normal directions. As a result of the continuous (rather than discrete) distribution of ray paths, nonducted whistler propagation is the dominant form of whistler propagation in the plasmasphere. Nonducted whistlers are rarely, if ever, observed on the ground because the generally large wave normal angles involved cause these waves to be refracted upward in the conjugate hemisphere, or to be internally reflected at the lower boundary of the ionosphere.

F. Satellite Observations

Since ground-based VLF stations do not observe most nonducted whistlers, the receiver must be placed in the magnetosphere. Earth orbiting satellites offer a unique platform from which to observe nonducted whistlers. Because we would like to be able to determine the regions of occurrence of nonducted whistlers, our satellite should make regular sweeps through the magnetosphere. The Orbiting Geophysical Observatory (OGO) series of satellites was initiated to measure the physical properties of the magnetosphere with a variety of scientific experiments. The OGO-1 and OGO-3 satellites each contained a broadband VLF (0.3 to 12.5 kHz) receiver and traveled over highly elliptical orbits. The initial orbit parameters for the satellites are given below.

<u>OGO-1</u>	<u>OGO-3</u>
Launch Date: September 5, 1964	June 7, 1966
Apogee: 149,000 km (alt.)	122,000 km (alt.)
Perigee: 282 km (alt.)	320 km (alt.)
Inclination: 31.15°	31°
Period: 64 hours	48.6 hours

The periods were such that the satellites would sweep through the inner magnetosphere every two to three days. Thus the satellites could sample the nonducted whistler activity with regularity. A sample orbit for OGO-3 is shown in Fig. 1.3. During the operating lifetime of each

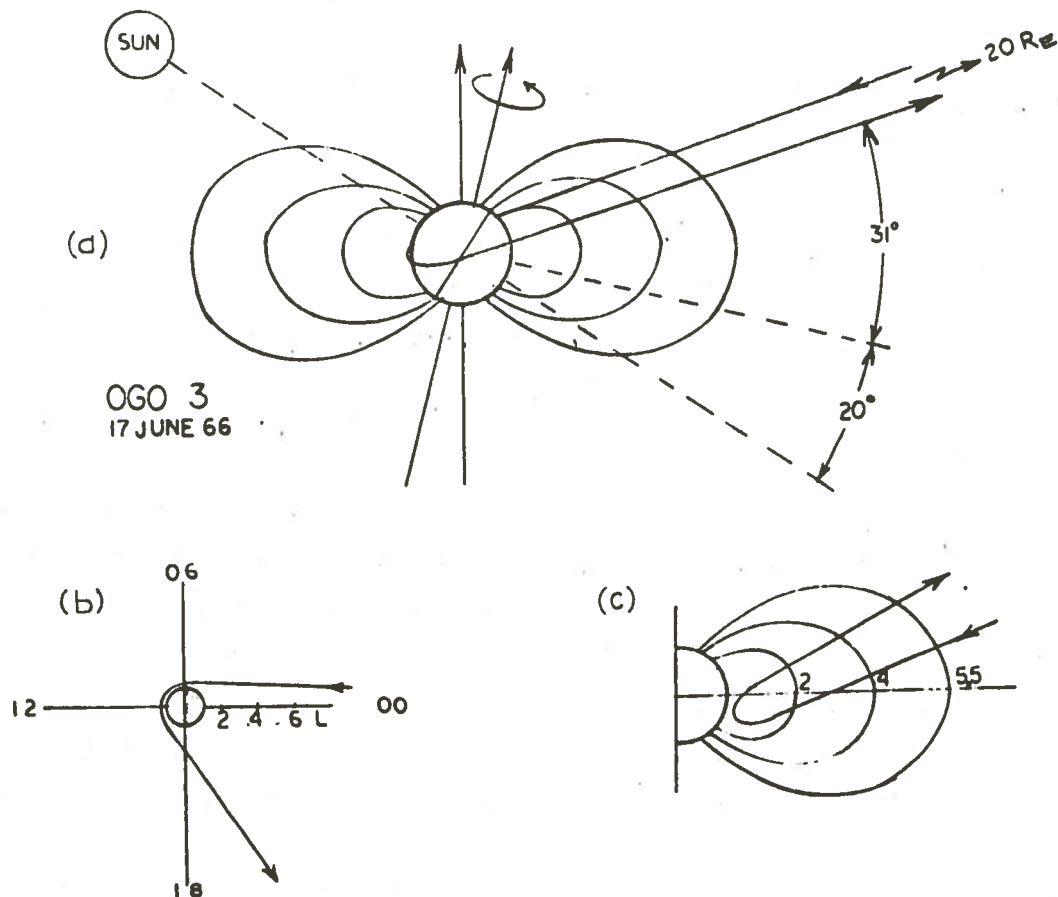


Fig. 1.3. TYPICAL ORBIT OF THE OGO-3 SATELLITE NEAR PERIGEE. (a) OGO-3 orbit on 17 June 1966 as the satellite sweeps through the inner magnetosphere. (b) Local time vs equatorial L-shell. (c) Orbit track in magnetic meridian.

satellite, the perigee moved higher in altitude. This behavior allowed the satellites to cover most of the inner magnetosphere. More detailed orbit information is given in Chapter IV.

The principal telemetry stations for the OGO-1 satellite were as follows:

<u>Symbol</u>	<u>Location</u>	<u>Geographic Latitude and Longitude</u>
ROS	Rosman, North Carolina	35°N, 83°W
JOB	Johannesburg, South Africa	28°S, 26°E
SKA	Unalaska, Alaska	54°N, 167°W

The abbreviation (ROS) in Fig. 1.4 refers to the OGO-1 telemetry station at Rosman, which received the telemetered VLF broadband data.

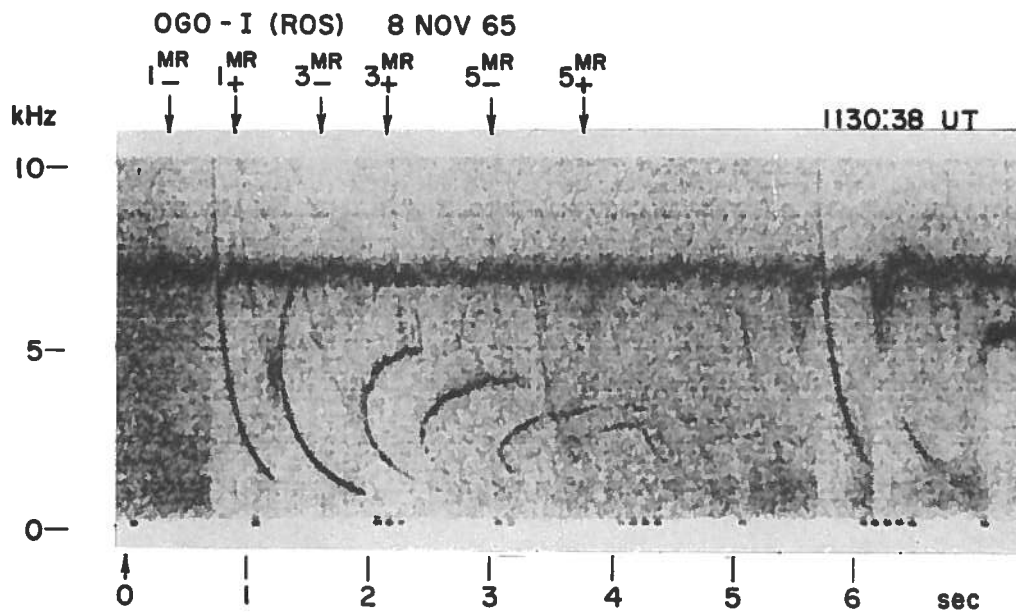


Fig. 1.4. FREQUENCY-TIME SPECTROGRAM OF A TYPICAL MAGNETOSPHERICALLY REFLECTED (MR) WHISTLER OBSERVED NEAR THE MAGNETIC EQUATOR AT $L \sim 2.4$. The dark band at 7 kHz is interference associated with the voltage-controlled oscillator used to indicate amplitudes. The labels associated with each MR component correspond to those in the ray path of Fig. 1.9.

G. The Magnetospherically Reflected Whistler

A very common nonducted whistler observed by the OGO-1 and OGO-3 satellites in the inner magnetosphere is the magnetospherically reflected (MR) whistler [Smith and Angerami, 1968]. An example of the MR whistler is shown in Fig. 1.4. The frequency-time spectrum usually consists of several traces or components spaced in a pattern determined by the satellite's location. The first trace shows a small dispersion and indicates that the path length between the lightning source and the satellite was short compared to the path lengths of the higher order components. The series of traces after the first exhibits "nose" frequencies or frequencies of minimum time delay. The nose frequency decreases with increasing component order. At first glance, one might conclude that the MR whistler is a result of an echoing process and that the VLF energy is being reflected somewhere in the magnetosphere.

H. Nonducted Whistler Ray Paths

Let us examine the various possibilities for nonducted whistler propagation in the magnetosphere. The propagation path of the whistler energy is determined by the refractive index along the path. As shown in Appendix A the refractive index (μ) is a function of the angle between the wave normal and the magnetic field, the frequency, the electron density, positive ion composition and the magnetic field strength. At any fixed point along the path, a refractive index surface can be drawn. The refractive index surface is the locus of the refractive index vector $\mu(\psi)$ as ψ is varied between 0° and 360° . The surface is formed by rotating this locus of points about the axis of the magnetic field direction. A typical sketch of $\mu(\psi)$ is shown in Fig. 1.5. The direction of the energy flow or ray direction for a particular wave normal angle ψ is given by constructing a normal to the surface at the end of the $\mu(\psi)$ vector [Stix, 1962; or Poeverlein, 1948]. Thus the ray path direction is dependent upon the behavior of the wave normal angle, and the types of ray paths which can exist in the magnetosphere can be classified by range of wave normal angles exhibited along the paths.

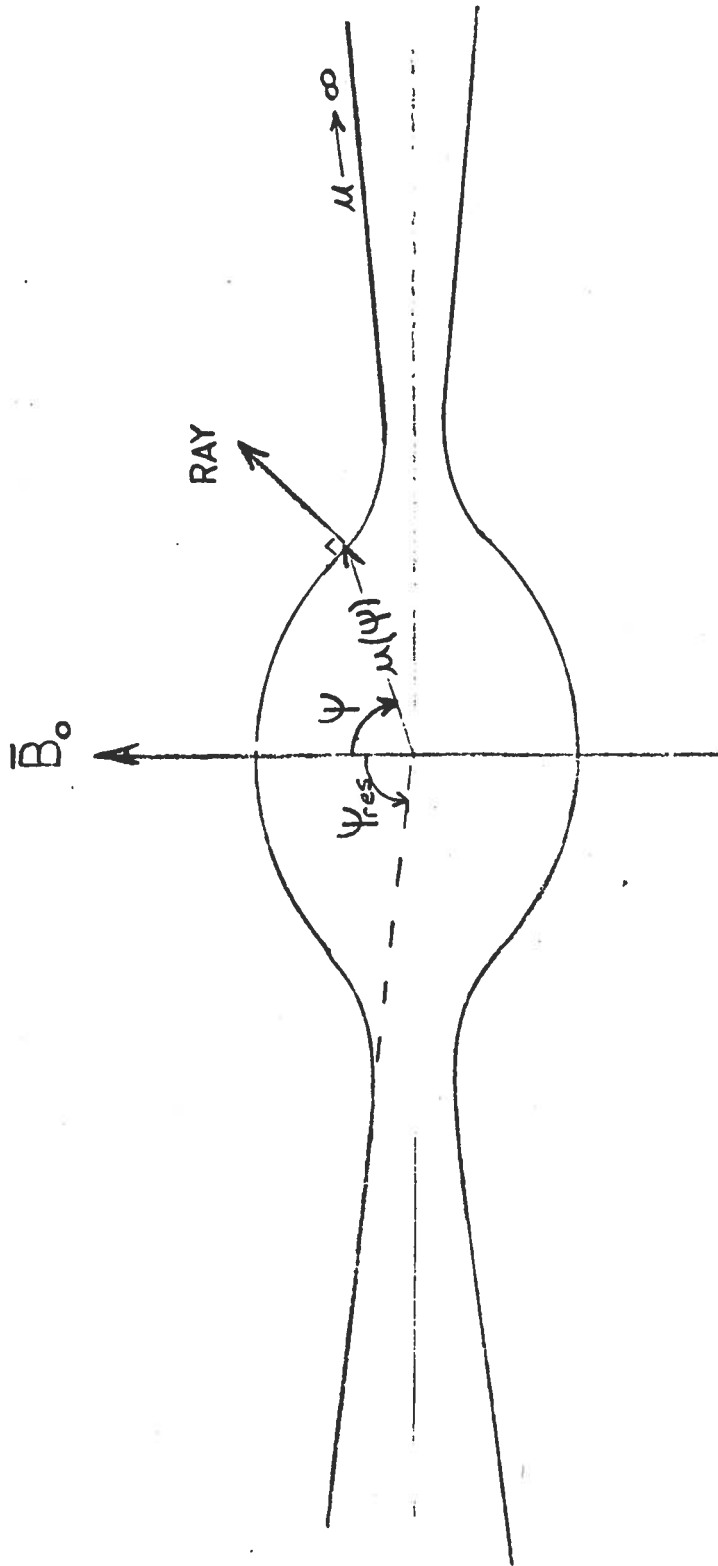


Fig. 1.5. SKETCH OF THE REFRACTIVE INDEX SURFACE $\mu(\psi)$ FOR ELECTRONS ONLY, WHICH IS OPEN AT WAVE NORMAL ANGLES NEAR 90° . $\mu(\psi)$ is symmetrical with respect to the vertical and horizontal axes and describes a figure of revolution around B_0 . The ray direction for a particular wave normal is perpendicular to the refractive index surface.

Consider first a magnetosphere composed of electrons and heavy ions, where the motions of the ions are ignored because of their inertia. Fig. 1.6 shows a typical whistler nonducted ray path computed by Yabroff [1961] neglecting the effects of ions in the calculations of $\mu(\psi)$. As the ray travels through the northern hemisphere, the wave normal lags behind the faster-rotating magnetic field direction. By the time the ray has entered the southern hemisphere, the wave normal rapidly approaches a limiting resonance cone at which μ goes to infinity. It can be seen from Fig. 1.6 that the ray path crosses a larger range of L-values in the northern

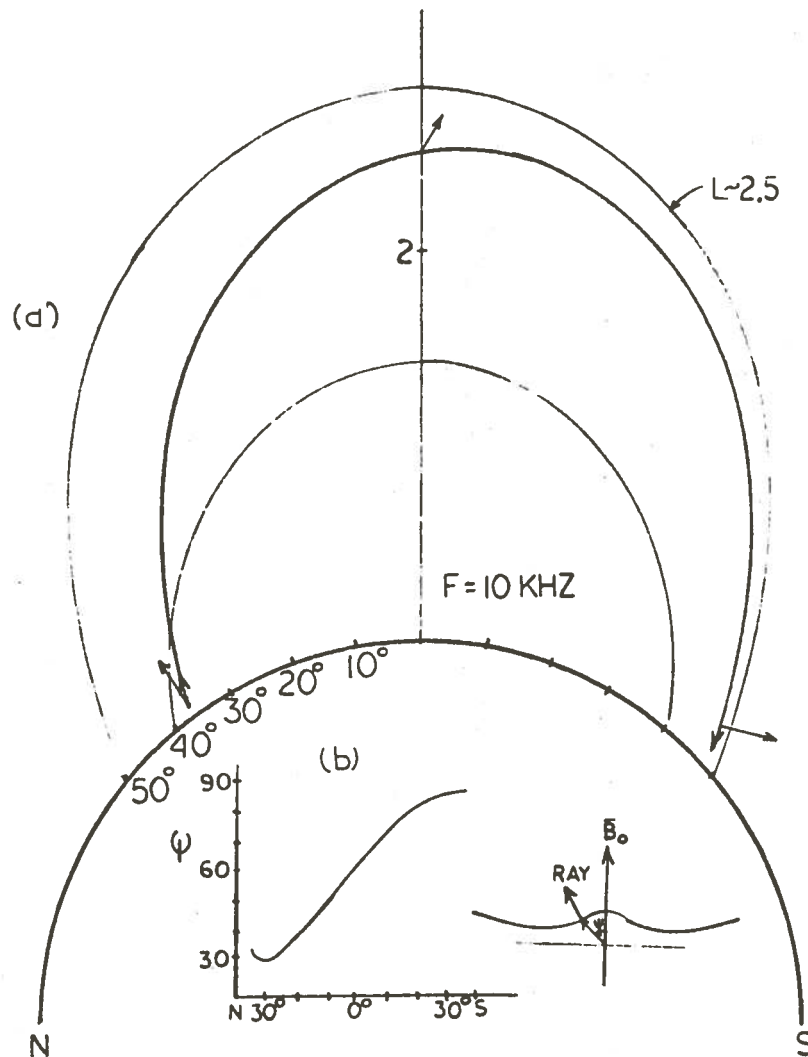


Fig. 1.6. (a) TYPICAL RAY PATH THROUGH A MODEL MAGNETOSPHERE WHEN THE EFFECT OF THE POSITIVE IONS ON THE REFRACTIVE INDEX μ HAS BEEN NEGLECTED. (b) Wave normal angle as a function of dipole latitude along path.

hemisphere, where the wave normal angles are small. But as the wave normal angle increases, the ray direction approaches closely the magnetic field direction. The large wave normal angle prevents the ray from propagating across the lower boundary of the ionosphere, hence this whistler could not be detected on the ground. The ray could undergo reflection at the ionosphere, but this reflection process is subject to ionospheric attenuation and would not produce the echoing appearance of the MR whistler.

I. Effect of Ions on Whistler Ray Paths

Hines [1957] first pointed out the significance of including the effects of ions in VLF ray path calculations. The addition of ions in refractive index calculations permits the refractive index surface to close for transverse propagation. The refractive index surfaces in Fig. 1.7 illustrate the difference between the electrons-only and the electrons-plus-ions calculations for a point in the magnetosphere. The inclusion of ions removes the resonance cone for frequencies lower than the "lower hybrid resonance" (LHR) frequency and allows the ray to be perpendicular to the magnetic field. The LHR frequency [Smith and Brice, 1964] is approximately given by $f_H/43$ (see Appendix A), where f_H is the electron gyrofrequency and 43 is the square root of the proton to electron mass ratio. In a typical plasmasphere extending to $L = 4$, the LHR frequency ranges between 10 kHz and .3 kHz. The sequence in Fig. 1.8 illustrates the frequency dependence of the refractive index surface for realistic magnetospheric models.

Using the Hines [1957] formulation of the refractive index, Kimura [1966] extended the ray path calculations of Yabroff [1961] to allow for ion effects. The ray path with ion effects showed significant deviations from the electron-only ray path as illustrated by Fig. 1.9. Successive portions of the ray in this figure are labeled 0^+ , 1^- , 1^+ , 2^- , 2^+ , etc., in analogy with ground-observed whistlers (1-hop, 2-hop, etc.). This nomenclature will be used throughout. The ion ray path virtually duplicates the electron-only path in the northern hemisphere, for in either case the refractive index surfaces are nearly identical for small wave normal angles. In the southern hemisphere the electron

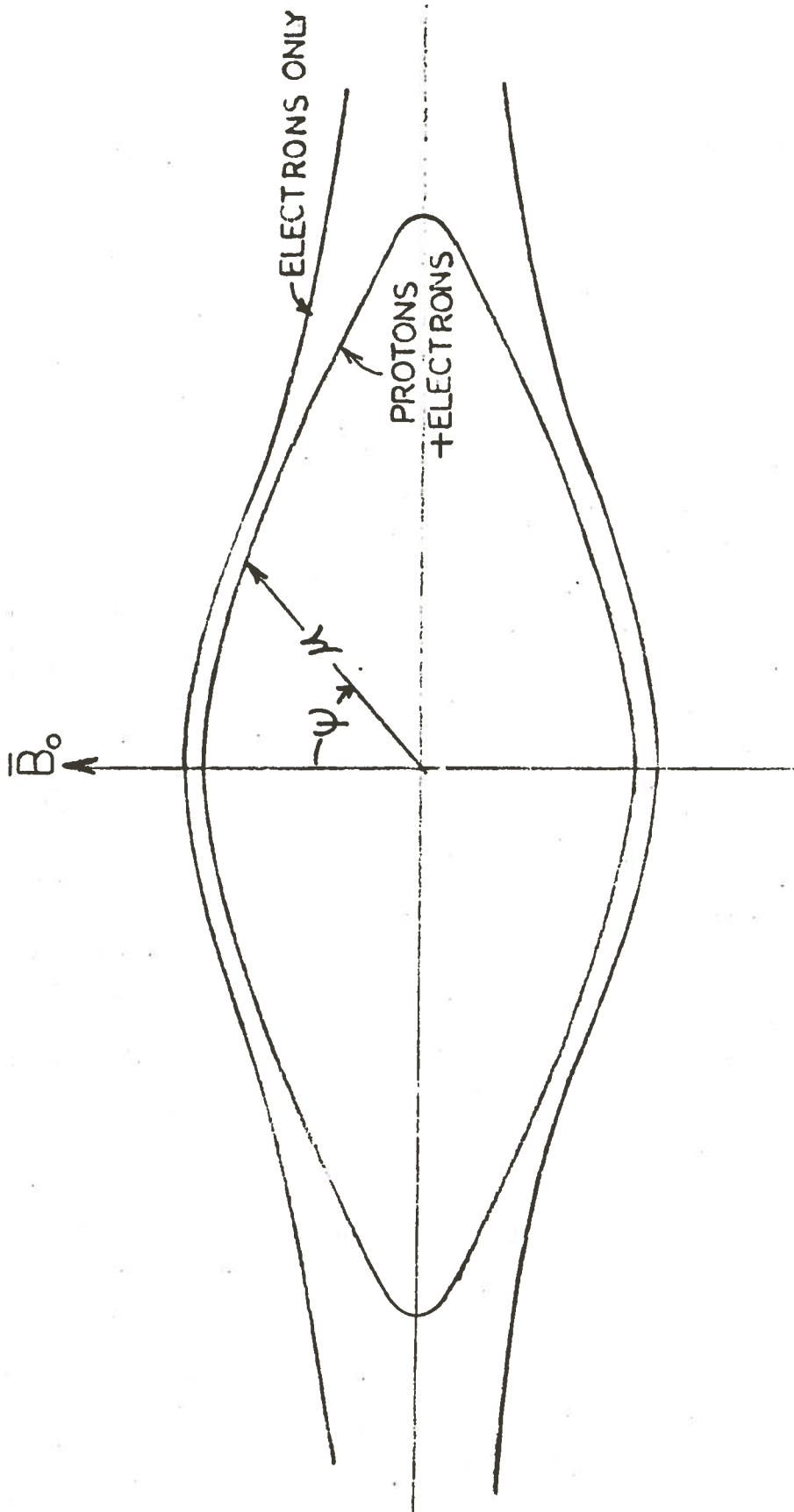


Fig. 1.7. SKETCHES OF REFRACTIVE INDEX SURFACES FOR IONS PLUS ELECTRONS, AND FOR ELECTRONS ONLY (c.f. Hines [1957]).

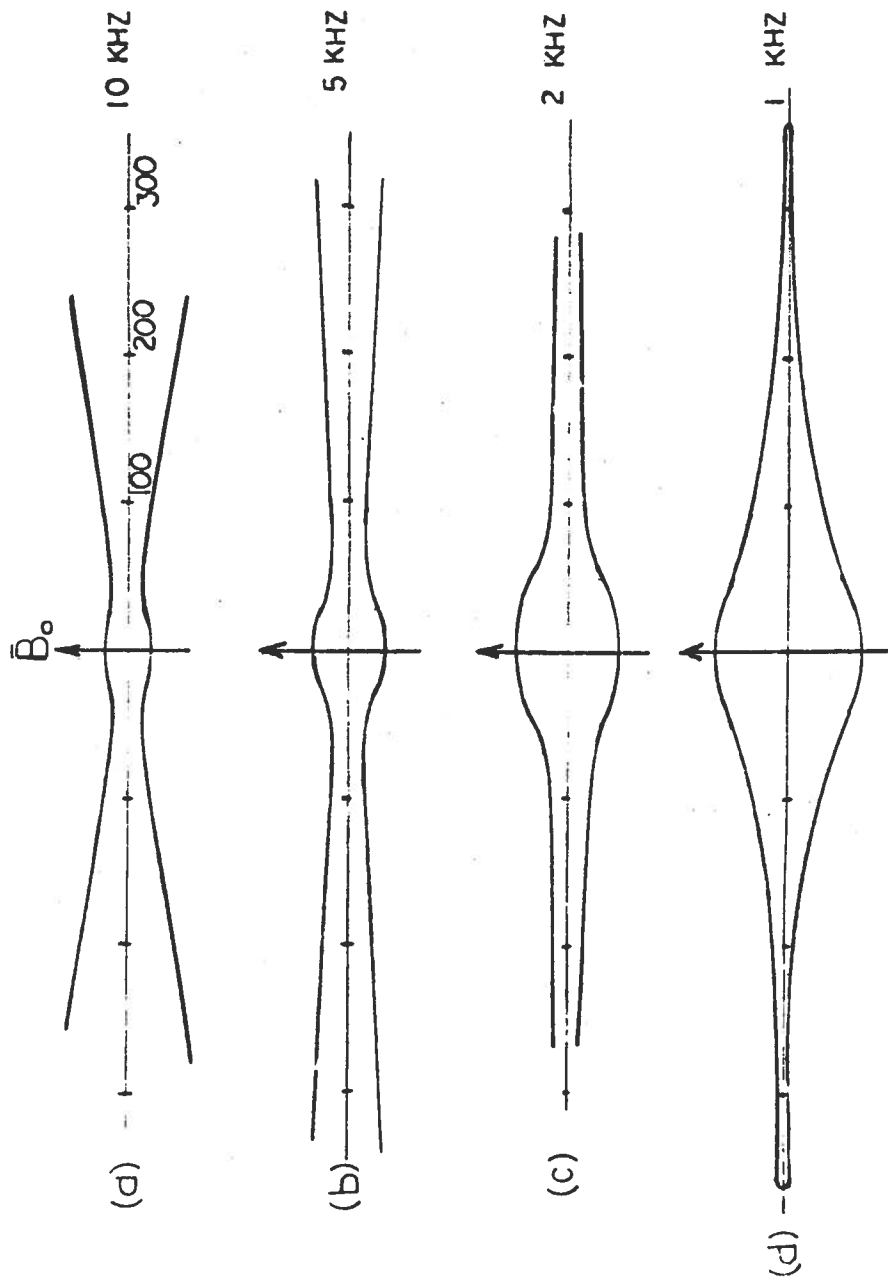


Fig. 1.8. SEQUENCE OF REFRACTIVE INDEX SURFACES AT SEVERAL FREQUENCIES FOR A POINT ON THE EQUATOR AT $L \sim 2.4$. The calculations assume that only protons and electrons are present. (a) 10-kHz refractive index curve. The resonance cone angle is 72° . (b) and (c) 5-kHz and 2-kHz refractive index curves show the rotation of the resonance cone toward 90° . (d) 1-kHz refractive index curve shows the closed nature of the surface for frequencies below the LHR frequency.

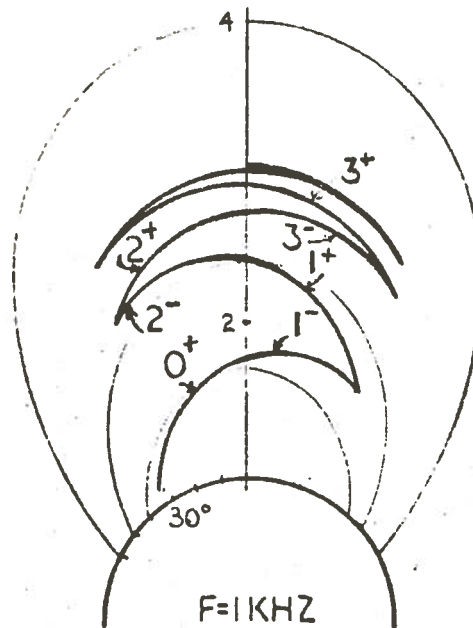


Fig. 1.9. TYPICAL RAY PATH THROUGH A MAGNETOSPHERE COMPOSED OF POSITIVE IONS AND ELECTRONS (c.f. Fig. 6, Kimura [1966]). The ray oscillates back and forth across the equator as it moves out in L space, and eventually reaches an L-shell where it remains trapped.

ray path becomes nearly field aligned as the wave normal rotates toward the resonance cone, but the ion ray path makes an abrupt turn-around near a latitude of -25° . The radical departure of the ion ray path results from the closing of the refractive index surface, which allows the wave normal to rotate through 90° . Reexamining the ion-plus-electron refractive index surface in Fig. 1.7, we find that the ray direction can change by almost 180° as the wave normal angle ψ rotates from 80° to 100° . Since the abrupt turnaround occurs in a small region, the process can be characterized as a "reflection." After reflection the ray travels back to the northern hemisphere where it is again reflected resulting in a ray path that oscillates about the magnetic equator. The successive "bounces" or "hops" of the ray path seem to offer a basis for the explanation of the echo-like traces on the magnetospherically-reflected whistler spectrogram of Fig. 1.4. Smith and Angerami [1968] used the ray tracings of Kimura [1966] to give a qualitative explanation of the MR whistler.

J. Organization Plan

In this introductory chapter we have presented background information about MR whistler propagation through the magnetosphere and about the gross structure of the magnetosphere. Chapter II is concerned with the MR whistler as it is observed in a smooth or slowly varying magnetosphere. In Chapter III we look at the effects on MR whistler ray paths and MR whistler spectrograms, of various narrow field-aligned density structures in the plasmasphere. Chapters II and III lay the groundwork for interpreting the spectral appearance of MR whistlers in terms of magnetospheric structure. In Chapter IV the occurrence rates of MR whistler observations are presented as a function of satellite position in order to set bounds on the extent of MR whistler propagation in the magnetosphere. In Chapter V we examine the effects upon MR whistler propagation of magnetic activity, which is responsible for creating much magnetospheric density structure. In Chapter VI we deduce features and lifetimes of post-storm magnetospheric density structure which inhibits the observation of MR whistlers. In Chapter VII we summarize the conclusions of this dissertation, deduce the long term magnetospheric density structure, and make suggestions for future experiments.

K. Contributions of the Present Investigation

The contributions of this investigation can be outlined as follows:

1. The gross features of magnetospherically-reflected whistlers are explained. This was done by matching observed MR whistler spectra in simple cases with that predicted by ray tracing in a smooth magnetospheric model containing ions and electrons (Chapter II.F). The nose frequency characteristic of an MR component is explained in terms of wave normal behavior in the regions of reflection (Chapter II.C), and the spacing patterns of the MR components are shown to be a function of satellite latitude (Chapter II.B).
2. The occurrence of MR whistlers with complex spectral characteristics is interpreted in terms of propagation through field-aligned electron density irregularities. The double traces and irregularities in MR spectra are interpreted in terms of small

cross-L density dropoffs and field-aligned troughs and enhancements of ionization, respectively. The cross-L dropoff in density allows two distinct rays to reach the satellite after starting at different latitudes and traveling over topologically similar paths (Chapter III.B). The trough and enhancement density structures produce unique irregularities in MR spectra and thus may be detected unambiguously in the satellite VLF broadband data (Chapter III.C, G). Such data have led to the detection of an enhancement at $L \sim 2.2$ which extends over 50° of longitude. The absence of MR whistlers (Chapter V) above $L \sim 2.4$ (well inside the plasmopause) for periods up to 12 days after a severe magnetic storm is explained in terms of trapping of whistler rays by very pronounced cross-L dropoffs (typically at $L = 1.8$ and $L = 2.4$) (Chapter VI). The field-aligned density structure (dropoffs, enhancements, and troughs) between $L = 1.8$ and $L = 3.0$ deduced from MR whistler spectra is thought to be the vestigial remains of the structure created by magnetic storms. This structure has been observed to persist for several weeks during quiet periods after a magnetic storm (Chapter VI.G).

3. The upper frequency cutoff observed on MR spectra is interpreted in terms of trapping of whistler rays by very pronounced cross-L density dropoffs. The trapping restricts the available starting latitudes from which MR whistlers can be excited. Introducing this input latitude restriction into the ray tracing calculations reproduces the observed upper frequency cutoff pattern in the MR whistler spectra without the need of Landau damping as proposed by Thorne [1968] (Chapters II.H and VI).

II. MR WHISTLER PROPAGATION IN A SMOOTH MAGNETOSPHERE

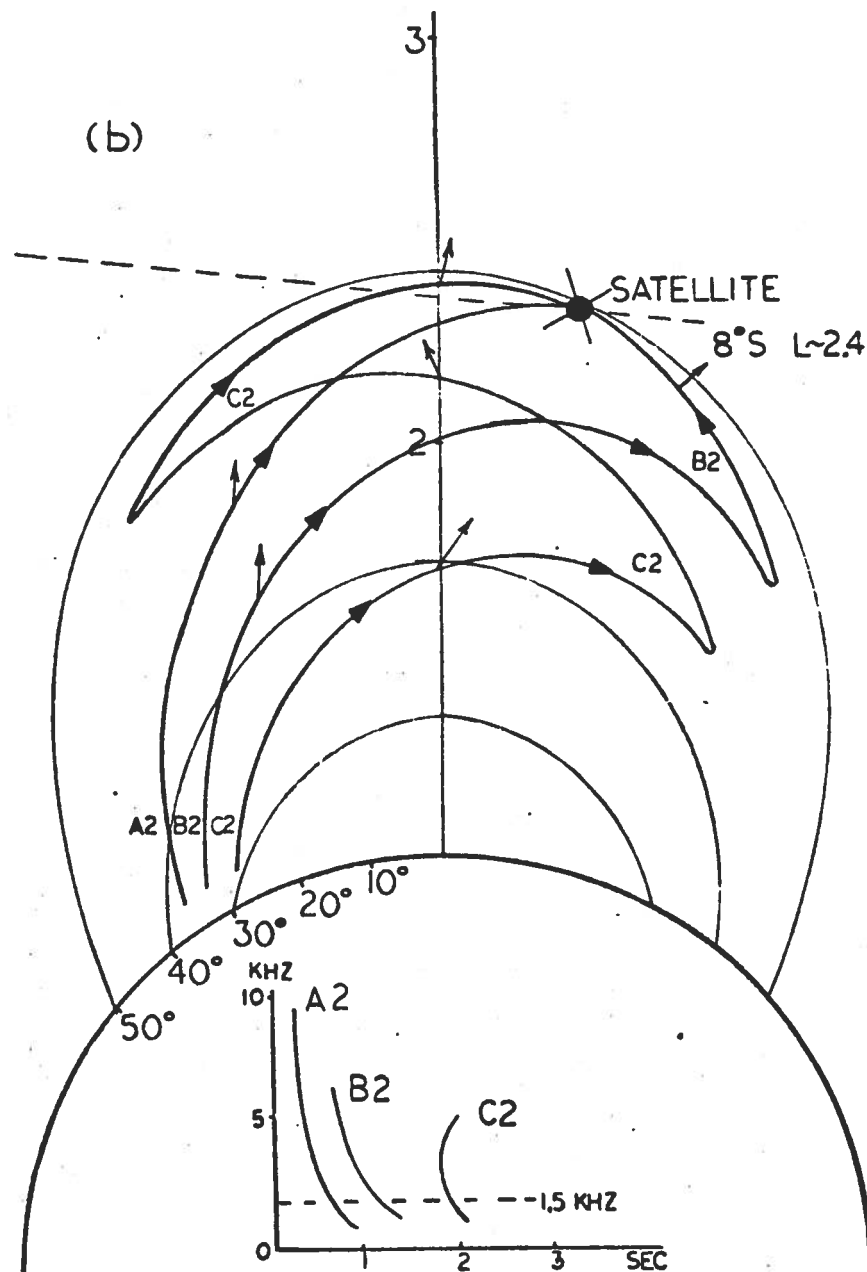
A. Introduction

Examination of VLF broadband (0.3 to 12.5 kHz) data from the OGO-1 and 3 satellites shows a wide variety of spectral forms of the MR whistler. The spectral dispersion characteristics are closely related to the location of the satellite in the plasmasphere and the plasma characteristics between the ground and satellite. In this chapter we will first examine the salient features of MR whistler ray paths in a smooth magnetosphere (i.e., free of any sharp density changes). We will assume that the distribution of ions and electrons follows diffusive equilibrium along the field lines and that the base level density at 1000 km is constant inside the plasmasphere. The study of MR propagation in a smooth magnetosphere constitutes a "first order" approach to the general problem of MR whistler propagation in a structured magnetosphere. We will demonstrate in this chapter that many of the observed frequency-time characteristics can be predicted from calculations based on first order smooth models of the magnetosphere. Based on the study of the deviations between observed and first order calculated MR whistler dispersions, appropriate perturbations in the smooth magnetospheric density models can then be inserted into the ray path calculations in order to reproduce the observed dispersions.

In the following sections we will focus on the dependence of MR whistlers upon satellite location, the formation of the nose of an MR whistler component, and the frequency dependence of the reflection process.

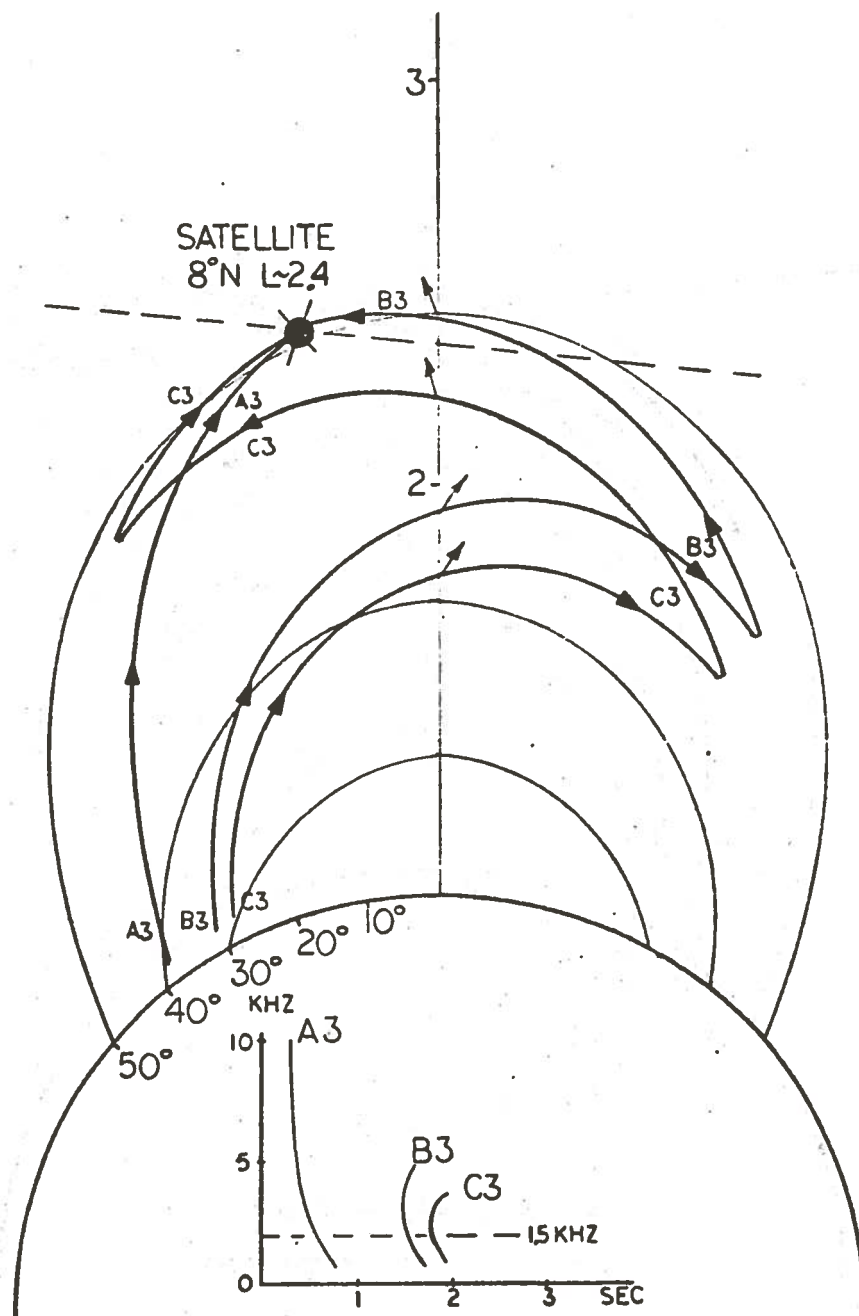
B. Spacing Patterns in MR Whistler Components

One of the most noticeable characteristics of MR whistlers is the change in MR component spacing on a frequency-time spectrogram with changes in satellite location in the magnetosphere. For the sake of illustration, we have taken a typical orbit of OGO 1 during the Fall of 1965 and have computed the ray paths and resulting spectra of MR whistlers which would be observed at geomagnetic latitudes of 18°S, 8°S, 8°N, 18°N as shown in Figs. 2.1a-d. The ray path calculation utilized



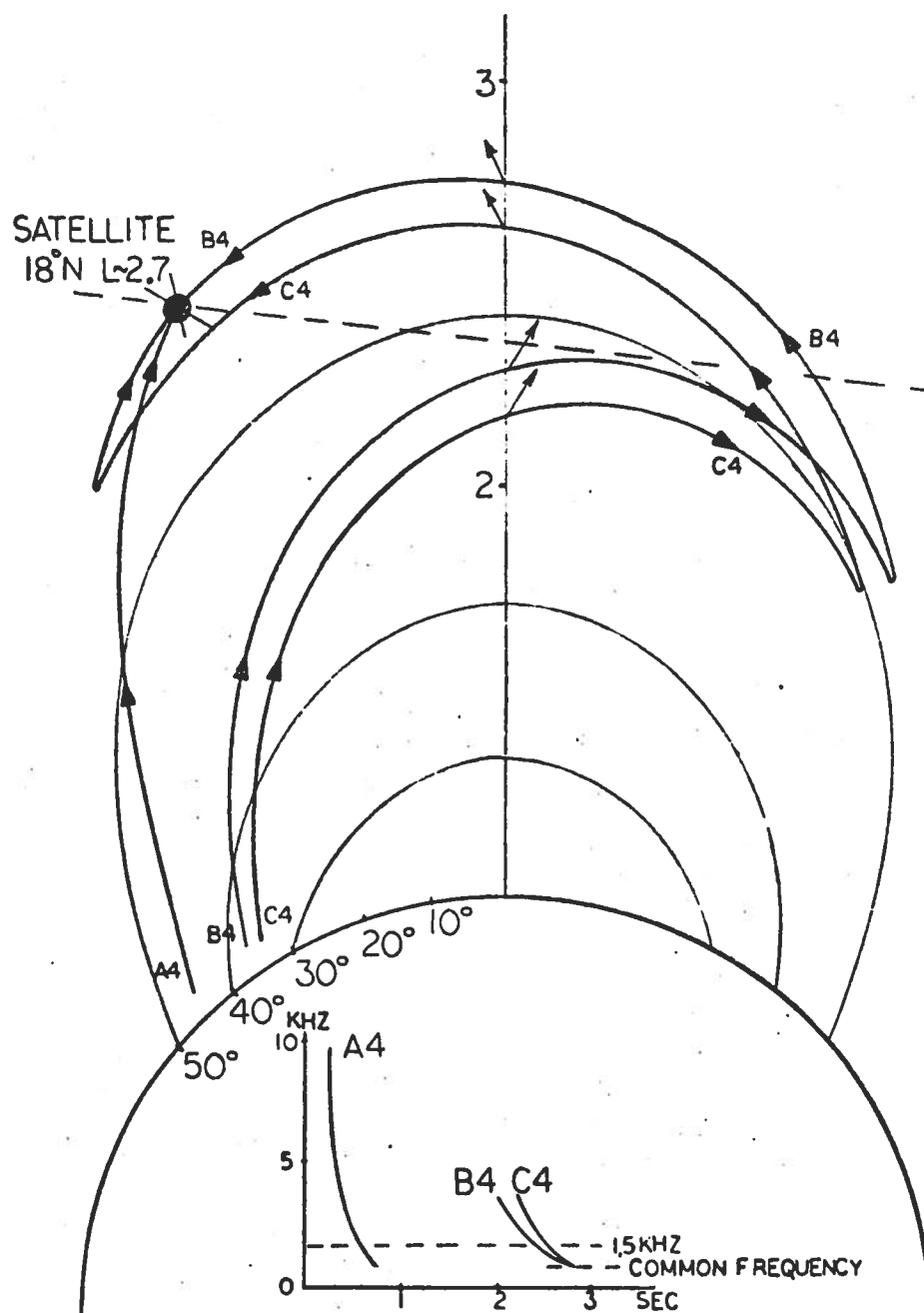
(b) 8°S, L~2.4

Fig. 2.1. CONTINUED.



(c) 8°N, L~2.4

Fig. 2.1. CONTINUED.



(d) 18°N, L~2.8

Fig. 2.1. CONTINUED.

a VLF ray tracing computer program with ion effects taken into account, first devised by Kimura [1966] with improvements by Smith [1968] and Walter [1969]. The program consists of the numerical integration of five partial differential equations formulated by Haselgrove [1954]. The program listing and the explanation of the individual subprograms has been given by Walter [1969]. All ray paths displayed in Fig. 2.1 are for the same frequency (1.5 kHz), and other frequency components would correspond to ray paths similar but not identical to the paths illustrated in the figure. The frequency dependence of the ray paths results from the effect of frequency upon the shape of the refractive index surface (c.f. Fig. 1.8). The ray paths shown in Fig. 2.1, of course, do not end at the satellite but continue on as illustrated by Fig. 1.9.

Referring to Fig. 2.1a, ray paths A1, B1, and C1 are shown for 1.5 kHz, with the MR whistler which would be observed at 18°S. Ray paths A1 and B1 closely parallel each other until the satellite is reached. Ray path B1 under-shoots the satellite location, reflects, and reaches the satellite position shortly after ray A1. However, ray C1 travels over a path which is markedly different and longer than rays A1 and B1. The resultant spectrogram shows traces A1 and B1 paired and trace C1 separated noticeably from the first two traces.

As the satellite moves to 8°S in Fig. 2.1b, paths A2 and B2 are not as close to each other as in the previous case. The resultant spectra shows that trace B2 has moved slightly in relation to A2 in the direction of trace C2. But there still exists a definite pairing between traces A2 and B2 although now to a lesser degree. When the satellite is situated on the geomagnetic equator (not illustrated), the paths are more nearly symmetrical about the equator, and thus the second trace is approximately equidistant from the first and third traces.

As the satellite crosses into the northern hemisphere, the spacing pattern between the traces continues to change. Ray paths B3 and C3 in Fig. 2.1c now parallel each other, and thus traces B3 and C3 are paired in the spectrogram. At 18°N the pairing between traces B4 and C4 in Fig. 2.1d becomes quite pronounced and the two traces actually

join together at their lowest frequency. At this "common" frequency, the turnaround point occurs at the satellite location. The trace is nonexistent below the common frequency because the ray paths for these frequencies make their turnaround above the satellite. Thus the cutoff at the common frequency is due to propagation effects.

The spacing pattern described in the preceding paragraphs is very easily observed in the satellite data. By knowing the hemisphere of the satellite, one can tell from the trace pairings whether the causative lightning source is in the northern or southern hemisphere. We will use the labels 0^+ , 1^- , 1^+ , 2^- , 2^+ , etc., to classify MR components as to their respective ray paths. Referring to Fig. 1.9, a whistler which propagates to the satellite without crossing the magnetic equator is called a 0^+ whistler (or a fractional hop whistler). One which has crossed the magnetic equator but which has not suffered a reflection is termed a 1^- whistler. The 1^+ ray path has undergone one reflection but has not recrossed the magnetic equator. The 2^- ray path is that between the magnetic equator and the second reflection. For example, ray paths A1, B1, and C1 (c.f. Fig. 2.1a) correspond to 1^- , 1^+ , and 3^- paths, respectively. Likewise ray paths A4, B4, and C4 correspond to 0^+ , 2^- , and 2^+ paths.

C. The Reflection Process

In general there are three cases of turnaround ray paths for MR whistlers. The first detailed description of the turnaround was given by Walter [1969] and covered two of the cases to be discussed below (cases 1 and 3). The other case (2) not considered by Walter, is however very important because it plays a part in the formation of the MR nose frequency. In this section we explain these three cases, using a geometrical Snell's law construction. The quantitative form of Snell's law states that

$$\mu_1 \sin \Delta_1 = \mu_2 \sin \Delta_2 \quad ,$$

where the angles $\Delta_{1,2}$ are measured from the normal to the plane of stratification as shown in Fig. 2.2a. The plane of stratification is defined as the locus of points which have the same refractive index, holding the wave normal direction constant. Appendix D results show that for a simple diffusive equilibrium density model (with the density at a base level constant in latitude) the planes of stratification lie almost along the radius vector for nearly transverse wave normals. Therefore we will assume that the magnetosphere is radially stratified in the region of the turnaround. Figure 2.2b illustrates the conservation of $\mu \sin \Delta$ using the geometric form of Snell's law during a turnaround. Since the turnaround region is small, we may assume that the normal to the stratification stays the same throughout the turnaround.

1. Case 1 (Low Frequency Case)

Case 1 covers the situation where the frequency (f) is lower than the local LHR frequency along the whole ray path. The refractive index surface is always closed, and the ray is always directed outward with respect to the magnetic field. Performing the Snell's law construction in Fig. 2.3a, we find that the ray direction rotates almost 180° as the wave normal passes through 90° . The distance between points 1 and 5 on the ray path in Fig. 2.3c, called the cross-field penetration of the ray in the turnaround region, is the largest in the low frequency case. For low frequencies ($f < f_{\text{LHR}}$) this type of turnaround always produces a ray path which walks outward in the manner of Fig. 2.1.

2. Case 2 (Gendrin Mode)

If $f > \text{local } f_{\text{LHR}}$ over much of the equatorial ray path of an MR whistler, the ray must propagate to lower altitudes in order to reach a region where $f < f_{\text{LHR}}$. In Fig. 2.4b as a ray propagates in the equatorial region where $f > f_{\text{LHR}}$, the ray direction is nearly parallel to the magnetic field. The wave normal is thus near the Gendrin angle [Gendrin, 1961] which is defined as the nonzero wave normal angle whose associated ray direction is parallel to the magnetic field. So for case 2, we will assume that the wave normal always lies inside the Gendrin angle.

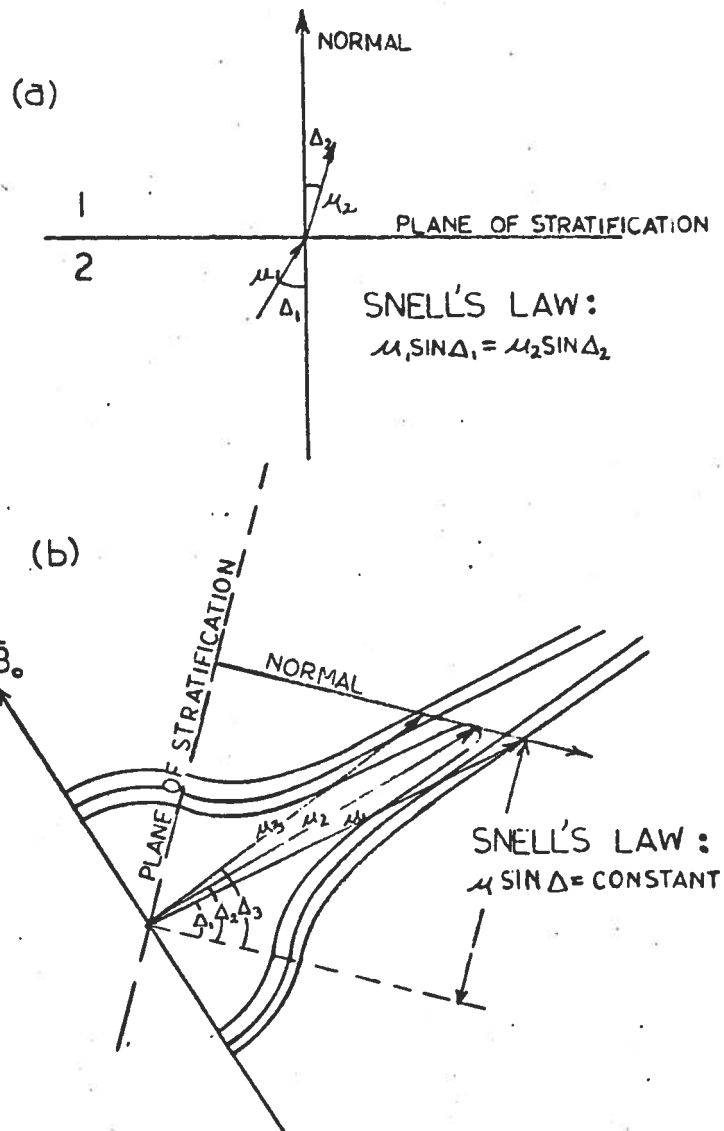


Fig. 2.2. (a) SNELL'S LAW FOR A SIMPLE CASE INVOLVING A SHARP PLANE BOUNDARY BETWEEN TWO DIFFERENT REGIONS. The regions may be either anisotropic or isotropic. (b) Geometric Snell's law construction illustrating the conservation of the refractive index component along the local stratification. The stratification refers to a fixed wave normal direction. For the case illustrated which refers to typical conditions near the turnaround the stratification is nearly radial (Appendix D).

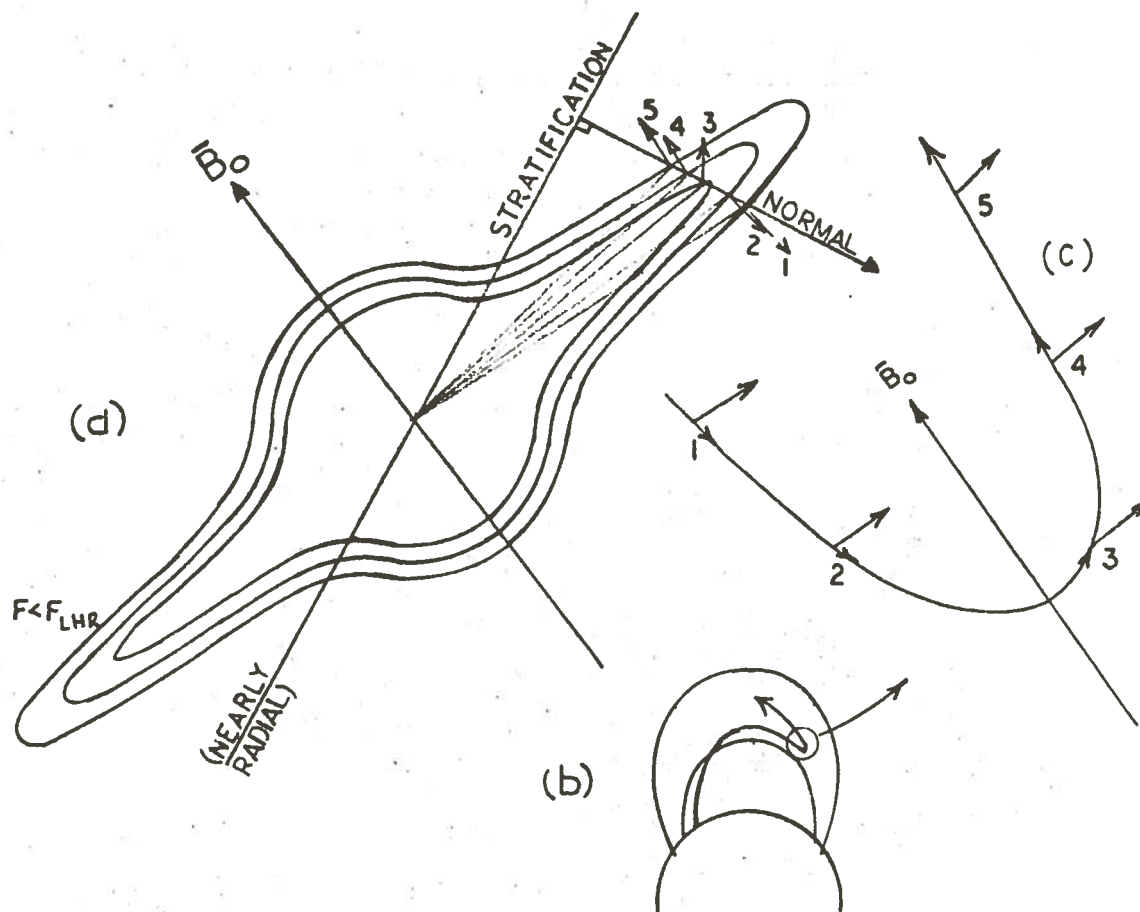


Fig. 2.3. CASE 1 TURNAROUND ("LOW FREQUENCY CASE"). (a) Sketch of the Snell's law construction during turnaround of the ray path. The refractive index surfaces remain closed throughout, and the ray remains directed outward from \vec{B}_0 before and after the turnaround. (b) Ray path in the magnetosphere. (c) Enlarged view of ray path in (b) of the turnaround region with ray directions and wave normals.

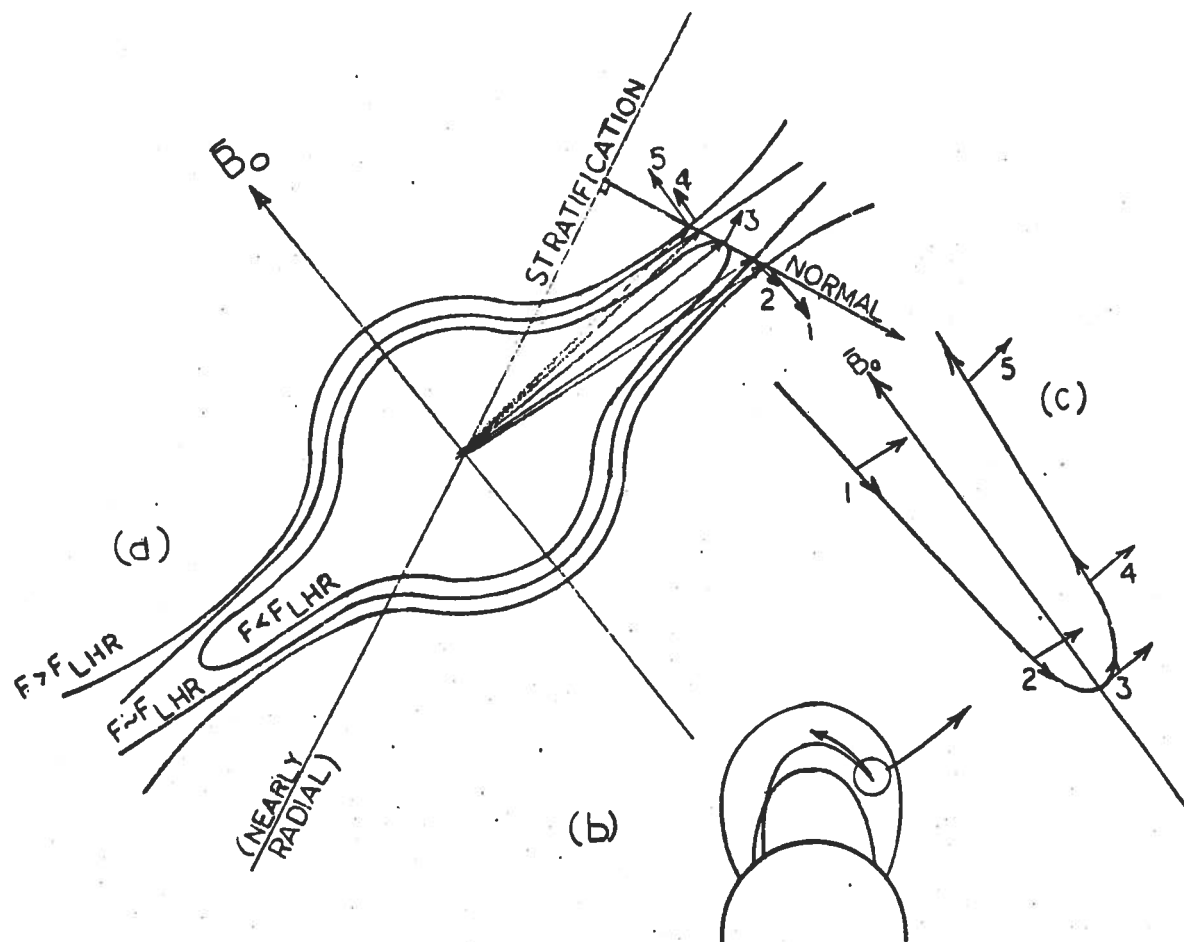


Fig. 2.4. CASE 2 TURNAROUND ("GENDRIN MODE"). (a) Sketch of the refractive index surfaces showing the opening of the surfaces as the local f_{LHR} becomes smaller than f . (b) Ray path in the magnetosphere illustrating how the ray is tightly bound to the magnetic field. (c) Enlarged view of the turnaround.

If the wave normal at Point 1 in Figs. 2.4a and c is at the Gendrin angle, then the wave normal of Point 5 lies slightly inside the Gendrin angle after turnaround, and the ray direction is directed slightly outward at Point 5. The cross-field penetration between Points 1 and 5 along the ray path is much smaller than in Case 1, and thus the ray path is more tightly bound to a particular field line than in the previous case.

3. Case 3 ("High" Frequency Case)

If f is considerably greater than the local LHR frequency as the ray traverses the equatorial region, the ray must propagate to much lower altitudes to reflect than in Case 2. The wave normal will rotate past the Gendrin angle, and the ray becomes directed inward toward lower L-shells as shown in Fig. 2.5b. As illustrated by Fig. 2.5a, we will start the Snell's law construction at a wave normal which lies well outside of the Gendrin angle. The resultant ray path loops back on itself as the resonance cone reasserts its influence on the ray direction after reflection.

In summary the three cases present the salient features exhibited by MR whistler turnaround ray paths. The reflection process is also examined with a more quantitative approach in Appendix C. The important fact is that the very low frequencies have large cross-field penetrations during turnaround as compared to higher frequencies.

After a ray is excited by an atmospheric on the ground, it may go through one, two or all of the three types of turnarounds depending on its frequency and starting latitude as it travels through the magnetosphere. In Fig. 2.6, the parameters for a typical MR ray path are plotted vs travel time. At the beginning of the ray path the wave normal is approximately half way between the longitudinal and transverse directions. During the early part of the ray path, the cross-field penetration is the largest as shown by positive slope of the L-shell plot (Fig. 2.6c). As the travel time increases the range of wave normals becomes highly restricted about the transverse position (Fig. 2.6a,b). By the fourth turnaround, the wave normal is in the Gendrin mode, and the cross-field penetration is very small. After the fifth turnaround, the wave normal

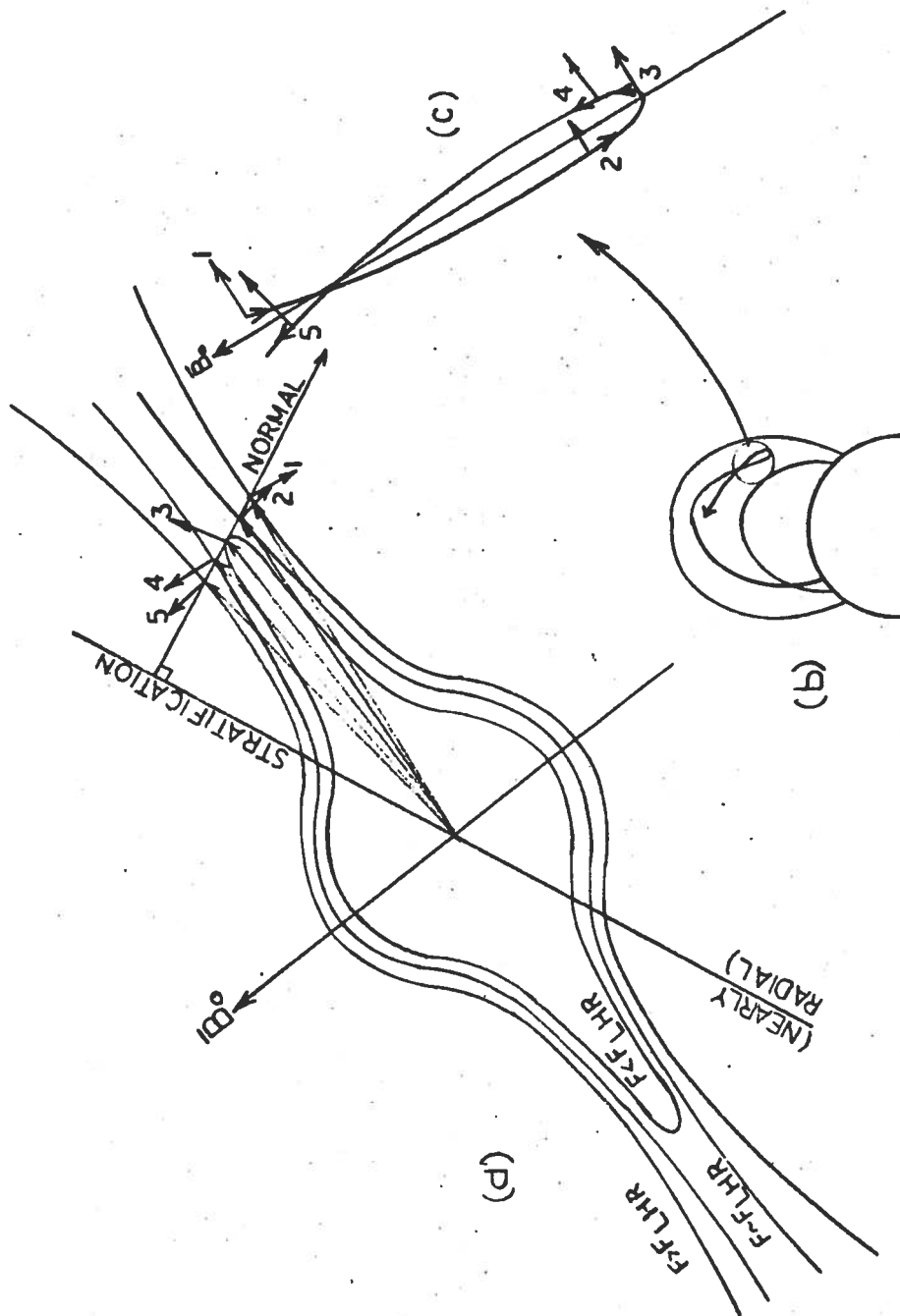


Fig. 2.5. CASE 3 TURNAROUND ("HIGH FREQUENCY CASE"). (a) Sketch of the refractive index surfaces showing the initial wave normal near the resonance cone. (b) Magneto-spheric ray path showing looping inward behavior of the ray path. (c) Enlarged view of the ray path crossing itself in the turnaround region.

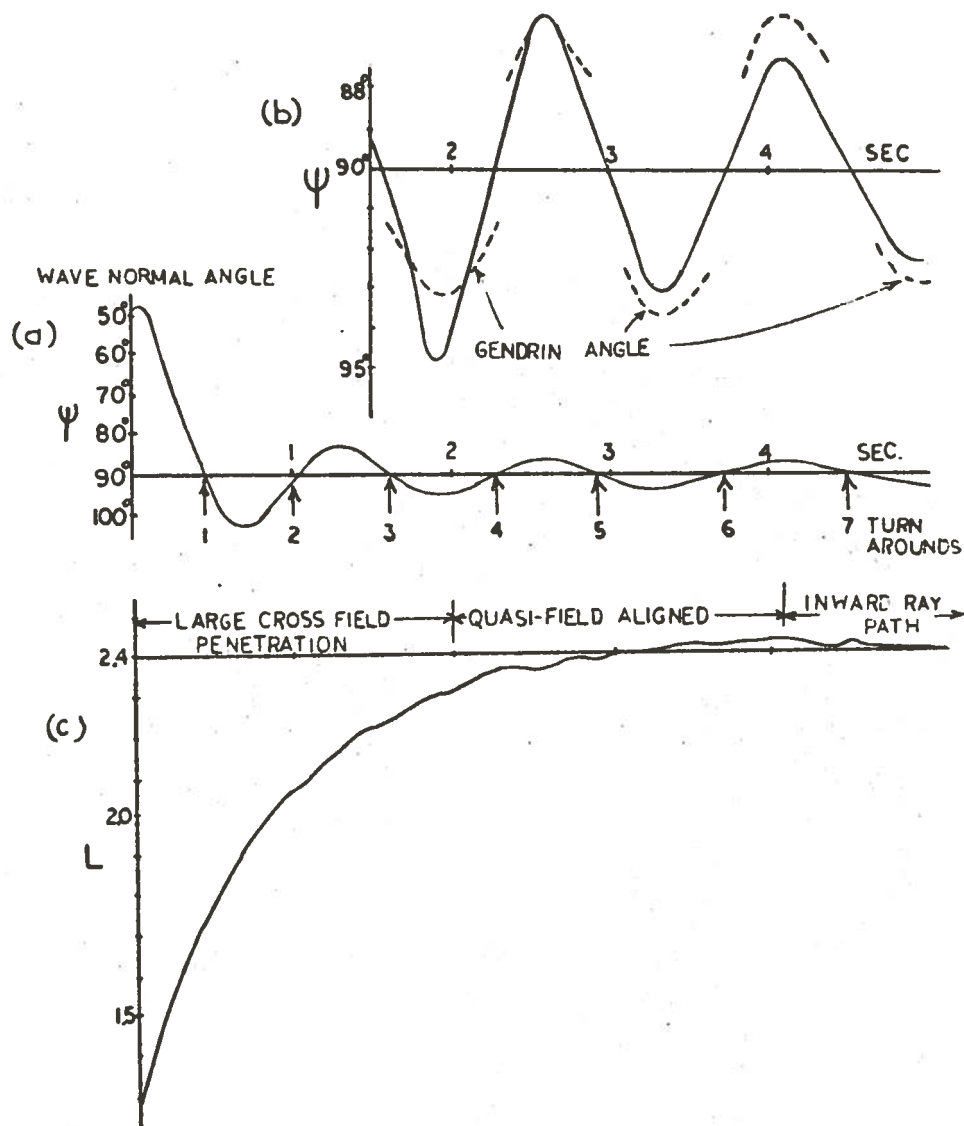


Fig. 2.6. TIME HISTORY OF WAVE NORMAL BEHAVIOR ALONG AN MR RAY PATH ILLUSTRATED FOR A WAVE AT 2 kHz. (a) Wave normal angle variation along path. The wave normal angle tends to oscillate about 90°. (b) Enlarged view of (a) showing the wave normal passing through the Gendrin angle. (c) Ray path L-shell vs travel time. The ray crosses a large range of L-shells at the beginning of the path, but after several turnarounds it tends to become trapped at some maximum L-shell. As the wave normal in (b) passes through the Gendrin angle, the L-shell along the path tends to decrease slowly.

has rotated past the Gendrin angle and the ray is very nearly field-aligned. But by the seventh turnaround, the ray path is decreasing in L-shell and looping inward on itself. So we see that for a typical example, the ray path undergoes several changes in character, all determined by the wave normal behavior.

D. Formation of the MR Nose Frequency

The formation of the nose frequency or frequency of minimum travel time of an MR whistler component occurs at the frequency which minimizes the time delay integral over the ray path. The group ray time delay is given by [Helliwell, 1965]

$$t_g(f) = \frac{1}{c} \int_{\text{path}(f)} \mu_{gr}(f) ds ,$$

where

t_g = time delay over the ray path (from the point of origin to the point of observation)

c = speed of light

μ_{gr} = group ray refractive index (see Appendix B)

ds = differential path element

$\text{path}(f)$ = ray path

Figure 2.7a illustrates the path dependence of a 1^+ component upon frequency whereby the higher frequencies travel over longer paths than do the lower frequencies. The particular example is a 1^+ MR component observed at the equator at $L \sim 2.4$. The 1.5 kHz ray path is located in the lower magnetosphere where the local LHR frequency is always greater than 1.5 kHz. The path length for 1.5 kHz is shorter than for the other two frequencies, and the corresponding turnaround is similar to Case 1 discussed in the previous section.

The 4 kHz ray path is somewhat longer than the 1.5-kHz path and is more nearly field-aligned. The equatorial portion of this path lies in

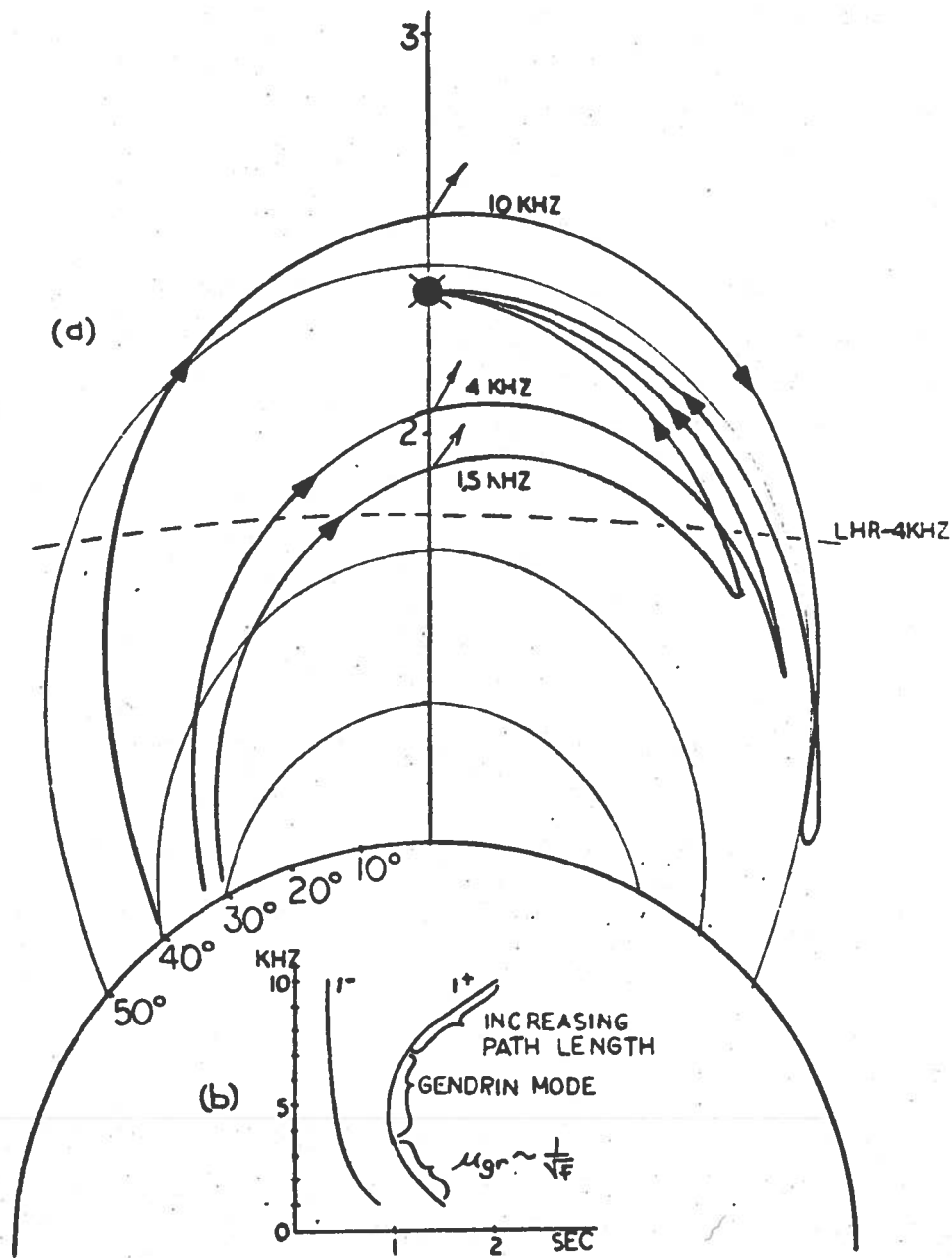


Fig. 2.7. (a) RAY PATHS FOR THE 1^+ SECOND COMPONENT OF AN MR WHISTLER AS A FUNCTION OF FREQUENCY FOR A SATELLITE LOCATION AT THE EQUATOR, $L \sim 2.4$. (b) Computed spectra corresponding to the ray paths in (a).

a region where the local LHR is less than 4 kHz, and therefore the ray must propagate to lower altitudes until the local LHR exceeds 4 kHz. Since the ray path for 4 kHz is nearly field-aligned, the wave normal lies near the Gendrin angle, and the turnaround for this frequency is described by Case 2.

The 10-kHz ray path is longer than those at the lower two frequencies, because the magnetospheric region where the LHR equals 10 kHz is located just above the topside ionosphere. The longer ray path for 10 kHz also causes the wave normal to rotate past the Gendrin angle, resulting in the type of turnaround described by Case 3. The ray loops inward on itself, causing the starting latitude to be significantly higher than at the lower frequencies.

Now we will examine the frequency dependency of the group ray refractive index and how μ_{gr} varies along the ray paths. As shown in Appendix B, μ_{gr} is also dependent upon the wave normal angle and the plasma and gyro frequencies along the path. We will use dipole latitude along the path as our independent variable because it seems to unify all these different parameters. Figure 2.8a,b shows the variations of the wave normal angle and μ_{gr} for several frequencies as functions of dipole latitude along each path. Since ray path for each frequency makes its first turnaround at a different latitude, the wave normal curves show a discontinuity at the 90° wave normal angle. The 10 kHz ray path reflects at -40° latitude and so the 10 kHz wave normal curve is continuous. The wave normal angle curves for the lower frequencies continues on the other side of -40°. The wave normal directions are similar for all frequencies near the equator but diverge in the turnaround and starting regions.

Figure 2.8b shows that for frequencies between 4 and 7 kHz μ_{gr} is essentially frequency independent in the equatorial region and is equal to

$$\mu_{gr} = 2 \frac{f_p}{f_H} ,$$

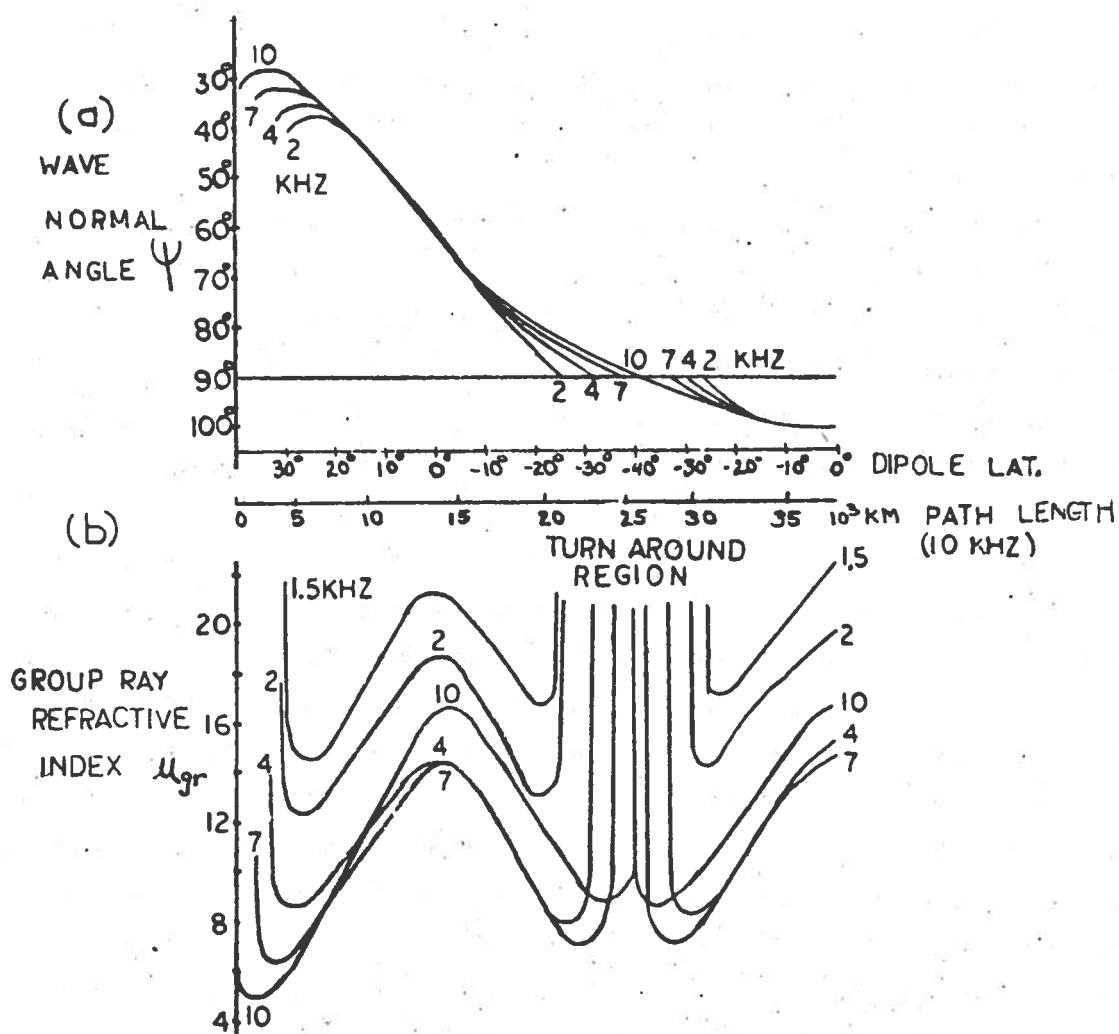


Fig. 2.8. (a) WAVE NORMAL BEHAVIOR FOR SEVERAL FREQUENCIES ASSOCIATED WITH THE RAY PATHS OF FIG. 2.7a. The wave normal angles are plotted vs dipole latitude along the path. Since the 10 kHz ray path has the maximum penetration into the southern hemisphere, its dipole latitude and path length are used as a reference for the other frequencies. The apparent discontinuities in the wave normal curve were introduced to clarify and unify the plots. (b) Group ray refractive index vs dipole latitude along the path. The Gendrin mode refers to frequencies traveling at the Gendrin velocity. The remarks about the apparent discontinuities in (a) also apply to (b).

the Gendrin [1961] mode group ray refractive index (see Appendix B). In the turnaround region the μ_{gr} curves peak off scale, generally at values greater than 100. For frequencies above the Gendrin mode frequencies μ_{gr} increases because the wave normal is approaching the resonance cone. For frequencies below the Gendrin mode frequencies μ_{gr} also increases, being inversely proportional to \sqrt{f} .

Thus the minimum value of the time delay integral occurs at the frequency whose group ray refractive index is a minimum along the entire path, and whose path length is the shortest among the band of frequencies which travel in the Gendrin mode. In our example, this nose frequency is approximately at 4.5 kHz as shown in Fig. 2.7b. The same description of the formation of the nose frequency may be applied to higher order components of MR whistlers. The ray paths for the third component along with the resultant spectra are illustrated in Fig. 2.9.

E. Density Models

For a first order approximation we will first assume that the magnetosphere can be represented by a simple diffusive equilibrium density model [Angerami and Thomas, 1964]. The electron densities are determined by

$$N_e = N_o \left[\sum_i \alpha_i \exp(-Z/H_i) \right]^{1/2}$$

where

$$Z = (r_b/r)(r - r_b)$$

r_b = reference geocentric radius

r = geocentric radius

α_i = fraction of the i^{th} ion at r_b

H_i = scale height of the i^{th} ion at r_b

N_o = reference level of electron density at r_b

N_e = electron density

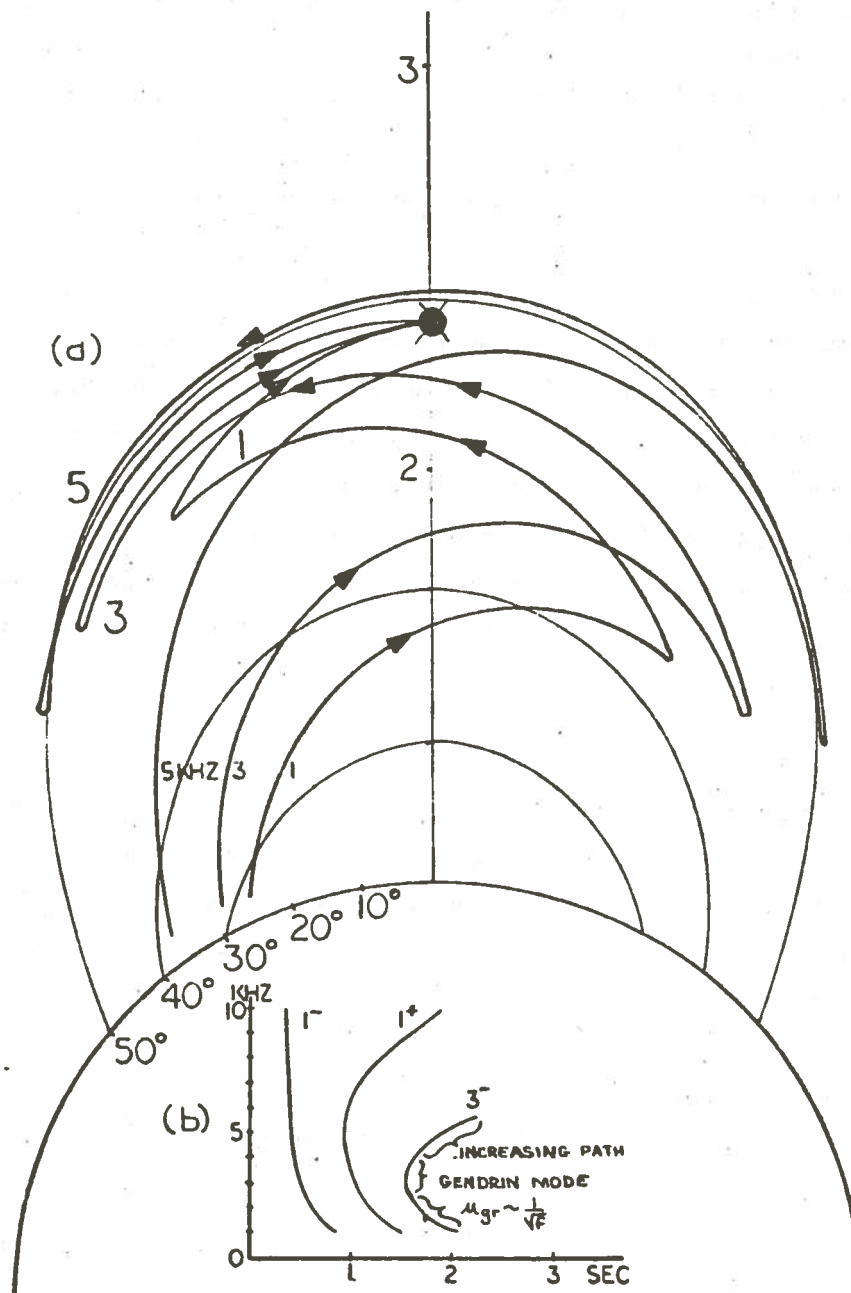


Fig. 2.9. (a) 3^- RAY PATHS FOR THREE FREQUENCIES. Notice that the 5 kHz path loops inward on itself at the second turnaround. The 3 kHz path is very nearly field aligned before and after the second turnaround; while 1 kHz path shows large cross-field penetration in its turnarounds. (b) Spectra corresponding to the ray paths in (a). The three different modes exemplified by the three frequencies are labeled on the 3^- component.

The ion densities for the i^{th} ion are given by

$$N_i = N_o \alpha_i e^{-Z/H_i} / \left[\sum_i \alpha_i e^{-Z/H_i} \right]^{1/2}$$

Two different magnetospheric models are presented in Fig. 2.10. These models differ only in ion composition and have been normalized to 10^4 el/cm³ at 1000 km altitude.

During 1965, several other satellites were making density measurements in the topside ionosphere at 1000 km altitude. Brace et al [1967], Mayr et al [1967], and Taylor et al [1968] have given ion compositions, electron temperatures, and electron density information for solar minimum during 1965 to 1966. From these sources a reasonable daytime model of the magnetosphere was composed, consisting of a 50% H⁺, 50% O⁺ ion mixture and a density of 1.15×10^4 el/cm³ at 1000 km, with a uniform temperature of 1600°K.

F. Ray Tracing Calculations

Calculation of the ray paths in the simple daytime magnetospheric model were made for 1.0, 1.5, 2.0, 3.0, 4.0, 5.0, 7.0, and 10.0 kHz and for starting latitudes between 20° and 40°, utilizing the computer ray tracing program including ion effects [Walter, 1969]. The wave normals at the starting altitude of 500 km were assumed to be vertical. This assumption results from applying Snell's law to a horizontally stratified lower ionosphere with a high refractive index.

An OGO-1 pass on 8 November 1965 at local dawn was selected to test the daytime model. On this pass there were many excellent examples of multicomponent MR whistlers to test the spacing pattern described earlier in this chapter. When the comparison between calculated and observed MR spectrograms for a particular satellite position were made using the satellite dipole latitude given by the OGO-1 ephemeris, the calculated spacing pattern was found to be slightly different from the observed spacings. This difference is shown by the second component in Fig. 2.11 (broken vs solid line). However, when the MR spectra was

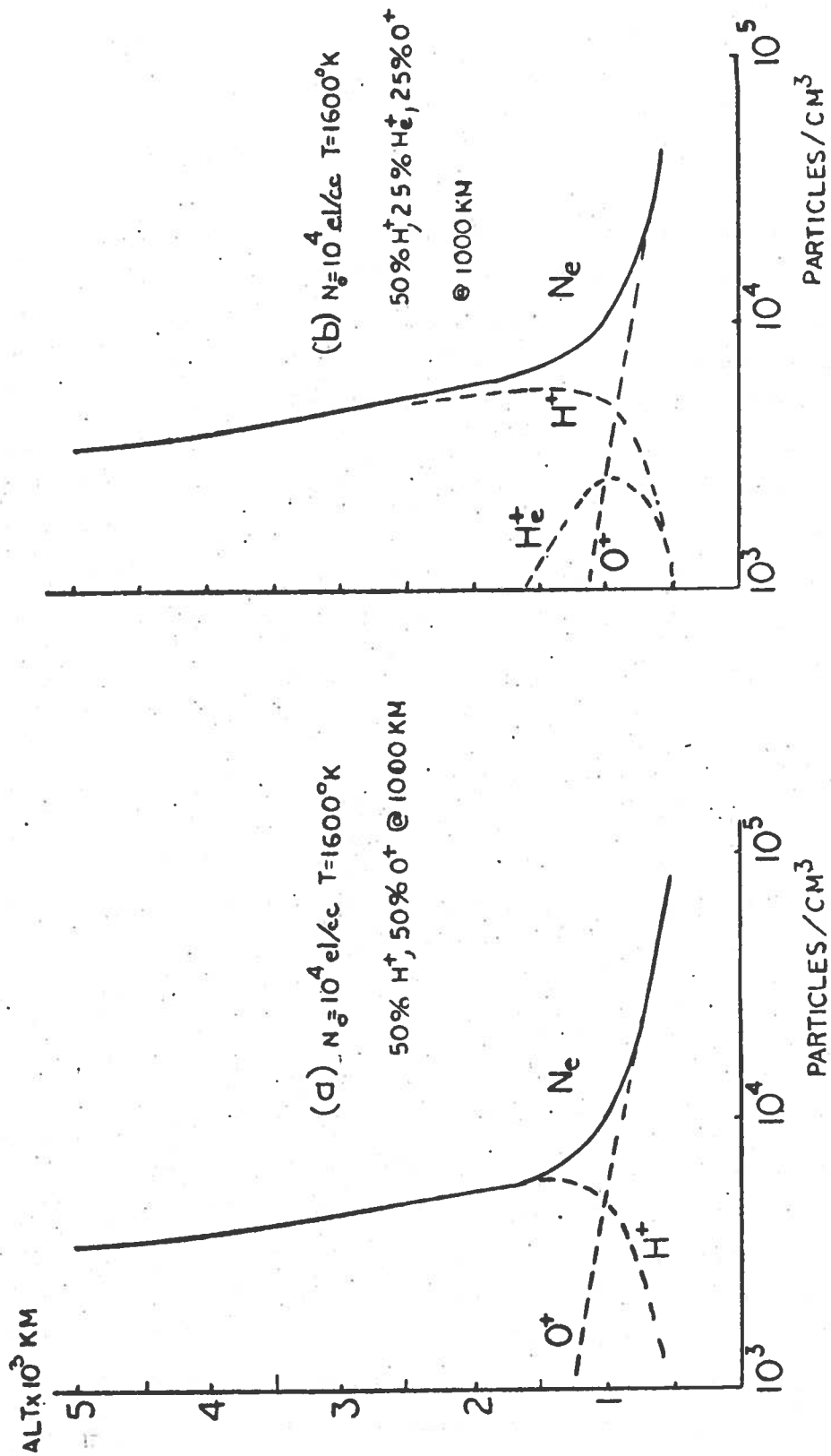


Fig. 2.10. DIFFUSIVE EQUILIBRIUM MODELS. (a) "Daytime" model contains 50% H^+ and 50% O^+ at 1000 km altitude with a uniform temperature of 1600°K . (b) "Nighttime" model contains 50% H^+ , 25% He^+ , and 25% O^+ at 1000 km altitude with a uniform temperature of 1600°K . Both models are normalized to 10^4 el/cc at 1000 km.

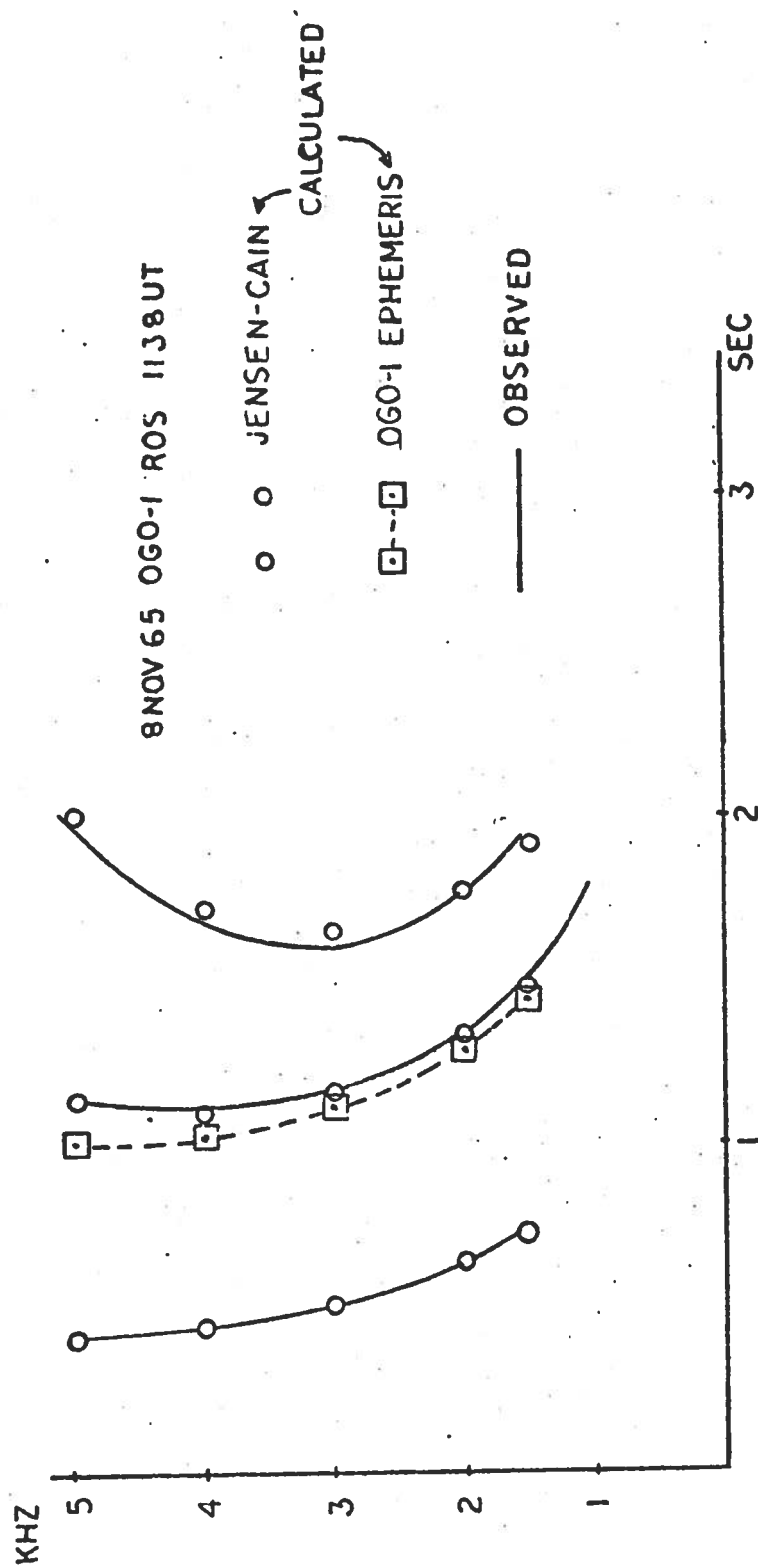


Fig. 2.11. EFFECT OF SHIFTING THE SATELLITE LATITUDE ON MR SPECTRA CALCULATIONS. Using the satellite magnetic latitude as given the Jensen-Cain magnetic field model gives a better match between calculated and observed spectrograms as opposed to that resulting from the dipole latitude for the satellite location given by the OGO-1 ephemeris.

recalculated using a satellite magnetic latitude as given by the Jensen-Cain [1962] spherical harmonic model of the geomagnetic field, a much better agreement was found between observed and calculated spectrograms (circles vs solid line). The difference between the ephemeris dipole latitude and the Jensen-Cain magnetic latitude for a given satellite location was approximately 1.4° . This difference shows that the spacing pattern of MR whistlers is very sensitive to the satellite location relative to the magnetic equator.

The predicted MR spectrograms are compared with the observed MR whistlers at four latitudes in Fig. 2.12. The agreement is very good considering that very simple models of the magnetosphere were used. The match is better at the lower frequencies, as some time delay differences above the noses are evident. Referring to Figs. 2.7 and 2.9, we find that the rays for frequencies above the nose spend part of their travel time above the L-shell of the satellite location. The rays for frequencies below the nose, on the other hand, lie completely below the L-shell of the satellite. Therefore a more rapid decrease in the densities above the satellite L-shell should be included in the model to correct for the extra time delay predicted at the higher frequencies.

Since our diffusive equilibrium model only specifies the density along the field line, we are free to vary the density distribution across field lines. Thus we can multiply our simple diffusive equilibrium model by a correction factor $N_{cf}(L)$ which is a function of L-shell. Our corrected density model of the magnetosphere is of the form:

$$N(f, L) = N_{DE}(r) \cdot N_{cf}(L)$$

where

$N_{DE}(r)$ = smooth diffusive equilibrium model, a function of r only

$N_{cf}(L)$ = correction factor, a function of L only.

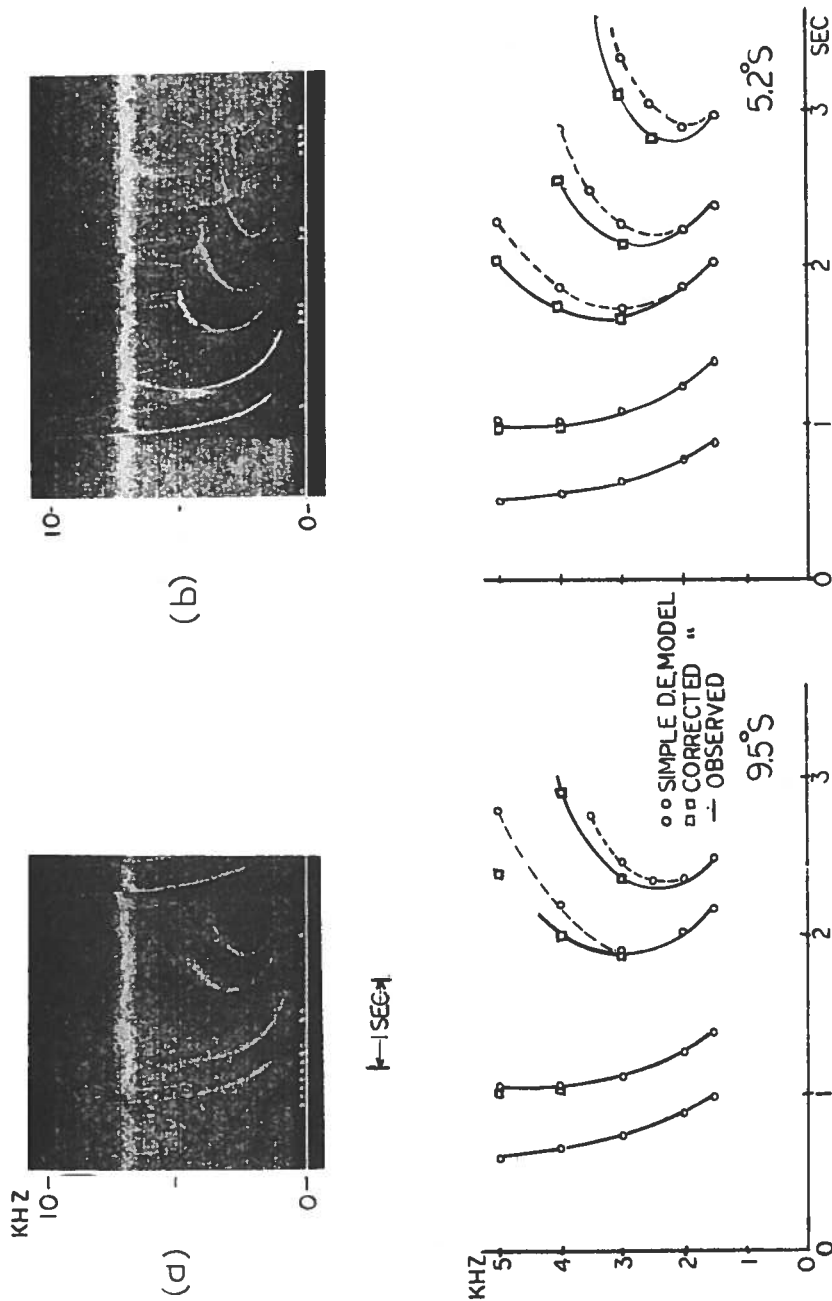


Fig. 2.12. COMPARISON OF COMPUTED (DOTS) AND OBSERVED (SOLID LINES) MR WHISTLER FREQUENCY-TIME SPECTRA FOR SEVERAL GEOMAGNETIC LATITUDES. The observations were made by OGO-1 on 8 November 1965 at local dawn. The daytime model of the magnetosphere consisted of 50% O^+ at 1000 km with a base level density of 1.15×10^4 el/cc and a uniform temperature of 1600°K. The dark line at about 7 kHz is interference associated with a voltage-controlled oscillator used to indicate amplitudes. The suppression of the background noise by the strong MR whistler components is due to the AGC of the satellite VLF receiver.

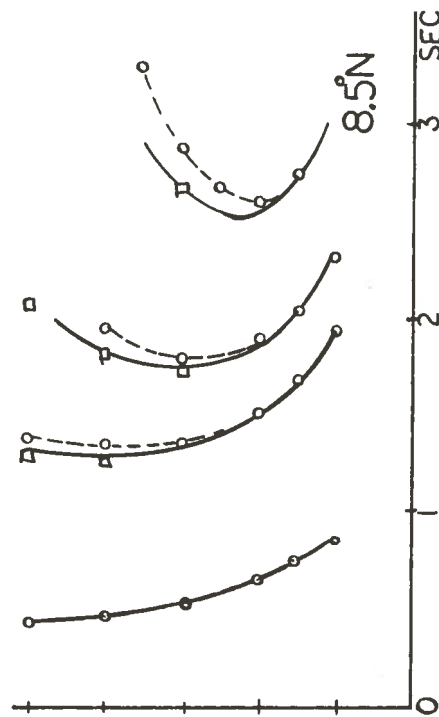
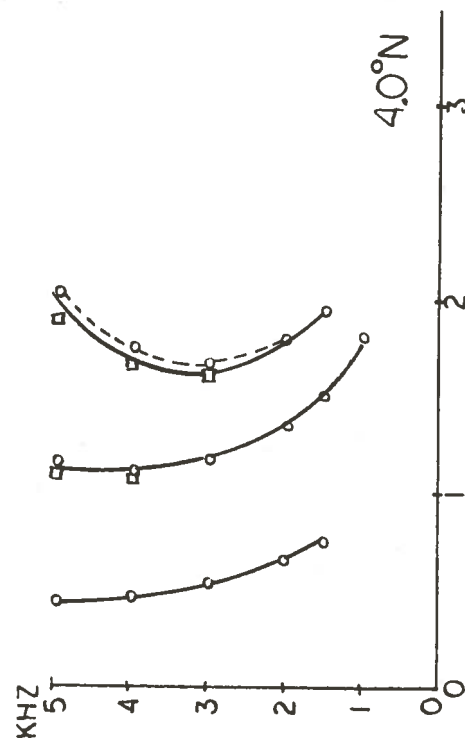
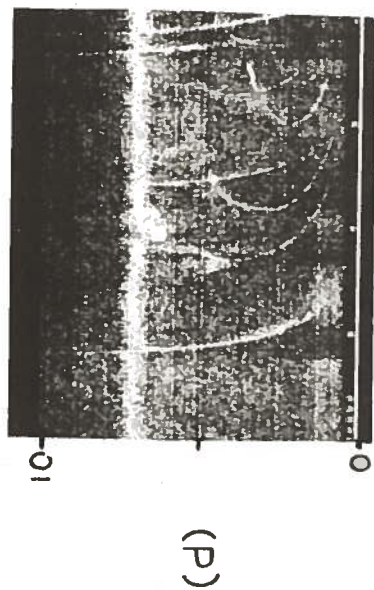
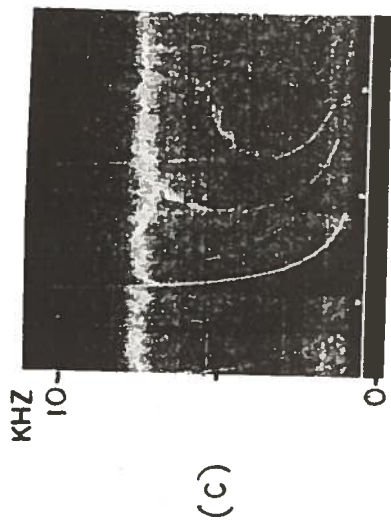


Fig. 2.12. CONTINUED.

The form of the correction factor was chosen to be

$$N_{CF}(L) = 1 - Ke^{-\frac{(L-L_o)^2}{2W^2}}$$

where

$$K = 0.9$$

$$L_o = 4.0$$

$$W = 0.8$$

which compares favorably with the normalized H^+ ion density measured by Taylor et al [1968b] during October 1965, as shown in Fig. 2.13. The corrected density model produces the desired result in reducing the calculated high frequency time delays to conform with the observed ones, as shown by the squares in the calculated spectra of Figs. 2.12a to d.

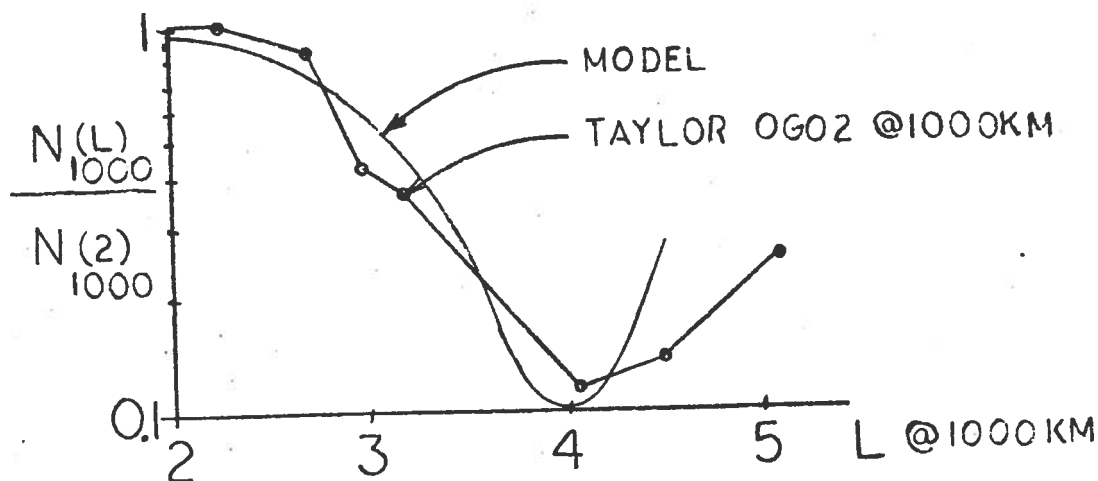


Fig. 2.13. (a) RELATIVE VARIATION OF THE ELECTRON DENSITY AT 1000 km UTILIZED IN THE RAY TRACING CALCULATIONS COMPARED TO ACTUAL PROTON MEASUREMENTS BY TAYLOR ET AL [1968b]. The proton measurements have been normalized to the proton density at $L \sim 2.0$ at 1000 km. (b) Comparison of computed spectra (dots) using the density variation in (a) to the observed MR whistler spectra.

G. Nighttime Models

An important parameter of the topside ionosphere which changes from day to night is the ion composition. Whereas during the day helium ions can be neglected, they become a very important constituent at night. This fact was pointed out by the OGO-2 ion measurements of Taylor et al [1968b]. A model composed of 50% H^+ , 25% O^+ , and 25% He^+ at 1000 km was tried in the ray tracing calculations and gave good agreement with MR whistlers observed after dusk during April 1965 as shown in Figs. 2.14a and b. The match between observed and predicted spectrograms shows a small time delay discrepancy at the high frequencies of the third and fourth components, which can be corrected for in the same way as outlined in the previous section.

The nose frequencies of MR whistlers observed at night do differ from those observed during the day. The nighttime noses are generally at lower frequencies due to the addition of helium in the models. The helium ions decrease the density gradient between 500 and 1000 km altitude (as shown in Fig. 2.10b), which is the important region where the wave normal is pulled inward. Therefore the wave normal angles in the nighttime models are larger and so are the travel times at high frequencies (cf. Section C).

H. Upper and Lower Frequency Cutoffs

If one accepts the "smooth" or slowly varying models of the magnetosphere as presented in an earlier section, then one cannot account for the upper and lower frequency cutoffs observed in the actual data. We can calculate a ray path and time delay for 1 kHz, but this frequency is generally not found in the higher order components, as shown in Figs. 2.12a to d. If we return to our previous calculations for a typical MR whistler frequency-time spectrogram, we can produce the MR whistler as shown in Fig. 2.15a. The lowest represented frequency of 1 kHz was arbitrary. The high frequency cutoff was determined by computation time. The integration step size becomes very small when the wave normal approaches the resonance cone, and thus computation time for the high frequencies becomes very long compared to that for lower frequencies.

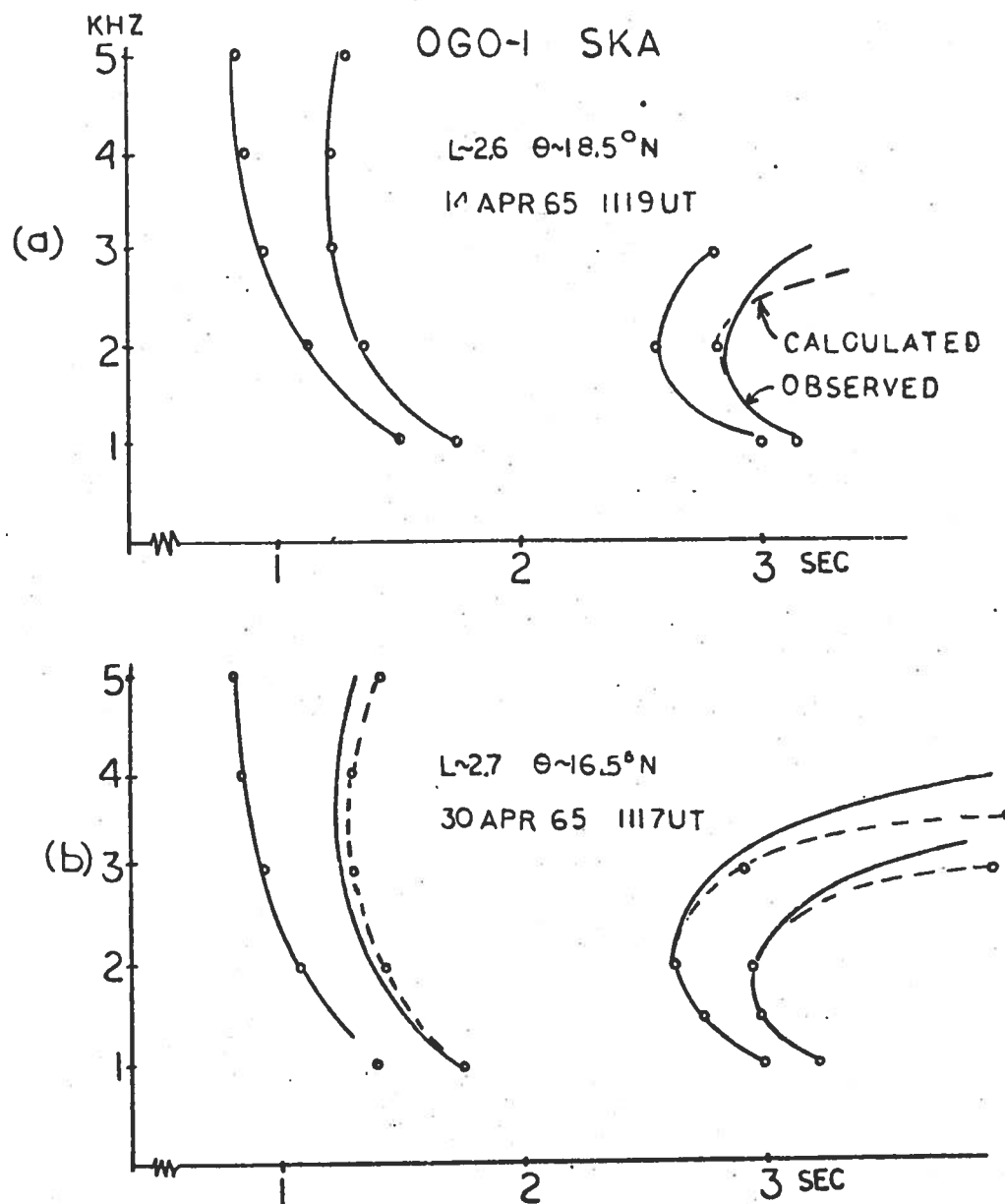


Fig. 2.14. COMPUTED AND OBSERVED MR WHISTLER SPECTRA USING THE NIGHTTIME MODEL OF 50% H^+ , 25% He^+ , AND 25% O^+ AT 1000 km WITH A BASE LEVEL DENSITY OF 10^4 el/cc AND A UNIFORM TEMPERATURE OF 1600°K . The two examples from separate OGO-1 passes in April 1965 were observed at local dusk. The match between observed and computed spectra is better on 14 April (a) than 30 April (b).

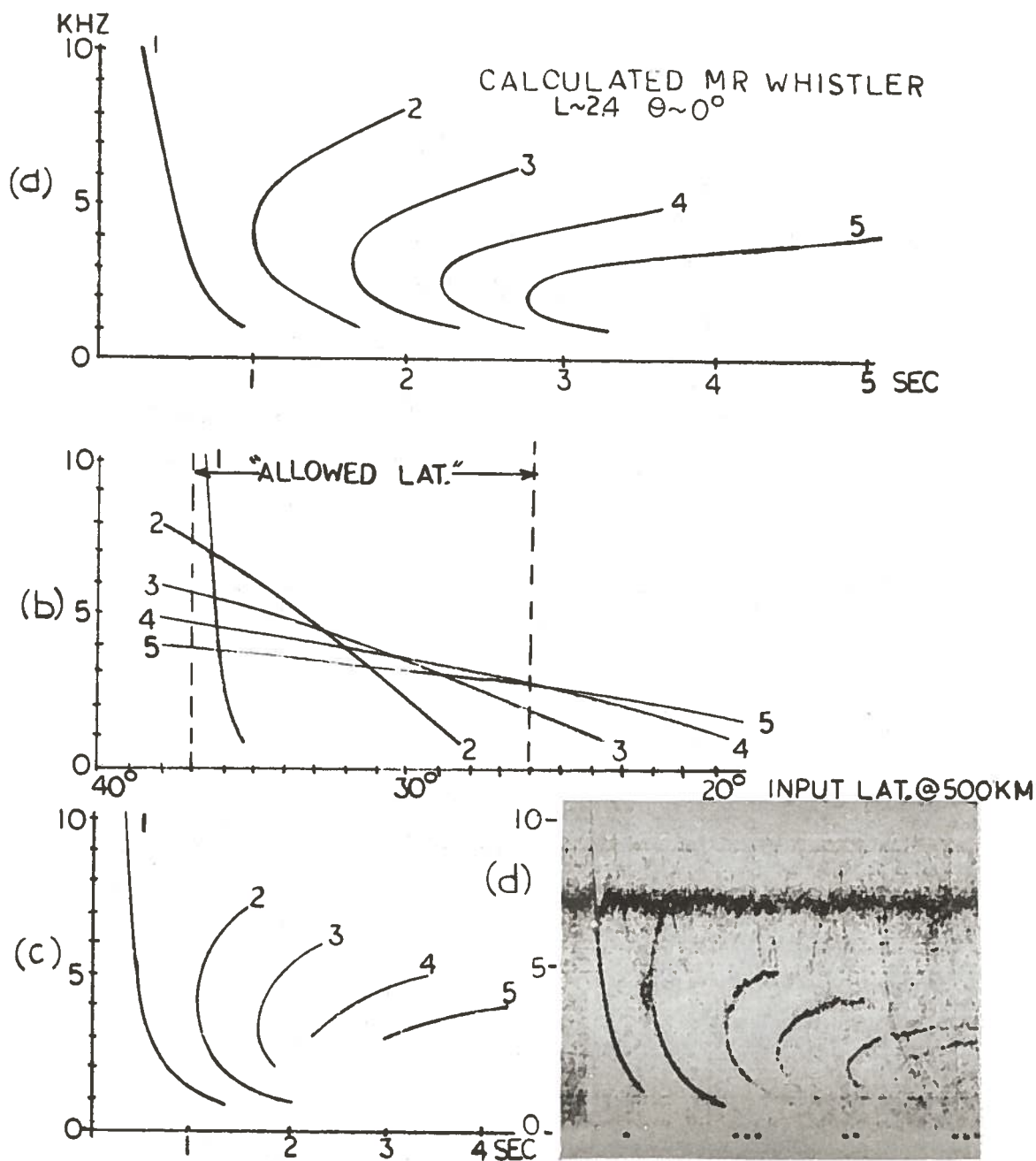


Fig. 2.15. UPPER AND LOWER FREQUENCY CUTOFFS. (a) Calculated MR spectrograms for five components with no restrictions on starting latitudes. (b) Input latitude at 500 km vs frequency for each component in (a). (c) Resulting MR spectrogram when the input latitudes are restricted to latitudes between 37° and 26° . (d) Observed MR whistler which shows upper and lower cutoff characteristics similar to (c).

The plot of input latitude at 500 km vs frequency and component number (Fig. 2.15b), shows that the high frequencies for a particular component are excited at much higher latitudes than the low frequencies. This result suggests that if one limits the input latitudes to a band of appropriate "allowed" latitudes and computes the resulting MR whistler spectrogram, upper and lower frequency cutoff patterns emerge which are similar to what is actually observed. The comparison between the actual and computed spectrograms is shown in Figs. 2.15c and d.

Examining Fig. 2.15d, we find that the upper cutoffs are very sharp for the 3rd, and 4th components but that the low frequency cutoffs are more gradual. The gradualness of the latter may be accounted by D-region absorption [Helliwell, 1965]. Calculations of the absorption loss of a vertically incident wave 2 kHz in a nighttime ionosphere show that the loss at 30° latitude is 4 dB but increases to 10 dB at 20° latitude. Since our lowest "allowed" latitude is 26°, our assumed loss mechanism for low frequencies seems to fit into this scheme of increasing absorption for decreasing input latitude. The explanation for the upper frequency cutoff mechanism is beyond the scope of this chapter but will be covered in Chapter VI.

Another loss mechanism is the defocusing suffered by a tube of rays which arrives at the satellite. The defocusing loss can be determined by taking the ratio of the input (at 500 km) and output (at satellite) cross-section areas of this tube of rays. Assuming that the rays remain in the same magnetic meridian, the defocusing loss can be expressed as

$$\text{Loss (dB)} = 10 \log \frac{d_2}{d_1} \cdot \frac{r_2}{r_1}$$

where

d_1 = separation between two adjacent rays at input altitude

d_2 = equatorial separation between the same two adjacent rays at the satellite

$r_1(r_2)$ = distance between the geomagnetic dipole axis and the input point (satellite position).

Based upon the calculated ray paths in a smooth magnetosphere, the defocusing loss for each component is listed for several frequencies in the table below.

Table 2.1
DEFOCUSING LOSS (dB)

Component No. f (kHz)	1	2	3	4	5
5	10.5	7.9	4.5		
4	10.6	8.2	6.4	4.0	2.2
3	10.6	9.6	7.1	6.0	4.5
1	10.2	10.1	8.1	7.1	6.5

The defocusing loss of the first and second components is roughly constant through the 1 to 5 kHz range, but for the higher order components, the lower frequencies undergo more defocusing than the higher frequencies. The lower frequency defocusing supplements the D-region absorption mentioned earlier. The minimal defocusing loss suffered by the upper frequency portions of the higher order components may partially account for their enhanced appearance on the spectrogram in Fig. 2.15d. This minimal defocusing would also tend to compensate for the attenuation occurring along the path due to collisions such as calculated by Kimura [1966].

I. Conclusions

Based upon the information developed in this chapter we conclude that:

1. The general characteristics of frequency-time MR whistler spectrograms can be successfully explained by VLF ray tracing calculations utilizing simple ion and electron density models of the magnetosphere.
2. The spacing patterns of MR whistler components are explained by the relative differences in ray path lengths for adjacent

components as a function of the magnetic latitude at the satellite and the hemisphere of the atmospheric source.

3. The reflection or turnaround behavior of the ray paths can be divided into three cases, depending on frequency. These three cases are the low frequency case (frequencies below the nose), the Gendrin mode case (near the nose frequency), and the high frequency case (frequencies above the nose).
4. The nose of a MR whistler component occurs in a band of frequencies propagating near the Gendrin condition in the equatorial region. The frequency of minimum travel time is approximately the lowest frequency in the Gendrin mode.
5. The upper and lower frequency cutoffs can be simply reproduced by restricting the range of input latitudes. The restriction on the lower latitude excitation could be attributed to ionospheric absorption. The enhanced amplitudes of the upper frequency portions of MR spectra could be due to minimal defocusing of MR ray paths.

III. EFFECTS OF SHARP IRREGULARITIES

A. Introduction

Frequently on MR whistler spectrograms there are extra traces of slightly different dispersions in addition to the traces predicted by ray tracing in a smooth magnetosphere. One class of this phenomenon is shown in Fig. 3.1a. There is a normal 1^- , 1^+ MR whistler pairing, with the 1^+ trace showing a large time delay at 10 kHz. However, a second faint trace labeled 1^+_{*} joins the regular 1^+ trace at 5 kHz and parallels the 1^- trace at higher frequencies.

Since our smooth magnetospheric models cannot produce this extra trace, we must modify our models slightly. The time delays based on the nighttime model discussed in the previous chapter closely duplicate the 1^- , 1^+ spectra. This model has a base level density of 10^4 el/cc at 1000 km (dashed line in Fig. 3.1f). Since the greatest contribution to the time delay occurs in the vicinity of the magnetic equator and a typical 1^+ path traverses the equatorial region beyond $L \sim 1.8$ (cf. Fig. 3.1e), it follows that the equatorial densities in our new model at L-shells above about 1.8 should not be modified. Another constraint on our new model is that it must produce an extra trace with nearly "longitudinal" characteristics since it parallels the 1^- trace. This new model must therefore produce a partial rotation of the wave normal toward the direction of the magnetic field to achieve this longitudinal characteristic. It can be shown by Snell's law [Smith, 1961] that a decrease in density across a field-aligned boundary is able to produce the desired rotation of the wavenormal toward the longitudinal direction.

B. Models

With this criterion for a density model, several density dropoff models were tried with varying degrees of success. The best results were obtained with a smooth 30% dropoff at $L = 1.8$. A ray starting near $L = 1.8$ (denoted by the broken line in Fig. 3.1e) encounters the density gradient at low altitudes, when the wave normal angle is

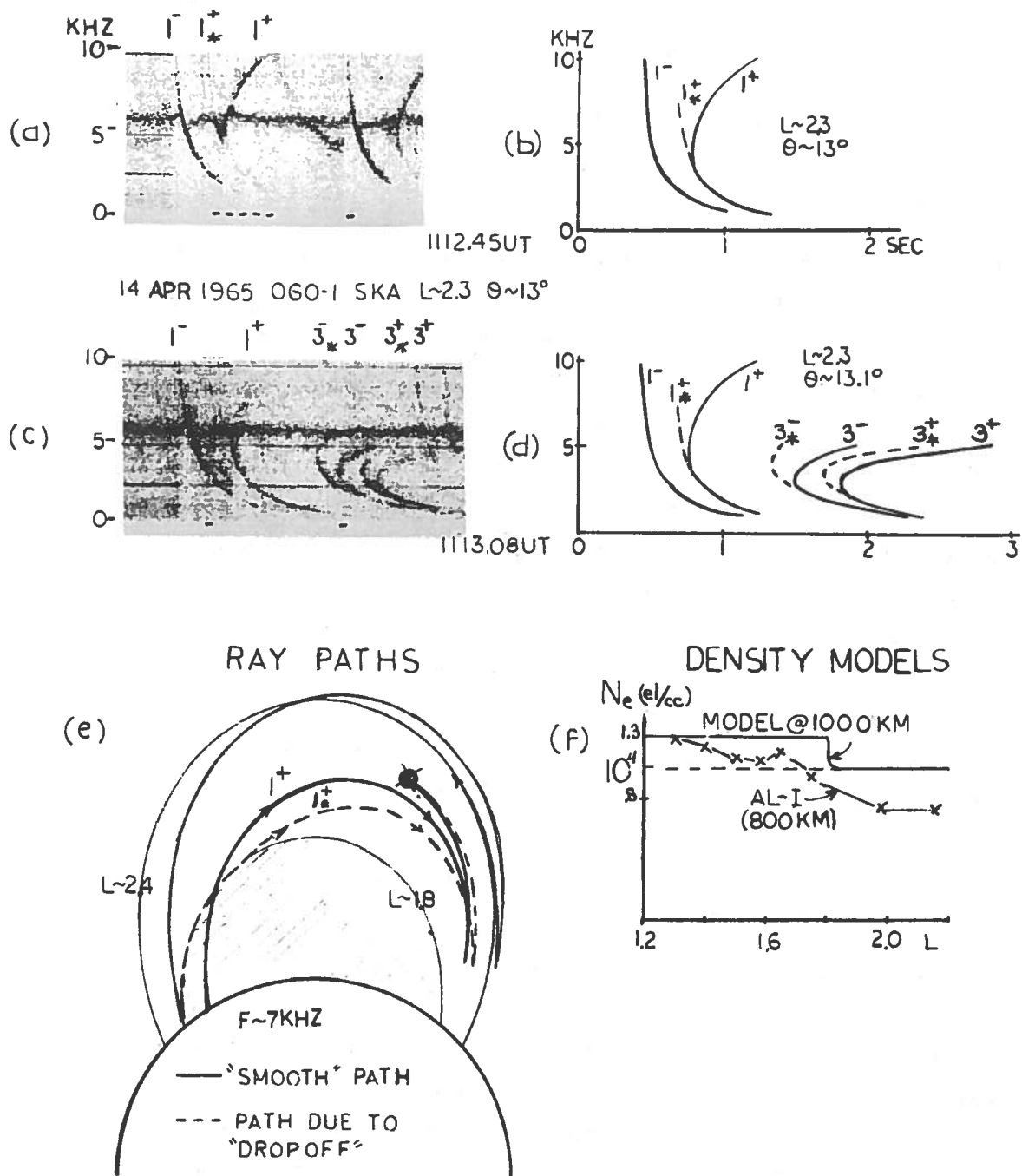


Fig. 3.1. ILLUSTRATION OF EFFECTS ON MR SPECTRA OF A RAPID DROPOFF IN DENSITY AT $L \sim 1.8$.

Fig. 3.1. ILLUSTRATION OF EFFECTS ON MR SPECTRA OF A RAPID DROPOFF IN DENSITY AT $L \sim 1.8$. (a) Observed spectra of an MR whistler exhibiting an extra 1^+_{*} component that parallels the 1^- trace. (The second event to the right of the figure does not show the 1^+_{*} trace.) (b) Spectra calculated using the electron density model represented by the solid line in (f). (c) Observed spectra of an MR whistler with extra 1^+_{*} , 3^-_{*} , and 3^+_{*} traces. (d) Spectra calculated using the model of f. (e) Ray paths for the 1^+ and 1^+_{*} MR whistler traces shown in (a) and (b). The solid line denotes the 1^+ ray path, which is not affected by the irregularity at $L \sim 1.8$. The dotted line represents the 1^+_{*} ray path, which is partially trapped by the dropoff in density at $L \sim 1.8$. This ray path is nearly field-aligned in the northern hemisphere, leading to the longitudinal characteristics of the 1^+_{*} component. (f) Profiles of the electron density models at 1000 km. The dropoff model is compared to the smooth magnetospheric model (dashed line) and to Alouette-1 sounder electron density measurements at 800 km [Bauer and Krishnamurthy, 1968] (crosses). The Alouette measurements show the existence of a density dropoff structure although it is not as sharp as the model.

still small. For this reason the wave normal direction is strongly affected by the gradient and initially rotates to the longitudinal direction producing a path which is nearly field-aligned along $L \sim 1.8$. However, since in the equatorial region the magnetic field gradient has a larger effect on the wave normal than the density gradient [Scarabucci, 1969], the ray escapes the influence of the density dropoff near the equator and propagates into the MR whistler mode. The regular MR ray path (denoted by the solid line in Fig. 3.1e) is only slightly affected by the density dropoff since the wave normal angle is large when the ray encounters the irregularity and the density gradient has greatest effect upon rays with small wave normal angles. At the satellite point above $L \sim 1.8$ the two ray paths, the regular (1^+) and the partially trapped MR modes (1_*^+), will meet producing two 1^+ components of slightly different dispersion at frequencies below about 7 kHz (cf. Fig. 3.1a).

At higher frequencies the travel time of the 1^+ ray will however increase, since the larger wave normal angle results in reflection at lower altitudes and consequent longer paths, as shown in Chapter II (compare rays at 4 and 10 kHz in Fig. 2.7). However, the 1_*^+ ray will not be strongly changed when the frequency is increased, since the wave normal angles are kept small by the density gradient, and therefore the travel time dependency on frequency is essentially through μ_{gr} . In other words, the behavior of the 1_*^+ component at higher frequencies follows the pattern of the low frequencies (Case 1 in Chapter II), for which $t \sim \mu_{gr} \sim 1/\sqrt{f}$ (cf. Fig. 2.7). The behavior just described can also be visualized referring to Fig. 3.1e. At the frequency of 7 kHz the illustrated rays reflect at nearly the same height and have therefore comparable lengths. However, at higher frequencies the reflection of the 1^+ will take place at lower heights, whereas the reflection height of the "nearly longitudinal" 1_*^+ will be nearly unchanged.

The predictions based on the above arguments have been amply fulfilled, as illustrated by a comparison of the calculated spectra of Fig. 3.1b with the data of Fig. 3.1a. Note also that when the satellite is at a higher altitude the 1^+ and 1_*^+ components will join at a lower frequency.

The irregularity will also produce higher order components as shown in Fig. 3.1c. The appearance of the 3^- , 3^+ components is such that the traces seem to experience splitting. Trace splitting can be predicted up to $L \sim 3$ in this model, and in the actual example of 14 April 1965 it was observed up to $L \sim 2.8$. When compared to an Alouette-1 pass [Bauer and Krishnamurthy, 1968] on the same day, longitude, and local time, the two density profiles in the topside ionosphere are somewhat similar, but the Alouette-1 profile does not show the sharpness of our model. But it does show a comparable decrease in density at $L \sim 1.65$.

Figure 3.1 shows that an MR whistler observed at one L-value can be affected by an irregularity located on a lower L-shell. This conclusion is important because satellite VLF data may only extend down to $L \sim 2.2$. The observation of trace splitting allows extrapolation of density structure information to well below $L = 2.2$.

C. Theoretical Basis for Other Types of Irregularities

It is an experimental fact that enhancements of ionization which are field aligned exist in the magnetosphere. This observation has been deduced from ground [Helliwell, 1965] and satellite observations of whistlers [Angerami, 1970]. It would be interesting to see theoretically the effects of enhancements or "ducts" upon the MR ray paths. In Fig. 3.2c we illustrate these effects produced by a model represented by a field aligned gaussian shaped duct placed at $L = 2.2$. The duct has a 30% enhancement and a half-width of .03 L-shell. These parameters were purposely chosen to be much sharper than normally observed whistler ducts so that its effects on the ray paths would be easily detected. As shown in Fig. 3.2c two rays starting 1° apart undergo radical defocusing as they encounter the duct. The ray starting at 33° encounters the increase in density just before the first reflection. The increase in density rotates the wave normal angle toward 90° . The ray direction becomes very field-aligned, and after reflection (still in the inner flank of the duct) the path starts to turn inward. The ray starting at 34° encounters the increase in density soon after crossing the equator. The wave normal is rotated by the increase in density toward 90° resulting in a very field-aligned path

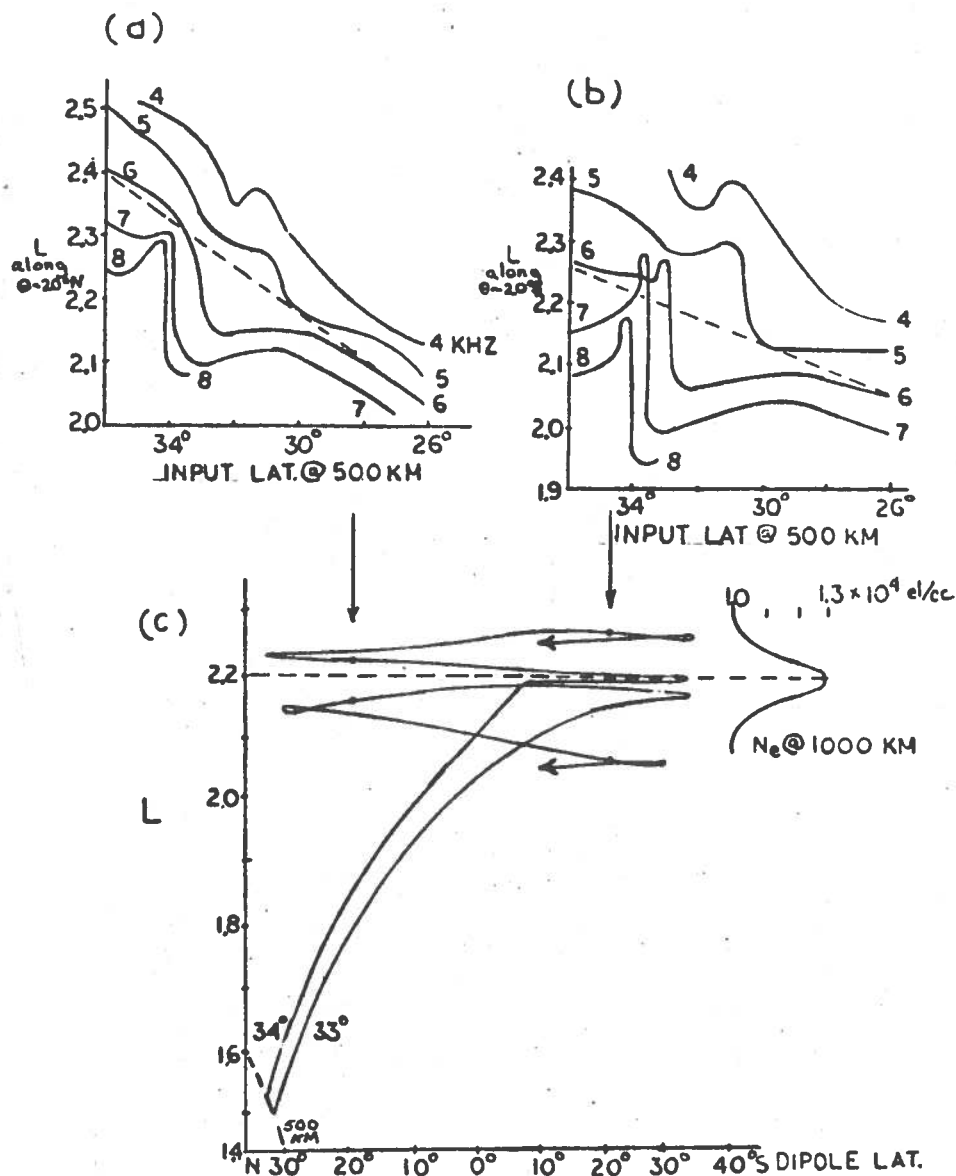


Fig. 3.2. THEORETICAL EFFECT OF AN ENHANCEMENT AT $L = 2.2$ UPON MR WHISTLER RAY PATHS. (a) Input latitude at 500 km vs satellite L-shell at 20° for the 2^- MR component. The observation point for the 2^- trace is varied between $L \sim 2.0$ and $L \sim 2.5$, and input-output curves are plotted for 4, 5, 6, 7 and 8 kHz. As a reference, the input-output curve for 6 kHz in a smooth magnetosphere is shown by a dashed line. The main effect of the duct is to perturb the smooth magnetosphere input-output characteristics over a limited range of L-shells near the duct resulting in defocusing and focusing of the ray paths. (b) The input-output characteristics for the 3^- MR component with the satellite position at -20° latitude. The defocusing region has expanded as compared to (a). (c) Paths of rays at 6 kHz starting at 33° and 34° latitude. The 33° ray makes its first turnaround under the influence of the density increase side of the enhancement, which guides the ray until it turns inward. The 34° ray path turns around at the center of the duct and crosses over to the other side. The duct causes the two rays to diverge from each other to cause the defocusing shown in (a) and (b).

until reflection. After reflection, however, the ray is on the density decrease side of the duct where the wave normal is rotated toward the longitudinal direction. Under the influence of the decreasing gradient, after the second turnaround the ray is still directed outward.

As shown in Fig. 3.2c, the duct essentially divides the raypaths much as an obstacle in the middle of a stream. It is also apparent that the amplitudes will be small along the regions illuminated by any of these two rays because of the strong defocusing. This can clearly be seen by looking at the input latitude vs the satellite L-shell along constant latitudes $\pm 20^\circ$ as illustrated in Figs. 3.2a and b. The effect is frequency dependent, showing a larger defocusing and focusing for the high frequencies than for the low frequencies. The spreading loss at 6 kHz between starting latitudes of 33° and 34° is approximately 8 dB. Normal spreading loss due to magnetic field spreading is less than 4 dB. The duct therefore implies that the 2^- component at $+20^\circ$ will have an extra attenuation of -4 dB at 6 kHz between $L \sim 2.17$ and 2.32 (Fig. 3.2a).

If we calculate the MR whistler spectrograms for a constant latitude of 20° varying only L-shell, then the sequence of Fig. 3.3 is arrived at. At L-shells above the duct center the 2^- , 2^+ traces have flattened tops. As the satellite approaches the duct from above, the flat tops of the traces begin to form a peak at the beginning of the flat portion. At the center of the duct, the peaks are still there, but the traces have started to elongate to higher frequencies. Below the duct the traces do not exhibit the sharp features, but they are still definitely distorted. Since this progression approximates the OGO-1 satellite path as it approaches perigee, we should be able to observe this continuous distortion of the traces as long as the satellite is in the vicinity of the duct.

The sequence of examples of MR whistler on the right side of Fig. 3.3 follows the progression shown by the calculated spectra on the left. The observed traces in Fig. 3.3a show top flattening as predicted by the model but do not demonstrate the extreme steepness in the first part of the 2^- trace as does the calculated spectrum on the right. A duct with wider dimensions would probably reduce this extreme steepness in the calculated spectrum since the steep portions of the traces are the portions

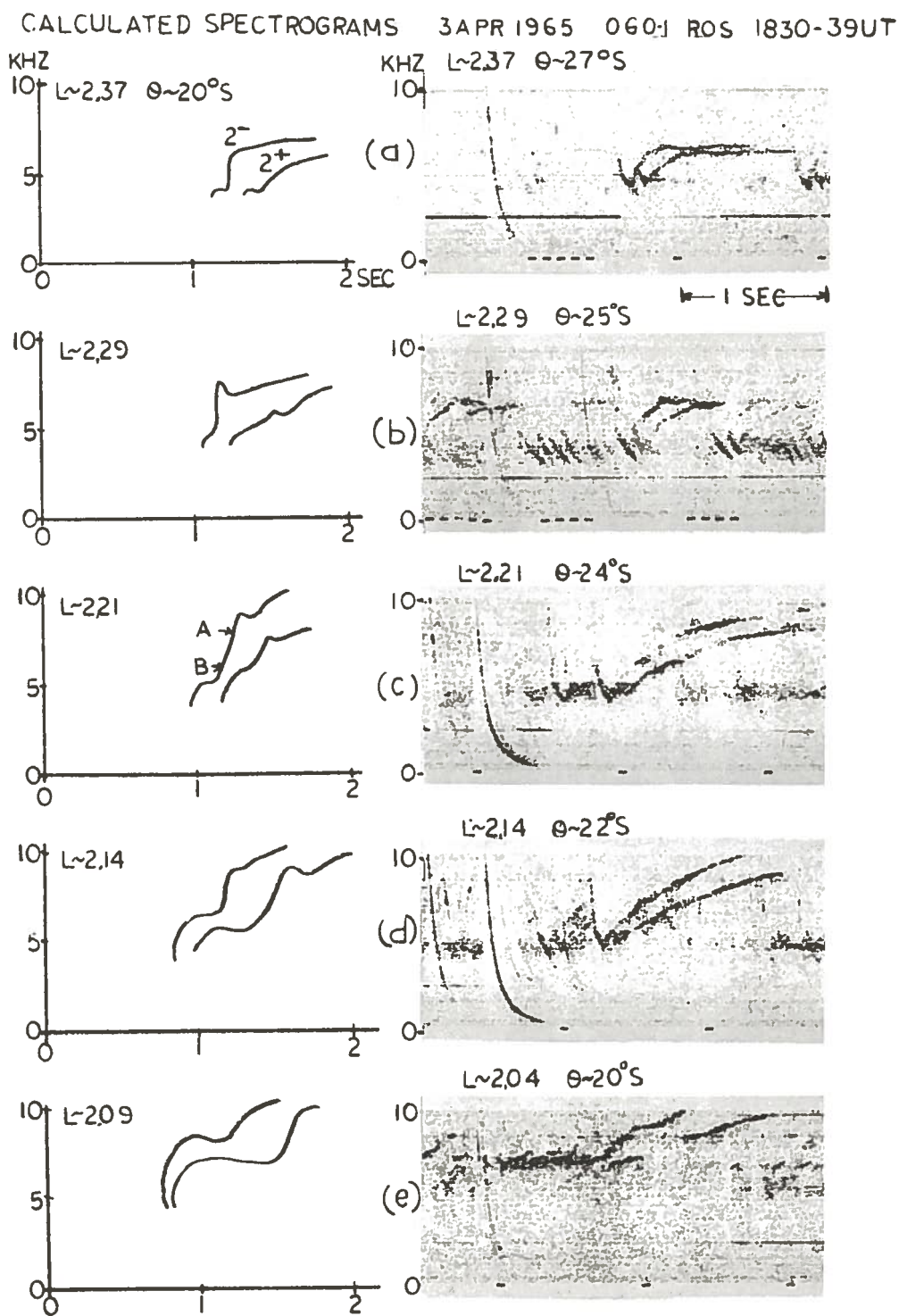


Fig. 3.3. SEQUENCE OF CALCULATED $2^- 2^+$ MR SPECTROGRAMS FOR THE DUCT MODEL OF FIG. 3.2 COMPARED TO A SEQUENCE OF OBSERVED $2^- 2^+$ MR WHISTLERS WHICH SHOW SIMILAR SPECTRAL DISTORTIONS.

strongly affected by the defocusing of the rays by the duct. The defocusing occurs at the center of the duct. The gap in the spectra in Fig. 3.3c corresponds to the frequency range A and B in the calculated spectra, which shows the greatest defocusing. The peaking of the traces indicates that the satellite is above the duct center. Examining the observed spectrogram on the right of Fig. 3.3c, we see that there are gaps in the traces which indicate strong attenuation. The correspondence between the predicted defocusing and the gaps in the observed spectra is one more piece of evidence of the validity of our model. Below the duct center the traces become "wavy" as shown by the calculated and observed spectra of Fig. 3.3c and d. Extrapolating from these examples one can approximately locate the L-shell of the duct center by observing the type and sequence of trace distortion.

The extra traces which join the regular 2^- , 2^+ traces in the observed spectrogram of Fig. 3.3a are produced by a dropoff in density at $L \sim 1.8$. The sharp lower cutoff in the observed spectrograms indicates on the basis of Fig. 3.2a that MR whistler ray paths were not excited at starting latitudes below 30° (cf. Section II.H). The cause of the noise band just above this propagational cutoff is not known but may be related to Landau growth [Thorne, 1968].

D. Comparison with Other Models

The comparison between predicted and observed MR whistlers in Fig. 3.3 provides good circumstantial proof of duct interactions with MR whistlers. The case for such would be greatly enhanced if no other simple model can be shown to produce such distortions in the spectrograms. In Fig. 3.4, the duct model is compared to other models which have 30% increase, 30% decrease, and no variation at $L \sim 2.2$. The time delay for the 3^- MR component at 6 kHz is plotted vs satellite L-shell position at -20° latitude for the four models in Fig. 3.4a. As would be expected, the "smooth" model curve is relatively straight; whereas the other models produce considerable deviations. Figure 3.4b shows, for the four models, the L-value along $20^\circ S$ corresponding to the 3^- MR component at 6 kHz, plotted as a function of initial latitude. Since the rays starting at 33° and below do not cross the center of the duct,

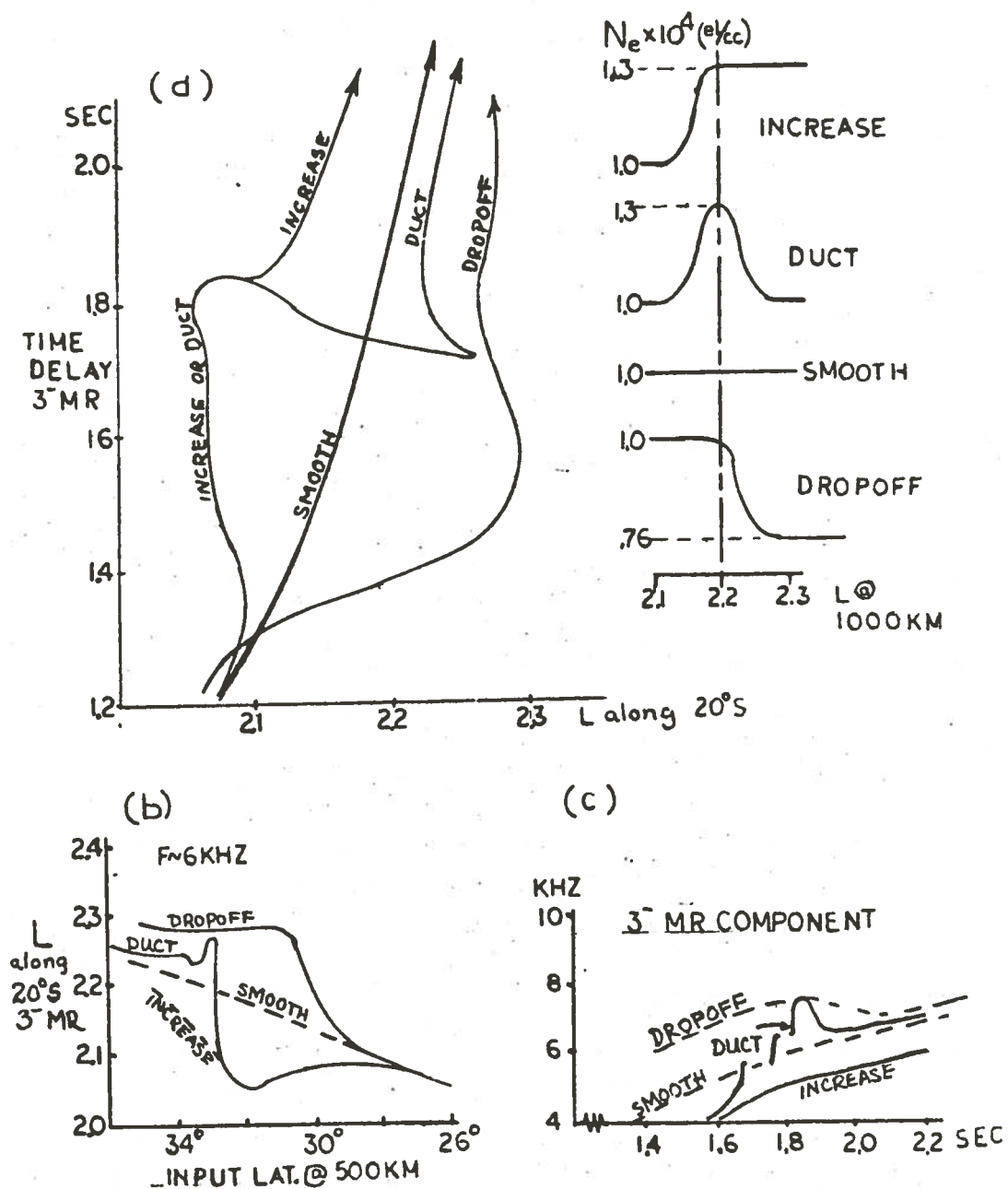


Fig. 3.4. CHARACTERISTICS OF THE 3^- MR COMPONENT AS PREDICTED BY FOUR MAGNETOSPHERIC DENSITY MODELS. (a) Comparison of time delays at 6 kHz for the 3^- MR component after propagating through the four magnetospheric models. (b) Input latitude vs satellite L-shell at -20° latitude for $f = 6$ kHz. (c) Calculated spectrograms of 3^- MR observable at $L = 2.2$, 20° S in the four models. The duct-affected trace shows the most significant characteristics.

their behavior is identical in either the "duct" or "increase" models (Figs. 3.4a and b). Above 34° the two models deviate widely. The increase model has no gradient above $L = 2.2$ and accordingly the corresponding time delay parallels that of the smooth model. However, for starting latitudes greater than 34° , the rays in the duct model encounter a sharp decrease in density and the time delay curve must take on the characteristics of the dropoff model.

The transition between the dominance of the increasing and decreasing densities produces a time delay curve of unique nature which is given by no other irregularity model investigated here. In this transition region, there occurs a minor yet observable phenomenon; bands of frequencies 0.75 kHz wide experience the same time delay at the satellite position. In Fig. 3.4a, this constant time delay over a band of frequencies occurs near the transition between the "increase" and "duct" models (1.84 sec). Although the full explanation of the phenomenon is not available at this time, it is closely related to the defocusing of the ray paths occurring around the duct. Of all the predicted 3^- MR traces for the four models shown in Fig. 3.4c, the duct trace exhibits the sharpest variation and thus is easily recognizable on a spectrogram.

In Fig. 3.5 there is further evidence of duct interaction with MR whistlers. The examples in Fig. 3.5 are 1^- , 1^+ , 3^- , and 3^+ MR whistlers observed by OGO-1 on several passes during April 1965. Below and in the duct center, the peaking of the $3^- 3^+$ traces is reduced but is still recognizable. The time banding phenomenon shows up as discrete blobs on the leading portions of the $3^- 3^+$ traces in Figs. 3.5d and g. This phenomenon does not show up on the $2^- 2^+$ traces of Fig. 3.3 because it is apparently dependent upon the extreme defocusing of the $3^- 3^+$ components. In Fig. 3.5c, the frequencies between points A and B suffer this extreme defocusing, and as shown in Fig. 3.5d, a gap in the 3-trace exists where a peak theoretically should be. The identification of the duct center based on these examples thus relies on the observation of the peaks on the 3^- and 3^+ components and of the gap in the spectra.

The 1^+ trace dispersion also shows the effects of the duct. Below the duct, there is no observable effect as shown in Fig. 3.5d, but above the duct center the 1^+ trace is bent back at the high frequencies, as in

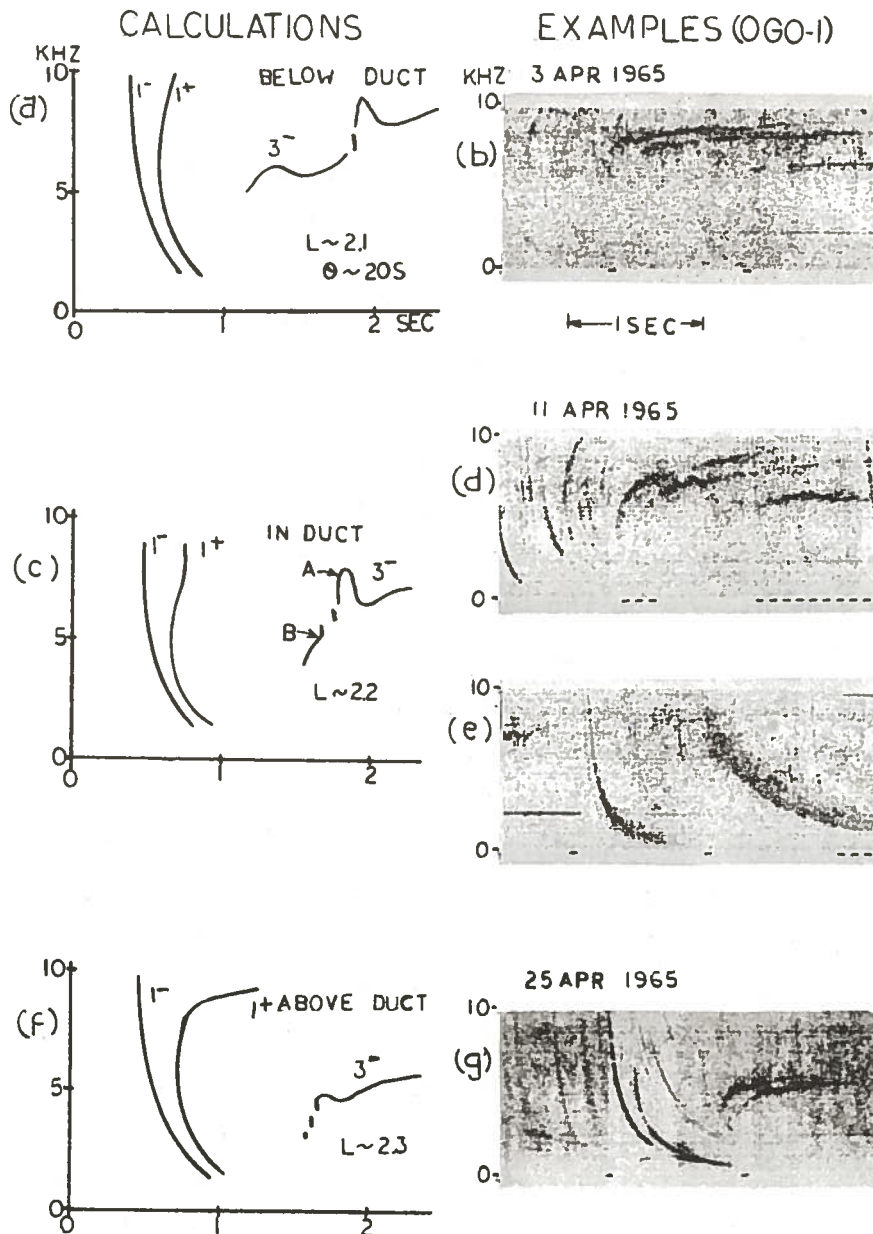


Fig. 3.5. DUCT (ENHANCEMENT) INTERACTION WITH $1^- 1^+$, $3^- 3^+$ MR WHISTLERS. (a) Calculated MR spectrogram for $L \sim 2.1$ showing the effects of a duct at $L \sim 2.2$ (same model as in Figs. 3.3 and 3.4). (b) Example of an MR whistler observed below a duct. (c) Calculated MR whistler for a satellite location at the duct center. (d) Example of an MR whistler seen in the center of a duct. Note the prominent peak on the 3^+ trace. (e) Ducted whistler seen in the duct of the example of (d). (f) Calculated MR whistler observed above a duct. (g) Example of MR whistler observed above a duct. Note the wavy 3^- trace which shows no prominent peaking.

Fig. 3.5f. An example of this bending of the 1^+ trace is demonstrated by the spectrogram of Fig. 3.6a. The ray path pattern for 1^+ rays in Fig. 3.6b display an ordered focusing and defocusing as the rays encounter the enhancement of density. Since the frequencies above the 1^+ nose travel along paths which are nearly field-aligned as shown in Chapter II, their paths are situated in the enhancement for a satellite position slightly above the duct center. The resultant time delays of the frequencies above the nose are increased in respect to the time delays predicted by a smooth magnetospheric model.

The focusing of the 1^+ rays in Fig. 3.6a results from the rotation of the wavenormal angle toward 90° by the density increase. The higher wavenormal angle of the rays as they enter the turnaround region near -30° latitude produces very field-aligned 1^+ paths for the rays starting at 31° , 32° , and 33° . The direction of the 34° ray path is only slightly affected as it crosses the enhancement, but the larger cross-field penetration of the 34° ray path compared to the 33° ray path produces defocusing of the 1^+ rays as shown in Fig. 3.6c.

E. Detection of Ducts by MR Whistlers

Since the duct interactions with MR whistlers produce recognizable distortion of the traces, one can track the duct as the satellite passes through it. Since the satellite is simultaneously changing longitude and local time as it changes altitude, it is possible to determine a lower bound for the longitude width of a duct. The example illustrated on the right of Fig. 3.3 extends from -13.7° to 7.5° longitude. However as the satellite record continues, the whistler activity changes from $2^- 2^+$ MR to $1^- 1^+$, $3^- 3^+$ MR traces. The latter example can be tracked to 33° longitude. Thus the duct extends from -13.7° to 33.1° . This 46.8° longitude width in local time is quite large. Ducts observed at $L \sim 4$ have widths less than 5° longitude [Angerami, 1970]. Thus this observation of extremely wide ducts is quite significant.

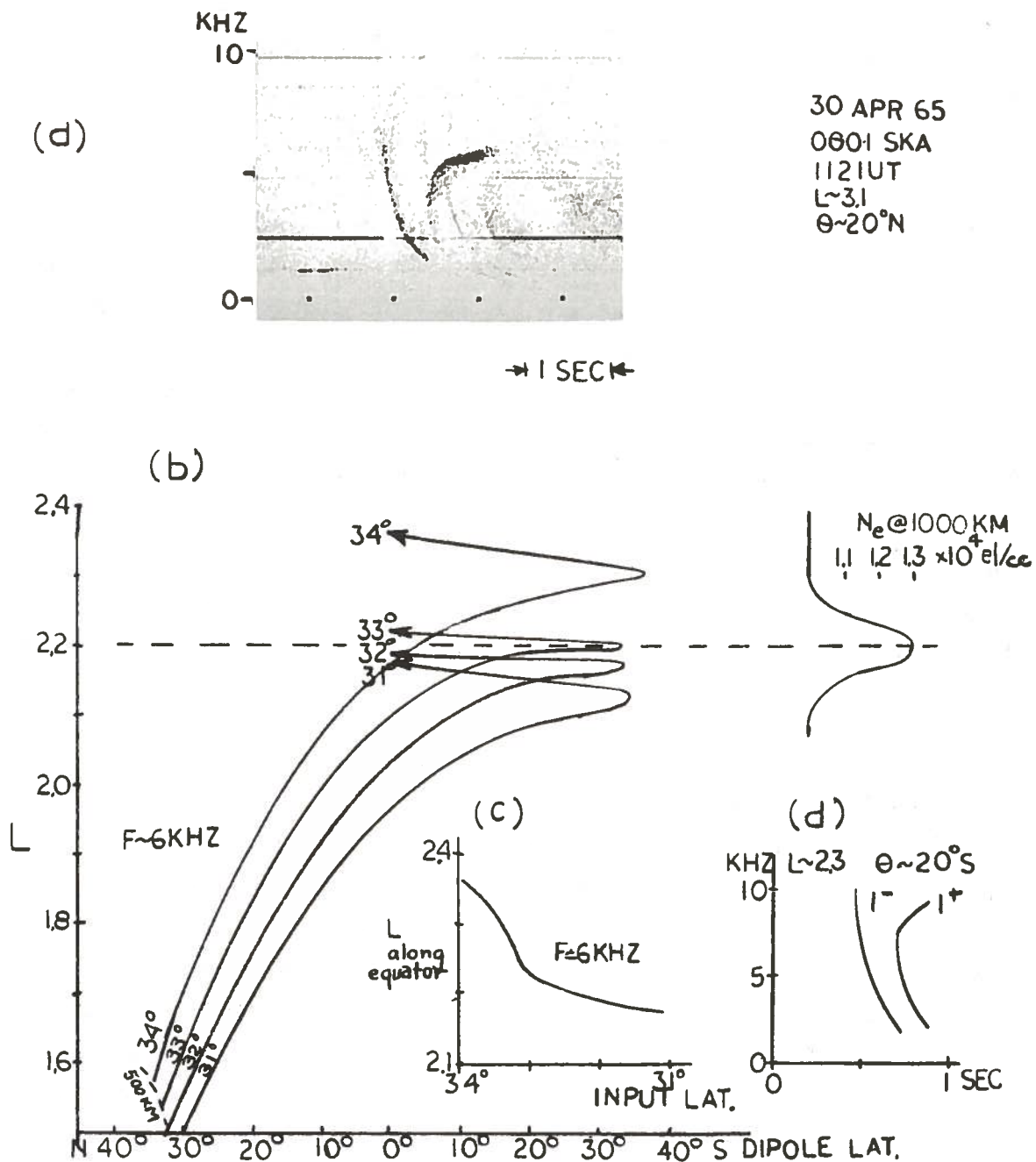


Fig. 3.6. EFFECTS OF AN ENHANCEMENT ON 1⁺ MR RAY PATHS AND SPECTROGRAMS. (a) Observed MR whistler 1⁻ 1⁺ traces showing duct effects (satellite, date, time, position). (b) 1⁺ ray paths starting between 31° and 34° latitude showing defocusing effects of a duct at L ~ 2.2. (c) Input latitude vs 1⁺ equatorial L-shell crossing point for the ray paths in (b). (d) Calculated MR spectrogram for 1⁻ 1⁺ traces showing the bending back effect on the 1⁺ component.

F. Detection of Ducts and Dropoffs

If we observe trace splitting and peaking in the MR whistler, it is possible by suitable ray tracing to determine the locations of the dropoff and duct L-shells. In Fig. 3.7b an extreme example of trace splitting is shown. The latitudes near 30° are in the region where the 2^- ray paths reflect. The $2^*_$ paths reflect at slightly different latitudes than the 2^- regular paths, and the two pairs of traces will separate. Our model places the dropoff at $L \sim 1.8$ to produce the separation of traces at $L \sim 2.5$ in Fig. 3.7a. The observation in Fig. 3.7b is at $L \sim 2.3$, and therefore a more accurate model would have the density dropoff at a slightly lower L-shell than 1.8. Also the regular 2^- , 2^+ traces in Fig. 3.7b display a distortion of the type closely resembling the duct interaction examples of Fig. 3.3c. Other 2^- , 2^+ whistlers observed on 18 March 1965 also follow the sequence illustrated by Fig. 3.3. Since the example of Fig. 3.7b was observed at $L \sim 2.3$, below the duct center, the center of the duct is probably located at $L \sim 2.4$. Thus the deduced profile for 18 March 1965 would have a density dropoff at $L \sim 1.7$ and a duct enhancement at $L \sim 2.4$.

A density profile can also be deduced for the examples in Fig. 2.10a to d. As illustrated by the example observed at $L \sim 2.4$ in Fig. 3.8a, the second and third components have faint extra traces which display longitudinal dispersions, and the third, fourth, and fifth components have discrete blobs at frequencies above the nose frequencies and slight peaks following the discrete blobs on the traces. These signatures on the components indicate that there is a density dropoff at $L \sim 1.9$ on a duct enhancement at $L \sim 2.4$. As shown in Chapter II the gross spectral details of Fig. 3.8a can be closely reproduced with the exception of the small perturbations of the traces by ray tracing calculations in a smooth magnetosphere. Therefore the enhancement factor of the duct must be very small compared to the examples of Fig. 3.5. The deduced density profile is portrayed in Fig. 3.8b.

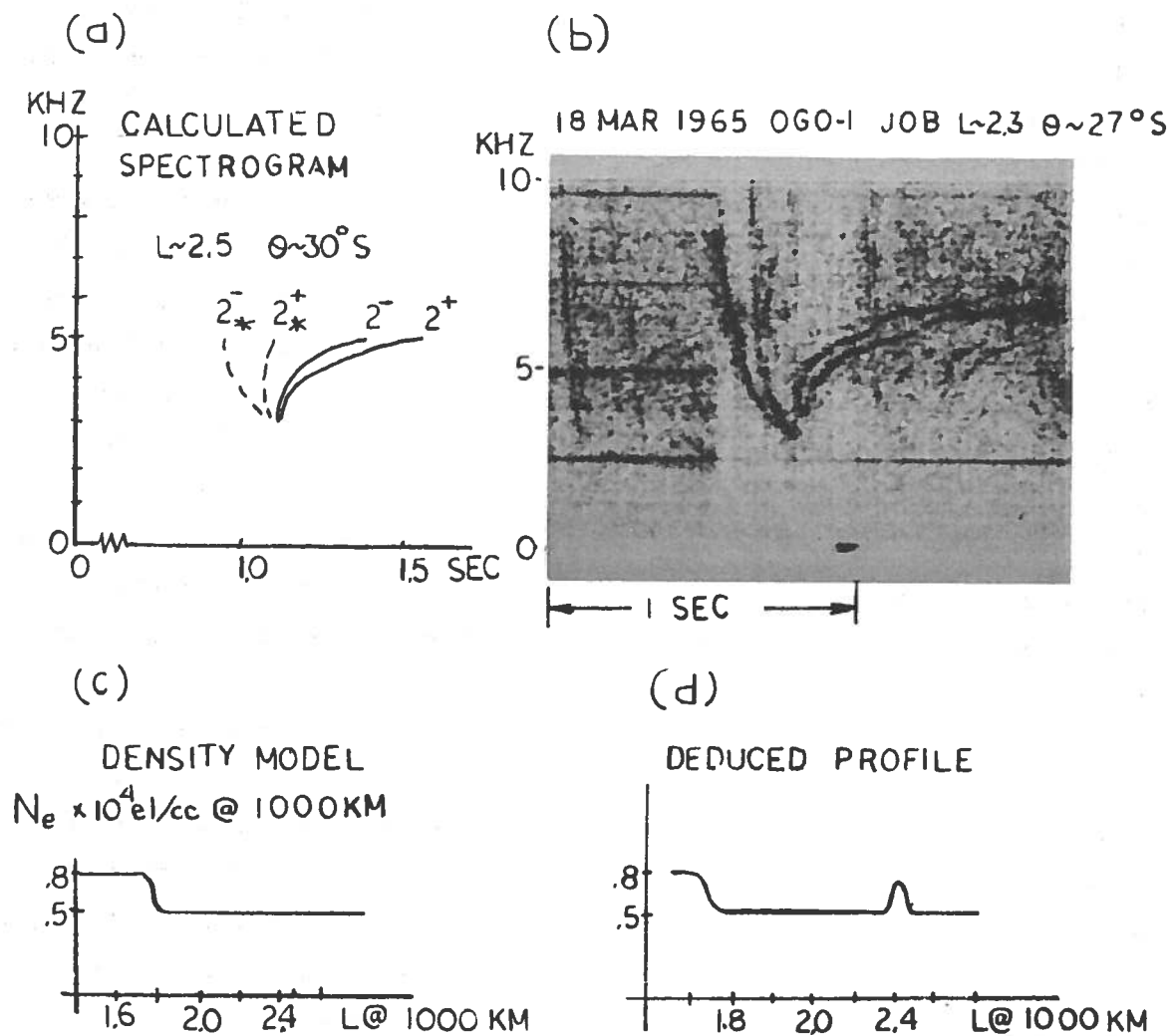


Fig. 3.7. DUCT AND DROPOFF DENSITY STRUCTURE EFFECTS. (a) Calculated frequency-time spectrogram of a $2^- 2^+$ MR whistler with extra $2_*^- 2_*^+$ traces produced by a density dropoff at $L \sim 1.8$ [model represented in (c)]. Note the separation between the $2^- 2^+$ and $2_*^- 2_*^+$ traces. (b) An MR spectrogram with observed extra traces similar to those predicted in (a) but exhibiting distortion in the regular traces near 6 kHz. These distortions indicate the presence of a duct, as shown in the profile of (d). (d) Deduced profile at 1000 km of the density based upon the spectrogram in (b).

KHZ 10- 5- 0- 8 NOV 1965 ROS 060-1 L-2.4 $\theta \sim 5^\circ S$

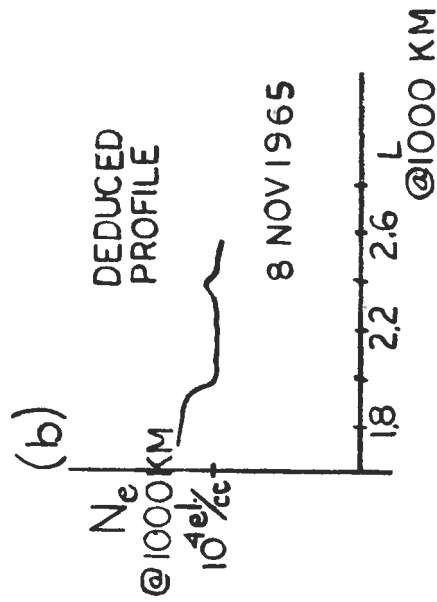
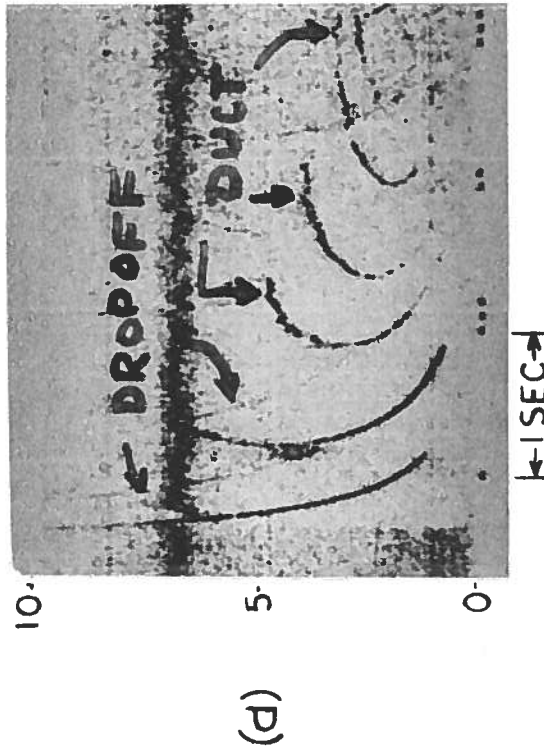


Fig. 3.8. (a) MR SPECTROGRAM SHOWING EFFECTS OF A CROSS-L DENSITY DROPOFF AT $L \sim 1.9$ AND A SMALL DUCT AT $L \sim 2.4$. (b) Sketch of the density profile at 1000 km deduced from (a).

G. Effects of a Field-Aligned Trough on MR Whistlers

In this section we will examine the effects of a field-aligned depression or "trough" of ionization on MR whistler spectra and ray paths. The primary effect of a trough on a 1^- , 1^+ MR whistler is to put a "wavy" signature into the upper frequency portion of the 1^+ trace as shown in Fig. 3.9a. The irregularity in the MR spectra comes about as a consequence of the disordering effect of the trough on MR ray paths after the first reflection. As illustrated in Fig. 3.9b, a gaussian trough at $L \sim 2.2$ (same dimensions as duct in Fig. 3.6b) disorders MR whistler rays originating from latitudes between 31° and 34° . The ray starting at 32° crosses the equator out of sequence with the other rays after the first reflection. The 32° ray sees a decrease in density before its first reflection which slows down the wavenormal rotation through 90° and causes the ray path to have a larger cross-field penetration than the other ray paths. The 33° and 34° ray paths both see an increase in density before their first reflection which speeds up the rotation of the wave normal through 90° and causes the ray paths to be tightly bound about the magnetic field direction. This ray path behavior allows three 1^+ paths at a particular frequency to exist (cf. Fig. 3.9c) and gives rise to the wavy signature of the 1^+ trace (cf. Fig. 3.9d).

Since the disordering of the ray paths by a trough begins at the first reflection (as opposed to the case of a duct which disorders the ray paths after the second reflection, cf. Figs. 3.2a and 3.6c), the 2^- and higher order MR whistler components will display a different set of irregularities in their spectra than in the duct case. Calculating the spectra of 2^- and higher order components based on the trough density model of Fig. 3.9b, we find that the trough introduces a double wiggle into the upper frequency portion. This type of signature becomes more pronounced in the 3^- , 3^+ components. Unfortunately, no clear example of this spectral irregularity was found in the available data. But the trough effects on the 1^+ MR spectra are easily recognized such that the higher order components add no new information.

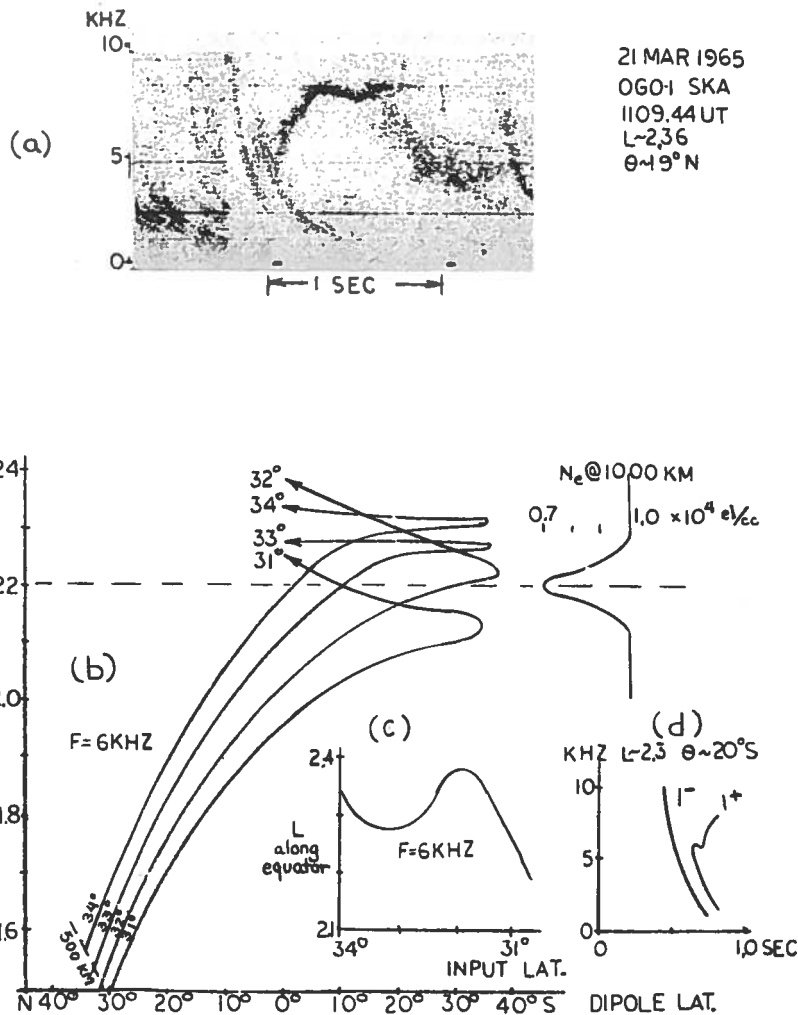


Fig. 3.9. (a) EXAMPLE OF A MR WHISTLER WITH IRREGULAR SPECTRA CAUSED BY A FIELD-ALIGNED TROUGH. The wavy upper frequency portion of the trace shows the primary effects of the trough. There is also evidence of a density dropoff at a lower L-shell due to the presence of a 1⁺ trace. (b) Effect of a trough at L~2.2 on MR whistler rays which have undergone one reflection. The trough disorders the rays starting between 31° and 34° such that above L~2.2 the satellite would observe three separate 1⁺ rays arriving at different times. (c) The input latitude vs output L-shell along the equator characteristics for the ray paths in (b) show that there is a general focusing of the rays above the trough center allowing for three 1⁺ rays to cross the satellite point at L~2.3. (d) A calculated MR spectrogram using the trough model of (b). The irregularity in the 1⁺ trace corresponds to that observed in (a).

H. Summary

In this chapter we have found that three types of field-aligned density structure produce recognizable irregularities in MR whistler spectra. The cross-L dropoff in density produces double traces in MR whistlers observed at satellite locations above the density dropoff. The enhancement and trough contain both increasing and decreasing cross-L density gradients which causes considerable defocusing and focusing of the ray paths in the vicinity of the irregularity. As a result of the deformation of the ray paths, the enhancement and trough introduce recognizable signatures into the MR spectra observed in the vicinity of the density irregularity. The trough can be easily identified from the signature on the 1^+ component, but the duct structure can only be positively identified from the 2^- , 2^+ or higher order components. As a result of the latter, a very wide duct has been detected at $L \sim 2.2$ which extends for at least 50° longitude. A cross-L density dropoff can produce double traces which show duct or trough effects. This type of MR spectra allows two types of density structure to be detected from the same MR whistler. The means of detecting these three types of structure by a careful examination of MR spectra will be used in Chapter VI.

IV. OCCURRENCE OF MR WHISTLERS

A. Introduction

A fundamental question in the study of MR whistlers is what are the factors governing their occurrence. Three obvious factors are:

- (1) location of the satellite in the magnetosphere
- (2) local time at the subsatellite point
- (3) magnetic activity

We will examine the first two factors in this chapter and will treat magnetic activity effects in a later chapter.

All VLF broadband data of the OGO-1 and OGO-3 satellites were examined for passes below $L = 6$ for evidence of MR whistler activity. For OGO-1 this period included all available data from October 1964 to July 1967; the OGO-3 data spanned the period June 1966 to September 1967. From this survey it was decided to limit the detailed examination of the data to below $L = 4.0$ and between $+40^\circ$ and -40° geomagnetic latitude. Outside of these limits no MR activity was observed. These limits also place restrictions on the time span for the data. November 1966 was selected as the cutoff date for the data. After November 1966, the perigee of OGO-1 was above $L = 4$, and OGO-3 spends much of its orbit time below $L = 4$ outside of $\pm 40^\circ$.

During this two year period of data for OGO-1, the satellite perigee moved from a low of $L = 1.2$ to a high of $L = 3.8$. Because of power limitations on board OGO-1, the broadband data were available only for three to four month periods (Fall 1964, Spring 1965, Fall 1965, Spring 1966, and Fall 1966). However the different orbits encountered during the various spans gave very good coverage over the magnetosphere in the regions of interest. Figure 4.1 shows the changes of the OGO-1 orbit.

B. Occurrence of MR Whistlers in L-Shell--Latitude Space

The magnetosphere was divided into field aligned sectors for this study. Each sector measured 0.2 shell in width and extended 10° in

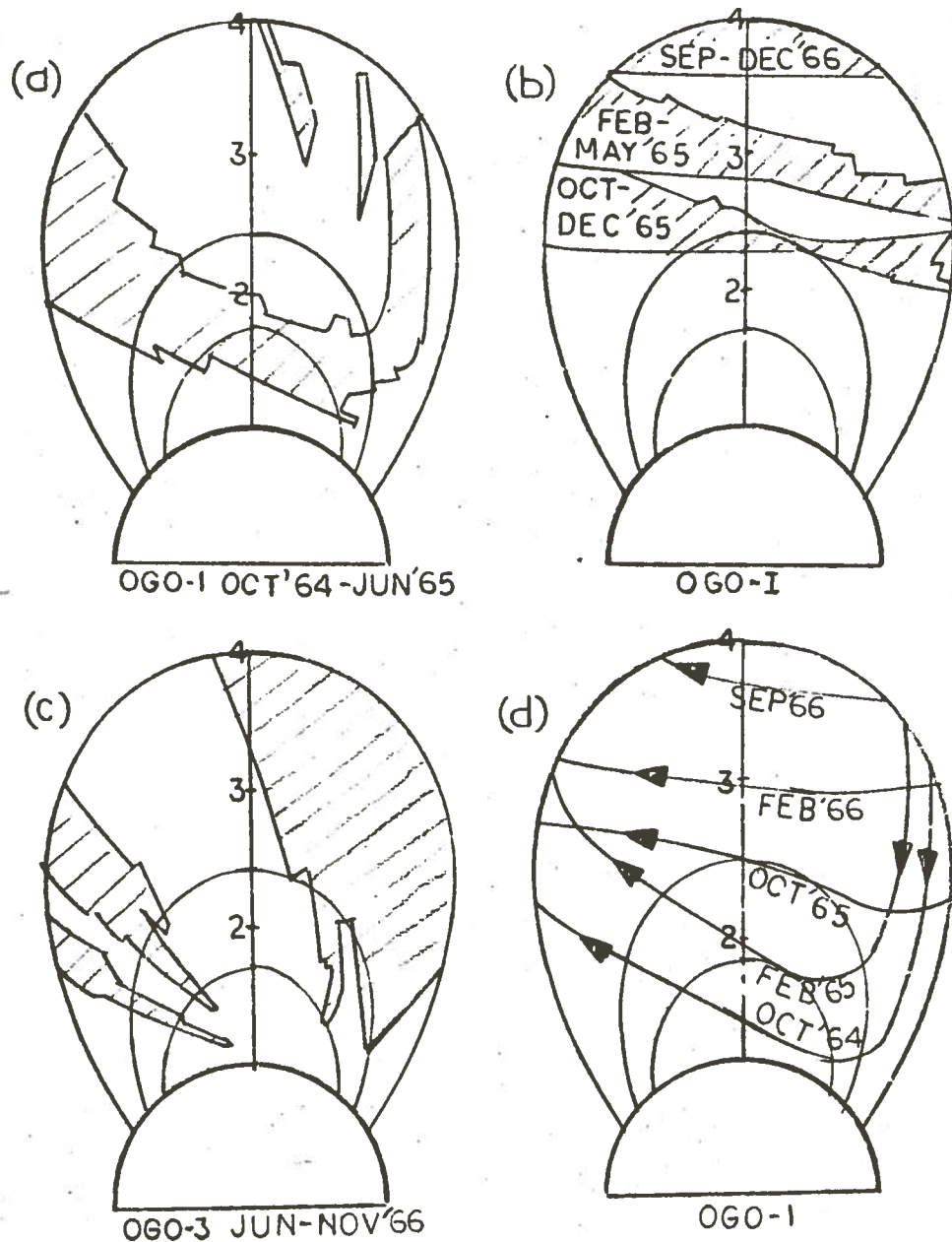


Fig. 4.1. CUMULATIVE DATA COVERAGE (SHADED PORTIONS) IN THE MAGNETIC MERIDIAN PLANE BY (a) OGO-1 during October 1964 to June 1965; (b) OGO-1 during October 1965 to December 1966; and (c) OGO-3 during June to November 1966. (d) Plots in the magnetic meridian plane of typical orbits of OGO-1.

latitude. The dipole field approximation was used for calculating the L-shell. In each sector the number of MR whistlers was counted and the time that the satellite spent in the sector was recorded. The occurrence rate of MR whistlers was defined as

$$\text{MR rate} = \frac{\sum \text{MR's}}{\sum \text{time}} \left(\frac{\text{whistlers}}{\text{minute}} \right) .$$

These calculated rates were then tabulated in Fig. 4.2. This procedure gives an average rate of occurrence for the total period of observation.

The highest rates occurred at the equator between $L = 2.2$ and $L = 2.4$ and in the southern hemisphere below $L = 2.8$ between -20° and -40° . The equatorial activity was primarily multicomponent MR whistlers. Below $L = 2.6$, the multicomponent MR activity seems to be most prevalent. The southern hemisphere activity was primarily "Nu" whistlers excited by southern sources and $1^- 1^+$ MR whistlers excited by northern sources. Often the individual occurrence rate on a particular pass was quite high, e.g., 20 to 40 whistlers/minute. The places of low activity are also of interest because they often occur next to regions of high activity. For example, the equatorial region above $L = 2.6$ shows low activity although just below $L = 2.6$ the activity was quite high. We shall examine this anomaly in the next chapter.

The change in the satellite orbits of OGO-1 and OGO-3 probably has some effect upon the occurrence rates. The Spring 1965 passes observe the high southern hemisphere activity; the Fall of 1965 orbits observed the high equatorial activity; and the Spring 1966 orbits observed the low equatorial activity above $L = 2.6$. Although the individual orbits do shape the occurrence rates, the overall pattern of activity does seem to be continuous. The lack of telemetry coverage of the satellite at the perigee during Fall 1964 and Spring 1965 prevents accurate determination of the lower altitude bounds of MR activity.

It is also interesting to view the occurrence rates as a function of L-shell, with the latitude dependence integrated out. This procedure eliminates the influence of the individual satellite orbit since its effect is primarily a latitude effect. As shown in Fig. 4.3, the activity slowly builds up to a peak at $L = 2.4$, where there is a significant

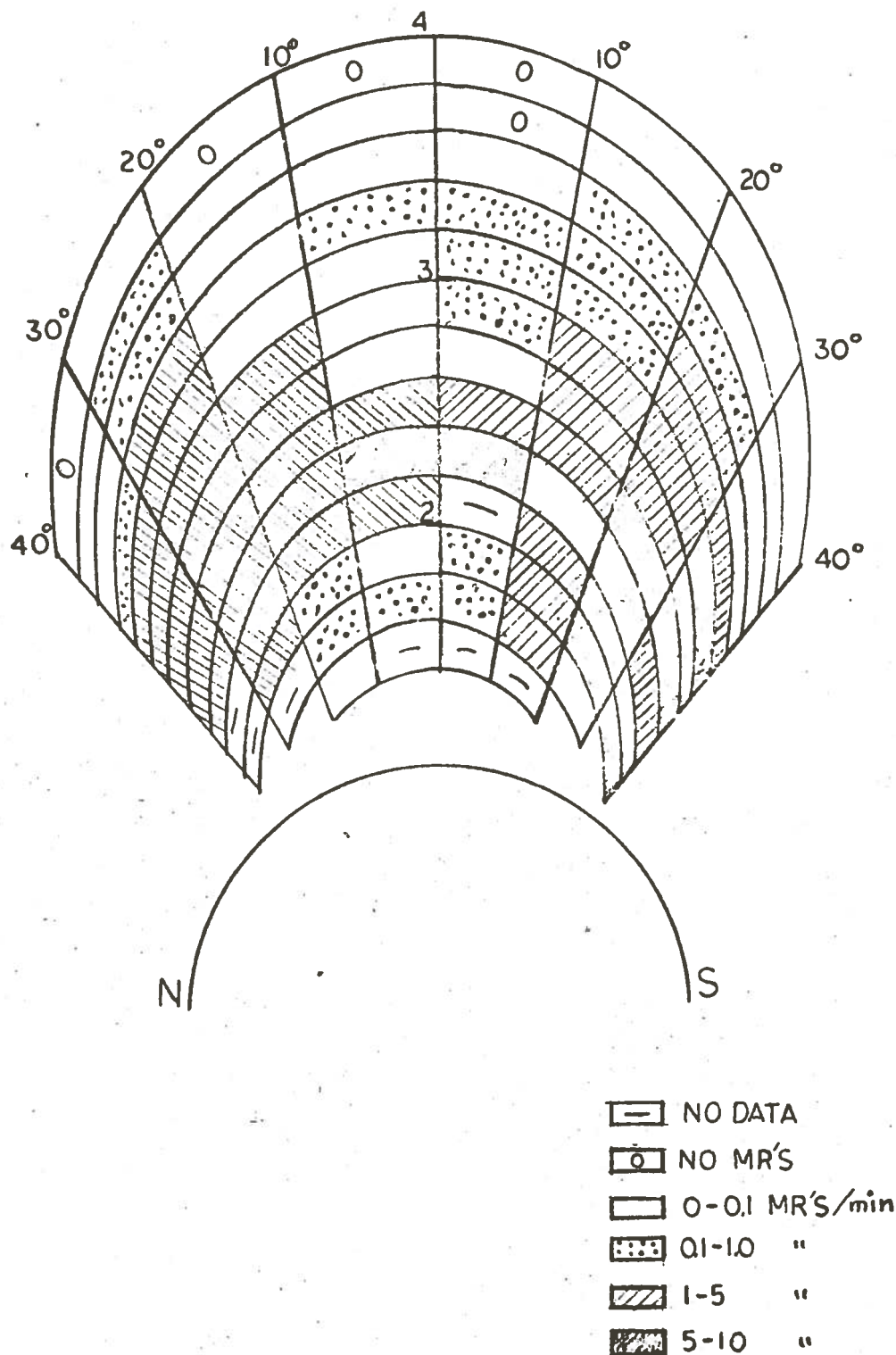


Fig. 4.2. AVERAGE OCCURRENCE LEVELS OF MR WHISTLERS FOR THE OBSERVATION PERIOD OCTOBER 1964 TO DECEMBER 1966 IN THE MAGNETIC MERIDIAN PLANE.

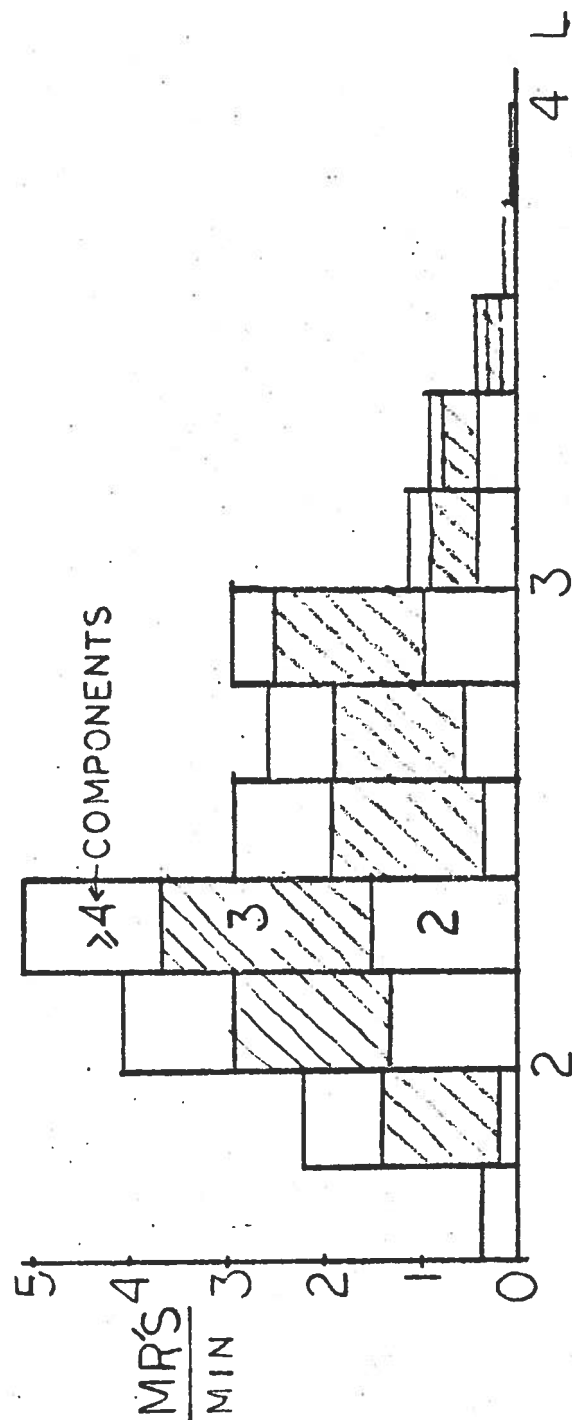


Fig. 4.3. AVERAGE OCCURRENCE RATES FOR MR WHISTLERS WITH DIFFERENT NUMBERS OF COMPONENTS PLOTTED VS L-SHELL.

drop in activity. At $L = 3$ there is another drop in occurrence. In each drop the activity is approximately halved.

C. Effect of the Plasmapause

It is useful to look at the dependence of MR activity on local time vs L shell (Fig. 4.4). The boundary of the plasmapause deduced from ducted whistler observations during the summer of 1963 [Carpenter, 1966] is also shown in this figure. Although for 1965 the plasmapause was generally at higher L-values [Taylor et al, 1965], the shape of the plasmapause follows the outer edge of the MR activity. The activity seems to be the highest near dusk and the lowest in the late morning sector. Again this difference in activity may be influenced by the satellite orbit, since there were twice as many passes in the dusk sector than in the later morning sector.

The maximum L shell for MR activity generally occurs well within the plasmapause. An ion mass spectrometer on board OGO-1 measured the proton density and the position where the proton density experienced a drop of several orders of magnitude [Taylor et al, 1965]. This drop was interpreted to be the location of the plasmapause. The following is an individual pass comparison between Taylor's plasmapause and the MR whistler activity. The 26 November pass seems to be the only pass that might be correlated with the plasmapause. All the others seem to cut off at much lower L shells than would be predicted from ray tracing calculations. In particular on 10 November, the MR activity stopped at $L = 2.4$ when the plasmapause was at $L = 4.61$. The relation of the plasmapause location to MR activity will be examined in Chapter V.

<u>Date of Pass</u> <u>1964</u>	<u>Plasmapause</u> <u>[Taylor et al, 1965]</u>	<u>Maximum L-Shell</u> <u>with MR Activity</u>
8 November	$L = 6.06$	$L = 3.4$
10 November	$L = 4.61$	$L = 2.4$
26 November	$L = 3.45$	$L = 2.8$
2 December	$L = 5.49$	$L = 3.4$
10 December	$L = 5.15$	$L = 3.6$

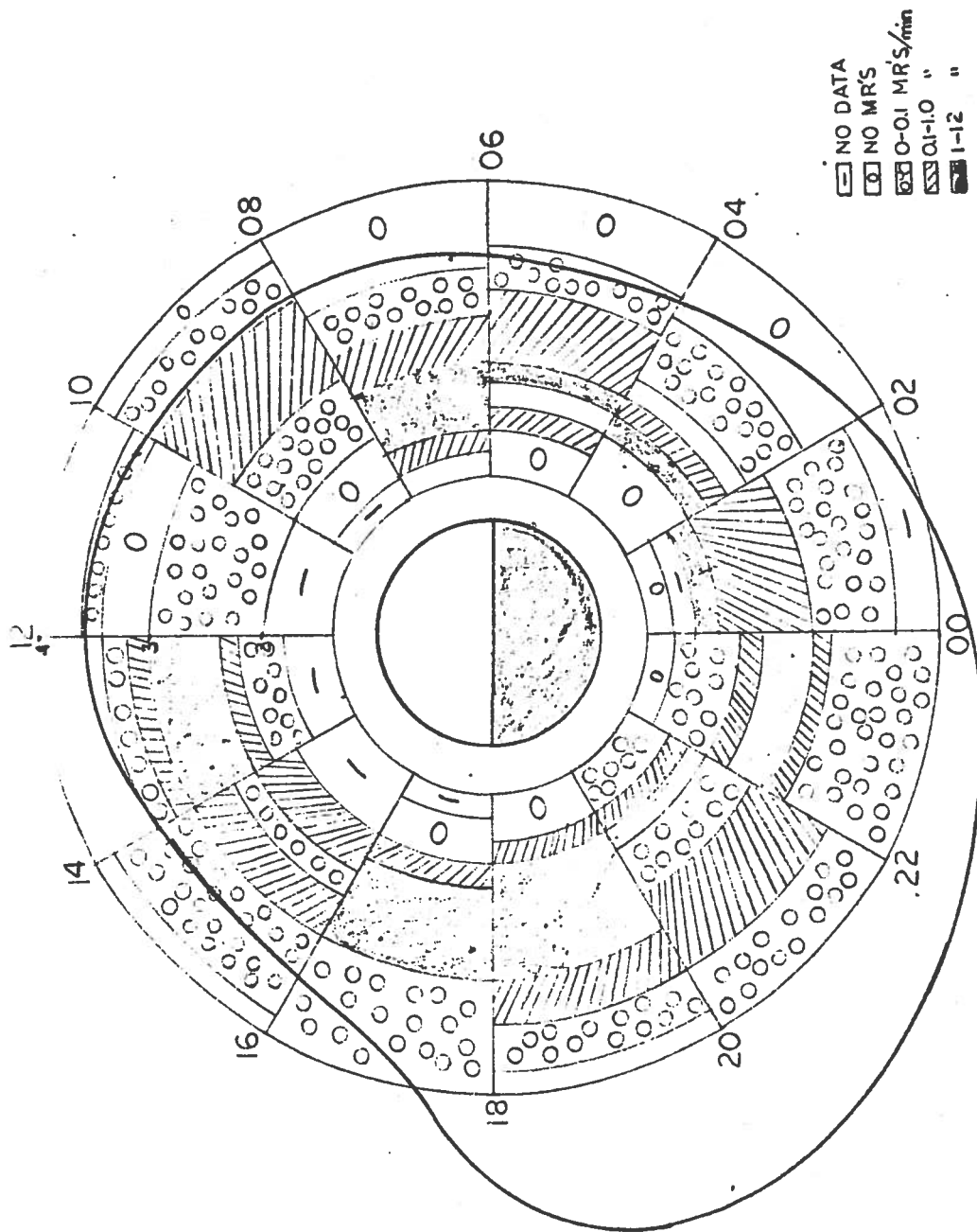


Fig. 4.4. AVERAGE OCCURRENCE LEVELS OF MR WHISTLERS IN LOCAL TIME VS L-SHELL. MR whistler occurrence in the blank regions was very minute. The cam-shaped curve marks the average position of the plasmopause given by Carpenter [1966].

D. Uses of the Data

For the data to be used effectively in the study of the magnetosphere, we require at least moderate whistler activity over several successive passes. Also we would like a small variation of the local time from pass to pass. The data observed by OGO-1 during March to May 1965 seem to fill these two requirements. These months contained several magnetic storms including a very large one on April 1965, all passes occurred between dusk and midnight and showed moderate to high MR whistler activity. Periods of successive passes extending over several weeks were available so that the long term effects of magnetic storms on MR whistlers could be easily observed. The data presented in Chapter V come primarily from this period.

V. MAGNETIC STORM EFFECTS ON MR WHISTLERS

A. Effect of Magnetic Storms on the Magnetosphere

Carpenter [1966] has shown that the inner magnetosphere is characterized by a dense thermal plasma region (plasmasphere) whose field-aligned outer boundary is generally located between $L = 4$ and $L = 6$. The outer region has much lower densities of electrons and protons than the plasmasphere. Typically the drop in densities across the plasmasphere outer boundary or plasmopause is an order of magnitude or greater. During periods of moderate to low magnetic activity the plasmopause is located beyond $L = 4$, but during magnetically disturbed periods it may move inward to between $L = 2$ and $L = 3$ [Carpenter, 1966; Taylor et al, 1968a]. The inner portion of the magnetosphere which is below the new plasmopause location remains relatively undisturbed, but the outer portion, between the new and old plasmopause locations, is initially depleted of plasma [Park, 1970]. The magnetosphere then goes into a recovery period in which the depleted portion is resupplied with plasma from the ionosphere diffusing upward along field lines.

B. A Case Study of MR Whistler Activity During the 17 to 18 April 1965 Magnetic Storm

In the following section we will examine the behavior of MR whistler activity before and after the great magnetic storm of 17 to 18 April 1965. During the period of 14 to 30 April, the OGO-1 satellite made seven passes through the magnetosphere. The broadband VLF receiver experiment was operative on five of these passes such that broadband data were available for the passes on 14, 22, 25, 27 and 30 April. In Fig. 5.1 the L-shell and dipole latitude of the satellite tracks are plotted for each of these passes. The fact that the pass orbit parameters are remarkably similar to each other will aid in the comparison of the data from one pass to the next.

The 17 to 18 April 1965 storm was the strongest storm occurring during 1965. K_p reached a maximum of 8₋ during the peak of the storm. In Fig. 5.2a the magnetic activity index A_p is plotted for the storm period. A_p peaks on the 18th but immediately decreases to a low value comparable

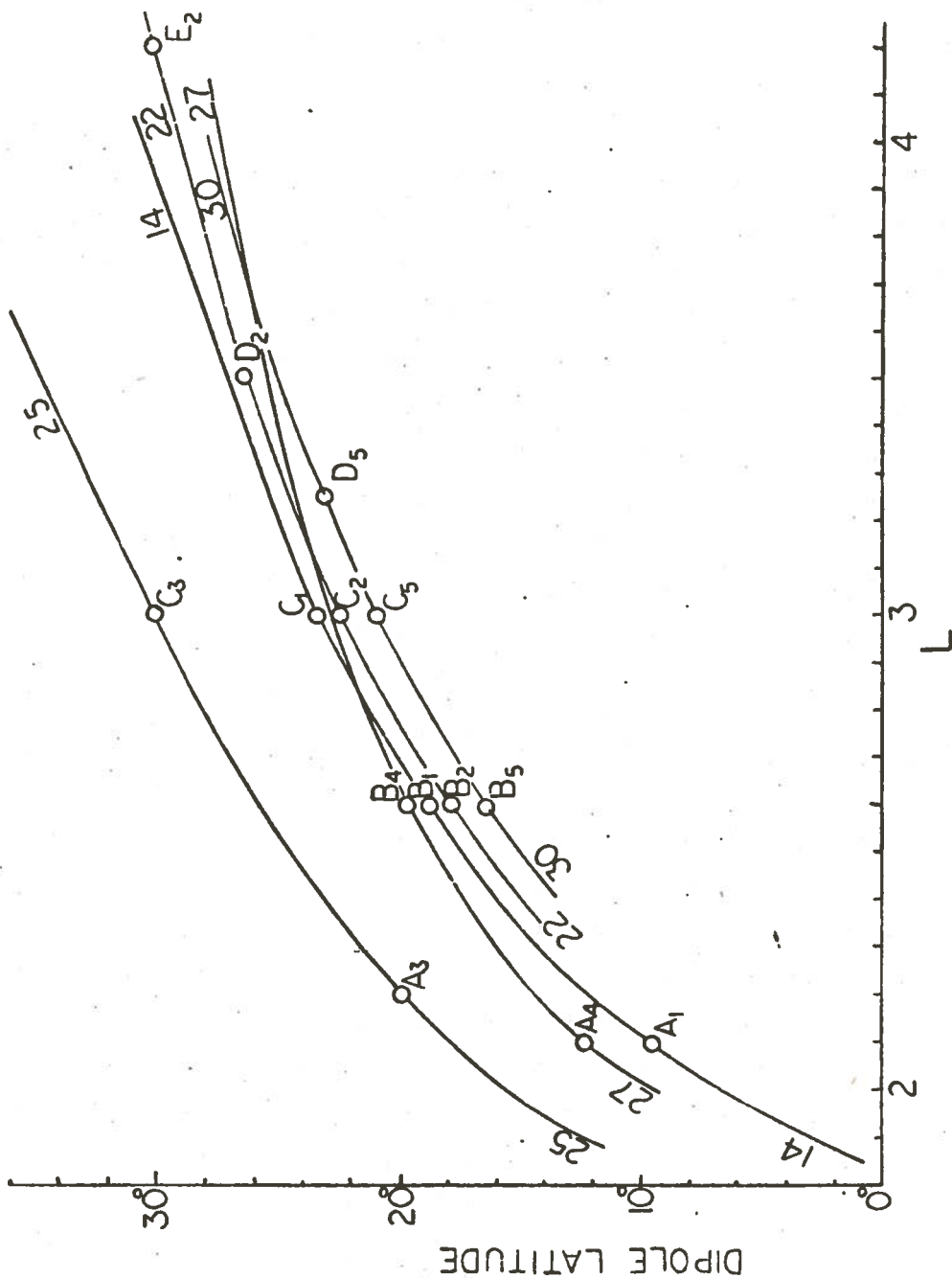


Fig. 5.1. L-SHELL-DIPOLE LATITUDE PLOT FOR APRIL 14, 22, 25, 27 and 30, 1965 OGO-1 PASSES. Notice that with exception of the 25th of April pass, the orbits are very close to each other. The subscripted letters refer to points along the orbit for which the whistler activity is illustrated (Fig. 5.4).

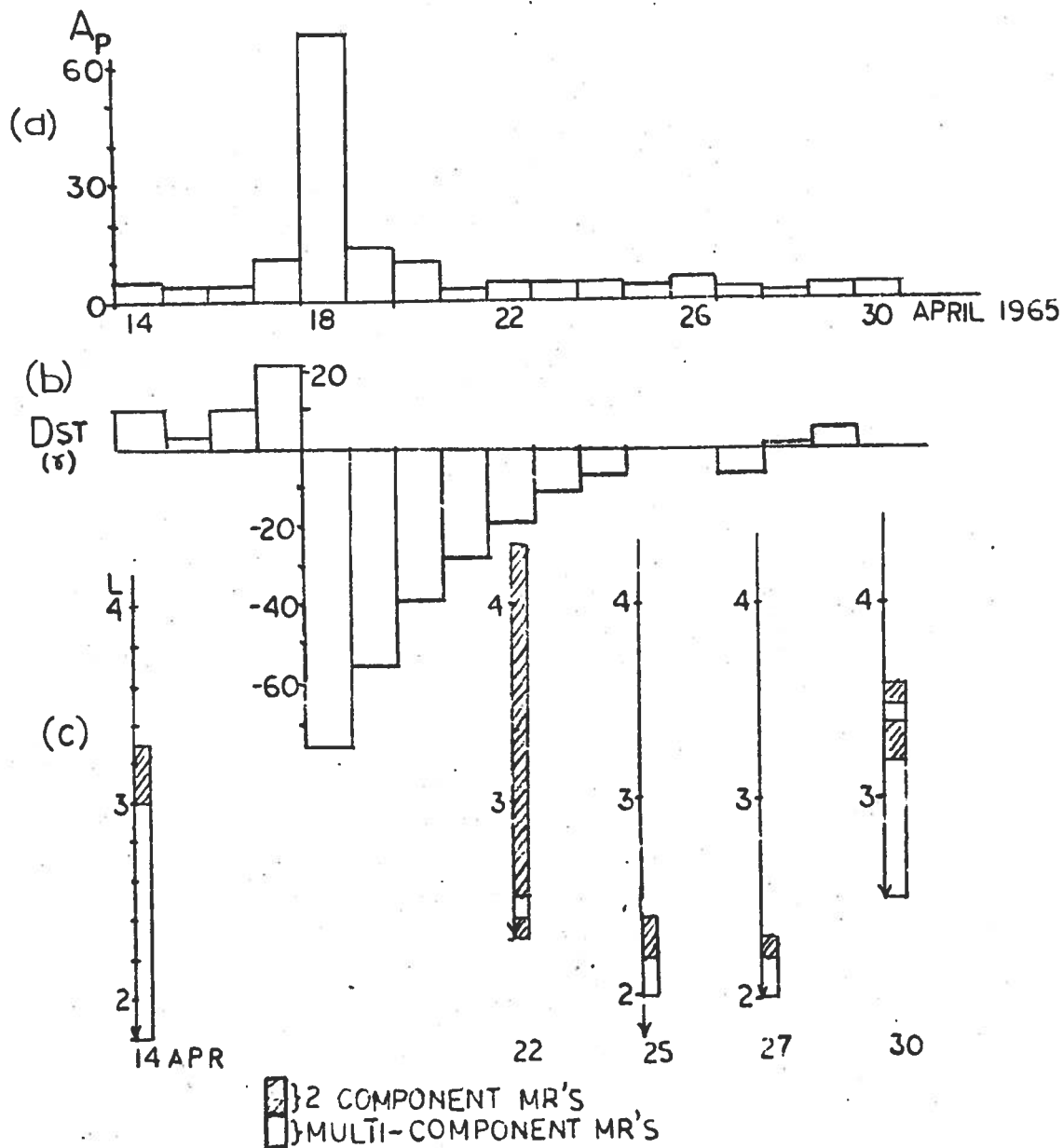


Fig. 5.2. GEOMAGNETIC ACTIVITY DURING THE APRIL 17 TO 18 STORM COMPARED TO THE OBSERVED OGO-1 MR WHISTLER ACTIVITY. (a) Average daily magnetic activity index A_p . (b) Average daily Dst index measured in γ . (c) MR whistler activity as a function of L-shell. No VLF data were available for passes on 17 and 19 April. The arrowhead marks the lower L range limit for the available data on each pass. The L-range where multicomponent MR whistlers were observed is indicated by the cross-hatched area.

to the pre-storm levels. Thus the injection of energetic particles into the magnetosphere is confined to a short period about the 18th. Another interesting indicator of magnetic storm effects is the Dst level [Sugiura and Cain, 1970] which is plotted in Fig. 5.2b. It features a large negative decrease on the 18th and a very slow recovery lasting for seven days. In Fig. 5.2c bar graphs of the MR whistler activity are plotted for the five OGO-1 passes. Before the storm MR activity on 14 April was observed from $L \sim 1.8$ to $L \sim 3.3$. After the storm peak MR whistlers on 22 April could be observed from $L \sim 2.3$ to $L \sim 4.3$. The characteristics of the whistler spectra on the 22nd showed unusual departures from the classic MR spectra presented in Chapter II and will be examined in greater detail in a later section. The MR whistler activity on 25 and 27 April featured a cutoff of whistler activity above $L \sim 2.3$ to 2.4. The nature of this cutoff is quite significant and will be also closely examined in this chapter. On 30 April the MR activity recovers to pre-storm levels. It can be noted from Fig. 5.2 that the activity levels of MR whistlers show effects of the magnetic storm well after the A_p and Dst indices have returned to quiet levels.

C. MR Whistler Activity Levels: 14 to 30 April 1965

In Fig. 5.3 and Fig. 5.4 the occurrence rates and spectra of MR and other whistler activity are illustrated. Referring to Fig. 5.3a, on 14 April there is considerable multicomponent MR whistler activity from $L \sim 1.8$ to $L \sim 3.3$. Above $L \sim 3.0$ the occurrence rate slowly decreases to zero. In Fig. 5.4, examples A_1 , B_1 , and C_1 illustrate the spectra of MR whistlers observed on 14 April. The spectrum of A_1 shows a seven component MR whistler with some bending back of top portions of the traces evident. Example B_1 features trace splitting of the third and fourth traces. As shown in Chapter III from examples taken from this same day, the trace splitting results from a sharp dropoff in density at $L \sim 1.8$ (cf. Fig. 3.1). The bending of the tops of the traces in example A_1 is probably due to the effect of this dropoff. Example C_1 is a $1^- 1^+$ MR whistler with the 1^+ trace showing the effect of some small irregularity, but the decrease in occurrence rates did not allow the type of irregularity to be deduced for certain. However, example C_1 does seem to fit the duct enhancement example of Chapter III (cf. Fig. 3.6).

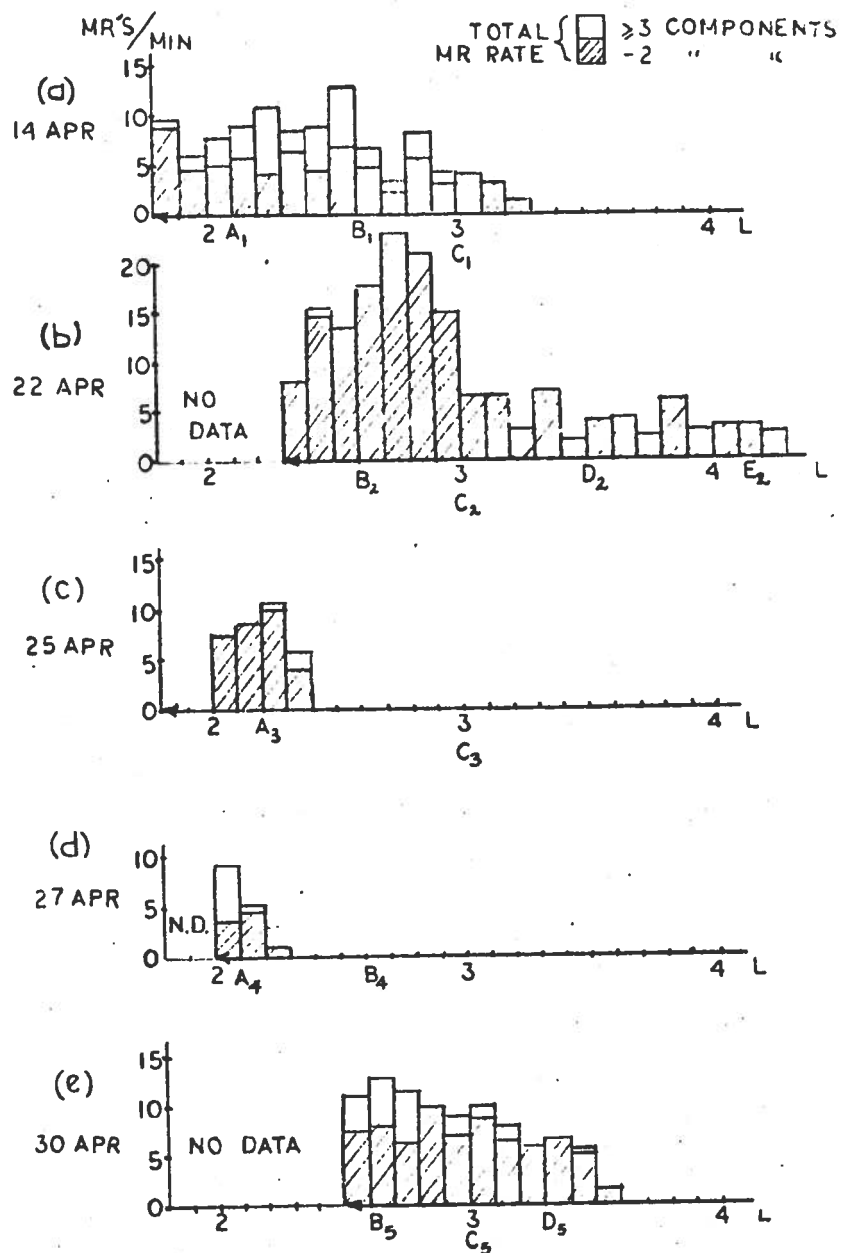


Fig. 5.3. OCCURRENCE RATES FOR MR WHISTLERS OBSERVED ON FIVE OGO-1 PASSES BEFORE AND AFTER THE 17 TO 18 APRIL STORM. The longitude and local time range for each pass were: (a) 151° - 173° W, 2100-0000 LT; (b) 160° - 180° W, 2200-0000 LT; (c) 107° - 78° W, 2000-2200 LT; (d) 20° - 50° E, 2000-2300 LT; (e) 155° - 170° W, 2100-2300 LT.

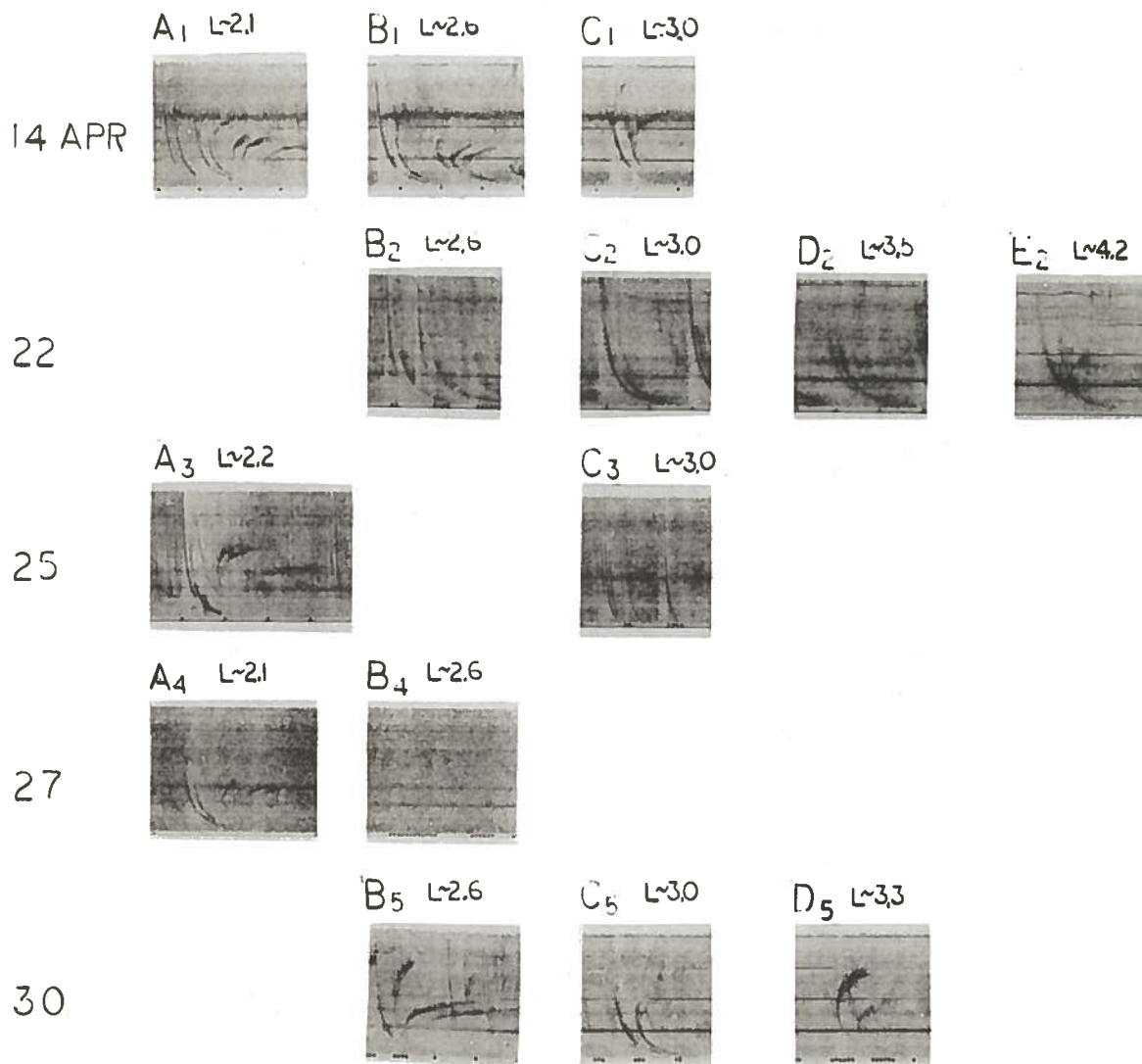


Fig. 5.4. FREQUENCY-TIME SPECTROGRAMS OF WHISTLERS (NOT ALL ARE MR's) OBSERVED BEFORE AND AFTER THE STORM. The details of each whistler are discussed in the text. (C3 does not refer to an MR whistler.)

The MR whistler activity on 22 April displayed high levels between $L \sim 2.3$ and $L \sim 3.0$ and continued at moderate levels between $L \sim 3.0$ and $L \sim 4.3$ as illustrated in Fig. 5.3b. In contrast to the classical MR spectra observed on the 14th, the whistler spectra in examples B_2 , C_2 , and D_2 , observed on the 22nd, consists of $1^- 1^+$ components with very "longitudinal" characteristics (without any nose frequency apparent in its spectral shape). (In these examples, the $1^- 1^+$ traces join at a common low frequency as the dipole latitude increases, a common feature of MR whistlers.) In Chapter III we saw how it was possible to form a 1^+ (cf. Fig. 3.1) longitudinal trace by introducing into the density model a rapid decrease of density across a field line. This field-aligned irregularity trapped a ray starting at a higher latitude than the 1^+ ray, into a partially field-aligned path before degenerating into the MR mode. Thus the 1^+ component in examples B_2 , C_2 , and D_2 must have initially traveled over a partially field-aligned path induced by an irregularity in the density structure. The model for the density structure seen by the $1^- 1^+$ whistlers of 22 April must produce a longitudinal 1^+ component over a wide range of L-shells (between $L \sim 2.6$ and $L \sim 3.5$) and must be consistent with the behavior of the density between the old and new plasmopause locations discussed by Park [1970].

The example E_2 is a $1^- 1^+$ MR whistler observed at $L \sim 4.2$ which does feature a nose and also trace splitting on the 1^+ component. The nose frequency is about 2 kHz higher than that predicted by MR propagation in a smooth magnetosphere. The 1^+ ray of example E_2 was probably partially trapped into a field-aligned mode, but after degeneration into the MR mode, the long path to $L \sim 4.2$ allowed the wave normal for high frequencies to rotate past the Gendrin angle. The partial trapping would introduce trace splitting and a higher nose frequency.

The only observation on the 22nd of a regular MR whistler (similar to the examples in Chapter II) was a $2^- 2^+$ MR whistler (not shown) at $L \sim 2.4$. This whistler displayed an upper frequency cutoff pattern consistent with an upper latitude restriction on whistler excitation approximately above 31° . On the basis of Chapter III.A, the longitudinal $1^- 1^+$ MR whistlers can be assumed to be excited at much higher latitudes than

the $2^- 2^+$ components. Thus MR whistler propagation excited from the lower latitudes (20° to 40°) is nonexistent above $L \sim 2.4$. The MR whistler activity on 25 April also shows this cutoff in occurrence at $L \sim 2.4$ as illustrated by Fig. 5.3c. Example A3 of Fig. 5.4 shows the presence of a duct enhancement, as evidenced by the spectral irregularities in the third and fourth traces (cf. Fig. 3.5). Between $L \sim 2.2$ and $L \sim 2.4$, the MR activity consists of $2^- 2^+$ components (not shown) similar to the $2^- 2^+$ MR whistler observed on 22 April. The upper frequency cutoff pattern observed on these whistlers also indicated a high latitude restriction on whistler excitation. This subject will be examined in more detail in Chapter VI. Above $L \sim 2.4$ the whistler activity consisted of 0^+ whistlers without any associated MR components as illustrated by examples C3. The 1^+ components observed on 22 April were not present.

The activity on 27 April was similar to that on 25 April but much fainter as shown in example A4. The MR activity stopped at $L \sim 2.3$ with very little 0^+ whistler activity beyond that L-shell as shown by example B4. The multicomponent MR whistler in A4 does show some spectral irregularity in the upper frequency portions of the traces, but the type of density structure cannot be determined with any certainty. The upper latitude restriction for MR whistler excitation was approximately 28° on 27 April. In summary, spectral data from three OGO-1 passes (22, 25, and 27 April) after the storm peak show that MR whistlers excited from the low latitudes are not observed above $L \sim 2.4$ to 2.3. This phenomenon is longitude-independent since the three passes cover three different sectors (see Figs. 5.3b, c, and d for longitude coverage).

On 30 April the MR whistler activity recovered to a level similar to that on 14 April as shown in Figs. 5.3a and e, with a high level of activity between $L \sim 2.5$ and $L \sim 3.6$. The examples B5, C5 and D5 show some evidence of spectral irregularities indicating that there is some density structure (cf. example of duct effects on a 1^+ component observed on this pass in Fig. 3.6a). Thus for the 17 to 18 April storm, MR whistlers which are excited at the lower latitudes are cut off above $L \sim 2.4$ for approximately 12 days after the storm peak. The extra traces and spectral irregularities observed on the MR whistlers indicate that there

is density structure which changes from pass to pass. This topic will be examined in the next section.

D. Models for Ray Tracing Calculations

In this section we will develop density models which would describe the structure of the magnetosphere for 14, 22, and 30 April. The data for these three passes were obtained by the same telemetry station in Alaska so that any longitude effects may be ignored. In Chapter II (cf. Fig. 2.14) it was shown that a simple diffusive equilibrium model with a constant density at 1000 km approximately describes the state of the magnetosphere up to $L \sim 2.7$ for the days of 14 and 30 April. The model parameters were:

Base level density $N_0 = 10^4$ el/cc

Uniform temperature $T = 1600^\circ\text{K}$

Ion concentration at 1000 km \doteq 50% H^+ , 25% He^+ , 25% O^+

The model for 22 April will however require additional development from the initial deductions of the previous section. Since the 22 April pass occurs four days after the storm peak, one would expect that the effects of the storm upon the structure of the magnetosphere would still be in evidence. Park [1970] has demonstrated for a similar storm in June 1965 that the magnetospheric plasma levels takes five to eight days to recover to prestorm conditions. Thus the major magnetospheric structure that would be observed between $L \sim 2.6$ and $L \sim 3.5$ would be that left by the plasmopause when it moved inward during the storm peak on 18 April. The plasmopause is characterized by a sharp decrease in density at its usual location at $L \sim 4$ during magnetic quiet periods. As the density levels recover after the storm peak, the structure about the point of inward most movement of the plasmopause probably changes from a sharp boundary to a less pronounced shape due to diffusion processes. Since we had deduced that the longitudinal appearance of the 1^+ traces observed on the 22nd was caused by some form of density decrease, we can hypothesize that the required decrease in density is the plasmopause structure left by the storm.

To test this hypothesis, we can compare the $1^- 1^+$ components observed on 22 April with corresponding ones observed on 14 April in Fig. 5.4. From examples B_1 , B_2 , C_1 , and C_2 in this figure, one observes that the first two traces differ in spectral shape at the frequencies above 4 kHz but are similar below this frequency. Since the separation time between the two components is proportional to the square root of the density along the field lines in the vicinity of the satellite location (Appendix C), we can use this time delay as a crude measure of the density levels on each pass. Comparing the time delay at low frequencies between the first two traces for examples B_1 and B_2 we find that the differential times are similar. But comparison of examples C_1 and C_2 , shows that the differential time delay is much less on the 22nd than on the 14th. Thus the $1^- 1^+$ MR whistlers of 22 April observe much lower density levels at $L \sim 3$ than the corresponding components on 14 April. Thus our hypothesis is substantiated by the experimental observation a decrease in density levels between $L \sim 2.6$ and $L \sim 3.0$.

As demonstrated in Appendix C the differential time delay between the 1^- and 1^+ components is a direct measure of the density levels encountered by the second component ray path as it passes under the satellite position, reflects, and returns to the satellite. Thus one can state that

$$\Delta t = K\sqrt{N} ,$$

where

Δt = time delay difference between the first two components at a constant frequency

K = constant of proportionality

N = average density along the turnaround path

Since the latitudes along the orbits on the 14th and 22nd are very similar (Fig. 5.1), K should be the same for these two days and we can eliminate it by taking the ratio between the corresponding time delay differentials:

$$\frac{\Delta t_{22}}{\Delta t_{14}} = \sqrt{\frac{N_{22}}{N_{14}}}$$

or

$$\frac{N_{22}}{N_{14}} = \left(\frac{\Delta t_{22}}{\Delta t_{14}} \right)^2$$

The above equation now gives us a crude tool for estimating the depletion of density on the 22nd as compared to the normal density levels on the 14th. Performing the time delay measurements at $f \sim 2.5$ kHz to avoid the influence of localized gradients at higher frequencies, one finds that there is a general decrease in density starting at $L \sim 2.4$. Since the orbit parameters of the 30th are also very similar to those of the 14th and 22nd, the ratio of the density levels on the 22nd and the 30th was also calculated. These curves, plotted in Fig. 5.5, show a general decrease in densities between $L \sim 2.4$ and $L \sim 2.9$ with a slight recovery between $L \sim 2.9$ and $L \sim 3.4$.

Using the result of Fig. 5.5 as a guide, we can formulate the following model for the 22 April magnetosphere:

$$N_{22}(r_2 L) = N_{14}(r) N(L) ,$$

where

$N_{22}(r_2 L)$ = density level on the 22nd

$N_{14}(r)$ = diffusive equilibrium model used for April 14

$N(L)$ = modifying factor which decreases the density in accord with Fig. 5.5

The form of $N(L)$ was chosen as

$$N(L) = \frac{1^+ \text{ Drop}}{2} - \frac{1^- \text{ Drop}}{2} \tanh \frac{L - L_0}{w} ,$$

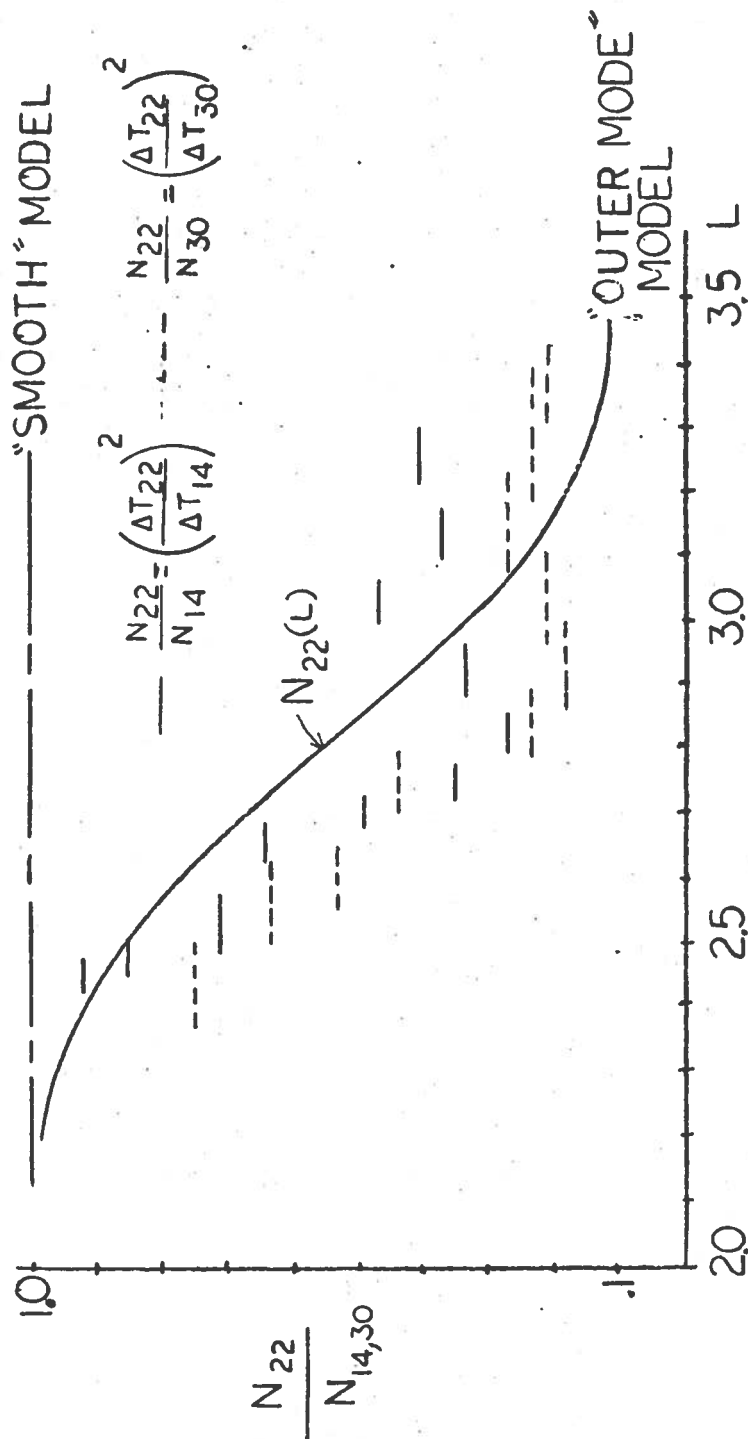


Fig. 5.5. MEASUREMENT OF THE DEPLETION OF DENSITY ON 22 APRIL ABOVE $L \sim 2.5$ AS COMPARED TO DENSITY LEVELS ON 14 AND 30 APRIL. The short solid and broken lines refer to individual MR whistler time delay measurements. $N_{22}(L)$ is the normalized density model at 1000 km for 22 April (determined by ray tracing) as compared to the normalized base level for the smooth magnetospheric density models.

with

Drop (fractional value of density present at higher L-shells) = 0.1

L_0 (center of the dropoff) = 2.8

w (width of the dropoff) = 0.35

and where

$$N(L) \rightarrow 1 \quad \text{when} \quad \frac{L - L_0}{w} \ll -1$$

and

$$N(L) \rightarrow \text{Drop} \quad \text{when} \quad \frac{L - L_0}{w} \gg 1$$

In Fig. 5.6, two ray paths which have undergone one turnaround are shown for a satellite position at $L \sim 2.8$, $\theta \sim 20^\circ$. The "inner" or regular MR ray path calculations are based on the simple diffusive equilibrium model with a constant density at 1000 km. Introduction of a decrease above $L \sim 2.4$ would not affect the ray path to any noticeable degree. Since the magnetic field gradients control the rotation of the wave normal over all of the "inner" path, the resultant MR spectrogram will display the characteristic MR whistler nose. The decrease in density would only affect the time delays experienced by the frequency components above the nose as shown in Chapter II (cf. Fig. 2.13).

If we use the $N_{22}(r, L)$ density model with a Drop factor of 0.1, a center location $L_0 \sim 2.8$ and a width factor $w = 0.35$ in our ray path calculations, we find that the ray paths starting at latitudes below 50° are similar to the "inner" mode. But for starting latitudes between 50° and 60° , the decreasing density gradient rotates the wave normal inward initially, causing the ray to be bent inward. The "outer" mode (so named because it starts at high latitudes) ray path travels to L-shells lower than $L \sim 2.4$ where the influence of the magnetic field rotates the wave normal into the MR whistler mode. The initial longitudinal character of the outer mode ray path allows the wave normal for all frequencies to lie

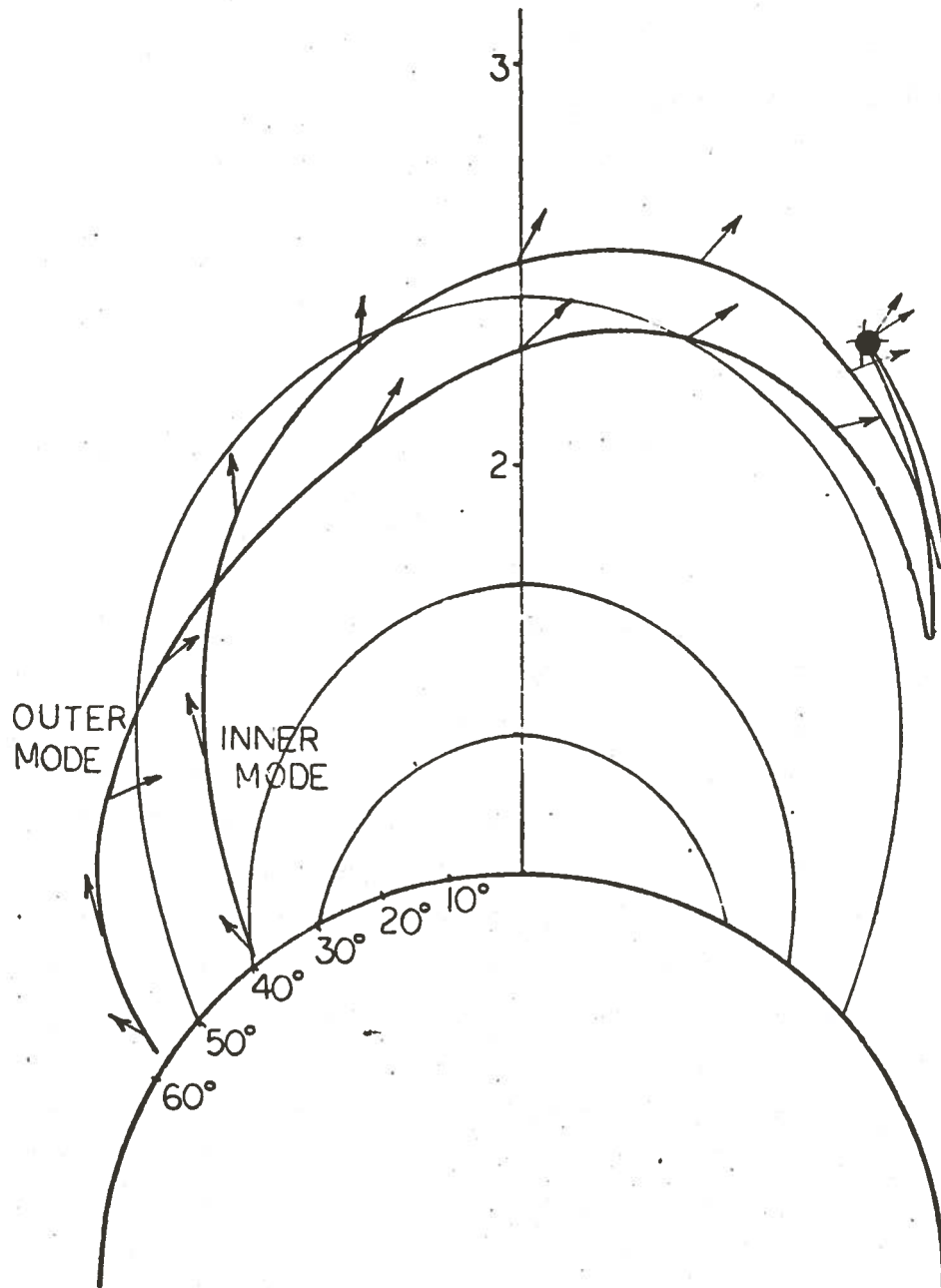


Fig. 5.6. RAY PATHS FOR THE OUTER AND INNER MR WHISTLER MODES, WITH WAVE NORMAL DIRECTIONS INDICATED BY THE ARROWS ALONG THE PATHS.

inside the Gendrin angle. The resultant spectra for the 1^+ trace does not exhibit a nose, and thus parallels the 1^- trace on the spectrogram.

Figure 5.7a shows the variation of wave normal angle for both modes. The "inner" mode wave normal rotates steadily toward 90° under the influence of the magnetic field. The outer mode wave normal initially experiences a very rapid inward rotation under the influence of the density decrease and then rotates outward into the MR mode. Figure 5.7b compares the spectra of the MR whistler component for the inner and outer modes.

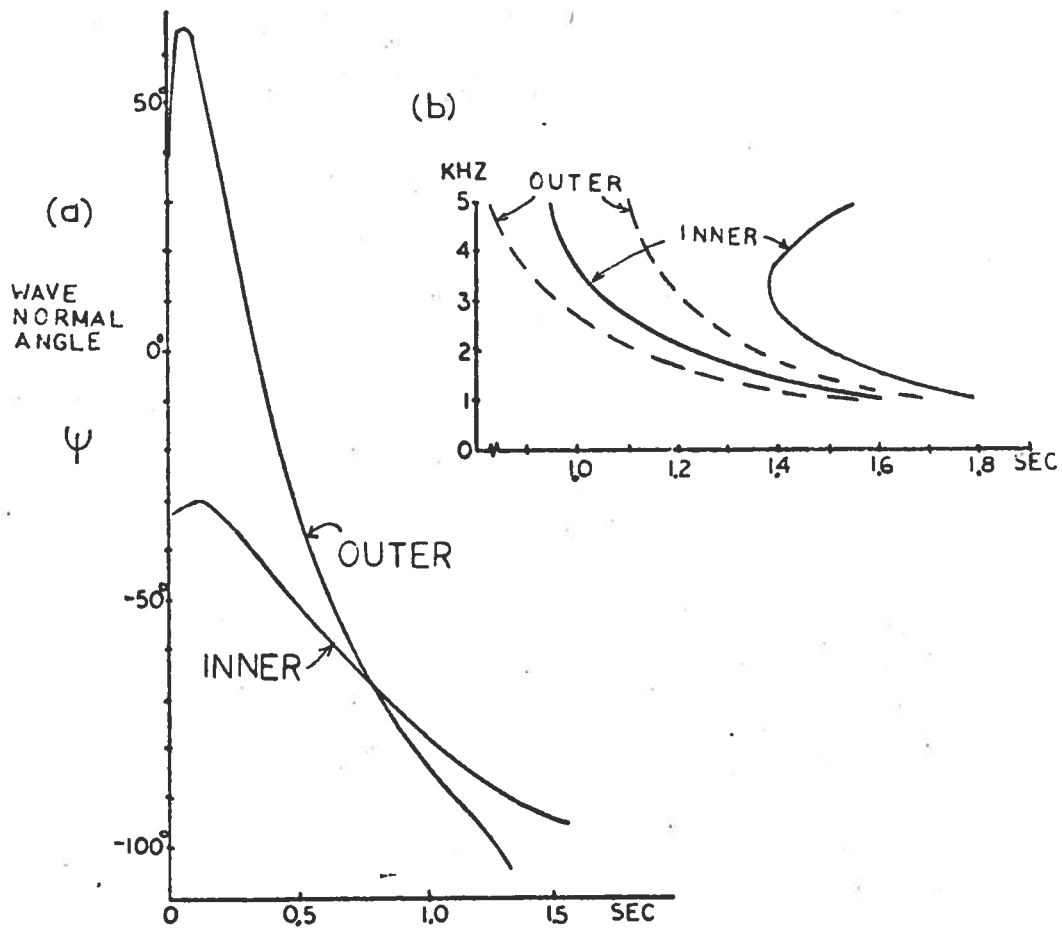


Fig. 5.7. (a) WAVE NORMAL ANGLE VARIATION ALONG THE OUTER AND INNER MODE MR RAY PATHS OF FIG. 5.6. (b) Calculated spectrograms for the outer and inner modes. The density model for the inner mode used a constant base level density, while the outer mode base level density was modified by the $N_{22}(L)$ factor (Fig. 5.5).

The inner mode time delays are based on the smooth diffusive equilibrium model; whereas the outer mode time delays are based upon the density decrease model. The inner mode spectrogram corresponds to the MR whistlers observed on 14 April (cf. example C1 in Fig. 5.4), and the outer mode spectrogram corresponds to the MR whistlers observed on 22 April (cf. example C2 in Fig. 5.4). The difference in the $1^- 1^+$ separation times between the two sets of whistlers in Fig. 5.7b substantiates our initial deductions about the change in density structure from 14 April (before storm) to 22 April (after storm peak).

On the basis of ray tracing calculations utilizing a density decrease between $L \sim 2.4$ and $L \sim 3.2$, both inner and outer modes would be observed in the magnetosphere. On 22 April, however, the lone example of the inner mode is a $2^- 2^+$ MR whistler (observed at $L \sim 2.4$). The rest of the MR whistlers observed were excited at the high latitudes. The disappearance of the outer mode on 25 and 27 April probably means that the density gradients which were responsible for this mode had declined substantially by the 25th. This is consistent with the filling of the magnetospheric density levels near $L \sim 4$, at least at the lower altitudes where most of the bending of the ray paths occurs (cf. Fig. 5.6 and Fig. 5.7). However inner and outer mode MR whistlers have been observed to coexist on at least one pass. This phenomenon was observed near $L \sim 3$ on 16 May 1965 during the initial phases of a magnetic storm. It has been well established by Carpenter [1966] that the plasmapause moves inward during periods of increasing K_p . Thus the mechanism causing the cutoff of the inner mode is present only after the peak of the 17 to 18 April storm.

As a further illustration of the effects of magnetic activity upon MR whistler occurrence levels, Fig. 5.10 plots K_p indices and the occurrence rates for 7 OGO-1 passes during a 22-day period in May 1965. The activity on 3 May is spotty but some MR whistlers were observed above $L \sim 3$. Immediately after the storm on 5 May no MR whistlers were observed from $L \sim 2$ to $L \sim 4$, but a high level of fractional hop whistlers were observed. The next pass on 10 May shows some isolated MR activity below $L \sim 3$ after five days of agitated magnetic activity. On 13 May during quiet magnetic conditions, the MR occurrence levels decayed to zero at

$L \sim 2.6$ much like the occurrence levels after the 17 to 18 April storm. The MR occurrence levels recovered above $L \sim 3$ on 16 May. Again after a storm MR whistlers disappeared above $L \sim 2.4$ on 19 May and recovered on 21 May. As seen from these examples the disappearance of MR whistlers above $L \sim 2.4$, 2.6 seems to occur during quiet magnetic periods after a storm.

E. Comparison of Computed and Measured Spectra

Figure 5.8 displays the computed and measured spectrograms for a majority of the MR whistlers in Fig. 5.4. The density model for the calculated spectrograms of 14, 25, 27, and 30 April is the simple D.E. model of Section D. The model for the 22nd is the D.E. model modified by the decreasing density factor $N(L)$ of the same section (and Fig. 4.5). The match between computed and measured spectra is the best on 14 April. The example B1 in Fig. 5.8 does not show the extra traces seen in the corresponding B1 example in Fig. 5.4 for reasons of simplicity (cf. Figs. 3.1b and d). The difference at the upper frequencies between calculated and measured time delay indicates that the base level density decreases slightly above $L \sim 2.6$. This conclusion is based on the results of Chapter II.F.

The close match in examples B2, C2, and D2 for 22 April demonstrates the validity of the $N_{22}(r, L)$ model in interpreting the MR whistler activity on this pass. The time delay separation between the first and second traces decreases from example B2 to D2 which can be interpreted in terms of the drop in density levels above $L \sim 2.5$. The match in examples A3 indicates that the density levels at $L \sim 2.2$ on 25 April are slightly lower than predicted by the simple D.E. model. However, on 27 April the match in A4 indicates that the density level at 1000 km is higher the model level. Notice, too, in examples A3 and A4 that the range between upper and lower frequencies of the third and fourth traces are severely limited indicating a limitation in excitation latitudes. The examples B5 and C5 for 30 April show the recovery of the MR whistler activity beyond $L \sim 2.4$ and also indicate that there is a decrease in density above $L \sim 2.6$ similar to that on the 14th. Notice that although

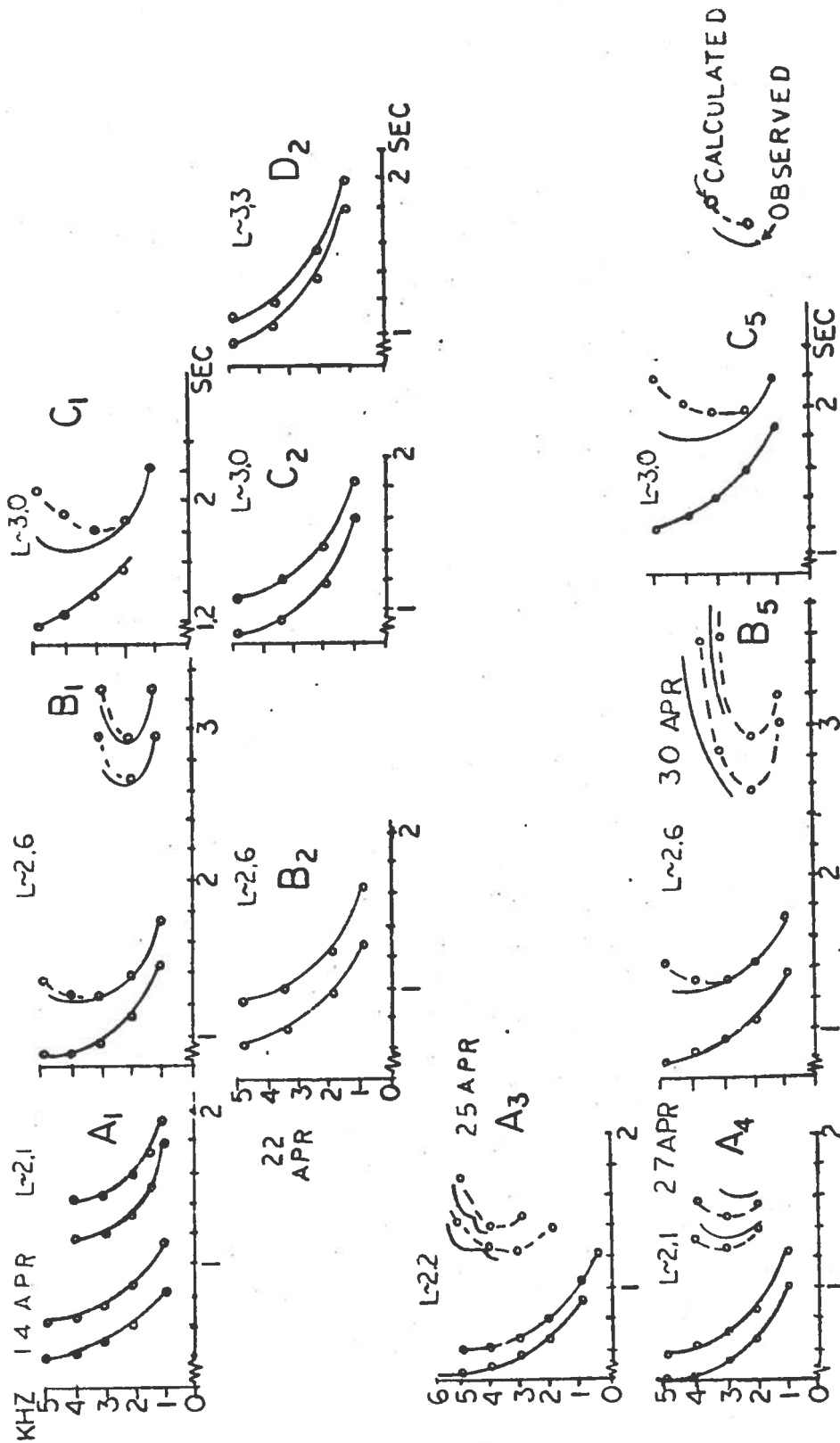


Fig. 5.8. COMPARISON OF COMPUTED AND MEASURED SPECTROGRAMS. The computations for the 14th, 25th, 27th, and 30th of April used the simple D.E. model. The calculations for the 22nd of April used the same D.E. model but modified by the dropoff factor (Fig. 5.5).

the upper frequencies for the third and fourth traces on example B5 extend for long time delays, the lower frequencies do not extend below the nose. This phenomenon indicates that the lowest latitude of excitation is approximately 31° which is higher than that for 14 April.

F. Alouette Topside Density Data

Bauer and Krishnamurthy [1968] used Alouette I topside density data to study the state of the ionosphere before and after the April storm. These data are sketched in Fig. 5.9. In this figure the density profile for 14 April contains a dropoff in density at $L \sim 1.7$ (this density structure was deduced in Fig. 3.1). The density level remains fairly constant between $L \sim 2$ and $L \sim 3$ and decreases beyond $L \sim 3$. When the storm peaks on the 18th, the density profile inflates to higher levels, and a trough appears at $L \sim 2.2$. At a different longitude on the 18th the density levels are not as inflated, but there exists several peaks and valleys between $L \sim 2$ and $L \sim 3.5$. Well after the storm peak, the density profile for 25 April is "flat," i.e., shows little or no variation in L-shell at 800 km. From this presentation, one could conclude that the storm creates density structure during the storm peak, but this disappears by the 25th. However, as shown by example A3 in Fig. 5.4, there is very strong evidence for density enhancement at $L \sim 2.2$. Suggestions for resolving the conflict between MR whistler deduced densities and the Alouette data will be presented in Chapter VI.

G. Behavior of MR Whistlers during Other Magnetically Disturbed Periods

As was demonstrated in previous sections, the lifetime of the inner mode cutoff at $L \sim 2.4$ after the 17 to 18 April 1965 storm is approximately 12 days. After storms of lesser magnitude, the inner mode usually remains cut off for three to six days. These lifetimes are very dependent on how the magnetic activity decays after the storm peak. On many occasions the magnetic activity extends several days beyond the initial storm peak, and this phenomenon usually extends the cutoff lifetime to larger than normal values. For moderate storms (kp 4) the cutoff usually occurs between $L \sim 2.4$ to 2.6. For large magnitude storms the cutoff is at $L \sim 2.4$ or below.

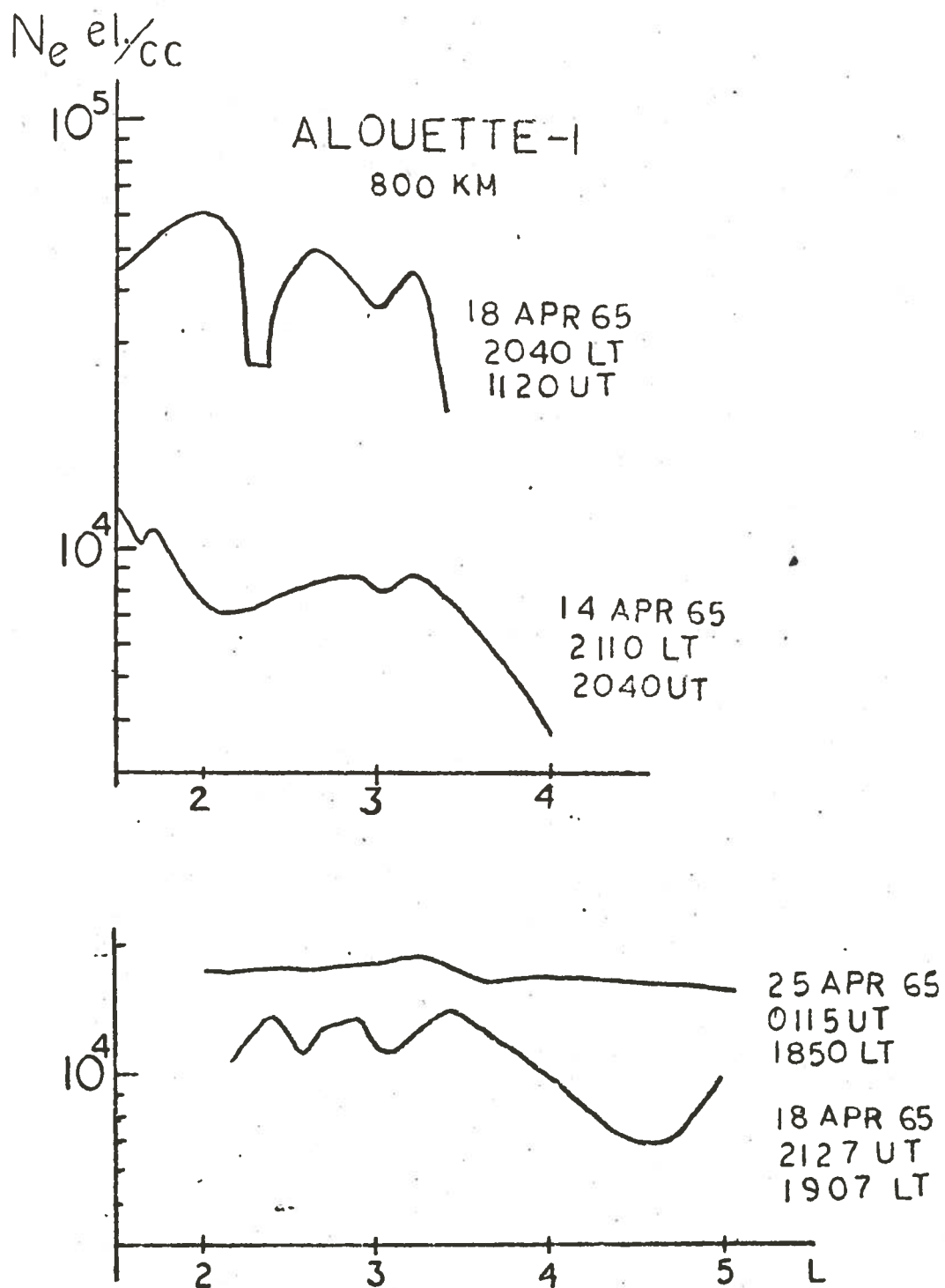


Fig. 5.9. DENSITY MEASUREMENTS AT 800 km MADE BY THE ALOUETTE-1 SATELLITE BEFORE, DURING, AND AFTER THE 17 TO 18 APRIL STORM.

Since successive passes of the OGO-1 satellite have different longitude coverage, the data from the 17 to 18 April storm demonstrates that the cutoff is longitude independent. The OGO-3 satellite sees approximately the same longitude coverage on successive passes. The MR whistler behavior as observed by OGO-3 after a storm displays a very similar pattern to that observed by OGO-1. However the trough, duct, etc. density structure deduced from MR spectral irregularities do show a definite longitude dependence. The outer mode MR whistlers are also longitude dependent, having only been observed over the Alaskan longitudes.

H. Summary

In this chapter we have presented a case study of the MR whistler behavior before and after the 17 to 18 April 1965 storm and have found that the MR whistler activity excited from the low latitudes totally disappears above $L \sim 2.4$ for up to 12 days after the storm peak. It is shown that under the special circumstances of the depletion of the outer plasmasphere $1^- 1^+$ MR whistlers with longitudinal spectral characteristics can be excited from the high latitudes near $L \sim 4$ during the period of the disappearance of the inner MR whistler mode. Comparison of the $1^- 1^+$ longitudinal MR whistler time delays to those of the inner mode MR whistlers observed before and well after the storm peak allows modeling of the decrease in density above $L \sim 2.6$. Ray tracing calculations using the model agree very well with the measured $1^- 1^+$ longitudinal MR whistlers. Inner mode MR whistlers observed below $L \sim 2.4$ show an upper frequency cutoff pattern consistent with a maximum input latitude of 28° to 31° .

The cutoff of inner mode MR whistlers above $L \sim 2.4$ was found to be longitude independent, however outer mode MR whistler occurrence had a strong longitudinal dependence. Examination of MR whistler behavior during other magnetically disturbed periods shows a similar cutoff of inner mode MR whistlers generally between $L \sim 2.4$ to 2.6 .

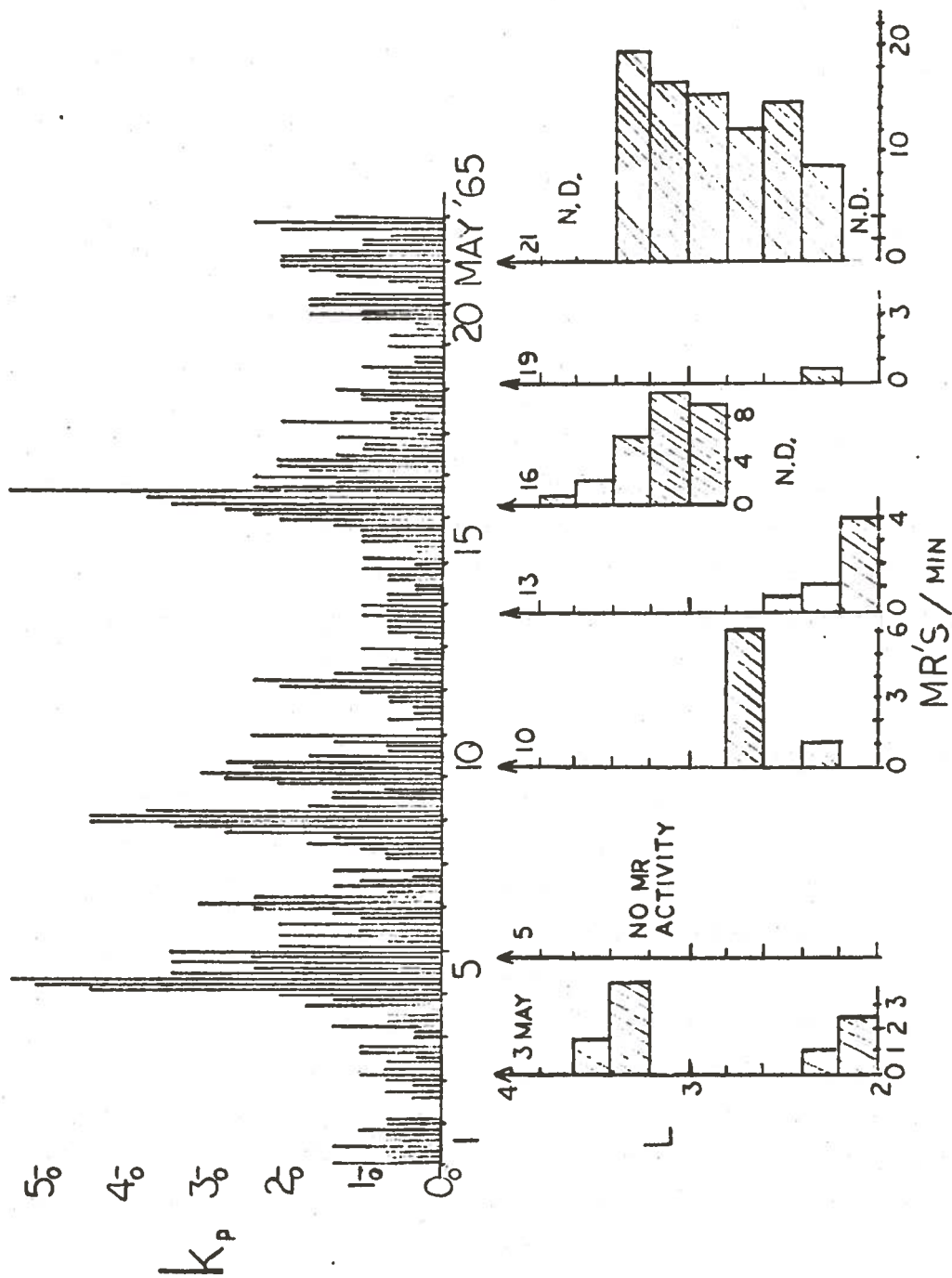


Fig. 5.10. MR WHISTLER ACTIVITY LEVELS DURING MAY 1965 CORRELATED WITH THE MAGNETIC ACTIVITY INDEX K_p . The occurrence levels display a wide variation from pass to pass which is related to magnetic activity.

VI. TRAPPING AND ITS RELATION TO THE STRUCTURE OF THE MAGNETOSPHERE

A. Introduction

In Chapter III on irregularities we saw how various density models changed the pattern of ray paths as compared to that predicted by a smooth model. In this chapter we will examine in more detail the effects of strong gradients on MR whistler propagation. As a reference for the discussion that follows, Fig. 6.1 plots the ray paths for 2 kHz starting

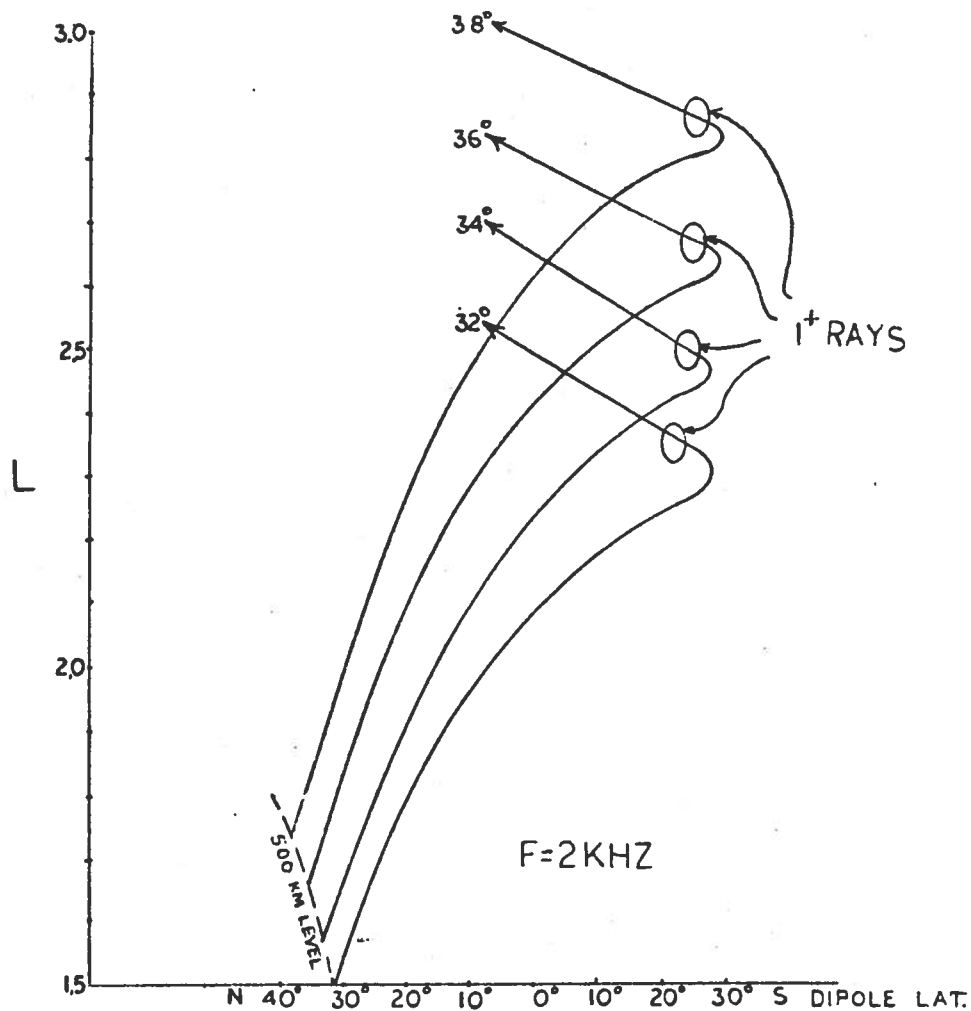


Fig. 6.1. TYPICAL RAY PATHS FOR 2 kHz IN A "SMOOTH" MAGNETOSPHERIC MODEL. The parameter indicated is the starting latitude at 500 km (indicated by dotted line) where the wave normal is vertical. The maximum in South dipole latitude corresponds to the first magnetospheric reflection or turnaround.

at latitudes of 32° , 34° , 36° , and 38° . The density model for the magnetosphere in this case is the simple smooth diffusive equilibrium nighttime model used in the second chapter. The L-shells for these starting latitudes ranged from 1.5 to 1.73. After the first magnetospheric reflection, the rays cross the equator between $L \sim 2.5$ and $L \sim 3.0$.

In contrast to the orderly pattern of rays in Fig. 6.1, Fig. 6.2 plots the ray paths based on the density dropoff model of Chapter III

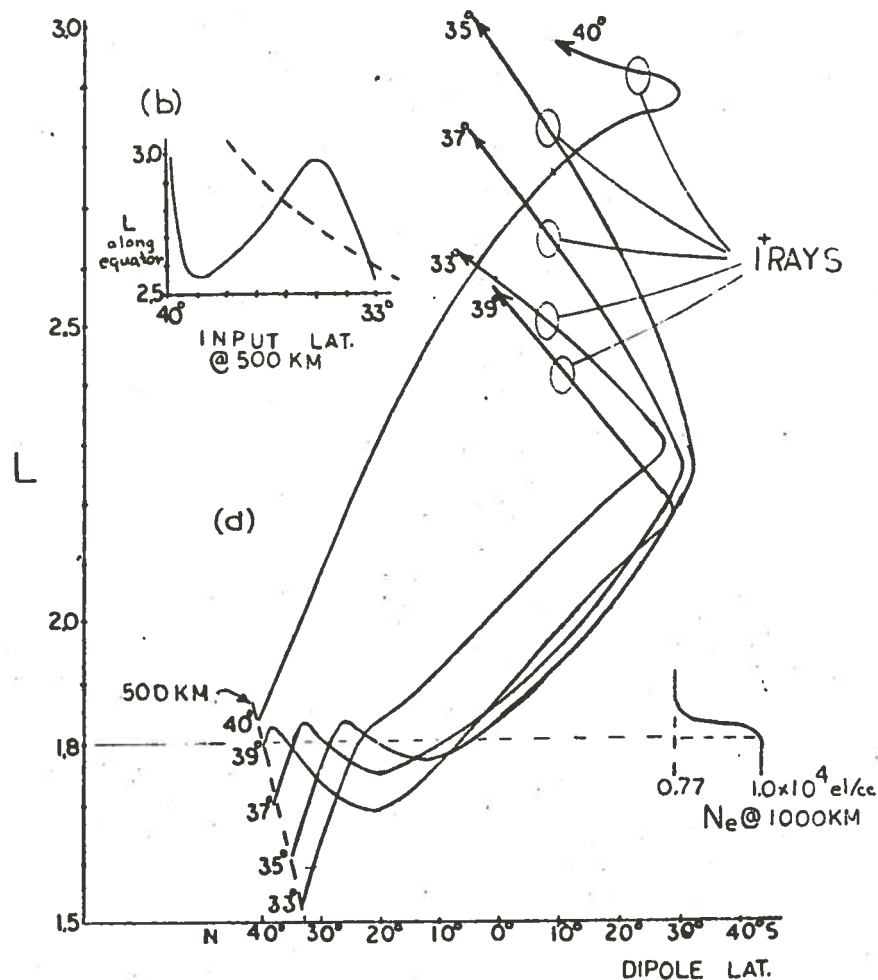


Fig. 6.2. (a) ILLUSTRATION OF THE EFFECTS OF AN ABRUPT DROP IN DENSITY ON THE RAY PATHS. The drop in electron density at 1000 km starts at $L \sim 1.8$ as shown in the lower right-hand of the figure. The pattern of rays crossing the equator after the first reflection is highly disordered resulting in some defocusing. (b) Input latitude vs L-shell along the equator. The steeper characteristic of the input-output curve as compared to that of a smooth magnetospheric model indicates defocusing.

(cf. Fig. 3.1). This model incorporates a 23% dropoff at $L = 1.8$ with a gaussian halfwidth of $.02L$. The ray starting at 33° is only slightly bent as it propagates through the dropoff, and after the first reflection, it crosses the equator at nearly the same point as the 32° ray in Fig. 6.1. However the 35° ray path is bent around after crossing $L \sim 1.8$. The 35° , 37° , and 39° ray paths make one complete oscillation about the $L \sim 1.8$ shell and, after the first reflection, cross the equator between $L \sim 2.5$ and $L \sim 3.0$. The 40° ray path does not cross the dropoff in density and follows a normal path through the magnetosphere. The rays cross the equator between $L \sim 2.5$ and $L \sim 3.0$ in a disordered pattern, which creates the situation where two distinct 1^+ rays may cross the satellite position each with a different time delay, thus creating double traces. This is illustrated in Fig. 6.2 by the 39° and 33° ray paths, which cross at the equator near $L \sim 2.55$. The disordering of the rays produces defocusing as illustrated by the steepness of the curve in Fig. 6.2b. Thus a satellite between $L \sim 2.5$ and 3.0 near the equatorial plane would observe trace splitting and a reduction in amplitudes due to defocusing in the MR whistlers, both evidencing a density dropoff at $L \sim 1.8$.

B. Trapping Conditions

Figure 6.3 gives a schematic view of how a ray is bent by a sharp cross-L density dropoff. This diagram is adapted from Fig. 4 of Smith et al [1960], who used it to explain trapping of rays by enhancements of ionization. Using the Snell's law construction of Fig. 6.3, they showed that the trapping condition for the case of $f \ll f_H$ is

$$\cos \psi_1 \geq \frac{N(P)}{N(O)} , \quad (6.1)$$

where

ψ_1 = initial wave normal angle

$N(O)$ = maximum density (inside density dropoff)

$N(P)$ = background density (where the ray becomes parallel to the field direction)

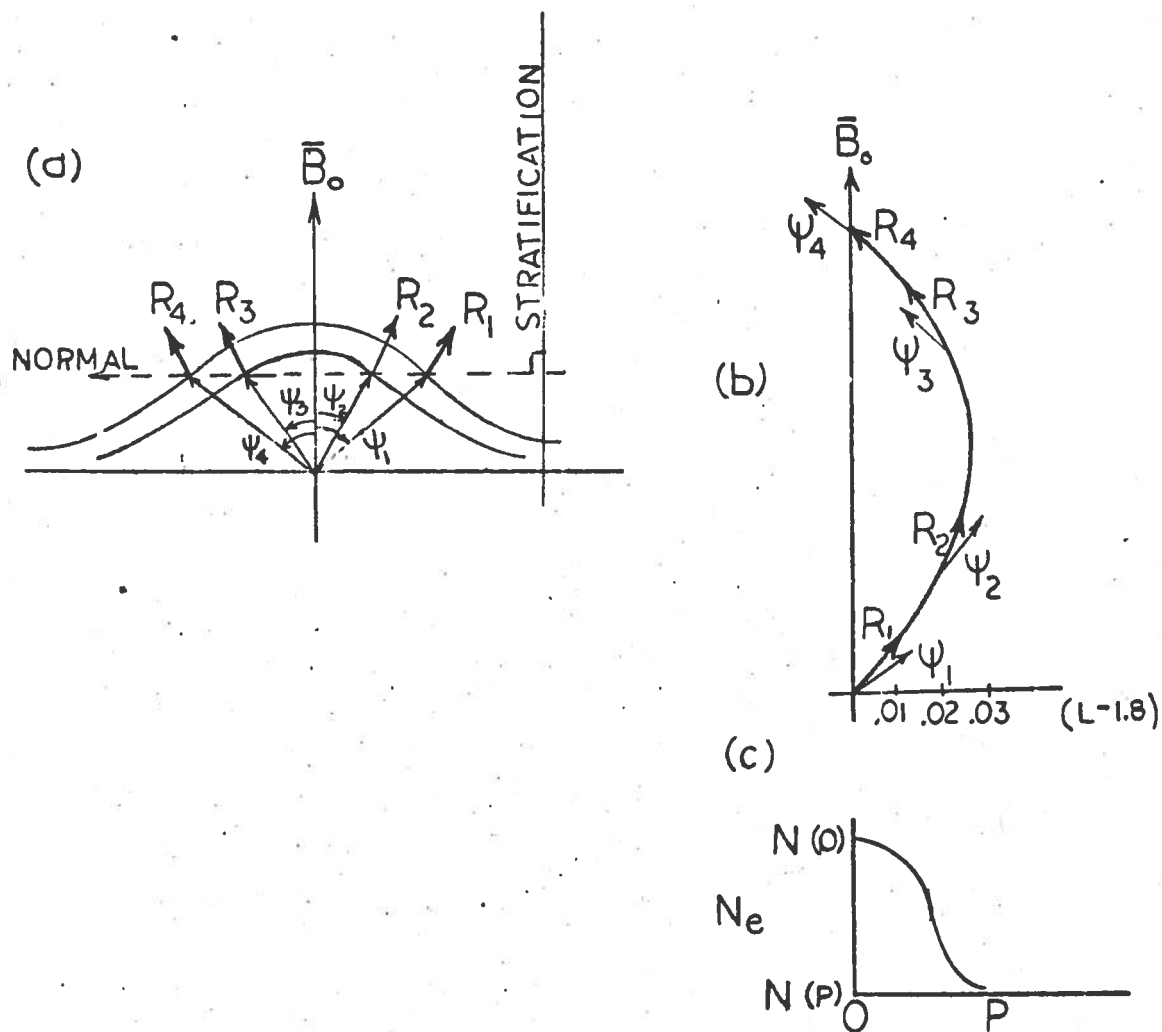


Fig. 6.3. CONDITION FOR TRAPPING A RAY BY A DENSITY DROPOFF. Adapted from Smith [1961] this trapping condition assumes a linear magnetic field with no curvature, ψ_1 is the maximum wave normal angle which can be trapped by a density droppoff characterized by a decrease in density from $N(O)$ to $N(P)$.

Equation (6.1) assumes no field curvature effects and gives the maximum wave normal angle of a ray that would be trapped. Rays with larger wave normal angles than ψ_1 would not be trapped and would require larger decreases in density between points O and P for trapping.

Referring to Fig. 6.2a again, we see that the 33° ray path is not bent or trapped by the cross-L density dropoff because its wave normal angle at $L \sim 1.8$ is apparently too large. However, the wave normal angle at $L \sim 1.8$ is 35° which is less than the trapping angle of 40° as predicted by Eq. (6.1). The 35° , 37° , and 39° rays are initially trapped at $L \sim 1.8$ but then escape into the MR mode at the equator. These rays should remain trapped by our simple trapping criterion which neglects all contributions of field line "curvature" to the gradient of μ . As shown in the next section, this contribution maximizes at the equator and would modify the orientation of the normal to the stratification of Fig. 6.3a.

C. Effects of Magnetic Field "Curvature"

In Fig. 6.4a, two ray paths starting at 35° are plotted to illustrate the effects of increasing the dropoff factor K from .3 to .5. The $K = .3$ ray path, denoted by the solid line, escapes in the equatorial region after making one oscillation about the $L \sim 1.8$ field line. However, the $K = .5$ ray path (dashed line) remains in a trapped mode at $L \sim 1.8$. The wave normal angles for both cases are plotted in Fig. 6.4b. The $K = .3$ curve makes a partial rotation toward the $\psi = 0^\circ$ line at the equator, but then it changes direction and rotates to higher negative wave normal angles, under the effect of the magnetic field gradients. When the ray for $K = .3$ first encounters the density dropoff at 30° latitude, the density gradient dominates any contribution of magnetic field curvature to the gradient of μ . Thus the trapping of the ray is described by Fig. 6.3. But at the equator, curvature effects are significant and will modify the trapping criterion. In the following discussion, we will give a quantitative examination of curvature effects at the equator.

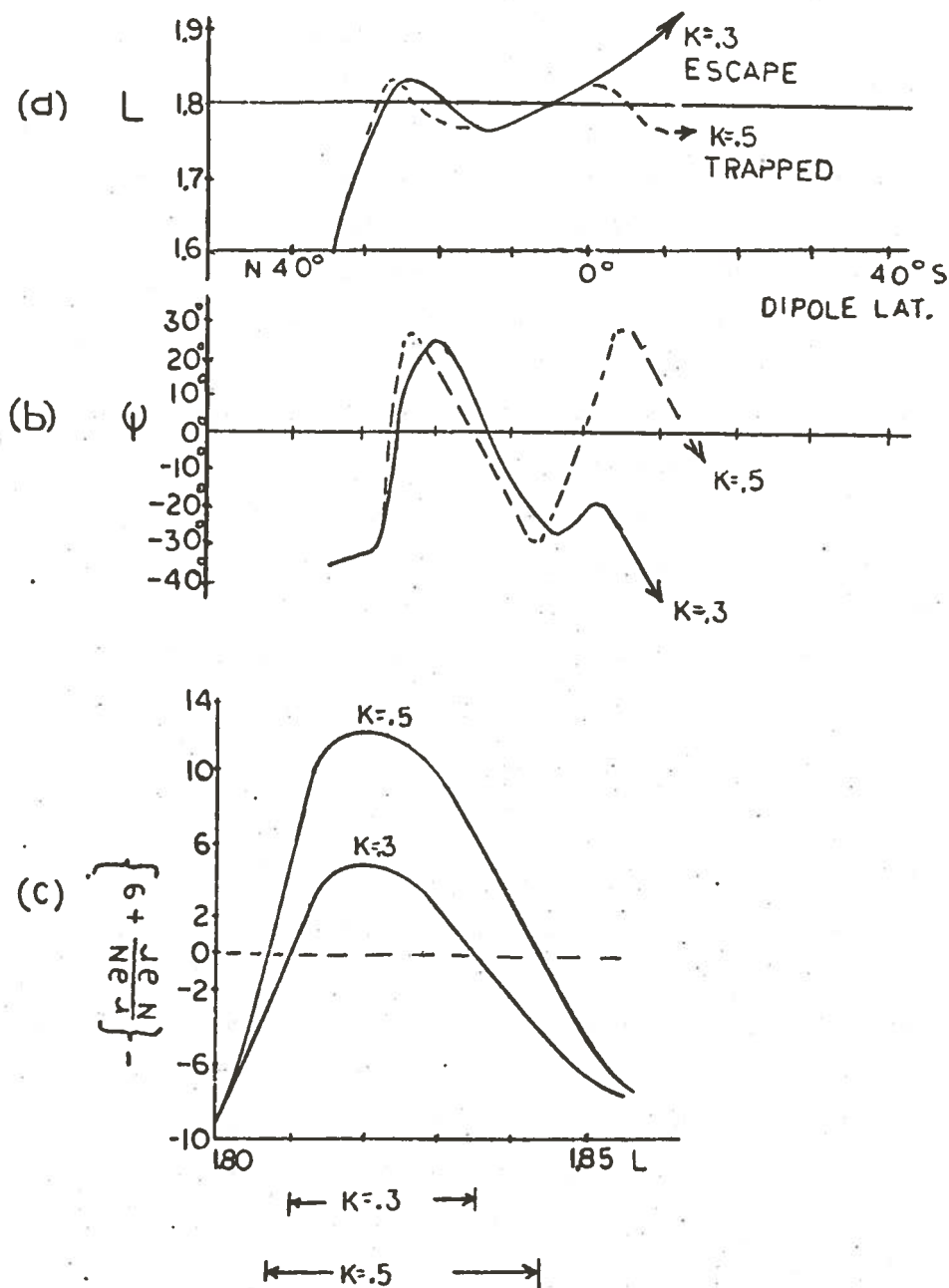


Fig. 6.4. EXAMPLES OF CURVATURE EFFECTS ON TRAPPING OF RAYS. (a) L-shell vs latitude plot of the ray path for two magnitudes of dropoffs in density at $L \sim 1.8$. (b) Wave normal angle variation for the ray path in (a) illustrating trapped and escaped modes. (c) Plot of the relative dominance of the density gradient vs the curvature gradients showing the density gradient range of control at the equator.

According to Scarabucci [1969], the variation of wave normal angle is governed by the following equation:

$$\frac{2\mu}{c} \frac{d\psi}{dt} = - \sin \delta \left\{ \frac{1}{N} \frac{\partial N}{\partial r} + \frac{3}{r} (m_c + m_y) \right\} + \frac{\cos \delta}{r} \left\{ \frac{1}{N} \frac{\partial N}{\partial \theta} + m_\theta \right\} \quad (6.2)$$

where

μ = refractive index

ψ = angle between wave normal and geomagnetic field

δ = angle between local vertical and wave normal

N = electron density

r = geocentric radius

θ = colatitude

t = time

The influence of the direction of the dipole geomagnetic field is given by

$$m_c = \frac{2(1 + \cos^2 \theta)}{1 + 3 \cos^2 \theta}, \quad (6.3)$$

and the influence of the gradient of magnetic field intensity over the wave normal angle ψ is given by

$$m_y = \frac{\cos \psi}{\cos \psi - f/f_H}, \quad (6.4a)$$

and

$$m_\theta = \frac{3 \sin \theta \cos \theta}{1 + 3 \cos^2 \theta} \cdot m_y \quad (6.4b)$$

At the equator ($\theta = 90^\circ$) the direction term (6.3) reaches its maximum value of 2. For the equatorial region, the density $N(r, L)$ reduces to a function of r and thus (6.1) reduces to

$$\frac{2\mu}{c} \frac{d\psi}{dt} = - \sin \delta \left\{ \frac{1}{N} \frac{\partial N}{\partial r} + \frac{3}{r} \left(2 + \frac{\cos \psi}{\cos \psi - f/f_H} \right) \right\} \quad (6.5)$$

If $\psi \leq 30^\circ$ and $\cos \psi \gg f/f_H$, then the above equation simplifies to

$$\frac{2\mu}{c} \frac{d\psi}{dt} = + \frac{\sin \delta}{r} \left\{ - \frac{r}{N} \frac{\partial N}{\partial r} - 9 \right\} = \frac{\sin \delta}{r} \{A\} \quad (6.6)$$

The derivative of N is negative if N decreases outward, and thus the derivative term may be greater than 9 if the decrease in density is sufficiently sharp. If A is positive, then the density gradients dominate, but for a negative value of A the magnetic field dominates.

In our density dropoff models we have used the following to describe the density variation.

$$N(r, L) = N_{DE}(r) \left\{ 1 + K \cdot \exp - \left[\frac{(L - L_o)^2}{2w^2} \right] \right\} \quad L > L_o \quad (6.7)$$

$$N(r, L) = N_{DE}(1 + K) \quad L \leq L_o$$

For $L > L_o$ the variation of the term in brackets in Eq. (6.7) is much faster than that of the $N_{DE}(r)$ factor, and the partial derivative of Eq. (6.6) may be approximated by

$$\frac{r}{N} \frac{\partial N}{\partial r} = - \frac{K(L - L_o) L}{w^2 \left\{ 1 + K \cdot \exp - \left[\frac{(L - L_o)^2}{2w^2} \right] \right\}}$$

and the quantity A becomes:

$$A = \frac{K(L - L_o) L}{w^2 \left\{ 1 + K \cdot \exp - \left[\frac{(L - L_o)^2}{2w^2} \right] \right\}} - 9 \quad (6.8)$$

The above quantity is plotted for the $K = .3$ and $.5$ cases in Fig. 6.4c. When $A > 0$, the density gradient is in control of the wave normal rotation, and this range of control is denoted at the bottom of Fig. 6.4c. In the $K = .3$ case, the ray initially crosses $L = 1.8$ near 30° latitude, where the $K = .3$ range of control extends to $L = 1.845$. But at the equator where the direction gradients maximize, the $K = .3$ range of control shrinks to an upper limit of $L \sim 1.835$ as shown in Fig. 6.4c. The outer bounds for the ray path and wave normal variation are set by the initial wave normal angle at $L = 1.8$ as shown in Fig. 6.4b. However in the $K = .3$ case the shrinking of the range of control at the equator slows the rotation of the wave normal back to the $\psi = 0^\circ$ direction. At $L \sim 1.835$ the density and magnetic field direction gradients are equal, and the wave normal sees no gradient to cause it to rotate as shown by point 1 in Fig. 6.4b. Above $L \sim 1.835$ the total gradient $d\psi/dt$ becomes negative and the wave normal rotates away from the $\psi \sim 0^\circ$ line and towards higher (negative) angles. Thus the ray for $k = .3$ escapes from the quasi-trapped mode into the MR mode at the equator because of field "curvature" effects. In the $K = .5$ case the range of control is wider than the maximum excursion of the ray from the $L = 1.8$ field line, and the ray remains trapped at the equator.

Figure 6.5a plots the ray paths calculated using a density dropoff model with $k = .5$ and $w = .02$ at $L = 1.8$. Rays starting between 32° and 38° are totally trapped by the density decrease. The ray starting at 31° crosses $L \sim 1.8$ with a wave normal angle sufficiently large to escape. The 39° ray sees the density dropoff immediately after entering the ionosphere. The wave normal always experiences a small partial rotation toward the longitudinal position due to the decrease in density between 500 km and 1000 km. Adding the density gradient of the abrupt density dropoff to the normal density gradient forces the wave normal to rotate well past the longitudinal position. Along the inward directed ray path there is no large density gradient ($L < 1.8$), and the magnetic field gradient rotates the wave normal outward. When the density dropoff at $L \sim 1.8$ is again encountered, the wave normal of the ray is too large to be trapped. From Fig. 6.5a we see that there is some 1^+ trace splitting at $L \sim 2.6$ near the equator, but the most important effect of the

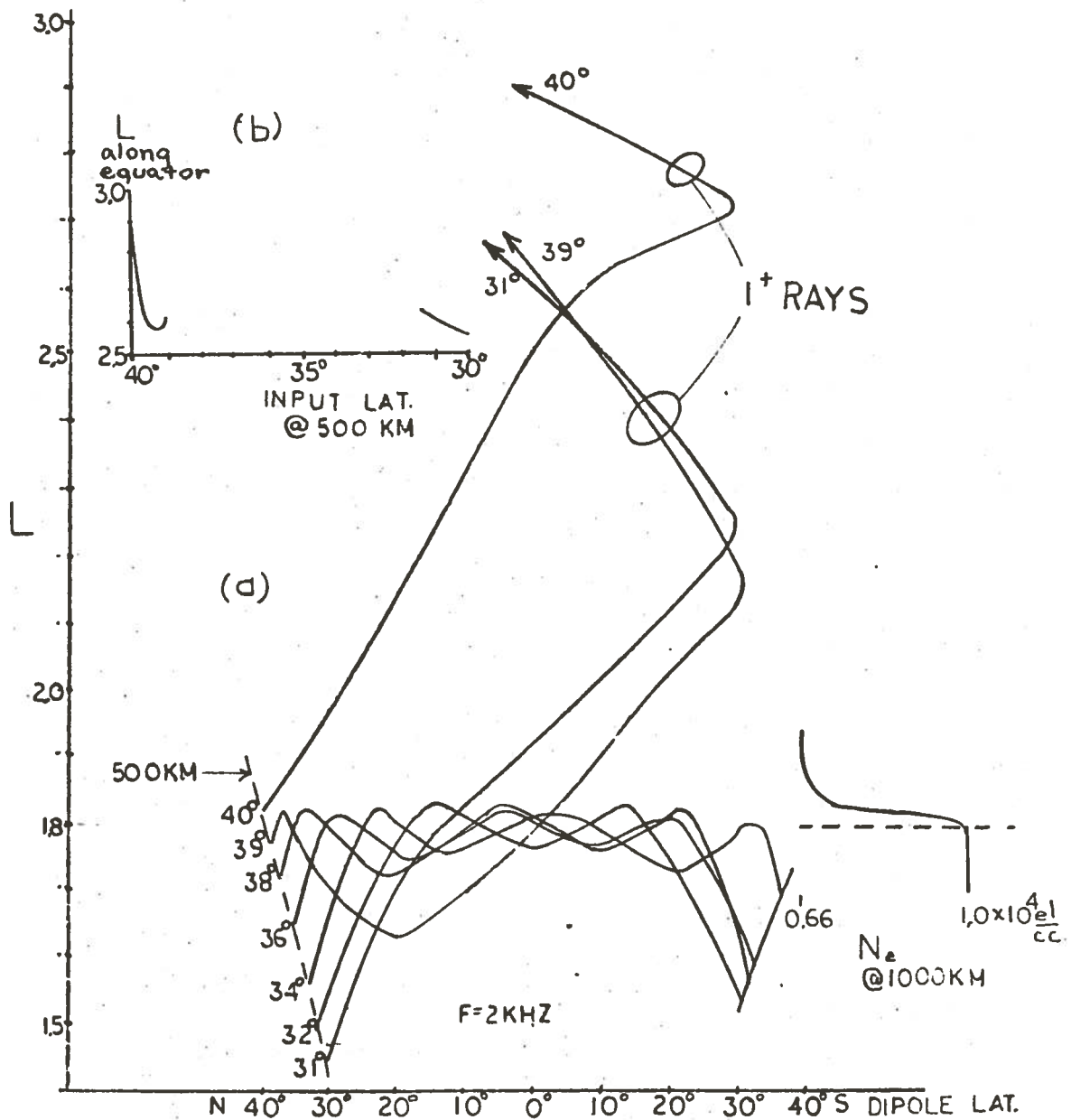


Fig. 6.5. (a) TRAPPING OF RAYS BY AN ABRUPT DENSITY DROPOFF AT $L \sim 1.8$. The rays starting between 31° and 39° are trapped totally. (b) Input latitude at 500 km vs output L-shell along the equator showing great defocusing for rays starting between 39° and 40° .

trapping is the extreme defocusing between $L \sim 2.6$ and $L = 3.0$, since only the rays starting between 39° and 40° are able to illuminate that wide region (see Fig. 6.5a or more detailed Fig. 6.5b).

The same type of trapping takes place with density dropoffs at higher L-shells as illustrated by Fig. 6.6. For $K = .5$ at $L = 2.4$ all rays starting between 39° and 48° are trapped. One might ask what would happen if we combine the two density dropoffs at $L = 1.8$ and 2.4 into one model. The trapping regions do overlap and the possibility exists that rays starting from 32° to 48° would be trapped. However, as illustrated by Fig. 6.7a rays beginning between 39° and 40° are partially trapped by the irregularity at $L = 1.8$, and by the time they reach $L = 2.4$, their wave normal angles are too high to be trapped by this second dropoff. If we wish to have complete trapping, we must allow these rays to traverse the $L \sim 1.8$ shell without being reflected. Since this partial trapping occurs only when the irregularity extends down into the ionosphere, we can modify our model by making K a function of altitude, such that it is small below 1000 km. When the rays that originate between 40° and 39° strike the $L = 1.8$ field line, they see a very small density gradient which is too small to cause trapping. These rays propagate outward as the corresponding 40° to 39° rays did in Fig. 6.6 and become trapped at $L = 2.4$ as shown in Fig. 6.7b. The primary difference between the ray paths in Figs. 6.7a and 6.7b is the leakage of the rays starting between 39° and 40° in the former. These rays in Fig. 6.7a are however highly defocused (cf. Figs. 6.5a and b) and thus the corresponding signals would have low amplitudes.

D. Consequence of Trapping

As was shown in the previous discussion, one can limit the range of latitudes of MR whistler excitation by inserting two cross-L density dropoffs into our model of the magnetosphere. In the model used in Fig. 6.7, the maximum latitude of MR whistler excitation is 31° . As previously demonstrated in Section II.H, the starting latitude limitation will affect the upper frequency portion of MR whistler components (Fig. 2.15b). Since the high frequencies tend to reach a maximum L-shell and then bounce inward, these frequencies would not be observed at the higher L-shells if

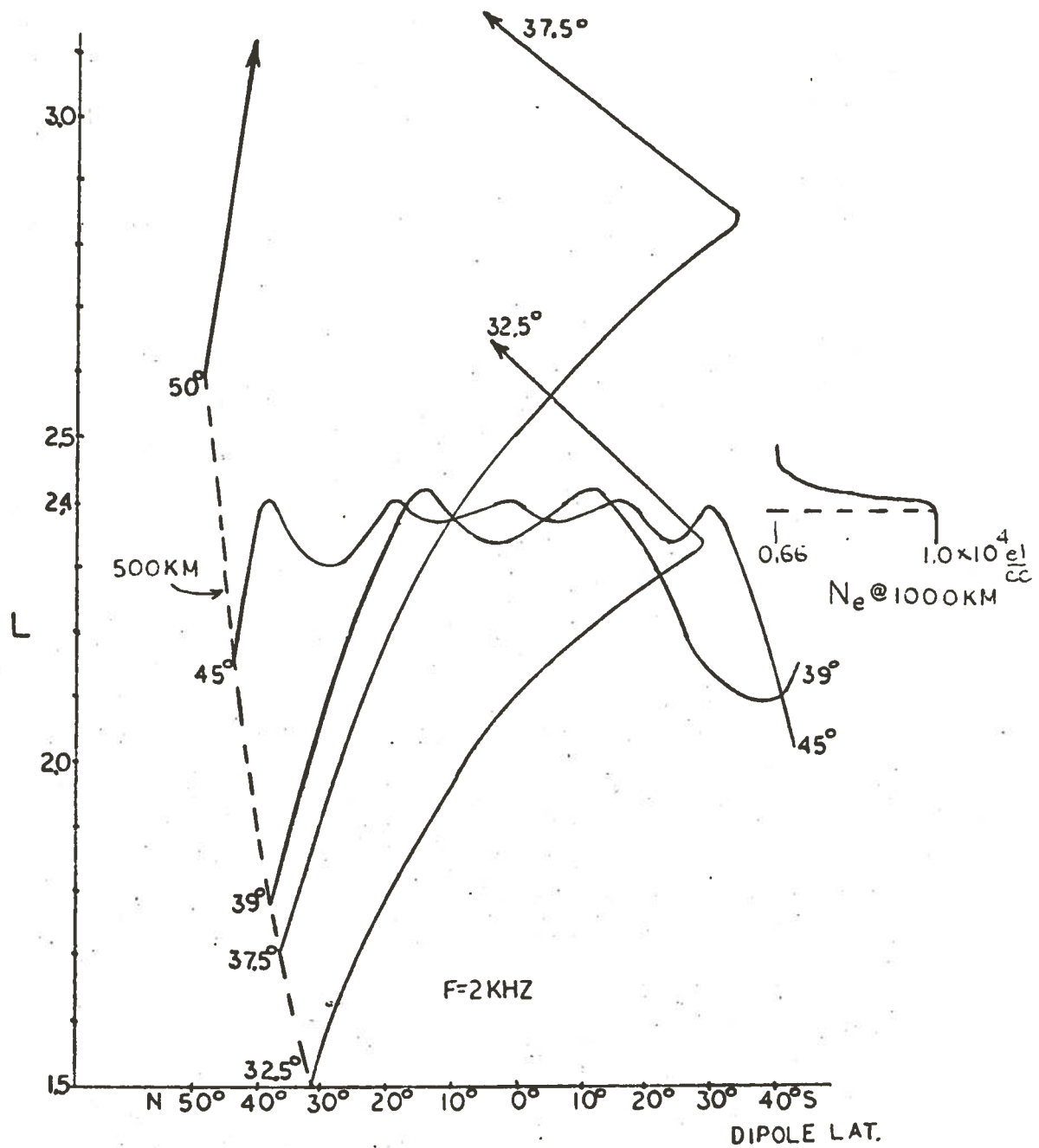


Fig. 6.6. TRAPPING OF RAYS BY AN ABRUPT DENSITY DROPOFF AT $L \sim 2.4$.
The trapping region occurs for the 39° to 48° latitudes.

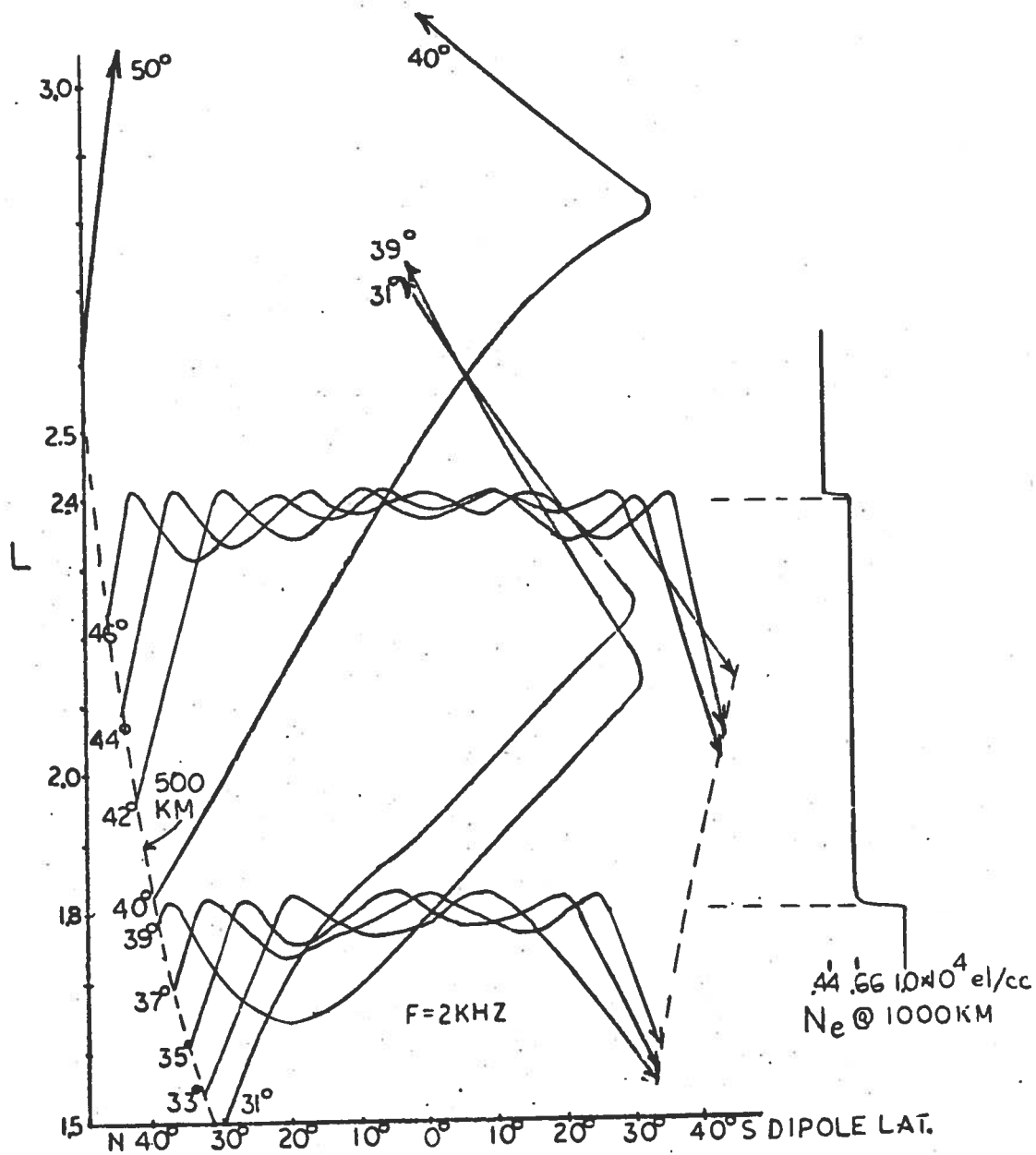


Fig. 6.7. (a) TRAPPING OF RAYS BY TWO DENSITY DROPOFFS AT $L \sim 2.4$ AND $L \sim 1.8$. Leakage rays, which are not trapped, start between 39° and 40° . (b) Trapping of rays by density dropoffs at the same location as in (a) but with an initial height variation. This allows the all rays starting between 31° and 48° to be trapped with no leakage.

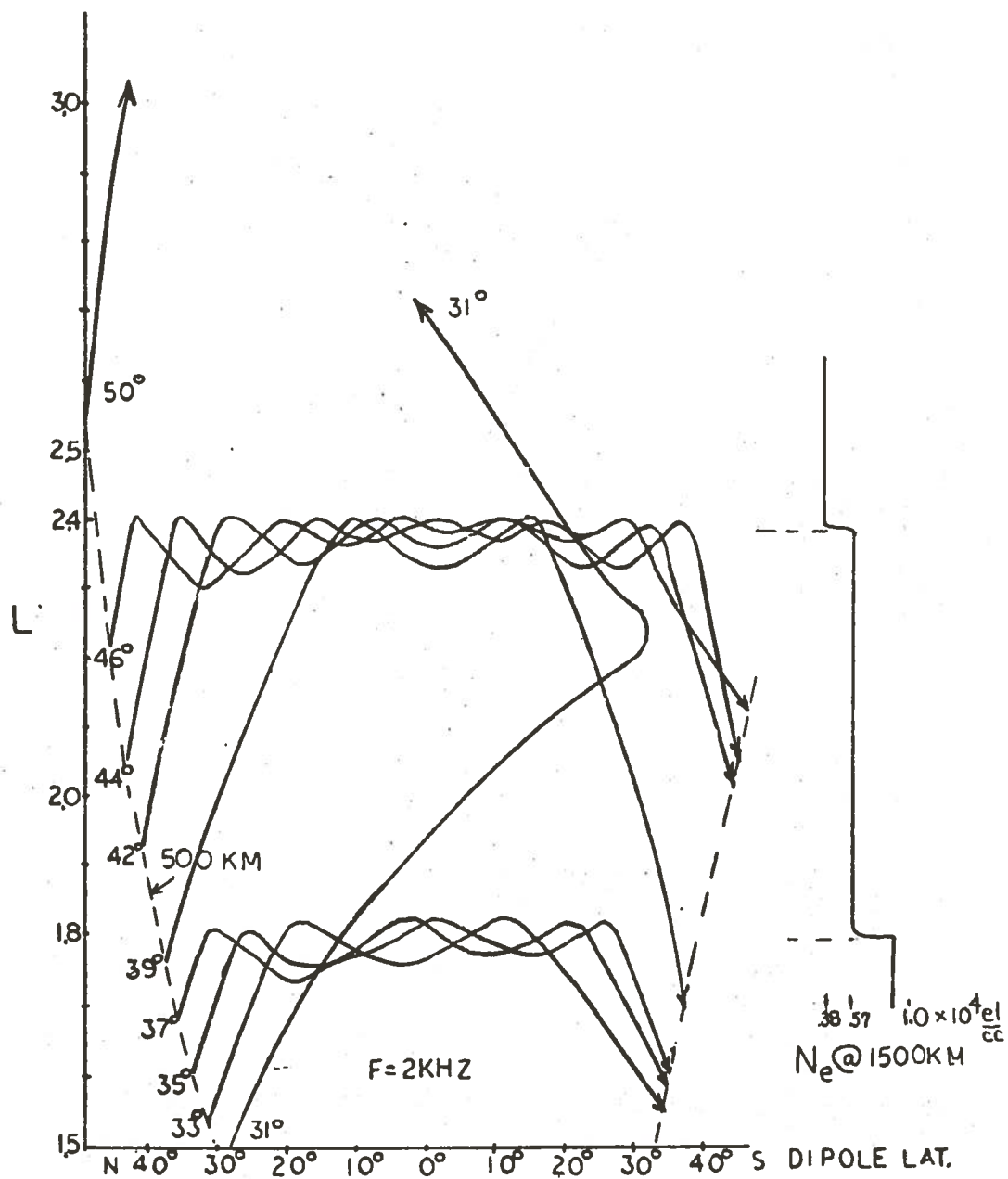


Fig. 6.7. CONTINUED.

there is an upper bound on excitation latitudes. The lower frequencies penetrate to much higher L-shells than the high frequencies as shown in Fig. 6.8. If only input latitudes below 31° are allowed for MR whistler excitation, then the upper frequency cutoff pattern of MR whistler components illustrated in Fig. 6.9 results. Theoretically within this model, one would only observe frequencies below 1 kHz above $L \sim 3$.

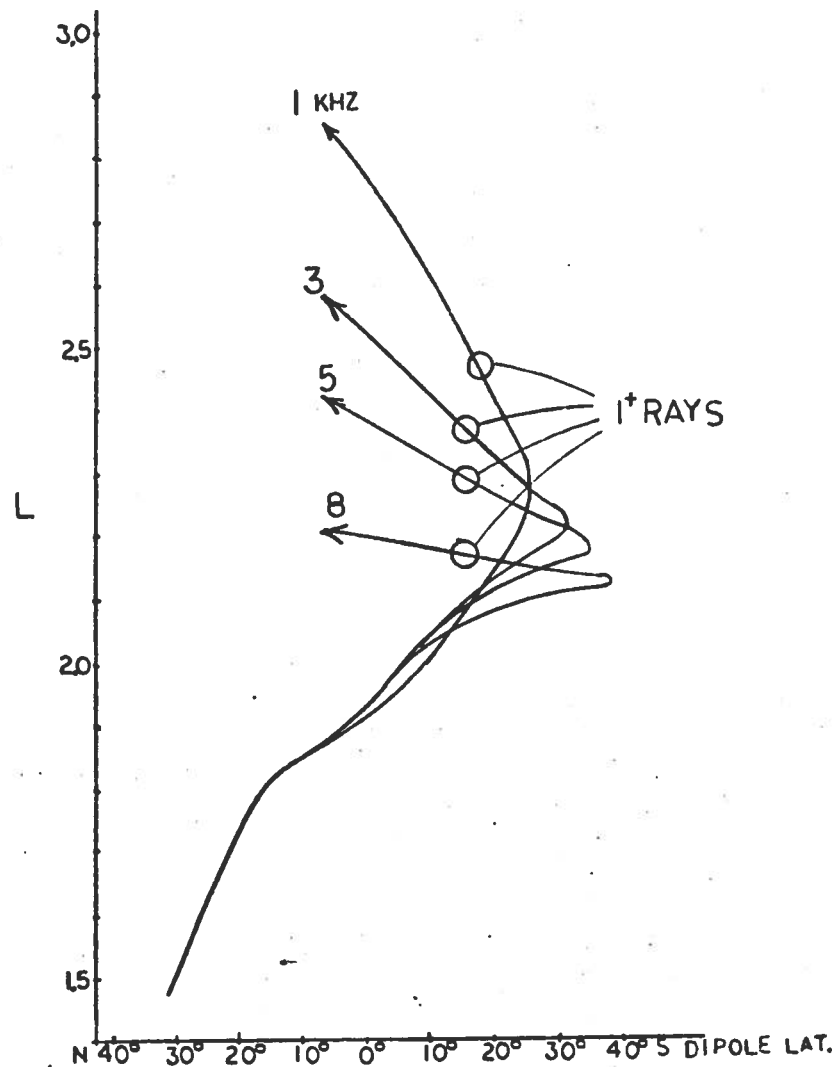


Fig. 6.8. CROSS-FIELD PENETRATION OF 1^+ RAY PATHS FOR A MAXIMUM STARTING LATITUDE AT 31° . The low frequencies have the greatest penetration into the magnetosphere.

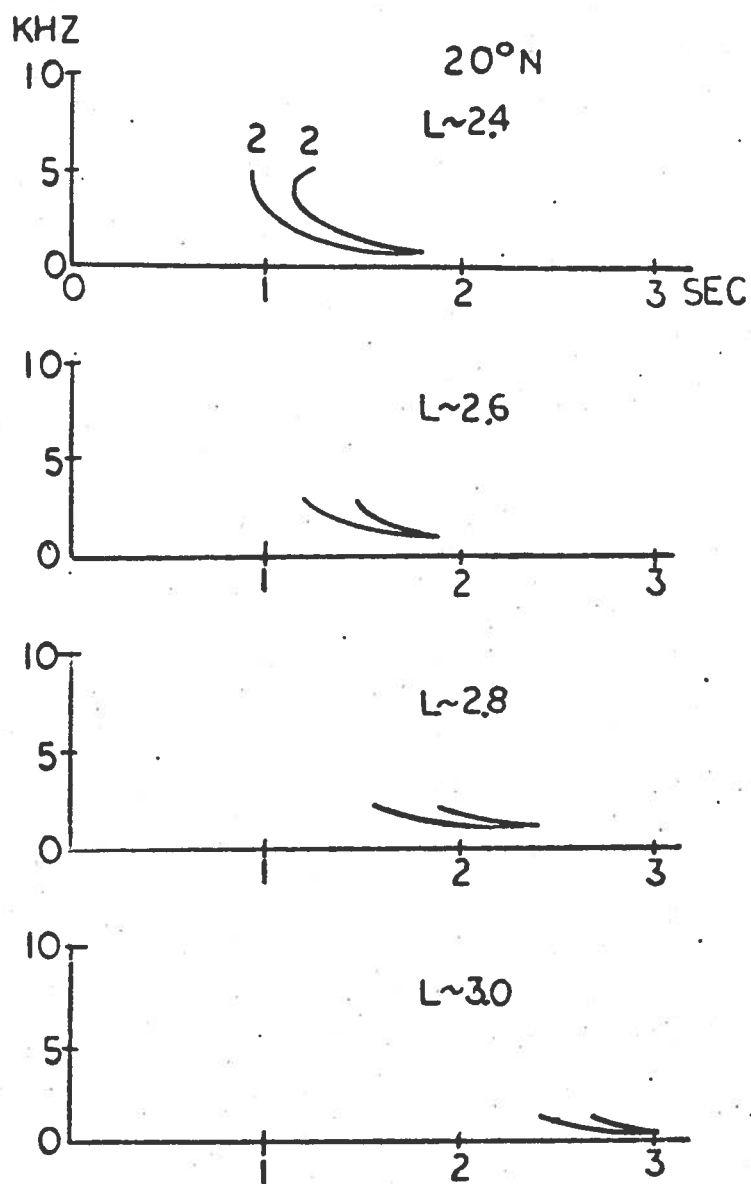


Fig. 6.9. $2^- 2^+$ MR WHISTLER SPECTRA PRODUCED BY RAY PATHS WHICH HAVE A MAXIMUM STARTING LATITUDE OF 31° . At the higher L-shells only the very low frequencies can be observed because of their greater cross-L penetration.

If we assume that the maximum input latitude is 31° in our smooth magnetospheric models and calculate the resulting spectra, we find that the upper frequency cutoffs are 2 kHz lower than those predicted by our dropoff model for comparable satellite positions in Fig. 6.9. This result shows that the predicted cutoff pattern is model-dependent. Thus any statement of maximum input latitude based on an observed MR whistler upper frequency cutoff pattern should also include magnetospheric density model specifications. To achieve the same upper frequency cutoff pattern for both models, the location of the two cross-L density dropoffs would have to be shifted down to $L \sim 1.7$ to 1.6 and $L \sim 2.2$ to 2.3 .

E. Comparison of Theoretical Results of Trapping with Observations

The following table summarizes the observations of MR whistlers after the 17 to 18 April 1965 storm as discussed in Chapter V, Section C.

Table 6.1

Date of Pass	L-shell Cutoff of Inner Mode MR's	Maximum Input Latitude Inferred from Smooth Model	Type of MR Whistler Activity (Component)
22 April	$L \sim 2.4$	31°	$2^- 2^+$ (one observation at $L \sim 2.4$)
25 April	$L \sim 2.4$	31°	$2^- 2^+$ (many observations at $L \sim 2.2$ to 2.4)
27 April	$L \sim 2.3$ to 2.2	28°	$1^- 1^+$ $3^- 3^+$ (many observa- tions at $L \sim 2.1$ to 2.2)

Examples of inner mode MR whistler spectra observed on 25 April are shown in Fig. 6.10. At $L \sim 2.2$ a strong multicomponent MR whistler was observed (Fig. 6.10a) and above $L \sim 2.2$ only $2^- 2^+$ MR whistlers were observed (Fig. 6.10b). The upper frequency cutoff for the $2^- 2^+$ example is approximately 4.5 kHz. Between 1.5 and 2.5 kHz the spectra signal strength remains at a strong level, but below 1.5 kHz there is a marked decrease in signal strength. Defocusing calculations for this example show that frequencies

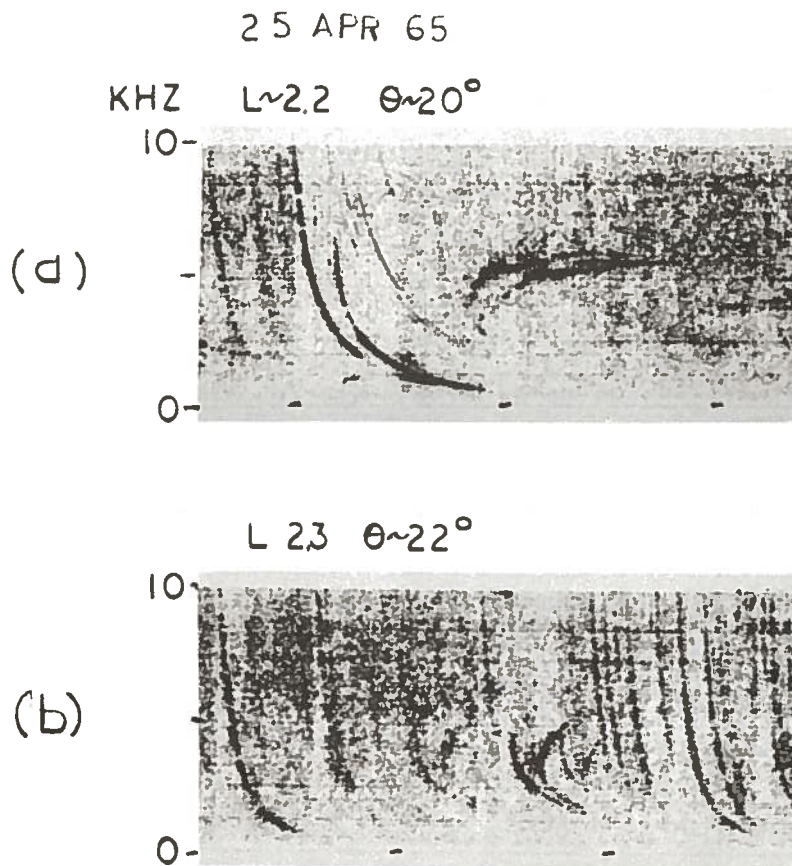


Fig. 6.10. MR WHISTLER SPECTRA FOR 25 APRIL 1965
 SHOWING THE PROGRESSIVE DISAPPEARANCE OF THE
 HIGH FREQUENCIES AS THE SATELLITE MOVES TO HIGHER
 L-SHELLS. (a) A four-component MR whistler with
 a duct (enhancement) interaction affecting the
 $3^- 3^+$ traces. (b) $2^- 2^+$ MR whistler with the
 upper frequency portions missing. Note that the
 upper cutoff is quite sharp whereas the low fre-
 quency attenuation is not as severe.

about the nose frequency suffer little loss (~ 1 dB), while at frequencies near the bottom portions of the spectra the defocusing may be ~ 5 dB.

The broadband VLF receiver on OGO-1 log-compresses incoming signals from an 80 dB to a 20 dB dynamic range. Furthermore the receiver has an instantaneous AGC action such that a very strong signal may suppress a weaker one. This arrangement allows very wide dynamic range but provides poor amplitude resolution. In addition the transferring of the broadened data through spectrum analyzers onto film records further distorts the amplitude information. Muzzio (private communication) has found that there may be only a 10 dB difference between the strongest signal on a spectrogram and the background noise. This finding is somewhat substantiated by the spectra of Fig. 3.3c whereby an enhancement of density defocuses a band of frequencies in the spectra by at least 4 dB (Chapter III, Section C). The defocusing produces a gap in the spectra. So it is entirely reasonable to assume that defocusing is responsible for the reduction of the lower frequency signal strength in Fig. 6.10b.

To account for the total disappearance of MR whistlers above a certain L-shell (e.g., $L \sim 2.4$ for 22 and 25 April) we propose the following explanation. The upper frequency cutoff shifts downward as the satellite moves upward in L-shell. The calculated shift for smooth models is about 1.5 kHz per 0.1 L-shell and may be more for other models. For the example of Fig. 6.10b as the satellite moves from $L = 2.3$ to 2.4 this would shift the upper frequency cutoff to below the nose. All frequencies in the resulting spectrum at $L \sim 2.4$ would suffer defocusing loss. Since there is a strong background of fractional hop whistlers, they would tend to wipe out any observable MR spectra due to the AGC of the receiver. For the example of Fig. 6.9 the defocusing loss would probably cause an observable disappearance of the MR spectra above $L \sim 2.6$. A similar progression of lowering upper frequency cutoff for $2^- 2^+$ MR whistlers due to a maximum input latitude of 28° is shown in Fig. 6.11. This figure approximates the conditions found on 27 April. The defocusing loss would probably cause a disappearance under normal conditions above $L \sim 2.3$.

Thorne [1968] hypothesized a secondary peak in the electron energy distribution near 10 keV which would allow Landau resonant particle

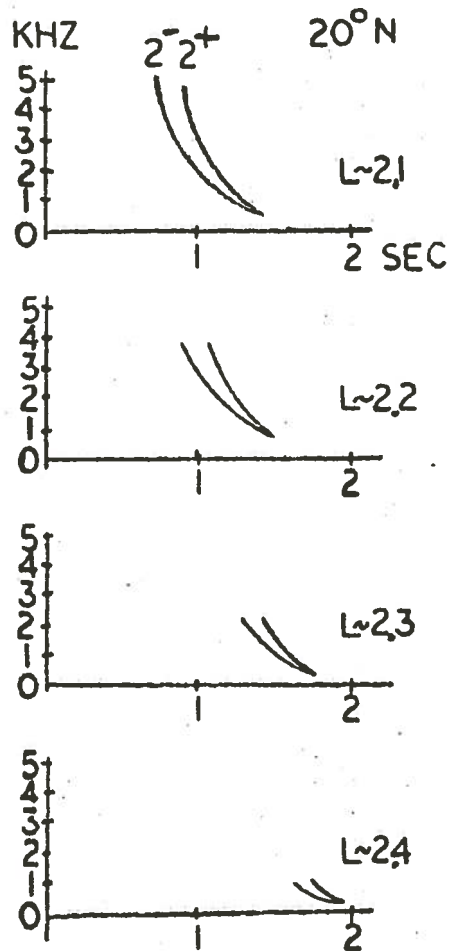


Fig. 6.11. $2^- 2^+$ MR WHISTLER
SPECTRA PRODUCED BY RAY PATHS
WITH A MAXIMUM STARTING LATI-
TUDE OF 28° . Note the extreme
frequency restriction of the
MR whistler at $L \sim 2.4$.

interactions with MR whistler waves. His approach used Landau growth and damping to quantitatively explain the upper and lower frequency cutoffs as well as the enhanced signal strengths. We have however shown that the MR whistler spectra observations can be explained by propagation in a cold plasma without the need of hot plasma particles. Landau particle interactions may be present, but at this time more quantitative work has to be done to predict exactly what the theoretical effects are.

F. Observation of Magnetospheric Structure by Satellites

Taylor et al [1971] has measured some very significant density structure with the OGO-4 H^+ detector, in the topside ionosphere. Immediately after a storm of 21 September 1967, the H^+ density profile exhibits a sharp dropoff at $L \sim 1.8$, a trough at $L \sim 2.2$, an enhancement at $L \sim 2.5$, another dropoff at $L \sim 2.7$, and a trough at $L \sim 2.9$. Figure 6.12 shows this density structure (A) compared to profile (B) which exhibits no significant sharp variations. The OGO-4 H^+ high resolution data indicates that the structure content varies as longitude changes and that the structure is observed in the topside ionosphere, lasts only for a day or two before it disappears. All measurements were made near local midnight on several OGO-4 passes ranging between $7^\circ W$ and $91^\circ E$ longitude.

The structure, reported by Taylor et al [1971], obviously contains the sharp cross-L density dropoffs required for trapping of whistler rays. However, Taylor's structure disappears in the topside ionosphere after about one day. The same phenomenon can be observed in the Alouette-1 electron density data and to the knowledge of the author has not been fully examined in the literature. As shown in Fig. 5.9 the Alouette-1 electron density profile during a storm peak shows much structure, yet several days later the density profile shows little variation with L-shell. The interpretation of the Alouette data is hampered by the fact that the O^+ -ion is a major constituent in the topside ionosphere and may obscure any significant H^+ ion density structure. The MR whistler data from 17 to 18 April 1965 storm (cf. Chapter V) indicates that the density structure can last up to 12 days. The apparent disagreement between the observed life times of the storm-induced structure can be partially resolved in the following discussion.

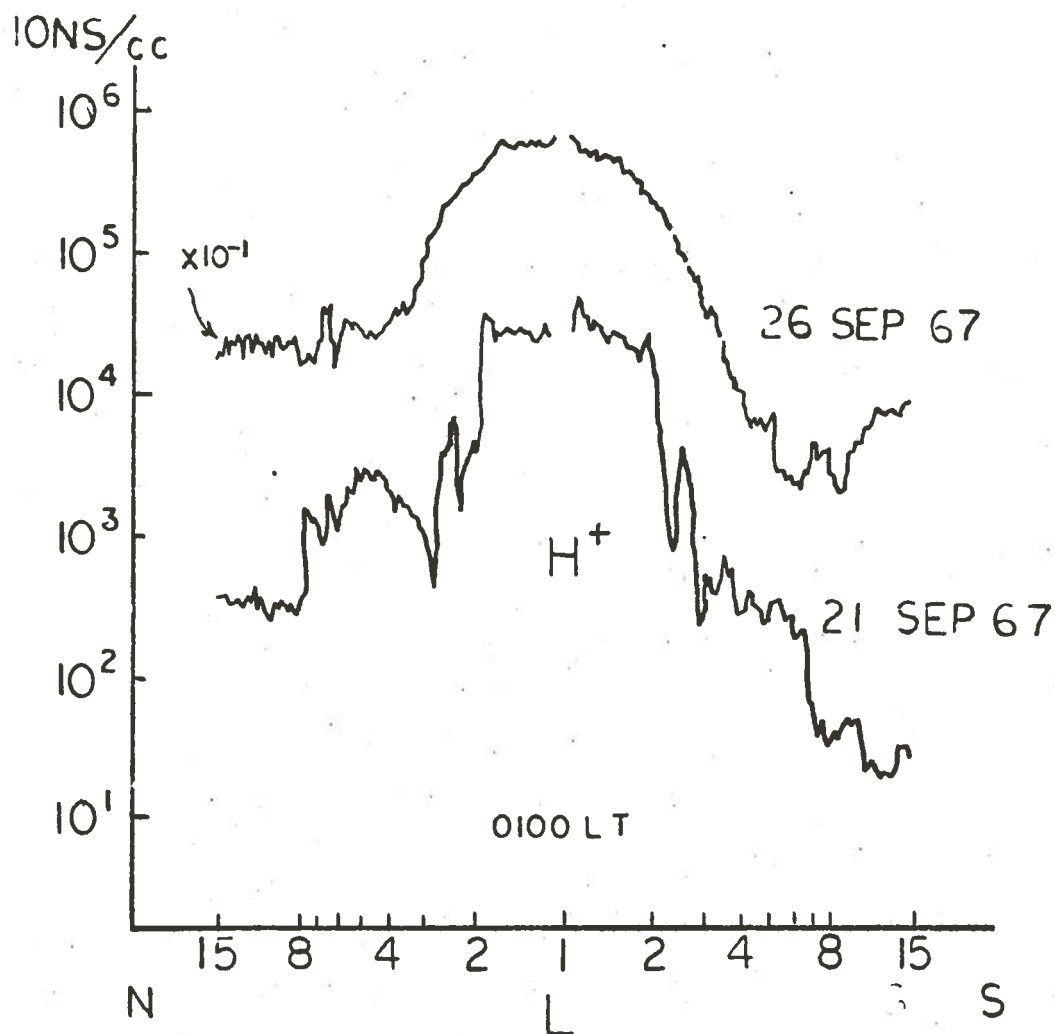


Fig. 6.12. A COMPARISON OF H^+ PROFILES. The profile of 21 September, measured immediately after the storm peak, shows significant density structure. The profile of 26 September, measured after five days of quiet magnetic conditions, shows none of the density structure of the 21 September profile [Taylor et al, 1971].

Grebowsky et al [1970] have presented a comparison between coincident H^+ measurements made by the OGO-4 satellite (topside ionosphere, 600 to 800 km) and the OGO-3 satellite (lower magnetosphere, 3000 to 6500 km). In one example (Fig. 2 of Grebowsky et al [1970]), the OGO-4 H^+ density profile is very similar to the B (quiet) profile of Fig. 6.12. The total ion density profile, corresponding to the electron density, shows very little variation with L-shell due to the presence of O^+ , which compensates for the low H^+ levels above $L \sim 4$. In contrast, the corresponding H^+ profile (their Fig. 4) in the lower magnetosphere contains sharp cross-L density dropoffs at $L \sim 1.7$, $L \sim 2.6$, and $L \sim 3.5$. Thus the H^+ and electron density profiles in the topside ionosphere may not indicate the true density structure of the magnetosphere.

The set of H^+ measurements from Grebowsky et al [1970] used in the previous discussion was taken on 8 August 1967. The last previous magnetic storm occurred nine days before this date. This time period is consistent with the MR whistler deduced 12 day lifetime of the gradient structure after the 17 to 18 April 1965 storm.

From an experimental and observational standpoint, we have demonstrated that different types of density structure can be measured in the magnetosphere and the topside ionosphere simultaneously. The disappearance of storm induced structure in the topside ionosphere may be due to the transition altitude being moved above the level of observation (1000 km). If the satellite density measurements are made below the transition height, the results are generally dominated by the O^+ ion. This transition height effect would uncouple the measurements made in the topside ionosphere from those made in the magnetosphere.

G. Summary

In this chapter we have demonstrated by ray tracing calculations that a sharp cross-L density dropoff will trap upgoing whistler rays, preventing them from becoming MR whistlers. It is shown that trapping by several density dropoffs will restrict the highest starting latitude for MR whistlers and will thereby create an upper frequency cutoff pattern on MR whistlers which reproduces the observed cutoffs in the spectrum without the need of the Landau damping mechanism [Thorne, 1968].

However, the overlap of upper frequency limiting effects with the defocusing of the lower frequencies is proposed to be responsible for the total disappearance of MR whistlers above $L \sim 2.4$ to 2.6 after a magnetic storm. Direct measurements of density structure by satellite show that the cross-L density dropoffs required for trapping are created by magnetic storms and that their lifetimes in the magnetosphere are consistent with MR whistler deduced lifetimes. The disappearance of the storm-created structure in the topside ionosphere is explained in terms of the upward movement of the transition height.

VII. CONCLUSIONS AND FUTURE WORK

A. Summary and Conclusions

Based on the data and research presented in this report, one can draw the following conclusions about MR whistlers and their relation to the structure of the magnetosphere.

- (1) MR whistler spectra are sensitive to various types of irregularities found in the magnetosphere. Field-aligned troughs and enhancements of ionization produce irregularities in the spectra of the MR whistler traces; whereas cross-L dropoffs in density produce double traces. By noting the type of distortion of the MR traces, one can deduce the type and location of the irregularity.
- (2) The absence of observations of MR whistlers beyond $L \sim 2.4$ for a period of 9 to 12 days after a severe magnetic storm can be explained by a combination of two abrupt dropoffs of density at $L \sim 1.8$ and $L \sim 2.4$. These two dropoffs limit the excursion of the upper frequencies of MR whistler components into the magnetosphere, whereas the lower frequencies are attenuated by defocusing.
- (3) By observing the MR whistler activity after it recovers to pre-storm levels, one can deduce the vestiges of magnetospheric density structure created by magnetic storms. This structure is very persistent and will remain (has been observed for up to 19 days) during quiet periods after a storm until the region is disturbed by another magnetic storm. The structure consists of strong enhancements and depressions which are present between $L \sim 2.0$ and $L \sim 3.0$.
- (4) OGO-4 observations of H^+ density in the topside ionosphere [Taylor et al, 1971] have shown that the peaks and troughs created by a magnetic storm are seen only immediately after the storm peak. However, the MR whistler activity yields evidence for a corresponding structure at higher altitudes lasting for up to 12 days after the storm peak.
- (5) The ability to explain the observed upper frequency cutoffs by raytracing casts doubt on the interpretation of these cutoffs in terms of Landau damping [Thorne, 1968]. The enhanced appearance of the upper frequency portions of MR whistlers on spectrograms is probably due to minimal defocusing loss. The possibility of caustics occurring should be investigated in future work.

B. Magnetospheric Density Structure

In Chapter III various isolated examples of magnetospheric density structure were deduced from MR whistler spectra. From the results of Chapters V and VI, we have established that magnetic storms create magnetospheric density structure which can trap whistler energy for up to 12 days after the storm peak. However, most of the examples of density structure were deduced from MR whistler spectra observed well after this post-storm period. In order to place the results of Chapter III into perspective with those of Chapters V and VI, we will examine the magnetospheric density structure deduced from MR spectra observed by OGO-1 during the six-week period preceding the 17 to 18 April 1965 storm.

After the magnetic storm ($K_p = 6$) of 3 to 4 March 1965, MR whistler activity disappeared above $L \sim 2.6$ as observed by OGO-1 passes on 5 and 8 March, but extended to $L \sim 3$ on 10 March. The MR whistler activity on the latter date consisted primarily of 1^- , 1^+ and 2^- , 2^+ components which contained many spectral irregularities whose type changed as the OGO-1 satellite descended from $L \sim 3.0$ to $L \sim 1.8$. The gross features of the magnetospheric density structure can thus be inferred from these spectral irregularities by the judicious utilization of the techniques evolved in Chapter III. The density profile deduced for 10 March 1965 is sketched in Fig. 7.1a. This profile incorporates a cross-L density dropoff at $L \sim 1.8$, a trough at $L \sim 2.1$, an enhancement at $L \sim 2.4$, and a trough at $L \sim 2.7$. These L-shell locations are reasonably accurate since the trough and enhancement structures induce the most recognizable spectral irregularities when the satellite is near the center of the structure.

The magnetic activity after the 3 to 4 March storm remained quiet for several weeks. During this quiet period OGO-1 passes occurring on 13, 18, and 21 March 1965 displayed MR whistler activity similar to that of 10 March. The density profiles inferred from these passes are sketched in Fig. 6.1. Since the passes of 10 and 18 March cover similar ranges of longitudes, the corresponding profiles were paired to illustrate their resemblance. The same was done for the 13 and 21 March profiles. The profile for 18 March is very similar to that for 10 March with the exception of the trough at $L \sim 2.1$. The cross-L density dropoff and enhancement

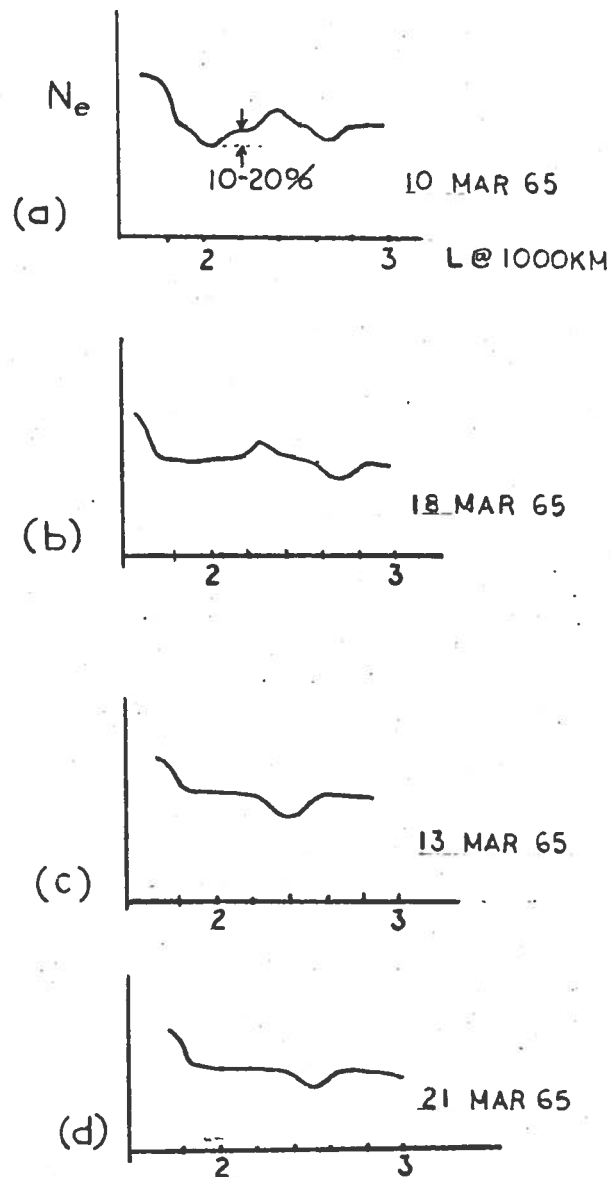


Fig. 7.1. SKETCHES OF ELECTRON DENSITY STRUCTURES DEDUCED FROM MR WHISTLERS OBSERVED ON FOUR OGO-1 PASSES. (a) 10 March 1965: this sketch shows a structure similar to Taylor et al [1971] (cf. Fig. 6.12). The longitude coverage for 10 and 18 March is similar (-35° to 45°). (b) 18 March 1965: this profile shows a close similarity to (a) but lacks an inner trough at $L \sim 2.1$. (c) 13 March 1965: at a different longitude range (-160° to -170°) from (a) and (b) the density structure only displays a dropoff and a trough. (d) 21 March 1965: this profile, measured 19 days after the storm, shows the same structure as (c) and the persistence of the structure in these longitudes.

structures were previously deduced in Fig. 3.7 for 18 March. The profiles for 13 and 21 March only display a trough structure near $L \sim 2.4$ and 2.5 along with a cross-L density dropoff near $L \sim 1.8$ (see Fig. 3.9 for example of trough effects on a $1^- 1^+$ MR whistler observed on 21 March). The persistence of different density structures at two different longitude ranges is taken as clear evidence that the magnetosphere retains vestiges of density structure created by magnetic storms.

The persistent observation of a density structure for several weeks after a storm implies that the level of ionospheric coupling between $L \sim 2$ to 3 is much lower than that measured by other investigators above $L \sim 3$. Otherwise the levels of ionization in the tubes of force which comprise the structure could have changed appreciably. Park [1970] has shown by ground whistler measurements that the upward electron flux between $L \sim 3.5$ and $L \sim 4$ is sufficient to fill these tubes in four to six days after a storm. This time period is in conflict with the observed persistence time of the density structure between $L \sim 2$ and $L \sim 3$. This paradox may imply that ionospheric coupling with the magnetosphere at the lower L-shells is very minimal. The only other mechanism for depleting the density structure is cross-L diffusion which is very slow and has a time constant of 10^3 days (C. Park, private communication). This question of ionospheric coupling at the lower L-shells should be the subject of further investigation.

C. Applications of the Structure

Grossi and Padula-Pintos [1971] reported echoes from an HF ground-based sounding line at $L \sim 1.8$ which are interpreted as propagation along a field-aligned enhancement. However, the severity of the path loss leaves the signals in the noise and requires time integration to recover the echoes. The reception of the echoes occurs only during local night. Since we have made repeatable observations of the density structure over a period of days at a particular longitude range, the structure should be observable at other local times. The HF mode should therefore be observable during the daytime. The absence of the MR mode is probably due to the fact that there is more absorption during the day

which could wipe out an already weak signal. As shown by our data, an HF ground-based sounding link could also be tried at $L \sim 2.2$ to 2.4 , since our data show enhancements in that region.

D. The Boomerang Mode: A Future Experiment

It has been suggested by Helliwell (private communication) that since it is possible for reflections to occur for naturally excited MR whistlers, we should be able to send a pulse of VLF electromagnetic energy between 0 and 10 kHz from the satellite and have the signal travel down the field line in the Gendrin mode, reflect, and return to the satellite location. The term boomerang is applied to this mode because the signal returns to the source somewhat like a boomerang which returns to the thrower.

To excite the boomerang mode from a satellite transmitter involves the excitation of the proper initial wave normal angle such that after reflection a ray would return to the satellite location. From Chapter II we know that there are three types of reflections. We can use this information to select the proper initial wave normal angle. Since the ray path must be approximately field-aligned to return to the satellite vicinity, the initial wave normal must be near the Gendrin angle. From case 1 (cf. Fig. 2.4), we know that if f is always below the local f_{LHR} , the ray path will always be directed outward in respect to the magnetic field and the return path will always pass the satellite latitude at a higher L-shell than that of the satellite. Thus for frequencies below the local LHR at the satellite a boomerang mode can not exist. From case 2 of Chapter II (cf. Fig. 2.5) if the initial wave normal lies well outside the Gendrin angle, the return ray path will cross itself and pass the satellite underneath at a lower L-shell. Thus with these last two ray paths, we have effectively straddled the satellite with return paths.

From the preceding discussion we can conclude that if we pick an initial wave normal which lies just outside of the Gendrin angle, the ray will return to the satellite location. In Fig. 7.2 the ray paths for three initial wave normals effectively straddle the satellite on

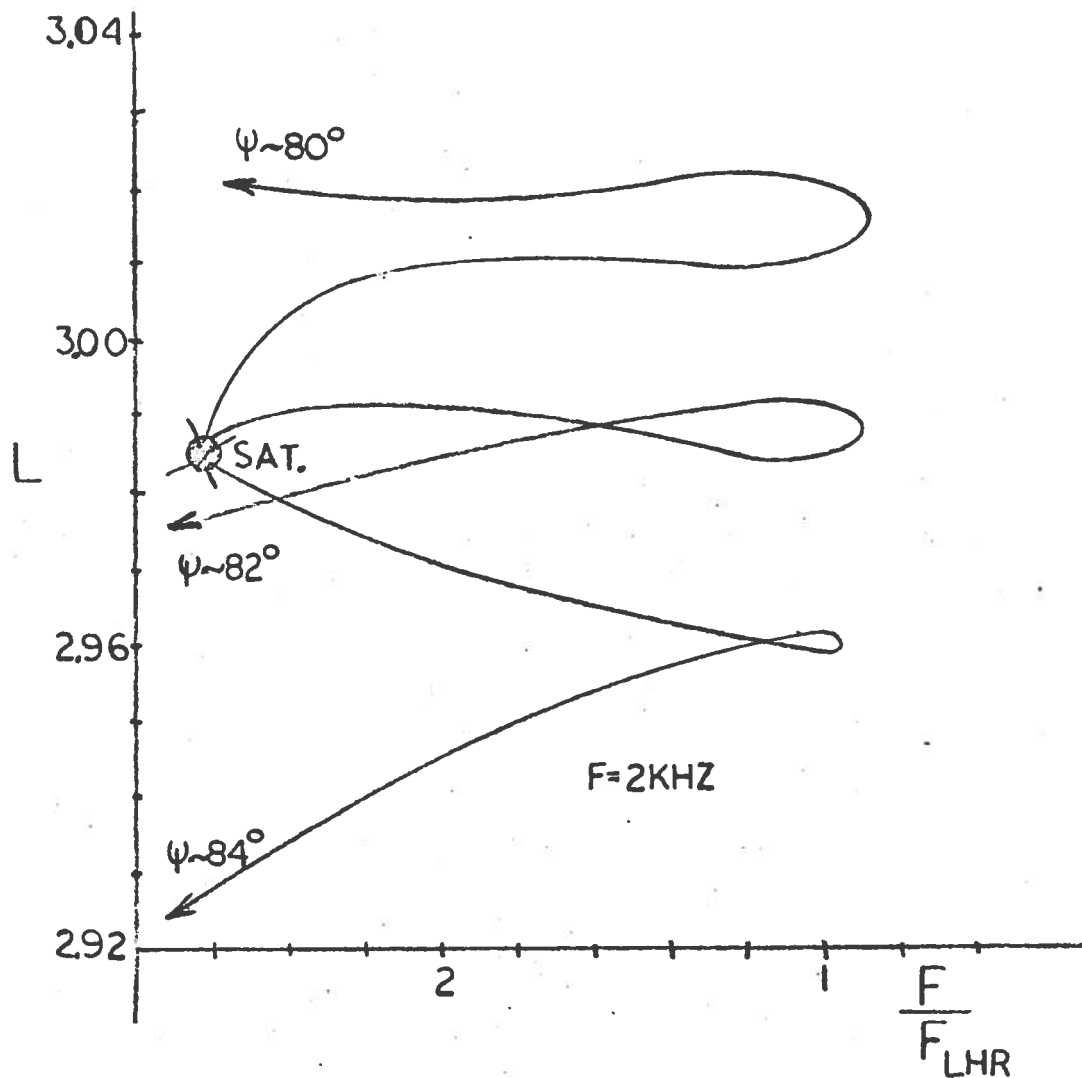


Fig. 7.2. SEVERAL BOOMERANG RAY PATHS FROM A SATELLITE AT THE EQUATOR, FOR THREE DIFFERENT VALUES OF INITIAL WAVE NORMAL ANGLE. The horizontal axis is measured in terms f/f_{LHR} for $f = 2$ kHz along the ray path.

the return path. The 82° initial wave normal path comes closest to the satellite, but this wave normal angle is less than 83° , the Gendrin angle at the satellite. However, the curvature gradients at the equator quickly rotate this initial wave normal into the Gendrin mode so that our original arguments are still valid.

Figure 7.3a shows the one hop boomerang path for an equatorial satellite position at $L \sim 3$. The spectrum for this path as it would be observed by a satellite receiver is illustrated in Fig. 7.3b. The one-hop trace essentially shows a constant time delay because all the frequencies are traveling in the Gendrin mode which is frequency independent. The additional time delay at the high frequencies is due to the longer paths traveled to reach regions where the local LHR exceeds the wave frequency.

From the spectrogram in Fig. 7.3b the electron density along the $L \sim 3$ path can be calculated from the time delays. Since the nose frequency has the most nearly field aligned path, one can assume to zeroth order that the nose frequency is traveling along the $L \sim 3$ field line at the Gendrin velocity. Using the appropriate expressions for μ_{gr} from Appendix B, one can integrate μ_{gr} along the field line down to the reflection, and using the time delay from Fig. 7.6 the electron density along the field line may be calculated.

The boomerang mode offers many advantages and opportunities in providing diagnostic tools for exploring the magnetosphere. First the boomerang mode is very easily excited by a VLF satellite transmitter because the power radiated by a short dipole is primarily concentrated near the resonance cone, which is close to the Gendrin angle [Wang, 1970]. Secondly electron density measurements made by the boomerang mode are path measurements and thus are not affected by spacecraft potential, etc. Thirdly the boomerang sounder mode would allow controlled experiments and would not be subject to the MR activity cutoff above $L \sim 2.5$ after a storm. Since we have shown that input latitude restrictions and not Landau effects determine the frequency range of MR components, observation of boomerang spectra would allow a full evaluation of possible Landau damping and growth effects on MR-type propagation. Landau effects would show up in the observed frequency range and number of reflections.

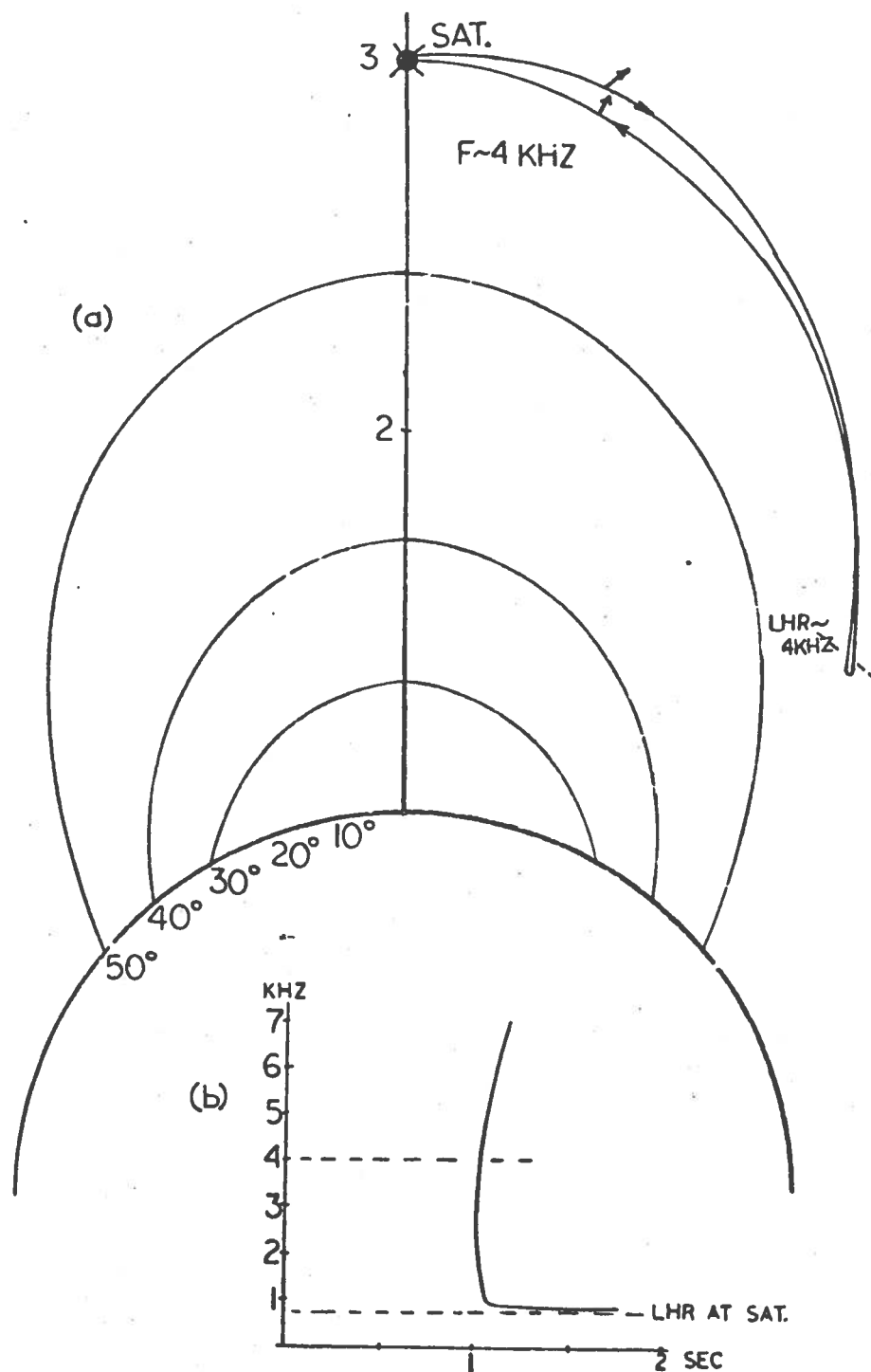


Fig. 7.3. (a) BOOMERANG RAY PATH FOR A SATELLITE SOUNDER AT $L \sim 3$ AT THE EQUATOR. (b) Corresponding spectrogram for the boomerang mode as seen by a satellite VLF receiver at the equator.

E. Future Theoretical Work on Boomerang Mode

As demonstrated in Chapter III, the MR whistler spectra are sensitive to field aligned troughs and enhancements of ionization. Similar irregularities in the boomerang spectra should also occur for propagation in troughs and enhancements. What these characteristics would be is a subject for future investigation. Also propagation effects due to the satellite proximity to the plasmapause should be investigated. To predict the possible Landau effects calculations similar to those of Thorne [1968] should be carried out.

F. Proposals for Future Work on MR Whistlers

There is a large quantity of OGO-3 broadband VLF data still not spectrum analyzed and investigated. There were adequate levels of MR whistler activity for application to magnetospheric structure diagnostics during June to December 1966. In 1967 the orbit of OGO-3 skirted the regions of normal MR activity. However, during 1968 the orbit was similar to that of OGO-1 during October to December 1965. The 1968 data have not been released by NASA due to budget restrictions. An effort should be made to obtain these data and to correlate them with the OGO-3 mass spectrometer experiment data. This effort would allow definitive work on magnetospheric structure diagnostics. Alouette-2 data should also be consulted.

Appendix A

THE REFRACTIVE INDEX AND THE LOWER HYBRID RESONANCE

Following the formalism given by Stix [1962], the refractive index (μ) is determined by the dispersion relation:

$$A\mu^4 + B\mu^2 + C = 0 \quad , \quad (A.1)$$

where

$$\begin{aligned} A &= S \sin^2 \theta + P \cos^2 \theta \quad , \\ B &= -RL \sin^2 \theta - PS(1 + \cos^2 \theta) \quad , \end{aligned} \quad (A.2)$$

$$C = PRL \quad ,$$

and

$$R, L = 1 - \sum_i \frac{\omega_{pi}^2}{\omega} \frac{1}{(\omega \pm \omega_{Hi})} \quad , \quad (A.3)$$

$$P = 1 - \sum_i \frac{\omega_p^2}{\omega^2} \quad ,$$

$$S, D = \frac{1}{2} (R \pm L) \quad .$$

Theta (θ) is defined as the angle between the wave normal and the static magnetic field direction. The plasma and gyrofrequencies ω_{pi} and ω_{Hi} are defined as

$$\omega_{pi}^2 = \frac{N_i Q_i^2}{m_i \epsilon_0} \quad , \quad \omega_{Hi} = \frac{Q_i B_0}{m_i} \quad ,$$

where

Q_i = charge of i^{th} particle (including sign)

N_i = number density of i^{th} particle

m_i = mass of i^{th} particle

B_0 = static magnetic field intensity

ϵ_0 = free space dielectric constant

The solutions to Eq. (A.1) can take two numerically equivalent forms,

$$\mu^2 = \frac{-B \pm \sqrt{B^2 - 4AC}}{2A} = \frac{2C}{-B \mp \sqrt{B^2 - 4AC}} \quad (\text{A.4})$$

The refractive index under certain conditions becomes infinite, a situation which is termed a resonance [Allis et al, 1963]. Considering the first form of Eq. (A.4), resonance occurs when $A = 0$. Neglecting ion effects and considering only electrons, A becomes

$$A = \left(1 - \frac{\omega_{pe}^2}{\omega^2}\right) \cos^2 \theta + \left(1 + \frac{\omega_{pe}^2}{\omega_{He}^2 - \omega^2}\right) \sin^2 \theta .$$

Setting A to zero, we find the following resonance condition for the electron-only case

$$\cot^2 \theta_{\text{res}} = \frac{1 + \frac{\omega_{pe}^2}{\omega_{He}^2 - \omega^2}}{\frac{\omega_{pe}^2}{\omega^2} - 1} .$$

Using the approximations for the whistler mode [Helliwell, 1965],

$$\frac{\omega_{pe}^2}{\omega^2} \gg 1, \quad \frac{\omega_{He}^2}{\omega^2} \ll 1,$$

results in the following whistler resonance condition

$$\cot^2 \theta_{res} = \frac{\omega^2}{\omega_{He}^2} \ll 1,$$

or for θ_{res} near 90° ,

$$\cos \theta_{res} \doteq \frac{\omega}{\omega_{He}}. \quad (A.5)$$

The angle θ_{res} is termed the resonance cone angle and is the limiting position for wave normal angles near 90° .

As the frequency is lowered, the resonance cone angle approaches 90° , but the contributions to the refractive index from heavy ions also become increasingly important. As pointed out by Hines [1957], at low frequencies the presence of heavy ions can cause the sign of S to change from positive (electron-only case) to negative. The transition of sign occurs at the lower hybrid resonance (LHR) frequency. At the LHR frequency the resonance cone is modified by the ions such that the refractive index becomes infinite at $\theta = 90^\circ$. Below the LHR frequency the resonance cone is no longer present and the refractive index is finite for all angles.

At $\theta = 90^\circ$, A equals S , Eq. (A.2), which is given by

$$S = 1 + \sum_i \frac{\omega_{pi}^2}{\omega_{Hi}^2 - \omega^2}.$$

For the case of protons and electrons, S becomes

$$S = 1 + \frac{\omega_p^2}{\omega_H^2 - \omega^2} + \frac{\omega_p^2/M}{\frac{\omega_H^2}{M^2} - \omega^2},$$

where

ω_H, ω_p = electron gyro and plasma frequencies

M = ratio of proton and electron masses ≈ 1840

Setting S to zero and solving for ω gives

$$\omega^4 - \omega^2 \left[\omega_p^2 \left(1 + \frac{1}{M} \right) + \omega_H^2 \left(1 + \frac{1}{M^2} \right) \right] + \frac{\omega_H^4}{M^2} + \frac{\omega_H^2 \omega_p^2}{M} \left(1 + \frac{1}{M} \right) = 0.$$

Since $1/M \ll 1$, we can approximate the above equation by

$$\omega^4 - \omega^2 \left(\omega_H^2 + \omega_p^2 \right) + \frac{\omega_H^4}{M^2} + \frac{\omega_H^2 \omega_p^2}{M} = 0,$$

or $\omega^4 - b\omega^2 + c = 0$, where

$$b = \omega_H^2 + \omega_p^2,$$

$$c = \frac{\omega_H^4}{M^2} + \frac{\omega_H^2 \omega_p^2}{M}.$$

The discriminant of the above biquadratic equation is

$$b^2 - 4c = \left[\omega_p^4 + 2\omega_p^2 \omega_H^2 \left(1 - \frac{2}{M} \right) + \omega_H^4 \left(1 - \frac{4}{M^2} \right) \right] \doteq \left(\omega_p^2 + \omega_H^2 \right)^2 = b^2$$

The solutions to the biquadratic equation are

$$\omega_{\text{LHR}}^2 = \frac{c}{b} = \frac{\omega_H^2}{M} \left(\frac{\omega_H^2/M + \omega_p^2}{\omega_H^2 + \omega_p^2} \right) \quad (\text{A.6})$$

and

$$\omega_{\text{UHR}}^2 = b = \omega_H^2 + \omega_p^2 \quad (\text{A.7})$$

Solution (A.6) gives the lower hybrid resonance, and solution (A.7) gives the upper hybrid resonance. The upper hybrid frequency is above the whistler mode frequencies and thus can be neglected for our purposes.

In the magnetosphere $\omega_p^2 > \omega_H^2 > \omega_H^2/M$, and solution (A.6) can be approximated by

$$\omega_{\text{LHR}} \doteq \frac{\omega_H}{\sqrt{M}} \doteq \frac{\omega_H}{43} \quad (\text{A.8})$$

Solving for $1/\omega^2$ in Eq. (A.6) gives the form as stated by Stix [1962]

$$\frac{1}{\omega_{\text{LHR}}^2} = \frac{1}{\omega_H^2/M} + \frac{1}{\omega_p^2/M + \omega_H^2/M^2} \quad (\text{A.9})$$

in which ω_H^2/M^2 and ω_p^2/M are the proton gyro and plasma frequencies squared. From Eq. (A.12) we can derive the expression for ω_{LHR}^2 as given by Brice and Smith [1964]. Since $\omega_p^2 > \omega_H^2$ for the magnetosphere

$$\frac{1}{M\omega_{\text{LHR}}^2} = \frac{1}{\omega_H^2} + \frac{1}{\omega_p^2} \quad (\text{A.10})$$

This form has been extended to several ion constituents by Brice and Smith to cover the situation as found in the ionosphere. For singly charged ions, ω_{LHR}^2 is given by

$$\frac{1}{\omega_{LHR}^2} \sum_i \frac{\alpha_i}{M_i} = \frac{1}{\omega_p^2} + \frac{1}{\omega_H^2} , \quad (A.11)$$

where

α_i = fraction of the ion density occupied by the i^{th} ion

M_i = ratio of i^{th} ion mass to that of the electron

1. Approximations for the Refractive Index

The refractive index expression as given in Eq. (A.1) is rather complicated, and thus approximations for the refractive index, necessary for simple calculations, are required. The solutions for (A.1) can be simplified by combining terms in the discriminant to give

$$\mu^2 = \frac{-B \pm F}{2A} = \frac{2C}{-B \pm F} , \quad (A.12)$$

where

$$F^2 = (RL - PS)^2 \sin^4 \theta + 4P^2 D^2 \cos^2 \theta ,$$

$$B = -RS(1 + \cos^2 \theta) - RL(\sin^2 \theta) ,$$

$$A = P \cos^2 \theta + S \sin^2 \theta ,$$

$$C = PRL .$$

To obtain good approximations valid over a wide range of wave normal angles, one must first examine the relative magnitudes of the individual terms for conditions in the magnetosphere. The smaller magnitude terms can be either dropped or used in a first-order expansion.

Using the standard ionospheric notation of X and Y where $X = \omega_p^2/\omega^2$ and $Y = \omega_H/\omega$, R , L , S , etc., can be defined as:

$$R = 1 - \frac{X}{1 - Y} - \frac{X/M}{1 + Y/M} \doteq \frac{-X}{Y - (1 - Y^2/M)} \quad (\text{A.13})$$

$$L = 1 - \frac{X}{1 + Y} - \frac{X/M}{1 - Y/M} \doteq \frac{+X}{Y + (1 - Y^2/M)}$$

$$S = 1 - \frac{X}{1 - Y^2} - \frac{X/M}{1 - Y^2/M^2} \doteq \frac{X}{Y^2} \left(1 - \frac{Y^2}{M} \right)$$

$$P = 1 - X - X/M \doteq -X$$

$$D = \frac{XY}{1 - Y^2} - \frac{XY/M^2}{1 - Y^2/M^2} \doteq -\frac{X}{Y}$$

The approximations are valid when $X \gg 1$, $Y \gg 1$, $M \gg 1$, and $X/Y^2 > 1$ for a magnetosphere composed of protons and electrons. When Y^2/M equals one, the frequency is the lower hybrid resonance frequency. Thus $1 - Y^2/M$ is a small number when compared to Y in the denominator of R and L . The product of R and L now becomes

$$RL \doteq \frac{X^2}{Y^2},$$

and

$$RL - PS \doteq -\frac{X^2}{M},$$

2. The Quasi Longitudinal Approximation

When the approximations for R , L , etc., from (A.13) and (A.14) are used, the quantity F^2 becomes

$$F^2 = \left(\frac{X^2}{M} \right)^2 \sin^4 \theta + 4 \left(\frac{X^2}{Y} \right)^2 \cos^2 \theta.$$

The $\cos^2 \theta$ term dominates F^2 over a wide range of angles. The critical angle at which the two terms in F^2 are equal is defined by

$$\frac{\cos^2 \theta_c}{\sin^2 \theta_c} = \frac{\omega_H^2}{2\omega M^2} \quad (A.15)$$

Since ω_H/M is the ion gyrofrequency and is very small compared to ω , the angle θ_c is very close to $\pi/2$ and can be approximated by the following:

$$\varphi_c = \pi/2 - \theta_c$$

or

$$\varphi_c \doteq \frac{\omega_H}{2\omega M} \quad (A.16)$$

For frequencies near the LHR φ_c is of the order of 0.01.

For the Quasi Longitudinal (QL) approximation, we can drop the $\sin^4 \theta$ term.

Using the second form of (A.12), μ^2 then becomes

$$\mu^2 \doteq \frac{2PRL}{PS(1 + \cos^2 \theta) + 2PD \cos \theta} ,$$

or

$$\mu^2 \doteq \frac{RL}{S + D \cos \theta} , \quad (A.17)$$

assuming $1 + \cos^2 \theta \doteq 2$. From Eqs. (A.6) and (A.7) we know that S can be represented as

$$S = \frac{(\omega^2 - \omega_{HR}^2)(\omega^2 - \omega_{LHR}^2)}{(\omega^2 - \omega_H^2)(\omega^2 - \omega_{H/M}^2)}$$

where

$$\omega_{HR}^2 = \omega_p^2 + \omega_H^2 \gg \omega^2 ,$$

$$\omega_{LHR}^2 = \frac{\omega_H^2}{M} \left[\frac{\omega_H^2/M + \omega_p^2}{\omega_H^2 + \omega_p^2} \right] .$$

Since $\omega_H^2 \gg \omega^2 \sim \omega_H^2/M \ll \omega_H^2/M^2$, S becomes

$$S \doteq + \frac{(\omega_H^2 + \omega_p^2)(\omega^2 - \omega_{LHR}^2)}{\omega^2 \omega_H^2} , \quad (A.18)$$

or

$$S \doteq \frac{X}{Y^2} \left(1 + \frac{Y^2}{X} \right) \left(1 - \frac{\omega_{LHR}^2}{\omega^2} \right) .$$

Substituting Eqs. (A.18), (A.14), and (A.13) in Eq. (A.17) gives the following QL expression for μ^2 as

$$\mu^2 = \frac{X/Y}{\cos \theta - \frac{\delta}{Y} \left[1 + \frac{Y^2}{X} \right]} , \quad (A.19)$$

where

$$\delta = 1 - \frac{\omega_{LHR}^2}{\omega^2} .$$

For the magnetosphere where $X/Y^2 \gg 1$, Eq. (A.18) can be approximated by

$$\mu_{QL}^2 = \frac{X/Y}{\cos \theta - \frac{\delta}{Y}} . \quad (A.20)$$

This QL expression differs from the Helliwell [1965] form in which $\delta = 1$. For $\omega \gg \omega_{\text{LHR}}$, δ is approximately 1, but at frequencies where $\omega \sim \omega_{\text{LHR}}$ δ is close to zero. At these frequencies the resonance cone is modified by δ such that θ_{res} approaches $\pi/2$ as δ goes to zero. The importance of the δ term was first pointed out by Thorne and Kennel [1967].

3. The Quasi Transverse Approximation

For a zeroeth order approximation, let us approximate F^2 as

$$F^2 \doteq \left(\frac{x^2}{M} \right)^2 \sin^4 \theta . \quad (\text{A.21})$$

This approximation is good when

$$\frac{\cos \theta}{\sin^2 \theta} < \frac{\omega_H}{2\omega M} ,$$

or as stated earlier by Eq. (A.16)

$$\phi < \frac{\omega_H}{2\omega M}$$

where $\theta = \pi/2 - \phi$. Substituting Eq. (A.21) into (A.12) and simplifying yields the following quasi transverse (QT) approximation for the refractive index:

$$\mu^2 = \frac{RL \sin^2 \theta + PS \cos^2 \theta}{P \cos^2 \theta + S \sin^2 \theta} \quad (\text{A.22})$$

This approximation form as given by Allis et al [1963] was shown to be very inadequate for frequencies below the LHR frequency by Lyons and Thorne [1969].

To extend the refractive index approximation for quasi-transverse angles to frequencies below the LHR, Lyons and Thorne [1970] performed a first order expansion of F to obtain

$$F = F_T \left(1 + \frac{F_L^2}{F_T^2} \right)^{1/2} \doteq F_T + \frac{F_L^2}{2F_T}, \quad (\text{A.23})$$

where

$$F_T = (RL - PS) \sin^2 \theta$$

$$F_L = 2PD \cos \theta$$

Substituting (A.23) into the second form of Eq. (A.12) for μ^2 gives

$$\mu^2 = \frac{RL}{S - \frac{PD^2}{RL - PS} \cot^2 \theta}$$

or

$$\mu^2 = \frac{X/M}{\cot^2 \theta + \frac{1}{M} \left(\frac{Y^2}{M} - 1 \right)}. \quad (\text{A.24})$$

Letting $\theta = \pi/2 - \varphi$, where $\varphi < \omega_H/2\omega M$, Eq. (A.24) becomes

$$\mu_{\text{PLA}}^2 = \frac{X/M}{\varphi^2 + \Gamma}, \quad (\text{A.25})$$

where

$$\Gamma = \frac{1}{M} \left(\frac{Y^2}{M} - 1 \right)$$

4. Validity of the Refractive Index Approximations

The plasmaspheric large angle (PIA) approximation for μ^2 was found by Lyons and Thorne [1970] to give very good agreement with the general expression for μ^2 for $\varphi < \omega_H/2\omega_M$ and for many cases μ_{PIA}^2 gives good agreement for $\varphi \sim \omega_H/2\omega_M$ and for frequencies at and just below the LHR. At the LHR

$$\mu_{PIA}^2 = \frac{X}{M\varphi^2},$$

and

$$\mu_{QL}^2 = \frac{X}{Y \cos \theta}.$$

Substituting $\theta = \pi/2 - \varphi$ in μ_{QL}^2 gives

$$\mu_{PIA}^2 = \frac{X}{M\varphi^2}, \quad \mu_{QL}^2 = \frac{X}{Y\varphi}.$$

These two expressions are equal at

$$\varphi = \frac{\omega_H}{\omega_M}$$

which is twice the angle $\varphi_c = \omega_H/2\omega_M$. At $\varphi_c = \omega_H/2\omega_M$

$$\mu_{PIA}^2 = \frac{X}{\frac{5Y^2}{4M} - 1}, \quad \mu_{QL}^2 = \frac{X}{\frac{3}{2} \frac{Y^2}{M} - 1}$$

Since φ_c is the critical angle at which the two approximations violate their original assumptions, it is not unreasonable that they are not equal. However, their similarity would lead to the supposition that for very crude ray path calculations, one could join path solutions which use both expressions at φ_c without too much loss of generality.

The QL expression has one assumption which is violated for large θ . The assumption that $1 + \cos^2 \theta \doteq 2$ is not true for θ close to $\pi/2$. But this assumption seems to compensate for the dropping of the $\sin^2 \theta$ term when that term becomes important for large θ . The resonance cone condition from the QL expression is

$$\cos \theta_{\text{res}} = \frac{1}{Y} \left(1 - \frac{Y^2}{M} \right) . \quad (\text{A.26})$$

However, a close examination of A as defined in Eq. (A.2) yields a resonance condition of

$$\cos \theta_{\text{res}} = \frac{1}{Y} \sqrt{1 - \frac{Y^2}{M}} \quad (\text{A.27})$$

The two expressions are close for small Y^2/M or for frequencies above the LHR. The error involved in using (A.26) only becomes noticeable for $Y^2/M \sim 1$. We can view the QL expression as being a good compromise over all $\theta < \theta_{\text{res}}$. The QL expression has the virtue also that a $1 - Y^2/M$ term is much easier to manipulate than a square root term.

5. Further Approximation

Given that the general expression for the refractive index is

$$\mu^2 = \frac{RL \sin^2 \theta + PS(1 + \cos^2 \theta) \pm \sqrt{(RL - PS)^2 \sin^4 \theta + 4P^2 D^2 \cos^2 \theta}}{2(P \cos^2 \theta + S \sin^2 \theta)} ,$$

we would like to obtain a QL expression which would be accurate for large θ . Let us assume that $\sin^2 \theta \sim 1$ and $\cos^2 \theta$ term in the numerator can be ignored since it is second order. Thus,

$$\mu^2 = \frac{RL + PS \pm |2PD \cos \theta|}{2(P \cos^2 \theta + S)} \quad (\text{A.28})$$

Substituting the quantities from (A.13) and (A.14) into (A.28) gives a large angle (IA) approximation.

$$\mu_{IA}^2 = \frac{\frac{X}{Y} \left[\cos \theta + \frac{1}{Y} \left(1 - \frac{Y^2}{2M} \right) \right]}{\cos^2 \theta - \frac{1}{Y^2} \left(1 - \frac{Y^2}{M} \right)} \quad (A.29)$$

The denominator can be factored to yield

$$\mu^2 = \frac{\frac{X}{Y} \left[\cos \theta + \frac{1}{Y} \left(1 - \frac{Y^2}{2M} \right) \right]}{\left[\cos \theta - \frac{1}{Y} \sqrt{1 - \frac{Y^2}{M}} \right] \left[\cos \theta + \frac{1}{Y} \sqrt{1 - \frac{Y^2}{M}} \right]} \quad (A.30)$$

If $Y^2/M < 1$, then $[1 - (Y^2/M)]^{1/2} \doteq 1 - Y^2/2M$ and Eq. (A.30) becomes

$$\mu_{IA}^2 = \frac{X/Y}{\cos \theta - \frac{1}{Y} \left(1 - \frac{Y^2}{2M} \right)},$$

which is very similar to μ_{QL}^2 . The large angle μ^2 has the virtue of being easily programmable on a computer to give good accuracy, but has the drawback of too much complexity to be used in any hand calculations.

Appendix B

THE GROUP RAY REFRACTIVE INDEX

The knowledge of the group ray refractive index (μ_{gr}) behavior under typical conditions in the magnetosphere is important in determining the time delays for nonducted whistlers. The group ray refractive index can be derived in several steps given the phase refractive index (μ) as specified in Appendix A. First we have to determine the group refractive index (μ_g). This quantity is defined as [Helliwell, 1965]

$$\mu_g = \frac{\partial \mu f}{\partial f} = \frac{c}{v_g} ,$$

where

c = speed of light

f = frequency

v_g = group velocity

The group refractive index defines the velocity of an "energy packet" produced by the constructive interference of two plane waves having same wave normal direction but slightly different frequencies. The group velocity gives the velocity of propagation of this "energy packet" unbounded laterally, and is therefore directed along the wave normal.

Since the influence of the earth's static magnetic field upon the charged particles makes the magnetosphere an anisotropic medium, the path of true energy packets (produced by interference of waves at slightly different wave normal directions, and therefore laterally limited) is not along the wave normal direction. The angle from the wave normal to the ray direction, measured away from the static magnetic field, is [Helliwell, 1965]:

$$\tan \alpha = \frac{-1}{\mu} \frac{\partial \mu}{\partial \psi}$$

where

α = angular deviation of ray direction from the wavenormal

ψ = wave normal angle

Since the energy packet travels along the ray direction and not the wave normal direction, the group velocity along the ray path is increased by a factor $\sec \alpha$ that we define the group-ray velocity v_{gr} as

$$v_{gr} = v_g \sec \alpha .$$

The group ray refractive index similarly defined as

$$\mu_{gr} = \mu_g \cos \alpha .$$

Case 1.

Electrons Only, Quasi-Longitudinal Approximation. This case is covered extensively by Helliwell [1965]. We will state the results so that they can be used as a reference.

$$\mu_{ele}^2 = \frac{f_p^2}{f_H f} \cdot \frac{1}{\cos \psi - f/f_H}$$

The restrictions on this approximation are that

$$\frac{\cos \psi}{\sin^2 \psi} > \frac{f_H f_p}{2f^2} \quad \text{and} \quad f \gg f_{LHR}$$

The group refractive index is:

$$\mu_g = \frac{f_p}{2f_H^{1/2} f^{1/2}} \frac{\cos \psi}{(\cos \psi - f/f_H)^{3/2}}$$

The angle α between the ray direction and the wavenormal is defined by

$$\tan \alpha = \frac{\sin \psi}{2(\cos \psi - f/f_H)} ,$$

and μ_{gr} is given by

$$\mu_{gr} = \frac{f_p}{2\sqrt{f_H f}} \frac{\cos \psi}{\left[\frac{\sin^2 \psi}{4} (\cos \psi - f/f_H) + (\cos \psi - f/f_H)^3 \right]^{1/2}}$$

Case 2.

Electrons Plus Protons, Quasi-Longitudinal Approximation. Given the quasi-longitudinal approximation for μ^2 as derived in Appendix A,

$$\mu^2 = \frac{f_p^2}{f_H f} \frac{1}{\cos \psi - \frac{f}{f_H} \left(1 - \frac{f_H^2}{Mf^2} \right)} , \quad (B.1)$$

or

$$\mu^2 = \frac{f_p^2}{f_H f} \frac{1}{\cos \psi - \delta \frac{f}{f_H}} , \quad \frac{\cos \psi}{\sin^2 \psi} < \frac{f_H}{2fM}$$

the group refractive index is

$$\mu_g = \frac{f_p}{2\sqrt{ff_H}} \frac{\cos \psi + \frac{2f_H}{Mf}}{\left[\cos \psi - \delta \frac{f}{f_H} \right]^{3/2}} ,$$

$\tan \alpha$ is defined as,

$$\tan \alpha = \frac{\sin \psi}{2 \left(\cos \psi - \delta \frac{f}{f_H} \right)} \quad (\text{B.2})$$

and the μ_{gr} resulting from the above quantities is

$$\mu_{gr} = \frac{\frac{f}{p}}{2 \sqrt{ff_H} \left[\frac{\sin^2 \psi}{4} \left(\cos \psi - \delta \frac{f}{f_H} \right) + \left(\cos \psi - \delta \frac{f}{f_H} \right)^3 \right]^{1/2}} \quad (\text{B.3})$$

There are two changes going from the electron only case (1) to the ion plus electron case (2): The modification of the resonance cone angle by the δ term, and a small additive term in the numerator of μ_g and μ_{gr} .

Approximations for μ_{gr}

At the LHR frequency the ratio of f/f_H is approximately 1/43 or .0232. For the case of MR whistlers, the f/f_H ratio is 0.1 or less over the majority of the ray paths. So we can consider f/f_H as being very small. Also since the wave normal angles are generally greater than 75° , we can approximate $\sin^2 \psi$ as 1.0. That gives the following results for μ_{gr} .

$$\text{Case 1.} \quad \mu_{gr} = \frac{\frac{f}{p}}{\sqrt{ff_H} \left[\cos \psi - \frac{f}{f_H} \right]^{1/2}}, \quad (\text{electron}) \quad (\text{B.4})$$

and for

$$\text{Case 2.} \quad \mu_{gr} = \frac{\frac{f}{p}}{\sqrt{ff_H} \left[\cos \psi - \delta \frac{f}{f_H} \right]^{1/2}} \quad (\text{ion}) \quad (\text{B.5})$$

Although the two formulas for μ_{gr} differ slightly, they both have minima at the same point. If we take

$$\text{Case 1.} \quad \frac{\partial \mu_{gr}}{\partial \psi} \sim \frac{-\sin \psi \left[\cos \psi - \frac{f}{f_H} - \frac{\cos \psi}{2} \right]}{\left[\cos \psi - \frac{f}{f_H} \right]^{3/2}}$$

$$\text{Case 2.} \quad \frac{\partial \mu_{gr}}{\partial \psi} \sim \frac{-\sin \psi \left[\cos \psi - \frac{f}{f_H} + \frac{f_H}{Mf} - \frac{\cos \psi}{2} - \frac{f_H}{Mf} \right]}{\left[\cos \psi - \frac{f}{f_H} \right]^{3/2}}$$

Setting $\partial \mu_{gr} / \partial \psi$ to zero in each case we find that $\cos \psi = 2f/f_H$ satisfies both cases. This condition is the definition of the Gendrin angle as defined in the electron only case (1) [Gendrin, 1961]. The group ray refractive index becomes in both cases for $\cos \psi = 2f/f_H$:

$$\text{Case 1.} \quad \mu_{gr} = \frac{2f}{f_H} p$$

$$\text{Case 2.} \quad \mu_{gr} = \frac{2f}{f_H} p \left[1 + \frac{f_H^2}{Mf^2} \right]^{1/2}$$

In the Gendrin mode for case 1, the μ_{gr} is independent of frequency and the ray direction can be shown to be parallel to the static magnetic field B_0 . However, when ions are considered, the group ray refractive index is not independent of frequency when the frequency is close to the LHR frequency. Secondly for case 2, the ray direction is not parallel to \bar{B}_0 . For the ray to be parallel to \bar{B}_0 in case 2, the condition $\cos \theta = 2\delta f/f_H$ must be met. In this modified Gendrin mode, μ_{gr} becomes

$$\mu_{gr} = \frac{2f}{f_H} \frac{p}{\sqrt{1 - \frac{f_H^2}{f_M^2}}} \quad \cos \psi = \frac{2f\delta}{f_H}$$

This expression goes to infinity at $f = f_{LHR}$, which would lead one to believe that this mode is not to be found in the magnetosphere when f is near f_{LHR} . Of course, the modified Gendrin mode reduces to the original Gendrin mode when $f \gg f_{LHR}$.

When μ_{gr} is plotted in Fig. B.1a using the complete expression for case 2 keeping ψ constant, we find that μ_{gr} does indeed go through a minimum when $f = f_H/2 \cos \psi$. One can also see the nose frequency pattern as occurs with an MR whistler. The μ_{gr} axis can be multiplied by a distance factor to give time delay. The resulting figure would be similar to an MR whistler spectrogram. Figure B.1b shows a comparison between cases 1 and 2 and also shows how close the approximation for μ_{gr} is to the complete expression. The main deviation between the two cases is at the Gendrin condition or minimum μ_{gr} . The influence of the LHR causes a 40% increase in the μ_{gr} from the electron case to the ion case at $\cos \theta = 2f/f_H$. This increase in μ_{gr} becomes important when calculating accurate time delays for MR nose frequencies at high L values.

Case 3.

Plasmaspheric Large Angle Approximation. In this case as derived by Lyons and Thorne [1970] the refractive index is given by

$$\mu_{pla}^2 = \frac{f_p^2/f_M}{\varphi^2 + \Gamma} \quad , \quad (B.6)$$

where

$$\varphi = \pi/2 - \theta = \text{wave normal}$$

$$\Gamma = \frac{1}{M} \left(\frac{f_H^2}{f_M^2} - 1 \right) \geq 0$$

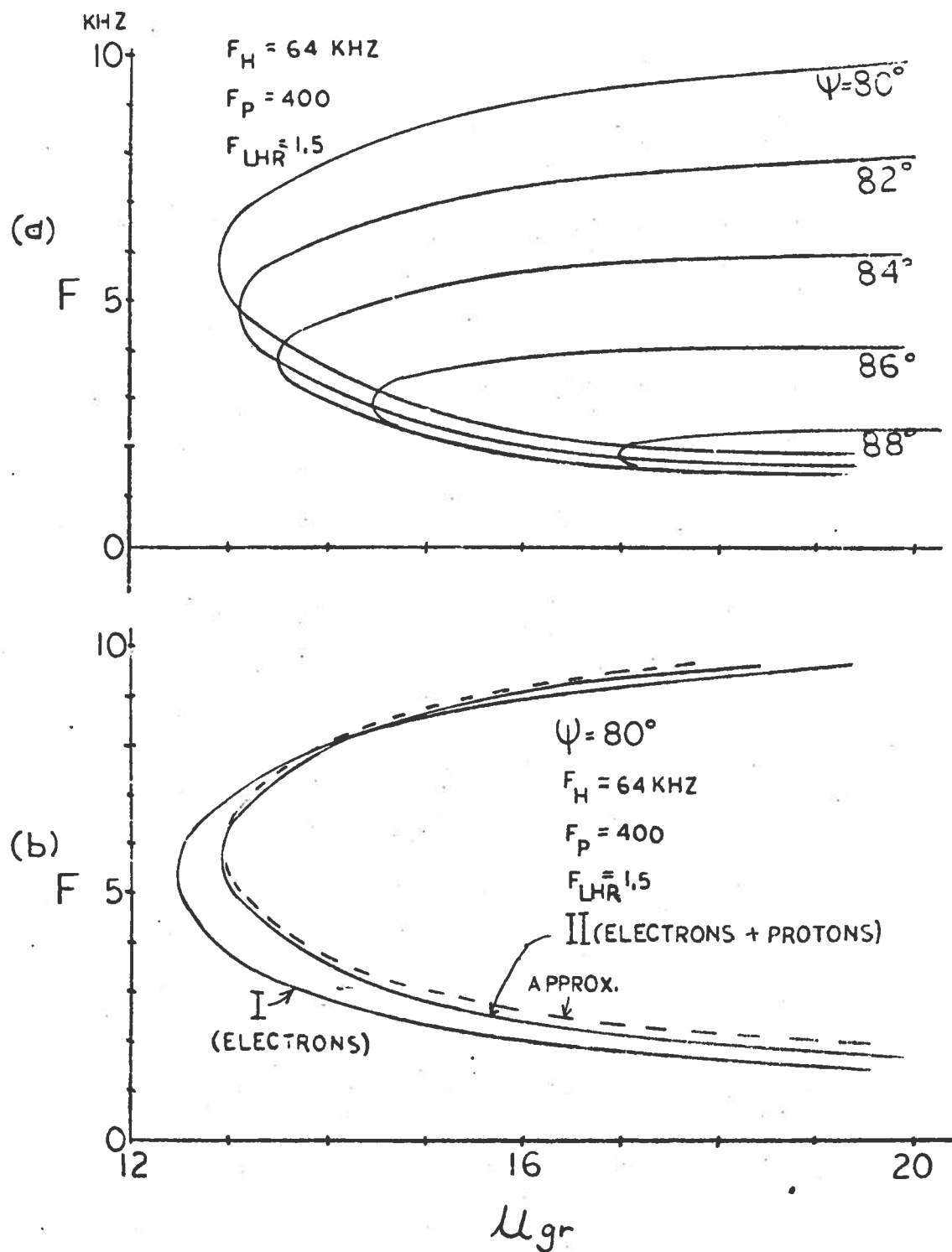


Fig. B.1. (a) GROUP-RAY REFRACTIVE INDEX AS A FUNCTION OF FREQUENCY AND WAVE NORMAL ANGLE. The "nose frequency" occurs at the Gendrin frequency $f = f_H \cos \theta/2$. (b) Comparison of the several expressions for μ_{gr} . The electron μ_{gr} underestimates the true μ_{gr} at the nose frequency; whereas the electron plus proton μ_{gr} approximation is very close to the true μ_{gr} .

and

$$\varphi < \frac{f_H}{2fM} .$$

The group refractive index is

$$\mu_g = \frac{f^2 f_H^M}{p^3} \frac{1}{[\varphi^2 + \Gamma]^{3/2}} ,$$

$\tan \alpha$ is defined as

$$\tan \alpha = \frac{\varphi}{\varphi^2 + \Gamma} \quad (B.7)$$

and the resulting μ_{gr} is

$$\mu_{gr} = \frac{f^2 f_H^M}{p^3} \cdot \frac{1}{[\varphi^2 + \Gamma]^{1/2}} \frac{1}{[(\varphi^2 + \Gamma)^2 + \varphi^2]^{1/2}} \quad (B.8)$$

Appendix C

SIMPLE MODELS OF THE TURNAROUND MECHANISM

The mechanism for the turnaround for an MR whistler ray has been heuristically described in Chapter II. The explanation was based upon computer calculated ray paths. Although the computer approach generates a great deal of digital data, there is a general lack of parameters for classifying the data. The purpose of this appendix is to provide some simple parameters which can describe the types of turnarounds encountered in Chapter II.

1. The Lyons and Thorne Approach

Lyons and Thorne [1970] (designated hereafter as L & T) provided the first good simple approach for modeling the turnaround mechanism. They first derived the plasmaspheric large angle (PLA) approximation for the refractive index which is valid for $f < f_{LHR}$ and $\theta \sim \pi/2$. This expression [Eq. (A.25) in Appendix A] is repeated for reference. Thus,

$$\mu_{pla}^2 = \frac{f_p^2 / f_M}{\phi^2 + \Gamma} \quad (C.1)$$

where

$$\Gamma = \frac{1}{M} \left(\frac{f_H^2}{f_M^2} - 1 \right)$$

The L & T approach assumes a localized magnetosphere in which the magnetic field lines are straight (violating the $\nabla \cdot \vec{B} = 0$ condition) and a uniform high density of protons and electrons. The direction of the magnetic field is taken to be along the x-axis of an x-y coordinate system, in such a way that the magnetic field intensity varies only along the x-axis. In this model the planes of stratification lie parallel to the y-axis. The normal to these planes is then parallel to the magnetic field direction. Snell's law implies that $\mu \sin \theta = \text{constant}$

throughout this region. Since $\theta \doteq \pi/2$, μ must remain constant. From Eq. (C.1), $\phi^2 + \Gamma$ is conserved along the ray path. Thus

$$\phi^2 + \Gamma = \phi_o^2 + \Gamma_o$$

where ϕ_o, Γ_o are defined at some point along the ray path. When $\phi=0$, the condition of turnaround, the quantity $\Gamma_{\max} = \phi_o^2 + \Gamma_o$ defines the maximum travel along a field line for an MR whistler ray path.

Using this model of the magnetosphere L & T investigated the turnarounds associated with the case 1 of Chapter II. The ray path is always assumed to be in a region where $f < f_{\text{LHR}}$. The angle α , defined as the angle between the wave normal direction and the ray direction, is given by

$$\tan \alpha = \frac{1}{\mu} \frac{\partial \mu}{\partial \theta} = \frac{\phi}{\phi^2 + \Gamma} \quad (\text{C.2})$$

The angle ψ between the ray direction and the magnetic field or x-axis is

$$\tan \psi = \tan (\theta - \alpha) = \frac{\Gamma}{\phi(1 + \phi^2 + \Gamma)} \quad (\text{C.3})$$

Tan ψ also gives the instantaneous slope of the ray path in this x-y coordinate system such that

$$\tan \psi = \frac{dy}{dx} = \frac{\Gamma}{\phi(1 + \phi^2 + \Gamma)} \quad (\text{C.4})$$

Since we have not specified exactly the x coordinate, let us use the following

$$\phi_o^2 - \phi^2 = \Gamma - \Gamma_o = \phi_o^2 x \quad ,$$

where

$$x = 0 \Rightarrow \varphi = \varphi_0$$

$$x = 1 \Rightarrow \varphi = 0$$

The above equation becomes

$$\frac{dy}{dx} = \tan \psi_0 \left(\frac{1 + kx^2}{\sqrt{1 - x^2}} \right),$$

where

$$\tan \psi_0 = \frac{\Gamma_0}{\varphi_0 (1 + \varphi_0^2 + \Gamma_0)}, \quad \Gamma_0, \varphi_0 \text{ evaluated at magnetic equator}$$

$$k = \frac{\varphi_0^2}{\Gamma_0}$$

The solution for the ray path equation is

$$y(x) = \tan \psi_0 \left\{ \sin^{-1} x + \frac{k}{2} \left[\sin^{-1} x - x(1 - x^2)^{1/2} \right] \right\}.$$

When $k \ll 1$ at low frequencies, the above equation becomes

$$x = \sin (y \cot \psi_0).$$

The ray paths for $k \ll 1$ depend upon the initial ray direction at the equator and oscillate about the $x = 0$ (y -axis) position in a sinusoidal fashion. The maximum excursion along a field line can be calculated from Γ_{\max} using the expansion

$$f_H = f_{\text{Heq}} \left(1 + \frac{9}{2} \lambda^2 \right)$$

where

$$\lambda = \text{magnetic latitude} < 20^\circ$$

$$f_{\text{Heq}} = f_H \text{ at magnetic equator}$$

The maximum latitude of travel, using the expansion, is

$$\lambda_{\text{max}} = \frac{\phi_o}{3} \cdot \frac{fM}{f_{\text{Heq}}} .$$

If we limit ϕ_o to the range of validity for the refractive index approximation ($\phi \leq f_H/2fM$), we find that λ_{max} is restricted below 10° latitude. The above equation can be extended to show the relation between x and λ , the dipole latitude. After some manipulation we have

$$\lambda = \frac{\phi_o}{3} \frac{fM}{f_{\text{Heq}}} \cdot \sqrt{x} .$$

The solutions for the ray paths are plotted in Fig. C.1 for several values of $f_{\text{Heq}}/f\sqrt{M}$. The minimum value of this ratio is 1.5 if we assume $\phi_o = 1^\circ$ and $\phi_o \leq f_H/2Mf$.

This figure shows that the cross field travel for the low frequencies is very large compared to the cross field penetration for $f \sim f_{\text{LHR}}$. At $f \sim f_{\text{LHR}}$, the ray path is very field aligned. Comparing this result to the ray tracing results of Chapter II, we find that the 1.5 kHz ray in Fig. 2.3 makes a very broad turnaround, but the 4 kHz ray has a very narrow turnaround.

L & T also investigated the effect of gradients upon the curvature of the ray paths. They found that the parallel gradients in the magnetic field intensity had the greatest effect upon ray curvature near turnaround. Other gradients due to field line curvature, density changes, and the change in the magnetic field across field lines were negligible.

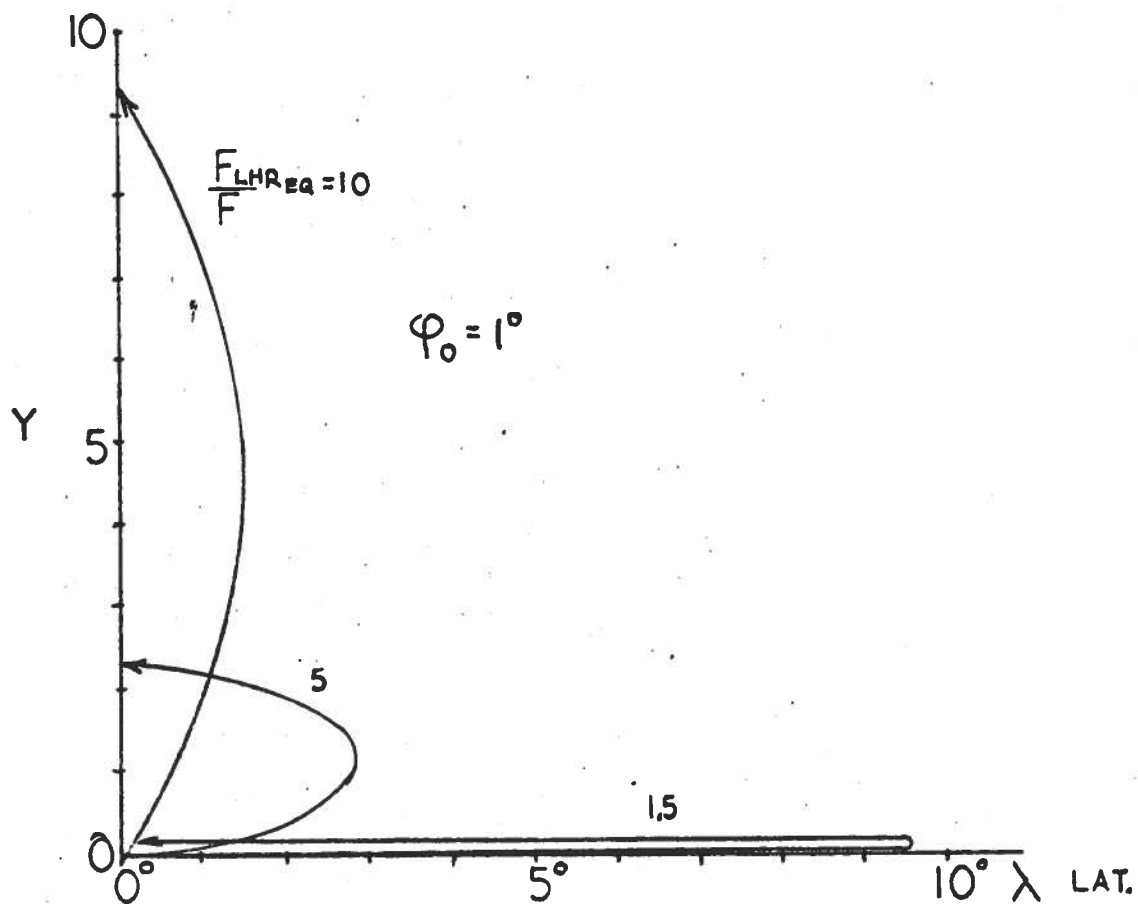


Fig. C.1. PENETRATION OF THE RAY PATH ACROSS AND ALONG THE FIELD USING THE LYONS AND THORNE APPROACH. (λ is latitude along the field line, in degrees, and γ represents distance across the field, in arbitrary units.)

2. Extension of the Lyons and Thorne Approach

One criticism of L & T's work is that they only considered the special case where $f < f_{LHR}$ over most or all of the ray path. This case is not typical of most frequencies observed in the spectral form of MR whistlers. The rays for the great majority of the frequencies observed travel down the field line until the $f = f_{LHR}$ surface is reached. The rays penetrate this surface, reflect, and propagate to a region where $f > f_{LHR}$.

To model this situation we will use the same assumptions as in the previous section, i.e., linear magnetic field, x-y coordinate system and, $\mu = \text{constant}$ along ray path. The big departure is that we will set the x coordinate to be equal to f/f_{LHR} . This choice has the advantage of giving us direct information about the location of the ray along the field line and about approximations which we can use for the refractive index.

Our approach can be outlined as:

- (a) Use the QL approximation for μ whenever ϕ , the wavenormal, is greater than $f_H/2fM$.
- (b) Use the PLA approximation for μ whenever $\phi < f_H/2fM$ and $x < 1$.
- (c) Join the ray path solutions from the two approximations at $\phi = f_H/2fM$.

3. The QL Ray Paths

The QL approximation as given by Eq. (A.20) in Appendix A is

$$\mu^2 = \frac{f_p^2}{f^2} \frac{f}{f_H} \frac{1}{\cos \theta - \frac{\delta f}{f_H}}, \quad (C.5)$$

where

$$\delta = 1 - \frac{f_H^2}{f_M^2}.$$

Tan α from Eq. (B.2) in Appendix B is

$$\tan \alpha = \frac{\sin \theta}{2 \left(\cos \theta - \frac{\delta f}{f_H} \right)} .$$

The angle $\psi = \theta - \alpha$, defined as the angle between the ray direction and the magnetic field on the x-axis is given by

$$\tan (\theta - \alpha) = \frac{\sin \theta (\cos \theta - 2\delta\Lambda)}{1 + \cos \theta (\cos \theta - 2\delta\Lambda)} \quad (C.6)$$

where

$$\Lambda = f/f_H .$$

Since $\theta \approx \pi/2$ in the turnaround region, we define the angle $\varphi = \pi/2 - \theta$ as being our wavenormal angle. Using the approximations that $\sin \theta \doteq 1$ and $\cos \theta \doteq \varphi$, Eq. (C.5) and (C.6) reduce to:

$$\mu^2 \doteq \frac{f^2}{2} \cdot \frac{\Lambda}{\varphi - \delta\Lambda} , \quad (C.7)$$

$$\tan \psi \doteq \varphi - 2\delta\Lambda . \quad (C.8)$$

Since $\mu = \text{constant}$ from Snell's law, we have

$$\frac{\Lambda}{\varphi - \delta\Lambda} = \frac{\Lambda_o}{\varphi_o} = \frac{1}{\epsilon} \quad (C.9)$$

where φ_o , Λ_o are defined at $f = f_{LHR}$. The quantity $\tan \psi$ combined with Eq. (C.9) becomes

$$\tan \psi = \Lambda(\epsilon - 1) + \frac{1}{\Lambda M}$$

Defining our x coordinate as

$$x = \frac{f}{f_{LHR}} = \frac{f}{f_H} M = \Lambda \sqrt{M} , \quad (C.10)$$

we can state

$$\frac{dy}{dx} = \tan \psi = \frac{x}{\sqrt{M}} (\epsilon - 1) + \frac{1}{\sqrt{M}} \frac{1}{x} \quad (C.11)$$

which is the differential equation governing the ray path in the QL region. The solution is

$$\sqrt{M} y = \frac{x^2}{2} (\epsilon - 1) + \ln x + \text{constant} . \quad (C.12)$$

3. Determination of Joining Point

Let us designate $x_1 = \Lambda_1 \sqrt{M}$ as the point where the QL ray path solution is to be joined to the yet to be derived PLA solution. From Snell's law:

$$\frac{\Lambda_1}{\phi_1 - \delta_1 \Lambda_1} = \frac{1}{\epsilon} ,$$

where

$$\phi_1 = \frac{1}{2\Lambda_1 M} , \quad \delta_1 = 1 - \frac{1}{\Lambda_1^2 M} .$$

Solving this equation for x_1^2 , we find

$$x_1^2 = \Lambda_1^2 M = \frac{3}{2(\epsilon + 1)} . \quad (C.13)$$

For $\epsilon \leq .5$, we stop the QL ray calculations at $x = 1$, since for $\epsilon \leq .5$, $x_1 \geq 1$ and the PLA approximation is not good for $x > 1$.

4. The PIA Ray Paths

From the previous section about the L & T approach we know that:

$$\mu^2 = \frac{f^2 p^2 / f^2 M}{\phi^2 + \Gamma} ,$$

where

$$\Gamma = \frac{1}{M} \frac{1}{\Lambda^2 M} - 1 ,$$

and

$$\frac{dy}{dx} = \tan \psi = \frac{\Gamma}{\phi(1 + \phi^2 + \Gamma)} .$$

From Snell's law, $\mu = \text{constant}$ and thus referring everything to the point x_1 we have

$$\phi^2 + \Gamma = \phi_1^2 + \Gamma_1 = \text{constant} .$$

Substituting for ϕ_1 and Γ_1 the appropriate values from the previous section, one obtains

$$\phi^2 + \Gamma = \frac{1}{M} \left[\frac{5}{6} (\epsilon + 1) - 1 \right] \quad (\text{C.14})$$

Designating x_2 as the point where $\phi = 0$, i.e., the turnaround point, Eq. (C.14) becomes

$$\Gamma_2 = \frac{1}{M} \left(\frac{1}{x_2^2} - 1 \right) = \frac{1}{M} \left[\frac{5(\epsilon + 1)}{6} - 1 \right] ,$$

or

$$x_2 = \sqrt{\frac{5(\epsilon + 1)}{6}} . \quad (\text{C.15})$$

Substituting $x = \Lambda\sqrt{M}$ in the equation for $\tan \psi$, we find the following:

$$\frac{dy}{dx} = \frac{\Gamma}{\Phi} = \frac{\frac{1}{M} \left[\frac{1}{x^2} - 1 \right]}{\sqrt{\frac{1}{M} \left[\frac{5(\epsilon - 1)}{6} - \frac{1}{x^2} \right]}}$$

or

$$\frac{dy}{dx} = \frac{1}{\sqrt{M} \sqrt{\frac{5(\epsilon + 1)}{6}}} \left[\frac{1}{x \sqrt{x^2 - \frac{6}{5(\epsilon + 1)}}} - \frac{1}{\sqrt{x^2 - \frac{6}{5(\epsilon + 1)}}} \right] \quad (C.16)$$

The solution for the above differential equation is

$$\sqrt{M} y = \frac{1}{\sqrt{\frac{5(\epsilon + 1)}{6}}} \left[\frac{1}{\sqrt{\frac{6}{5(\epsilon + 1)}}} \cos^{-1} \frac{1}{x} \sqrt{\frac{6}{5(\epsilon + 1)}} - \sqrt{x^2 - \frac{6}{5(\epsilon + 1)}} \right] + \text{constant} . \quad (C.17)$$

The above equation is plotted for several values of ϵ in Fig. C.2.

5. Estimation of Turnaround Time

Looking at the group ray refractive index for the PLA μ in Appendix B, we find that

$$\mu_{gr} = \frac{f_p f_H^2}{M^{5/2} f^3} \frac{1}{\sqrt{\varphi^2 + \Gamma}} \frac{1}{\sqrt{(\varphi^2 + \Gamma)^2 + \varphi^2}} \quad (C.18)$$

Since by Snell's law $\varphi^2 + \Gamma = \text{constant } (k)$, Eq. (C.18) becomes

$$\mu_{gr} = \frac{f_p f_H^2}{M^{5/2} f^3} \frac{1}{\sqrt{k}} \frac{1}{\sqrt{k^2 + \varphi^2}} .$$

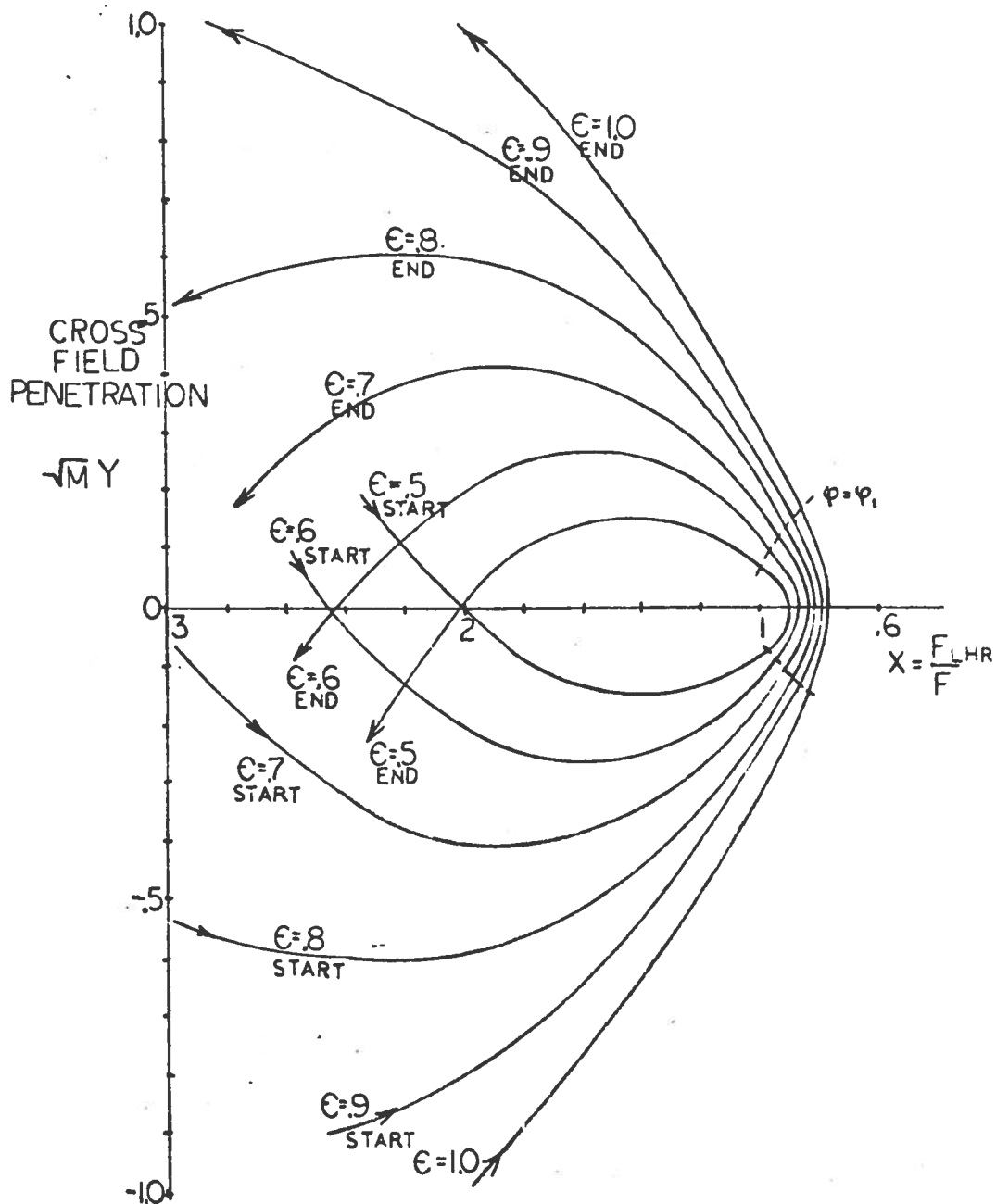


Fig. C.2. PENETRATION OF THE RAY PATHS DURING TURNAROUND ACROSS AND ALONG THE FIELD AS PREDICTED BY THE EXTENSION OF THE L & T APPROACH. The ray paths are centered on each other so that the relative cross field penetration can be compared. The ray paths start at $f/f_{LHR} = 3$. The turnarounds for $\epsilon = .5$ and $\epsilon = .6$ can be considered to be in case III (see Fig. 2.3) in that the ray path loops around on itself. The turnaround for $\epsilon = .8$ would be in case II, and the $\epsilon = .9$ and 1.0 turnarounds would be in case I.

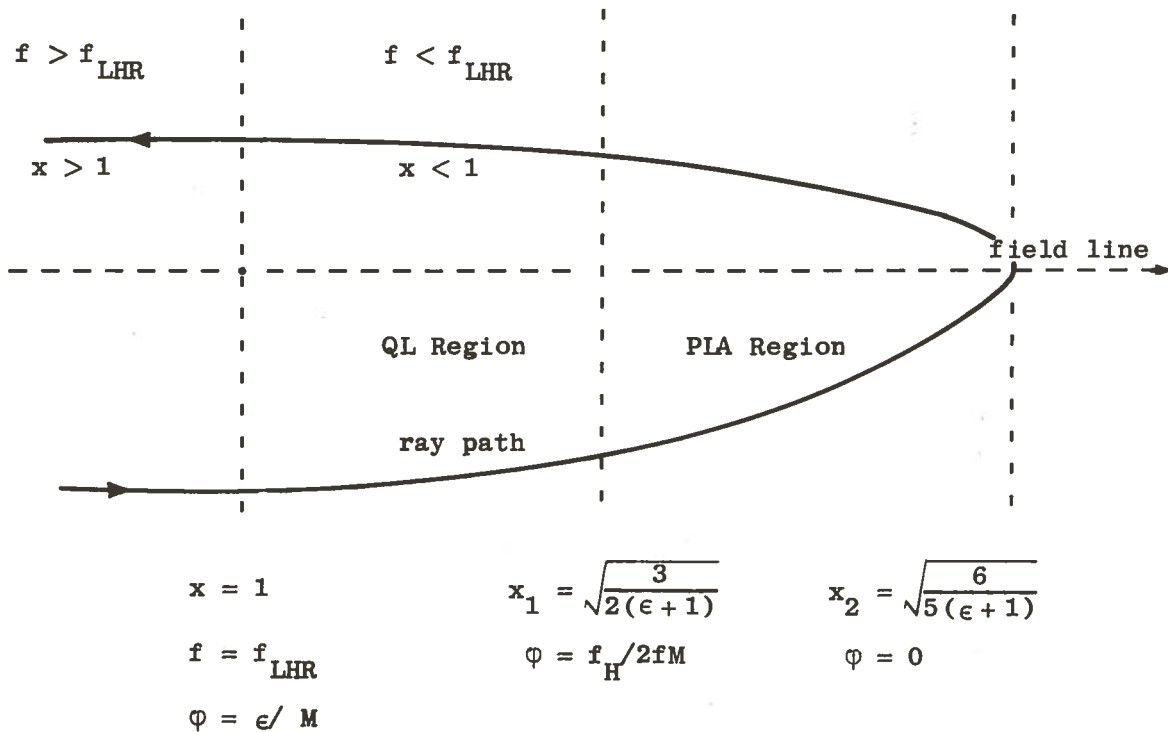
One can see that at $\varphi \sim 0$, μ_{gr} peaks strongly, and thus the ray velocity slows down at the turnaround point. Even though the turnaround takes place in a small region, the slowing down of the ray can not be ignored when calculating time delays for segments of the ray path.

The path for the turnaround region can more or less be considered field aligned, and thus the time delay can be calculated by integrating the μ_{gr} along the field line which is in the center of the ray path.

Since the Lyons and Thorne PLA refractive index form is not valid for $\varphi > f_H/2fM$, let us start the time delay calculations at the $f = f_{LHR}$ surface using the QL approximation. Then we can use the PLA expressions between $\varphi = f_H/2fM$ and $\varphi = 0$ (turnaround point). Using the coordinate system previously explained in this appendix, where

$$x = \frac{f M}{f_H} = \frac{f}{f_{LHR}},$$

we can separate our time delay calculations into their appropriate regions. From Eqs. (C.13) and (C.15) we can show this schematically



6. QL Region Calculations

The group ray refractive index for this region is given by Eq. (B.15) in Appendix B. Thus

$$\mu_{gr} = \frac{f_p}{\sqrt{f} f_H} \frac{\cos \theta + \frac{2f_H}{fM}}{\sqrt{\cos \theta - \delta \frac{f}{f_H}}}$$

Letting $\cos \theta \doteq \varphi$ and $\varphi - \delta f/f_H = \epsilon\lambda$, the above equation becomes

$$\mu_{gr} = \frac{f_p}{f_H} \frac{\epsilon + 1}{\sqrt{\epsilon}} + \frac{f_p f_H}{\sqrt{\epsilon} M f^2} . \quad (C.19)$$

The time delay for the QL region is

$$t_{g1} = \frac{2}{c} \int_{x=1}^{x=\sqrt{\frac{3}{2(\epsilon+1)}}} \mu_{gr} ds , \quad (C.20)$$

where

$$ds = r_0 L \sqrt{1 + 3 \sin^2 \lambda} \cos \lambda d\lambda$$

λ = dipole latitude

$$r_0 = 6370 \text{ km}$$

The expression for ds represents the incremental length along a field line [Angerami and Thomas, 1964].

Along a field line x varies as

$$x = \frac{f\sqrt{M}}{f_H} = \frac{f\sqrt{M}}{f_{Ho}} \frac{L^3 \cos^6 \lambda}{\sqrt{1 + 3 \sin^2 \lambda}} .$$

The function

$$F(\lambda) = \frac{\cos^6 \lambda}{\sqrt{1 + 3 \sin^2 \lambda}}$$

is very close to being a linear function for $20^\circ < \lambda < 35^\circ$. Thus

$$dx = \frac{f\sqrt{ML}^3}{f_{Ho}} \frac{\partial F(\lambda)}{\partial \lambda} d\lambda$$

or

$$dx = \frac{f\sqrt{ML}^3}{f_{Ho}} k_1 d\lambda, \quad k_1 \sim 1.35.$$

Also the function $\sqrt{1 + 3 \sin^2 \lambda} \cos \lambda$ remains almost constant for $20^\circ < \lambda < 35^\circ$. Therefore

$$\cos \lambda \sqrt{1 + 3 \sin^2 \lambda} = k_2 \approx 1.15.$$

The time delay integral Eq. (C.20) now becomes

$$t_{g_1} = \frac{2f}{c} \int_1^{\sqrt{3/2(\epsilon+1)}} \left[\frac{\epsilon + 1}{\sqrt{\epsilon}} \frac{x}{f\sqrt{M}} + \frac{f\sqrt{M}}{x} \frac{1}{Mf^2\sqrt{\epsilon}} \right] \frac{f_{Ho}}{f\sqrt{M}} \frac{r_o}{L^2} \frac{k_2}{k_1} dx.$$

Integrating over the limits of the QL region, we have

$$t_{g_1} = \frac{2f f_{Ho} r_o k_2}{c f^2 M L^2 k_1} \left[\frac{2\epsilon - 1}{4\sqrt{\epsilon}} + \frac{1}{2\sqrt{\epsilon}} \ln \frac{2(\epsilon + 1)}{3} \right] \quad (C.21)$$

7. PIA Region Calculations

From Eq. (C.18), the time delay integral for the PIA region is

$$t_{g_2} = \frac{2}{c} \int_{\sqrt{3/2(\epsilon+1)}}^{\sqrt{6/5(\epsilon+1)}} \frac{f_p f_H^2}{f_M^{3/2}} \frac{1}{\sqrt{\varphi^2 + \Gamma}} \frac{1}{\sqrt{(\varphi^2 + \Gamma)^2 + \varphi^2}} ds$$

Following the procedure of the QL region calculations, we have

$$dx = \frac{f\sqrt{M}}{f_{Ho}} L^3 k_1 d\lambda ,$$

$$ds = r_o L \sqrt{1 + 3 \sin^2 \lambda} \cos \lambda d\lambda .$$

From Snell's law,

$$\varphi^2 + \Gamma = \varphi_1^2 + \Gamma_1 = \frac{1}{M} \left[\frac{5}{6} (\epsilon + 1) - 1 \right] ,$$

and

$$\left(\varphi_1^2 + \Gamma_1 \right)^2 + \varphi^2 = \frac{\frac{5}{6} (\epsilon + 1)}{Mx^2} \left[x^2 - \frac{1}{\frac{5}{6} (\epsilon + 1)} \right] .$$

The time delay integral now becomes

$$t_{g_2} = \frac{2}{c} \frac{f_p}{f^2} \int_{\sqrt{3/2(\epsilon+1)}}^{\sqrt{6/5(\epsilon+1)}} \frac{r_o f_{Ho}}{M^2 L^2} \frac{k_2}{k_1} \frac{1}{\sqrt{\frac{5}{6} (\epsilon + 1) - 1}} \frac{1}{\sqrt{\frac{5}{6} (\epsilon + 1)}} x \frac{dx}{\sqrt{x^2 - \frac{1}{\frac{5}{6} (\epsilon + 1)}}}$$

or

$$t_{g_2} = \frac{2}{c} \frac{f_p f_{Ho} r_o}{f^2 M L^2} \frac{k_2}{k_1} \frac{1}{\sqrt{\frac{5}{6} (\epsilon + 1) - 1}} \cos^{-1} (4/5) \quad (C.22)$$

Combining Eq. (C.21) and (C.22) gives the total time delay for the turnaround. Thus

$$t_g = t_{g_1} + t_{g_2} = \frac{2f_p f_{Ho} r k_2}{cf^2 ML^2 k_1} \left[\frac{.47}{\sqrt{\frac{5}{6}(\epsilon + 1)} - 1} + \frac{2\epsilon - 1}{4\sqrt{\epsilon}} + \frac{1}{2\sqrt{\epsilon}} \ln \frac{2(\epsilon + 1)}{3} \right] \quad (C.23)$$

for $\epsilon \geq .5$.

For $\epsilon \leq .5$, ϕ is always less than $f_H/2fM$. Thus at $x = 1$, we can use the PIA approximations. From Snell's law

$$\phi^2 + \Gamma = \phi_o^2 + \Gamma_o \Big|_{x=1} = \phi_o^2 ,$$

$$\Gamma_{\max} = \phi_o^2 ,$$

or

$$x_{\min}^2 = \frac{1}{M\phi_o^2 + 1} = \frac{1}{\epsilon^2 + 1}$$

Since the time delay integral is almost the same as the processing section, we will only quote the results.

$$t_g = \frac{2f_p f_{Ho} r k_2}{cf^2 ML^2 k_1} \frac{1}{\epsilon} \cos^{-1} \frac{1}{\sqrt{\epsilon^2 + 1}}$$

for $\epsilon \leq .5$.

At $\epsilon = .5$, the solutions match up as

$$x_2^2 \Big|_{\epsilon=.5} = \frac{6}{5(\epsilon + 1)} \Big|_{\epsilon=.5} = .8 ,$$

$$x_{\min}^2 \Big|_{\epsilon=.5} = \frac{1}{\epsilon^2 + 1} \Big|_{\epsilon=.5} = .8 ,$$

and

$$\frac{1}{\epsilon} \cos^{-1} \frac{1}{\sqrt{\epsilon^2 + 1}} \Big|_{\epsilon=.5} = \frac{.47}{\sqrt{\frac{5}{6} (\epsilon + 1) - 1}} \Big|_{\epsilon=.5} = .94$$

As $\epsilon \rightarrow 0$,

$$\frac{1}{\epsilon} \cos^{-1} \frac{1}{\sqrt{1 + \epsilon^2}} \rightarrow 1 \quad \text{and} \quad t_g \Big|_{\epsilon \rightarrow 0} = \frac{2f f_{\text{Ho}} r_o k_1}{c f_{\text{ML}}^2 k_2} . \quad (\text{C.24})$$

The comparison of the theory with ray tracing results is illustrated in Fig. C.3.

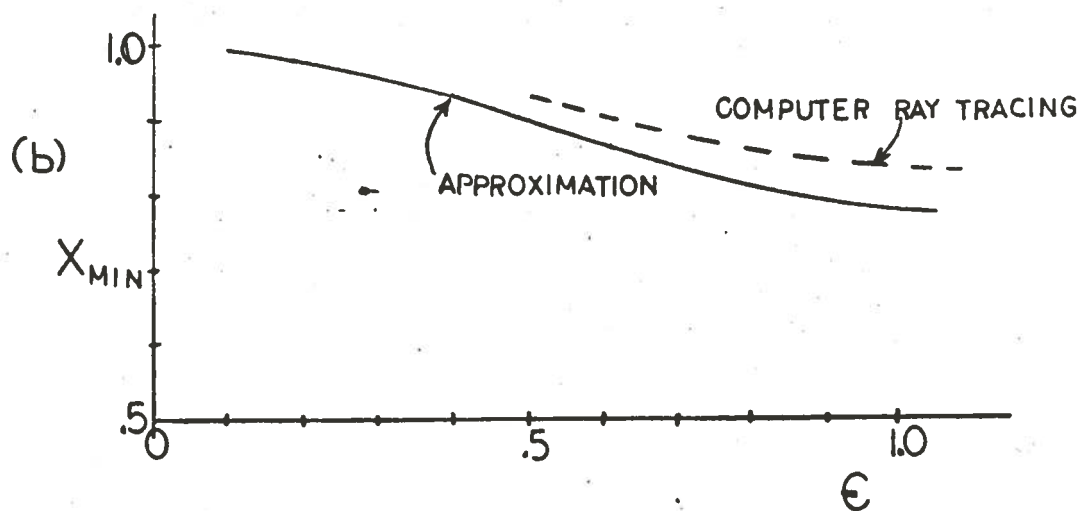
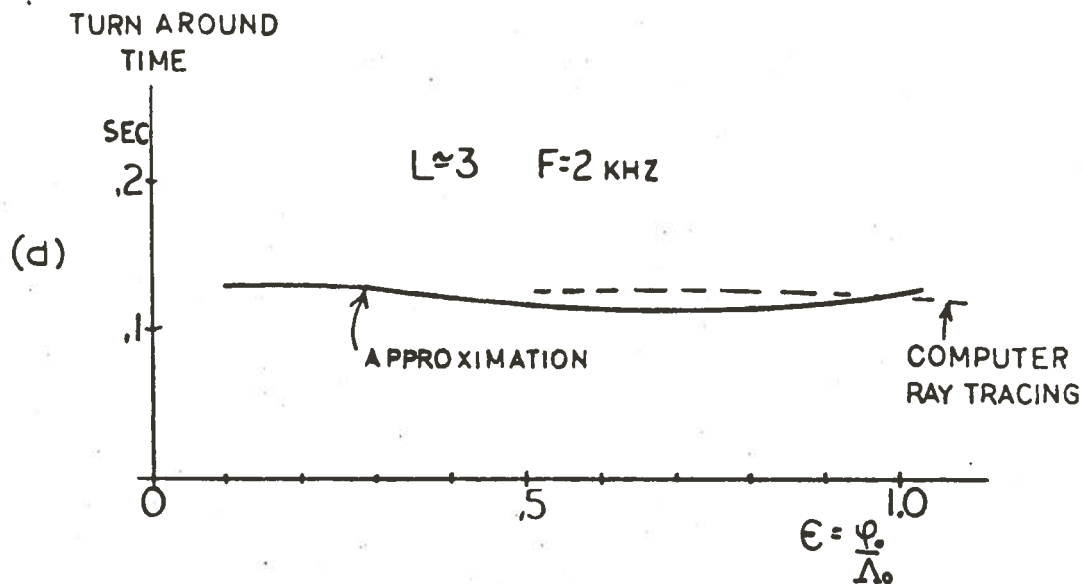


Fig. C.3. (a) TURNAROUND TIMES COMPARED USING RAY TRACING RESULTS AND OUR APPROXIMATE EXPRESSIONS (C.23) AND (C.24). Notice they are almost invariant with variations of ϵ . (b) The comparison of the maximum penetration of the ray path along a field line during turnaround as computed by ray tracing and from Eq. (C.15). The discrepancy is due to the fact that the dipole field used in the ray tracing calculations gives a different plane of stratification configuration than in our simple model.

Appendix D

DETERMINATION OF THE PLANE OF STRATIFICATION

As we have seen in Chapter II, the application of Snell's law depends on the normal to the plane of stratification. This appendix will outline a method of determining this normal direction. The plane of stratification is that plane specified geometrically by the normal direction. As given by Walter [1969], the plane of stratification for a given wave normal direction "is found by looking for the locus of points which have the same phase refractive index holding the direction of the wave normal constant." Since the local plane of stratification is the surface where $\mu = \text{constant}$, the normal to that surface is given by the local gradient of μ . However, since the wave normal direction is held constant, the calculation of the local gradient is slightly different from the usual ∇ (del) operator type of gradient. In a polar coordinate system, the gradient $\tilde{\nabla}\mu$ (given by Eq. (F.18) of Walter [1969]) can be written as

$$\tilde{\nabla}\mu = \left. \frac{\partial\mu}{\partial r} \right|_{\theta, \psi} \vec{a}_r + \frac{1}{r} \left(\left. \frac{\partial\mu}{\partial \theta} \right|_{r, \psi} - \frac{\partial\mu}{\partial \psi} \right|_{r, \theta} \right) \vec{a}_\theta \quad (\text{D.1})$$

for a dipole magnetic field. In this equation

r = radial distance

θ = colatitude (polar angle measured from the north magnetic pole)

ψ = angle between the magnetic field direction and the wave normal ("wave normal angle")

$\vec{a}_r, \vec{a}_\theta$ = unit vectors in a polar system

1. Finding $\tilde{\nabla}\mu$ in Magnetospheric Models

The electron density in a simple diffusive equilibrium model of the magnetosphere is given by [Angerami and Thomas, 1964] as

$$N = N_0 e^{-Z/2H} , \quad (D.2)$$

where

$$Z = (r_b/r)(r - r_b)$$

r_b = radial distance to the reference level (base)

$$H = \text{scale height at } r_b = KT/m_e g$$

N_0 = electron density at r_b , assumed here independent of latitude

The gyrofrequency of the dipole magnetic field is

$$f_H = f_{Ho} \left(\frac{r_e}{r} \right)^3 \sqrt{1 + 3 \cos^2 \theta} , \quad (D.3)$$

where

f_H = electron gyrofrequency

r_e = earth's radius = 6370 km

f_{Ho} = gyrofrequency at earth's magnetic equator = 870 kHz

The QL electron approximation for μ from Appendix A is given by

$$\mu = \frac{f_p}{\sqrt{f_H f}} \frac{1}{\sqrt{\cos \psi - f/f_H}} , \quad (D.4)$$

where f_p = plasma frequency (kHz) $\sim 9/N$, N in $\text{el} \cdot \text{cm}^{-3}$. The quantities $\partial\mu/\partial r$ and $\partial\mu/\partial\theta$ of Eq. (D.1) are given by

$$\frac{\partial\mu}{\partial r} = \frac{\partial\mu}{\partial f_p} \frac{\partial f_p}{\partial r} + \frac{\partial\mu}{\partial f_H} \frac{\partial f_H}{\partial r} , \quad (D.5)$$

$$\frac{\partial\mu}{\partial\theta} = \frac{\partial\mu}{\partial f_H} \frac{\partial f_H}{\partial\theta} ,$$

and

$$\left. \begin{aligned}
 \frac{\partial f_p}{\partial r} &= -f_p \frac{1}{4H} \left(\frac{r}{r}\right)^2 \\
 \frac{\partial f_H}{\partial r} &= -\frac{3f_H}{r} \\
 \frac{\partial f_H}{\partial \theta} &= -\frac{3f_H \cos \theta \sin \theta}{(1 + 3 \cos^2 \theta)} \\
 \frac{\partial \mu}{\partial f_p} &= \frac{\mu}{f_p} \\
 \frac{\partial \mu}{\partial f_H} &= \frac{\mu}{f_H} \frac{-\frac{1}{2} \cos \psi}{\cos \psi - f/f_H} \\
 \frac{\partial \mu}{\partial \psi} &= +\frac{\mu}{2} \frac{\sin \psi}{\cos \psi - f/f_H}
 \end{aligned} \right\} \quad (D.6)$$

Combining (D.5) and (D.6) and substituting the appropriate quantities in Eq. (D.1) gives

$$\tilde{\nabla}_\mu = A_r \vec{a}_r + A_\theta \vec{a}_\theta$$

where

$$A_r = \frac{\partial \mu}{\partial r} = -\frac{\mu}{4H} \left(\frac{r}{r}\right)^2 + \frac{\mu}{r} \frac{\frac{3}{2} \cos \psi}{\cos \psi - f/f_H}$$

$$A_\theta = \frac{1}{r} \left(\frac{\partial \mu}{\partial \theta} - \frac{\partial \mu}{\partial \psi} \right) = \frac{3\mu}{2r} \frac{\cos \psi \cos \theta \sin \theta}{(\cos \psi - f/f_H)(1 + 3 \cos^2 \theta)} - \frac{\mu \sin \psi}{2r(\cos \psi - f/f_H)}$$

Defining β as the angle between $\tilde{\nabla}\mu$ and the radius vector \bar{r} , $\tan \beta$ is determined by

$$\tan \beta = \frac{A_\theta}{A_r} = \frac{\frac{3}{2} \frac{\cos \psi \cos \theta \sin \theta}{(\cos \psi - f/f_H)(1 + 3 \cos^2 \theta)} - \frac{1}{2} \frac{\sin \psi}{(\cos \psi - f/f_H)}}{\frac{3}{2} \frac{\cos \psi}{(\cos \psi - f/f_H)} - \frac{r_b^2}{4Hr}} \quad (D.7)$$

Example 1

Letting $\cos \psi \doteq 2f/f_H$ for the Gendrin condition gives

$$\tan \beta = \frac{\frac{3}{2} \cdot \frac{2 \cos \theta \sin \theta}{1 + 3 \cos^2 \theta} - \frac{1}{2} \frac{\sin \psi}{f/f_H}}{3 - \frac{r_b^2}{4Hr}}$$

We can now look at the relative magnitudes of the terms.

$$\text{For all } \theta, \quad \frac{\sin \theta \cos \theta}{1 + 3 \cos^2 \theta} \leq 24$$

For $r > 12,000$ km, and a temperature of $\sim 1000^\circ\text{K}$,

$$\frac{r_b^2}{4Hr} \leq \sim \frac{(7,000)^2}{4 \times 1,000 \times 12,000} \sim 1.$$

$$\text{For the MR whistler case } \frac{f}{f_H} \ll .1,$$

which means $\sin \psi \sim 1.0$. Thus the expression is dominated by the anisotropy term $(1/2)[\sin \psi/(f/f_H)]$, which is at least an order of magnitude greater than any of the other terms. For typical point at $L \sim 2.5$, $\theta = 120^\circ$ (-30° latitude) and $f \sim 2$ kHz ($f/f_H = .01$), $\tan \beta \cong 50$, which means $\beta \sim 89^\circ$. Thus $\tilde{\nabla}\mu$ is perpendicular to the radius vector and the plane of stratification lies along the radius vector for this case.

BIBLIOGRAPHY

- Allis, W. P., S. J. Buchsbaum and A. Bers, Waves in Anisotropic Plasmas, MIT Press, Cambridge, Mass., 1963.
- Angerami, J. J., "Whistler Duct Properties Deduced from VLF Observations Made with the OGO-3 Satellite Near the Magnetic Equator," J. Geophys. Res. 75, 6115, 1970.
- Angerami, J. J. and D. L. Carpenter, "Whistler Studies of the Plasmapause in the Magnetosphere-2; Equatorial Density and Total Tube Electron Content Near the Knee in Magnetospheric Ionization," J. Geophys. Res. 71, 711, 1966.
- Angerami, J. J. and J. O. Thomas, "Studies of Planetary Atmosphere, 1, the Distribution of Electrons and Ions in the Earth's Exosphere," J. Geophys. Res. 69, 4537, 1964.
- Bauer, S. J. and B. V. Krishnamurthy, "Behavior of the Topside Ionosphere During a Great Magnetic Storm," Planet. Space Sci. 16, 653, 1968.
- Brace, L. H. and B. M. Reddy, "Early Electrostatic Probe Results from Explorer 22," J. Geophys. Res. 70, 5783, 1965.
- Brace, L. H., B. M. Reddy and H. G. Mayr, "Global Behavior of the Ionosphere at 1000 km Altitude," J. Geophys. Res. 72, 265, 1967.
- Brice, N. M. and R. L. Smith, "Recordings from Satellite Alouette 1, a Very-Low-Frequency Plasma Resonance," Nature 203(4948), 926, Aug 29, 1964.
- Carpenter, D. L., "Whistler Studies of the Plasmapause in the Magnetosphere," J. Geophys. Res. 71, 693, 1966.
- Colin, L. and K. L. Chan, "Global Electron Density Distributions from Topside Soundings," IEEE Proc. 57, 990, 1969.
- Gendrin, R., "Le Guidage des Whistlers par le Champ Magnetique," Planet. Space Sci. 5, 274, 1961.
- Gold, T., "Motions in the Magnetosphere of the Earth," J. Geophys. Res. 64, 1219, 1959.
- Grebowsky, J. M., N. K. Rahman, and H. A. Taylor, Jr., "Comparison of Coincident OGO 3 and OGO 4 Hydrogen Ion Composition Measurements," Planet. Space Sci. 18, 965, 1970.
- Grossi, M. D. and Victor H. Padula-Pintos, "Ground-Based Radio Sounding of the Earth Magnetosphere," J. Geophys. Res. 76, 3755, 1971.

- Haselgrove, J., "Ray Theory and a New Method of Ray Tracing," Rept. of the Physical Society Conference on Physics of the Ionosphere, Cambridge, England, pp. 355-364, Sep 1954.
- Helliwell, R. A., Whistlers and Related Ionospheric Phenomena, Stanford University Press, Stanford, Calif., 1965.
- Hines, C. O., "Heavy-Ion Effects in Audio-Frequency Radio Propagation," J. Atmos. and Terr. Phys. 11, 36, 1957.
- Jensen, D. C. and J. C. Cain, "An Interim Geomagnetic Field," J. Geophys. Res. 67, 3568, 1962.
- Kimura, I., "Effects of Ions on Whistler-Mode Ray Tracing," Radioscience 1, 269, 1966.
- Lyons, L. R. and R. M. Thorne, "The Magnetospheric Reflection of Whistlers," Planet. Space Sci. 18, 1753, 1970.
- Mayr, H. G., L. H. Brace and G. S. Dunham, "Ion Composition and Temperature in the Topside Ionosphere," J. Geophys. Res. 72, 4391, 1967.
- McIlwain, C. E., "Coordinates for Mapping the Distribution of Magnetically Trapped Particles," J. Geophys. Res. 66, 3681, 1961.
- Park, C. G., "Whistler Observations of the Interchange of Ionization Between the Ionosphere and Protonosphere," J. Geophys. Res. 75, 4249, 1970.
- Parker, E. N., Interplanetary Dynamical Processes, Interscience Publishers, New York, 1963.
- Poeeverlein, H., Strahlwege von Radiowellen in der ionosphäre, Sitzber. Bayer, Akad. Wiss., 1948.
- Ratcliffe, J. A., Magneto-Ionic Theory and Its Application to the Ionosphere, Cambridge University Press, Cambridge, England, 1959.
- Scarabucci, R. R., "Interpretation of VLF Signals Observed on the OGO-4 Satellite," Ph.D. Dissertation, Stanford University, Stanford, Calif., Oct 1969.
- Shkarofsky, I. P., "Accuracy of Langmuir Probe Measurements and Skin Potential on Satellites," J. Geophys. Res. 76, 3746, 1971.
- Smith, R. L., "Propagation Characteristics of Whistlers Trapped in Field-Aligned Columns of Enhanced Ionization," J. Geophys. Res. 66, 3699, 1961.
- Smith, R. L., "A Comment on Ray Tracing in an Anisotropic Medium," Radio Science 3, 13, 1968.

- Smith, R. L. and J. J. Angerami, "Magnetospheric Properties Deduced from OGO-1 Observations of Ducted and Nonducted Whistlers," J. Geophys. Res. 73, 1, 1968.
- Smith, R. L. and N. Brice, "Propagation in Multicomponent Plasmas," J. Geophys. Res. 69, 5029, 1964.
- Smith, R. L., R. A. Helliwell and I. W. Yabroff, "A Theory of Trapping of Whistlers in Field-Aligned Columns of Enhanced Ionization," J. Geophys. Res. 65, 815, 1960.
- Stix, T. H., The Theory of Plasma Waves, McGraw-Hill, New York, 1962.
- Sugiura, M. and S. Cain, Provisional Hourly Values of Equatorial Dst for 1964, 1965, 1966, and 1967, NASA-TN-D-5748, NASA/GSFC, Greenbelt, Md., May 1970.
- Taylor, H. A., Jr., H. C. Brinton and C. R. Smith, "Positive Ion Composition in the Magnetosphere Obtained from the OGO-A Satellite," J. Geophys. Res. 70, 5769, 1965.
- Taylor, H. A., Jr., H. C. Brinton and M. W. Pharo, III, "Contraction of the Plasmasphere During Geomagnetically Disturbed Periods," J. Geophys. Res. 73, 961, 1968a.
- Taylor, H. A., Jr., H. C. Brinton, M. W. Pharo, III, and N. K. Rahman, "Thermal Ions in the Exosphere; Evidence of Solar and Geomagnetic Control," J. Geophys. Res. 73, 5521, 1968b.
- Taylor, H. A., Jr., H. C. Brinton, and A. R. Deshmukh, "Observations of Irregular Structure in Thermal Ion Distributions in the Dusk-side Magnetosphere," J. Geophys. Res. 75, 2481, 1970.
- Taylor, H. A., Jr., J. M. Grebowsky and W. J. Walsh, "Structured Variations of the Plasmopause: Evidence of a Co-Rotating Plasmatail," J. Geophys. Res. 76, 6806, 1971.
- Thorne, R. M., "Unducted Whistler Evidence for a Secondary Peak in the Electron Energy Spectrum Near 10 keV," J. Geophys. Res. 73, 4895, 1968.
- Thorne, R. M. and C. F. Kennel, "Quasi-Trapped VLF Propagation in the Outer Magnetosphere," J. Geophys. Res. 72, 857, 1967.
- Walter, F., "Nonducted VLF Propagation in the Magnetosphere," Ph.D. Dissertation, Stanford University, Stanford, Calif., Oct 1969.
- Wang, T. N. C., "VLF Input Impedance Characteristics of an Electric Antenna in a Magnetoplasma," Ph.D. Dissertation, Stanford University, Stanford, Calif., May 1970.
- Yabroff, I., "Computation of Whistler Ray Paths," J. Res. NBS, D. 65D, 485, Sep-Oct 1961.

